Measurement of the W Boson Polarisation in $t\bar{t}$ Dilepton Events at $\sqrt{s} = 8$ TeV with the ATLAS Detector

Dissertation

zur Erlangung des mathematisch-naturwissenschaftlichen Doktorgrades
„Doctor rerum naturalium“
der Georg-August-Universität Göttingen

im Promotionsprogramm ProPhys
der Georg-August University School of Science (GAUSS)

vorgelegt von

Gvantsa Mchedlidze

aus Tiflis, Georgien

Göttingen, 2018

Betreuungsausschuss

Prof. Dr. Arnulf Quadt
Prof. Dr. Kevin Kröninger
Dr. Elizaveta Shabalina

Mitglieder der Prüfungskommission:

Referent:	Prof. Dr. Arnulf Quadt II. Physikalisches Institut, Georg-August-Universität Göttingen
Koreferentin:	Prof. Dr. Stanley Lai II. Physikalisches Institut, Georg-August-Universität Göttingen

Weitere Mitglieder der Prüfungskommission:

PD. Dr. Ralf Bernhard
II. Physikalisches Institut, Georg-August-Universität Göttingen

Prof. Dr. Laura Covi
Institut für Theoretische Physik, Georg-August-Universität Göttingen

Prof. Dr. Wolfram Kollatschny
Institut für Astrophysik, Georg-August-Universität Göttingen

Prof. Dr. Steffen Schumann
Institut für Theoretische Physik, Georg-August-Universität Göttingen

Tag der mündlichen Prüfung: 19.10.2018

Referenz: II.Physik-UniGö-Diss-2019/07

Measurement of the W Boson Polarisation in the $t\bar{t}$ Dilepton Events at $\sqrt{s} = 8$ TeV with the ATLAS Detector

Abstract

A measurement of the W boson polarisation in top quark decays is presented. The top anti-top pairs were produced at a centre of mass energy of $\sqrt{s} = 8$ TeV using proton-proton collisions at the LHC. The data sample corresponds to an integrated luminosity of $\int \mathcal{L} dt = 20.2$ fb^{-1} recorded by the ATLAS detector in 2012. The measurement was performed in the dilepton channel, which is characterised by two leptons (electron or muon) with opposite electric charge, missing transverse energy from two neutrinos, and at least two jets. One of these jets is required to be tagged as b jet. The W boson polarisation was studied using the angular distribution of the charged lepton in the rest frame of the W boson. The event is fully reconstructed using a kinematic reconstruction method. The three existing W boson polarisation state fractions are longitudinal, left-handed, and right-handed. The fractions were estimated from the data distribution using a binned likelihood fit. The W boson helicity fractions are obtained from a combined likelihood fit separately for different requirements on b-tag jet multiplicity. The best precision is obtained by requiring at least two $b-$tag jets at the final state. The corresponding fractions yield

$$
\begin{aligned}
F_0 &= 0.695 \pm 0.014(\text{stat.+bkg})^{+0.023}_{-0.024}\ (\text{syst.}),\\
F_L &= 0.291 \pm 0.009(\text{stat.+bkg})^{+0.011}_{-0.010}\ (\text{syst.}),\\
F_R &= 0.012 \pm 0.006(\text{stat.+bkg})^{+0.020}_{+0.021}\ (\text{syst.}).
\end{aligned}
$$

As the polarisation of the W bosons in top quark decays is sensitive to the Wtb vertex structure, limits on anomalous Wtb couplings are set. All results are in good agreement with the Standard Model predictions.

Contents

CHAPTER 1

Introduction

From ancient times, human being had an aspiration of explaining the behavior of nature. The understanding of one phenomenon rises other questions. As much as knowledge increases mankind realises how scarce it is. The fundamental questions like "How and when was the universe created?" and "What is it made of?" were the inspiration of going deeper and deeper into structure of matter and the era of particle physics began in the 19th century with the discovery of the electron. Numerous hadrons were discovered using cosmic rays as a source of high energetic particles produced in outer space. However, dramatic progress was made after design and construction of high energy particle accelerators and detectors, where more and more particles were discovered. Each new particle accelerator and detector helped answer the fundamental questions with better precision. A theory was needed which could describe the underlying structure behind the number of particles, that seems to be chaotic at first impression.
The Standard Model (SM) is the most successful theory in describing elementary particles and their interactions. In this theory, fundamental particles are classified as *fermions* (three generations of quarks and the same for leptons) and *bosons* as mediators of their interactions. The top quark is the heaviest elementary particle predicted by the Standard Model with a mass close to electroweak symmetry breaking scale. It is also the quark with the strongest Yukawa coupling, therefore the top quark is a very good "laboratory" to look for physics beyond the Standard Model. Only the high energy particle colliders are able to create such heavy particles. Therefore, the top quark was discovered only in 1995 by the CDF and D$\emptyset$ experiments at the Tevatron collider, and confirmed the three-generation structure of fundamental particles of the Standard Model. Due to it's high mass, the top quark decays before it can hadronise, therefore its properties, like charge and spin, are directly transferred to the decay products. By measuring these decay products, it is possible to answer fundamental questions about the structure of top quark decay vertices and the nature of its couplings.

In the Standard Model, the top quark almost exclusively decays into a W boson and a b quark. The decay vertex Wtb has *vector* minus *axial-vector* structure. This vertex structure could by modified by new physics processes beyond the Standard Model, therefore a precision measurement of the Wtb vertex is crucial. One possible way of testing the Wtb vertex is performing W boson polarisation measurements in pair production of top and anti-top quarks. Several properties of the top quark have already been explored by the Tevatron experiments like the mass, the charge, its lifetime, and the production cross sections. The structure of the Wtb vertex was also investigated together with the measurements of the W boson polarisation fractions. The centre of mass energy and the collected luminosity did not allow for precise measurements of these properties, except for the mass. At the Large Hadron Collider (unlike the Tevatron) the total production cross section of top-quark pair production is dominated by the gluon fusion process. According to the SM, top quarks can also be produced significantly through electroweak single top production. The data were taken at centre of mass energies of 7 and 8 TeV with integrated luminosities of 4.57 fb^{-1} and 20.2 fb^{-1}, respectively. Nowadays, the centre of mass energy has reached 13 TeV[1]. The aim of this thesis is to measure W boson polarisation fractions in top anti-top pairs ($t\bar{t}$) with dileptonic final states. The data has been recorded by the ATLAS experiment at a centre of mass energy of $\sqrt{s} = 8$ TeV using proton proton (pp) colliding beams at the Large Hadron Collider. In Chapter 2, the fundamental particles of the Standard model and the fundamental forces with the focus on the top quark physics and its decay vertex are introduced; Chapter 3 briefly describes the Large Hadron Collider and dedicated experiments on it, by focusing on the ATLAS experiment. The identification and reconstruction of the physics objects is given in Chapter 4, and followed by Chapter 5 with the description of the signal and background modelling using Monte Carlo simulation. The event selection and characteristics of full $t\bar{t}$ system reconstruction in the dilepton channel is given in Chapter 6. The strategy of the analyses and also study, evolution, and results of statistical and systematic uncertainties are given in Chapter 7. The results are summarised and discussed in Chapter 8.
Through this thesis, natural units are used ($\hbar = c = 1$) and, unless stated otherwise, energies, masses and momenta will be given in GeV.

[1]The design centre of mass energy is 14 TeV with instantaneous luminosity $10^{34}\text{cm}^{-2}\text{s}^{-1}$.

CHAPTER 2

Theoretical Overview

The Standard Model (SM) [1–5] has a great success in describing the available particle physics experimental data. Nevertheless, there is the necessity of existence of physics beyond the SM (BSM) to explain basic observations like gravity which could be hidden in the uncertainties of the experimental measurements. The top quark is the heaviest known elementary particle, which makes it the most difficult to produce. At LHC energies, the top quark production rate is high enough and its properties are studied with good precision. The following chapter reviews briefly the most relevant theoretical aspects to this work. Section 2.1 describes the SM, while Section 2.2 is dedicated to the top quark, focusing on its properties, decay modes and production mechanisms.

2.1. The Standard Model of Particle Physics

The Standard Model of particle physics is the theory that includes the best understanding of elementary particles [1], the fundamental forces, and their interactions. The basic concept of the SM is local gauge symmtery, the underlying gauge groups for electroweak and strong interactions are $SU(3) \times SU(2) \times U(1)$. The field theory with local symmetry breaking of the $SU(2) \times U(1)$ group, proposed by Glashow [1], Salam [2] and Weinberg [3], is known as the model of the electroweak interactions. This theory unifies the weak and the electromagnetic interactions. The strong interaction is described in a similar way by using the $SU(3)$ symmetry group [4].

[1] the particles without any substructure.

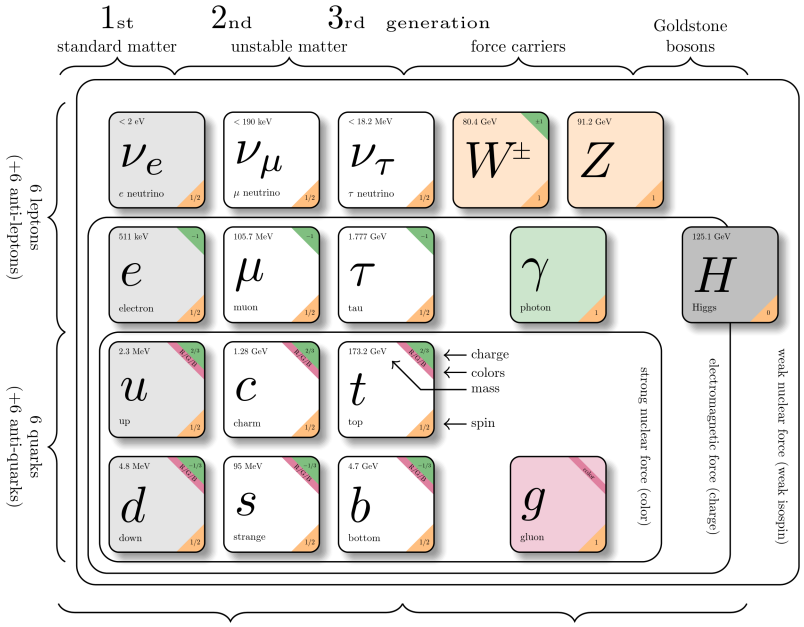

Figure 2.1.: Fermions and gauge bosons of the Standard Model and some of their basic properties.

Elementary Particles

The elementary particles are classified as matter particles, *fermions* (with spin $\frac{1}{2}$) and force mediator by gauge *bosons* (with spin 1). The *fermions* are divided in two groups: quarks interacting via the strong interaction and leptons which do not interact via the strong force. Quarks and leptons can be grouped into three generations (or families) as shown in Figure 2.1 which also contains the charges and masses of the particles. The difference in generations is the mass of the particles. The first generation particles are the lightest and the most stable while the second and the third generation are heavier and less stable. In each generation, quarks are paired as: "up type" quark with electric charge of $Q = +\frac{2}{3}e$[2] and its partner "down type" quark with $Q = -\frac{1}{3}e$. Additionally, each quark comes in three *colours*: *red, blue* and *green*. The colour charge is an additional degree of freedom needed to describe quarks and in QCD it is the equivalent to electric charge in electrodynamics. In contrast to quarks, leptons do not have *colour* charge. Furthermore, the neutrinos (which are leptons) carry a charge of $Q = 0e$, while electrically charged leptons (electron, muon and τ leptons) carry a charge of $Q = -1e$. Each *fermion* has a corresponding anti-particle with the same mass and opposite sign quantum numbers. The mediating gauge *bosons* for the interactions are:

[2] e is the absolute value of the charge of the electron.

- gluons (g) for the strong interaction. It only affects particles, carrying *colour* charge.
- photons (γ) for the electromagnetic interaction. It only affect particle, carrying electric charge.
- $W^{\pm}$ and Z^0 bosons for the weak interaction. The left-handed *fermions* interact with $W^{\pm}$.
- Higgs boson (H). The field of the Higgs boson causes the other elementary particles to acquire mass.

2.1.1. The Fundamental Forces

The elementary particles interact with each other through the four fundamental forces: the strong, the electromagnetic, the weak, and the gravitational force. The gravitation is not described by the SM. Compared to the other three forces, gravitation is by far the weakest and can be neglected in the description of elementary particle interactions. The relative strengths[3] of the forces are indicated in Table 2.1. The electromagnetic, weak, and strong forces are described by renormalisable Quantum gauge Field Theories (QFT). The Lagrange density is required to be invariant under local gauge transformations.

Force	Strength [3]	Mediating Boson	Spin	Mass [GeV]
Strong	1	Gluon g	1	0
Electromagnetism	10^{-3}	photon γ	1	$< 10^{-18}$
Weak	10^{-8}	W bosons $W^{\pm}$	1	80.4
		Z bosons Z	1	91.2
Gravity	10^{-37}	Graviton? G	2	$< 10^{-32}$

Table 2.1.: The four known forces of nature with the mass and the spin information of the mediating bosons. The relative strengths are approximate indicative values for two fundamental particles at a distance of 10^{-15} m (roughly the radius of a proton).

The Strong Interaction

The field theory of the strong interaction is Quantum Chromodynamics (QCD) which is invariant under $SU(3)$ local phase transformations,

$$\psi(x) \rightarrow \psi'(x) = \exp[ig_s\alpha(x)\cdot\hat{\mathrm{T}}]\psi(x), \tag{2.1}$$

where $\hat{\mathrm{T}} = T^a$ are the eight generators of the $SU(3)$ symmetry group, related to the Gell-Mann matrices: $T^a = \frac{1}{2}\lambda^a$; $\alpha^a(x)$ are eight functions of the space-time coordinates

[3] The strengths of the forces depend on the distance and energy scale being considered.

x and g_S is the strong coupling. Because the generators of $SU(3)$ are represented by 3×3 matrices, the wave function ψ must now include three additional degrees of freedom that can be represented by a three vector component. This new degree of freedom is termed as *colour* with *red, blue,* and *green* labelling the states. The required local gauge invariance can be asserted by introducing eight new fields $G^a_\mu(x)$, where the index $a = 1, ..., 8$. Each index corresponds to one of the eight generators of the $SU(3)$ symmetry. The Dirac equation, including the interactions with the new gauge fields, is invariant under local $SU(3)$ phase transformations. The new fields transform as:

$$G^k_\mu \rightarrow G^{k'}_\mu = G^k_\mu - \partial_\mu \alpha_k - g_s f_{ijk} \alpha_i G^j_\mu. \tag{2.2}$$

The last term in Equation 2.2 arises because generators of the $SU(3)$ symmetry do not commute and gives rise to gluon self-interactions. Therefore, QCD is known as a non-Abelian gauge theory. The f_{ijk} are the *structure constants* of the $SU(3)$ group defined by the commutation relations $[\lambda_i,\ \lambda_j] = 2if_{ijk}\lambda_k$. gs is related to the strong coupling constant α_s via: $g_s = \sqrt{4\pi\alpha_s}$. The coupling constant of the strong interaction, α_s, depends on the energy scale Q^2:

$$\alpha_s(Q^2) = \frac{12\pi}{(11n_c - 2n_f)\ln(\frac{Q^2}{\Lambda^2_{QCD}})}, \tag{2.3}$$

where n_c is the number of colours, n_f is the number of quark flavours that can be produced at the energy Q^2 ($Q^2 \leq m^2_q$) and Λ_{QCD} is the energy scale, $\Lambda_{QCD} = 200$ MeV. Equation 2.3 shows that the coupling constant decreases with large energies and therefore at small distances i.e. at small distances the quarks are *asymptotically free* [6], while the force between them increases with the distance. Free quarks have never been observed directly. This is explained by the hypothesis of *colour confinement*, which states that coloured objects are always confined to colour singlet states that only objects with non-zero colour charge can propagate as free particles. *Colour confinement* is believed to originate from the gluon-gluon self-interactions that arise because the gluons carry colour charge [7]. The measured value of the strong coupling constant is: $\alpha_s(m^2_Z) = 0.1184 \pm 0.0007$ [4] [8].

The Electroweak Interactions

The model of electroweak unification was proposed by Glashow [1], Salam [2] and Weinberg [3] (GSW), which unifies weak and electromagnetic forces of non-Abelian $SU(2)$ and Abelian $U(1)$ gauge groups, respectively.
The charged-current weak interaction is invariant under $SU(2)$ local phase transformations:

$$\varphi(x) \rightarrow \varphi'(x) = \exp[ig_W \alpha(x) \cdot \mathbf{T}]\varphi(x), \tag{2.4}$$

[4] A common reference for quoting the value of α_s is the mass of the Z boson. At this energy scale, the number of possible quark flavours is five: all quarks, except the top quark can be produced.

where $\mathbf{T}$ are the three generators of the $SU(2)$ group that can be written in terms of the Pauli spin matrices, $\mathbf{T} = \frac{1}{2}\sigma$ and $\alpha(x)$ are three functions which specify the local phase at each point in spacetime. In order to satisfy the required local gauge invariance, three gauge fields, W_k^μ with $k = 1, 2, 3$, are introduced, with corresponding three gauge bosons: $W^{(1)}, W^{(2)}, W^{(3)}$. The wave function $\varphi(x)$ is written in terms of two components (a weak isospin doublet), because the generators of the $SU(2)$ gauge transformation are the 2×2 Pauli spin-matrices.
In QFT, quarks and leptons are represented by spinor fields. For obtaining left-handed (LH) and right-handed (RH) components of the field $P_L = \dfrac{1-\gamma^5}{2}$ and $P_R = \dfrac{1+\gamma^5}{2}$ projection operators are defined. The weak charged-current interaction couples only to LH chiral[5] particle states and RH chiral antiparticle states. RH particle and LH antiparticle chiral states are placed in weak isospin singlets and are therefore unaffected by the $SU(2)$ local gauge transformation. The weak isospin doublets are composed only of LH chiral particle states and RH chiral antiparticle states and are affected by the gauge transformation of Equation 2.4. Therefore the symmetry group of the weak interaction is referred to as $SU(2)_L$. The physical W bosons can be identified as the linear combinations of $W^{(1)}$ and $W^{(2)}$:

$$W_\mu^\pm = \frac{1}{\sqrt{2}}(W_\mu^{(1)} \mp iW_\mu^{(2)}) \tag{2.5}$$

According to the Cabibbo hypothesis, the weak interactions of quarks have the same strength as the leptons, but their weak eigenstates differ from the mass eigenstates. The *Cabibbo-Kobayashi-Maskawa* (CKM) [9,10] unitary matrix relates the weak and the mass eigenstates of quarks by:

$$\begin{pmatrix} d' \\ s' \\ b' \end{pmatrix} = \begin{pmatrix} V_{ud} & V_{us} & V_{ub} \\ V_{cd} & V_{cs} & V_{cb} \\ V_{td} & V_{ts} & V_{tb} \end{pmatrix} \begin{pmatrix} d \\ s \\ b \end{pmatrix}. \tag{2.6}$$

The CKM matrix elements are determined experimentally and the diagonal elements have been found to be close to unity. The weak interaction vertex has *vector* minus *axial vector* (V-A) structure: For $W^\pm$ boson, it has the form:

$$\frac{-ig_W}{2\sqrt{2}}\gamma^\mu(1-\gamma^5)V_{ij} \tag{2.7}$$

and for Z boson

$$\frac{-ig_Z}{2}\gamma^\mu(c_V - c_A\gamma^5), \tag{2.8}$$

where V_{ij} is a CKM matrix element, γ^μ are the Dirac matrices, $g_{W,Z} = \sqrt{4\pi\alpha_{ew}}$ the weak coupling constants. c_V is the vector and c_A is the axial vector coefficients of the coupling.
$SU(2)$ gauge symmetry implies the existence of positive and negative weak charged

[5] Chirality defined as the eigenvalues of the chirality operator γ^5.

currents (exchanging $W^{\pm}$ boson) as well as weak neutral-currents (exchanging Z boson). It has been shown experimentally that the physical Z boson couples to both left- and right-handed chiral states (although not equally). Of the four mediating gauge bosons the photon and the Z boson are electrically neutral. Consequently, it is reasonable that they can be expressed in terms of quantum state formed from two neutral bosons as follows:

$$A_\mu = +B_\mu \cos\theta_W + W^3_\mu \sin\theta_W, \tag{2.9}$$

$$Z_\mu = -B_\mu \sin\theta_W + W^3_\mu \cos\theta_W, \tag{2.10}$$

where A_μ and Z_μ are the corresponding photon and Z boson fields; W_μ is associated with the $SU(2)_L$ local gauge symmetry and B_μ is associated with the $U(1)_Y$ local gauge symmetry. θ_W is the weak mixing angle. The GSW model of electroweak unification implies that the couplings of the weak and electromagnetic interactions are related. The weak hypercharge Y is given by: $Y = 2(Q - T_3)$.
All four gauge bosons described in the electroweak interaction are obtained from linear combinations of massless gauge fields. It has been experimentally observed that W and Z bosons are massive. This fact indicates that the underlying symmetry of the electroweak theory is broken by some mechanism that gives mass to the particles exchanged in weak interactions.

Electroweak Symmetry Breaking

The particles of the SM acquire their masses by breaking the $SU(2) \times U(1)$ local gauge symmetry of the electroweak theory, by introducing the *Higgs mechanism* [11–14]. The simplest Higgs model consists of a weak isospin doublet complex scalar field ϕ :

$$\phi = \frac{1}{\sqrt{2}} \begin{pmatrix} \phi+ \\ \phi_0 \end{pmatrix} = \frac{1}{\sqrt{2}} \begin{pmatrix} \phi_1 & +i\phi_2 \\ \phi_3 & +i\phi_4 \end{pmatrix}. \tag{2.11}$$

The corresponding Higgs potential has the following form:

$$V(\phi) = \mu^2 \phi^\dagger \phi + \lambda (\phi^\dagger \phi)^2. \tag{2.12}$$

The vacuum state is the lowest energy state of the field ϕ and corresponds to the minimum of the potential of Equation 2.12. λ must be positive for the potential to have a finite minimum. The shape of the potential depends on the sign of μ^2. If $\mu^2 > 0$, the resulting potential has a minimum at 0. If $\mu^2 < 0$, the potential energy function has two minima at $\frac{\mu^2}{2\lambda} = \frac{v^2}{2}(\pm v = \pm\sqrt{-\mu^2/\lambda})$, where v is the non-zero vacuum expectation value of the Higgs field. A graphical representation of the potential is shown in Figure 2.1.1 for both cases ($\mu^2 > 0$ and $\mu^2 < 0$). The choice of the vacuum state leads to the spontaneous breaking of the electroweak symmetry. For the option where $\phi_1 = \phi_2 = \phi_4 = 0$ and $\phi_3 = v$ ($v \neq 0$) , the vacuum state defined as:

$$\phi_0(v) = \frac{1}{\sqrt{2}} \begin{pmatrix} 0 \\ v \end{pmatrix} \tag{2.13}$$

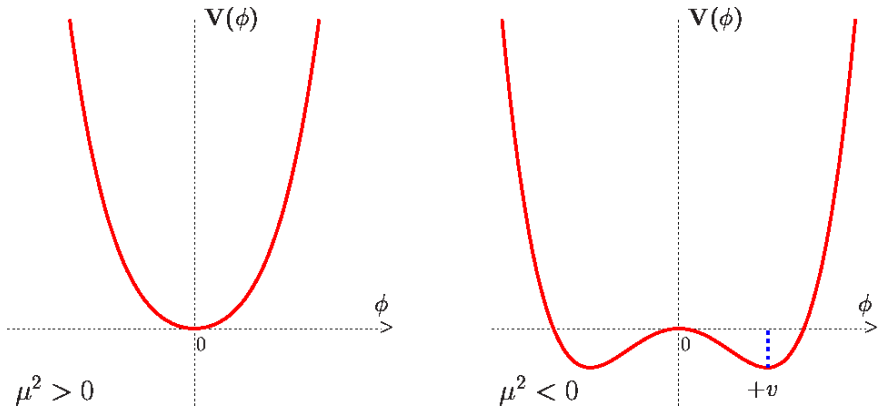

Figure 2.2.: Graphical representation of the potential $V(\phi)$ of a scalar real field for $\mu^2 > 0$ left and for $\mu^2 < 0$ right.

which is invariant with respect to the underlying $U(1)$ symmetry. The neutral scalar field, expanded around the chosen ground state, for the scalar Higgs $SU(2)$ doublet takes the form:

$$\phi(x) = \frac{1}{\sqrt{2}} \begin{pmatrix} 0 \\ v + h(x) \end{pmatrix}, \tag{2.14}$$

where $h(x)$ is the Higgs field. The $SU(2) \times U(1)$ symmetry is spontaneously broken but the $U(1)$ symmetry is kept, which implying, the photon is massless. The spontaneous breaking of the symmetry gives masses to real bosons via the interaction with the Higgs field. The particle associated to the Higgs field is called the Higgs boson. The SM Higgs boson has spin 0 and mass $m_H = \sqrt{2\mu}$. Furthermore, the masses of $W^{\pm}$ and Z bosons, respectively, are given by:

$$m_W = \frac{1}{2} v g \text{ and } m_Z = \frac{1}{2} v \sqrt{g^2 - g'^2}. \tag{2.15}$$

The Higgs mechanism also takes care of the generation of *fermion* masses by the coupling of the *fermions* to the Higgs field. This coupling is known as Yukawa coupling and is denoted y_f. The relation between the masses of the *fermions* and the Yukawa coupling is: $m_f = \frac{1}{2} v y_f$. The vacuum expectation value is related to the Fermi coupling constant G_F via: $v = \frac{1}{\sqrt{\sqrt{2} G_F}} \approx 246$ GeV. Because the Yukawa coupling is proportional to the particle mass it is clear that the coupling to the top quark is the largest one and hence the top-Higgs Yukawa coupling is close to unity. The mass of the Higgs boson is not predicted by the theory. The Higgs boson mass, measured experimentally, is $m_H = 125.09 \pm 0.21(stat.) \pm 0.11(syst.)$ GeV [15].

The Standard Model and beyond

The SM of particle physics has a great success in describing the wide range of precise experimental measurements. However, there are many questions that can not be answered by the SM. The Standard Model of particle physics has about 25 free parameters that must be put in by hand. These are: masses of the neutrinos[6], the twelve Yukawa couplings to the Higgs field (masses of the *fermions*), the three coupling constants describing the strengths of the gauge interactions (α, G_F and α_s), the Higgs potential described by the two parameters and eight mixing angles and phases of PMNS[7] [16,17] and CKM matrices [7]. The SM does not include gravity. Furthermore, cosmological observations from different sources show that ordinary matter can only account for 5% of the observed energy and matter in the universe, the rest is assumed to be dark matter and dark energy. The dark matter could be explained by the existence of a weakly interacting massive particle, that is not provided by the SM. Also there is no explanation of the matter-antimatter asymmetry of the universe. There are several other open questions that are not covered by the SM. There are several attempts to extend the SM, for example: supersymmetry, large-scale extra dimensions, and string theory. These BSM processes modify the SM predictions. The study of the Wtb vertex is one of the possible ways to probe BSM physics.

2.2. Top Quark Physics

The top quark is the heaviest elementary particle described by the SM. It was predicted already in 1973 by Kobayashi and Maskawa as the electroweak isospin partner of the bottom quark (discovered in 1977). The top quark was discovered in 1995 by the CDF and DØ collaborations [18,19] at the Fermilab Tevatron, a proton-antiproton ($p\bar{p}$) collider at a centre of mass energy of $\sqrt{s} = 1.8$ TeV. The mass of the top quark was measured very precisely and the first world combination of the Tevatron and LHC experiments results is: $m_t = 173.34 \pm 0.27(stat.) \pm 0.71(syst.)$ GeV [20]. The mass is close to electroweak symmetry breaking scale ($v \approx 246$ GeV). It indicates that the top quark may be able to open a window to new physics beyond the SM. Furthermore, as a consequence of its large mass the top quark decays before it can hadronise. The lifetime of the top quark is $\approx 0.5 \times 10^{-24}$s [8] [8]. The top quark can be studied as *bare* quark that transfers its properties directly to the decay products.
In Section 2.2.1 the production mechanisms of the top quark at the LHC are discussed. The decay modes of the top quark are discussed in Section 2.2.2 and its properties in Section 2.2.3, focusing on the (V-A) structure of the Wtb vertex.

[6] In the SM neutrinos are massless.

[7] The unitary Pontecorvo Maki Nakagawa Sakata (PMNS) matrix. In the three-flavour treatment of neutrino oscillations, the three weak eigenstates are related to the mass eigenstates by the 3×3 matrix and the elements of this matrix are fundamental parameters of the lepton flavour sector of the Standard Model.

[8] The hadronisation time is $\approx 10^{-23}$s.

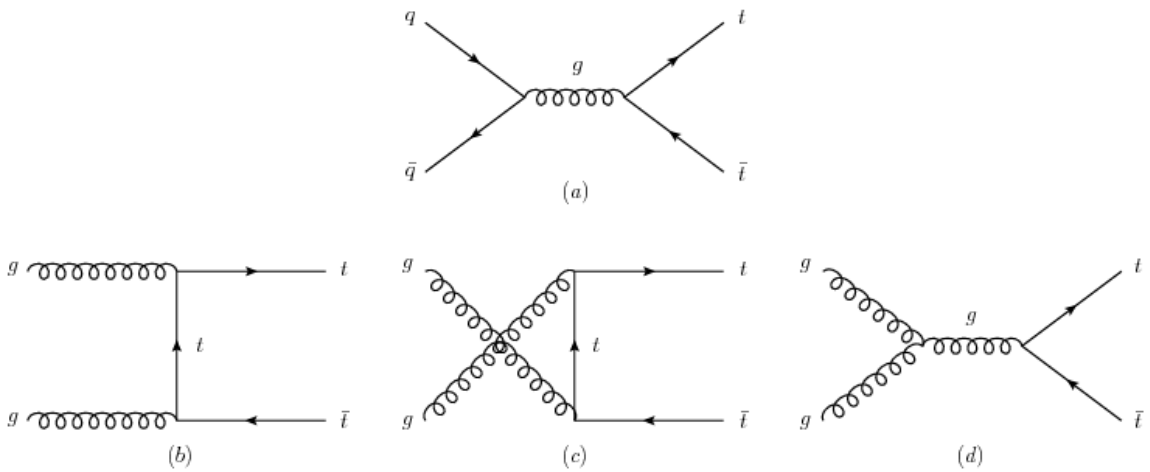

Figure 2.3.: The LO Feynman diagrams of the top quark pair production via the strong interaction.

2.2.1. Top Quark Production

At hadron colliders, top quarks can be produced via the electroweak interaction resulting in single top quarks or top quark pairs $t\bar{t}$ via the strong interaction.

Top Quark Pair Production

The dominant production process of top quarks at the LHC is the top quark pair production, via strong interactions through quark-antiquark annihilation and gluon-gluon fusion. The leading-order (LO) Feynman diagrams of top quark pair production are shown in Figure 2.3, where a) corresponds to quark-antiquark ($q\bar{q}$ and $q = u, d, s, c$) annihilation and b), c), d) correspond to gluon-gluon fusion. The total tree level $t\bar{t}$ cross section at the LHC is a convolution of the parton distribution functions (PDFs) for the incoming protons and the cross section for the partonic processes $q\bar{q}, gg \to t\bar{t}$. Using the factorisation theorem [21–24] the cross section takes the form:

$$\sigma_{q\bar{q},gg\to t\bar{t}}(\sqrt{s},\ m_t) = \sum_{i,j} \int dx_i dx_j f_i(x_i,\ \mu_F^2) f_j(x_j,\ \mu_F^2) \cdot \sigma_{i,j}(\sqrt{\hat{s}},\ m_t,\ \alpha_s(\mu_R^2),\ \mu_R^2), \tag{2.16}$$

where i, j are the possible combinations of incoming partons, $f(x,\ \mu_F^2)$ are the PDFs evaluated at some factorisation scale μ_F. In top quark analyses, the top quark mass is used as factorisation scale ($\mu_F = m_t$) . The PDFs can not be predicted by QCD , therefore they are measured experimentally, for example in ep collisions at HERA, in $p\bar{p}$ collisions at the Tevatron and in pp collisions at the LHC. The partonic subprocess cross

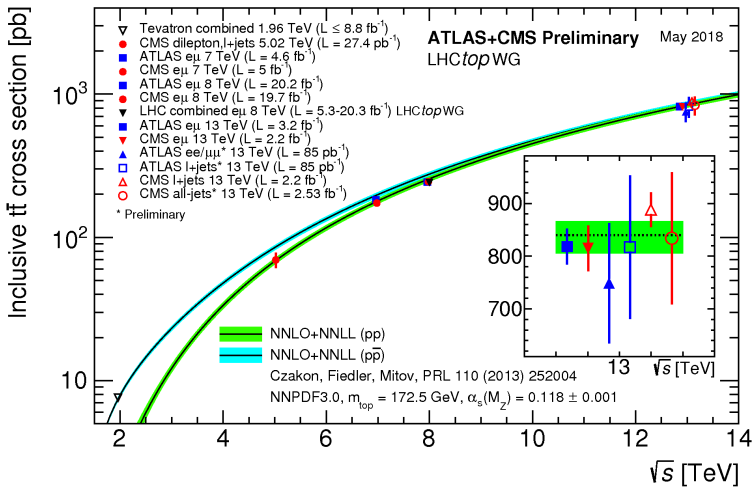

Figure 2.4.: Summary of LHC and Tevatron measurements of the top quark pair production cross section as a function of the centre of mass energy compared to the NNLO QCD calculation complemented with NNLL resummation (top++2.0 [28]). The theory band represents uncertainties due to renormalisation and factorisation scale, parton density functions, and the strong coupling [29].

section σ is a function of the centre of mass energy $\hat{s} = x_j x_j s$ (parton-parton collision), the mass of the top quark, and the QCD strong coupling constant, α_s, evaluated at the renormalisation scale μ_R. In top quark analyses, the renormalisation scale is set to the top quark mass ($\mu_R = m_t$). For producing $t\bar{t}$ pairs, s $\geq 4m_t^2$ is required. At the LHC, the dominant $t\bar{t}$ production mechanism ($\simeq$ 80 % at $\sqrt{s} = 7$ or 8 TeV) is gluon-gluon fusion, because in pp collisions the antiquarks are only available as sea quarks.
The theoretical calculation for top quark pair production cross section at next-to-next-to-leading-order (NNLO, QCD) including resummation of soft gluon terms with next-to-next-to-leading-logarithmic (NNLL) accuracy for pp collisions at a centre of mass energy $\sqrt{s} = 8$ TeV is: $\sigma_{t\bar{t}} = 252.89^{+6.39}_{-8.64}(\text{scale})^{+7.38}_{-7.33}(m_t) \pm 11.67(\text{PDF} + \alpha_s)$ pb [22, 25, 26]. The LHC (combined ATLAS and CMS) $t\bar{t}$ cross section measurement for $\sqrt{s} = 8$ TeV is $\sigma_{t\bar{t}} = 241.5 \pm 1.4(\text{stat}) \pm 5.7(syst) \pm 6.2(\text{lumi})$ pb [27]. Also the top quark pair production cross section was measured at all available centre of mass energies at the LHC with uncertainties of less than 5 % . The summary of LHC and Tevatron measurements compared to the NNLO QCD+ NNLL calculations of top quark pair production as a function of the centre of mass energy is presented on Figure 2.4

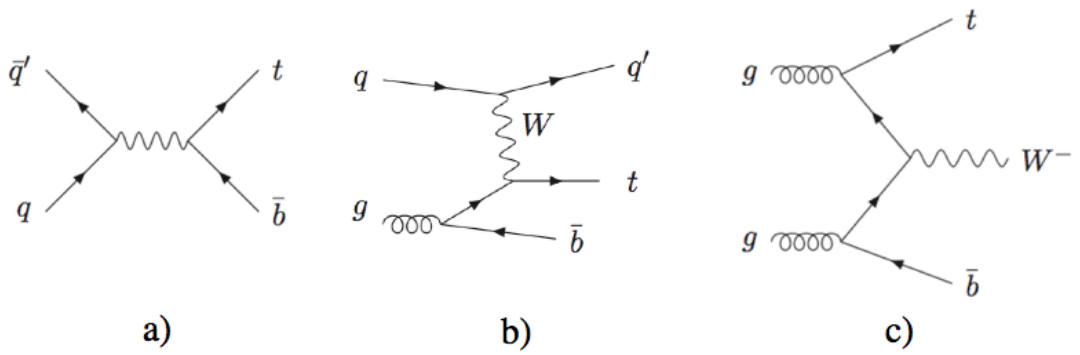

Figure 2.5.: Feynman diagrams for electroweak single top quark production. Represented are (a) a LO s-channel diagram, (b) a NLO t-channel diagram, and (c) a NLO Wt production diagram.

Single Top Quark Production

Top quarks can also be produced as single top quarks via the weak interaction. Several mechanisms can be measured individually due to the different final state:

- The s-channel production of a top quark and bottom quark;
- The t-channel production of a top quark and a light quark;
- The Wt-channel associated production of a top quark and an on-shell W boson.

The corresponding Feynman diagrams are shown in Figure 2.2.1. Compare to the top quark pair production, the single top quark production cross section is low and the process suffers from large backgrounds. At the LHC, the t-channel [30] and the Wt-channel [31] were observed, while only upper limits have been set on the s-channel production cross section [9] [32]. Figure 2.6 summarises the ATLAS and CMS measurements of the single top production cross-sections in various channels as a function of the centre of mass energy. The single top quark production gives direct access to the electroweak coupling of the top quark in form of the CKM matrix element $|V_{tb}|$. It has been extracted from the t-channel and Wt-channel cross section by comparing the measured cross section to the theoretical value: $|V_{tb}|^2 = \frac{\sigma_{meas}}{\sigma_{theory}}$. Figure 2.7 summarises the ATLAS and CMS extractions of the CKM matrix element V_{tb} from single top quark measurements.

[9] t-channel and s-channel production are dominant at the Tevatron, while the Wt-channel cross section is very low.

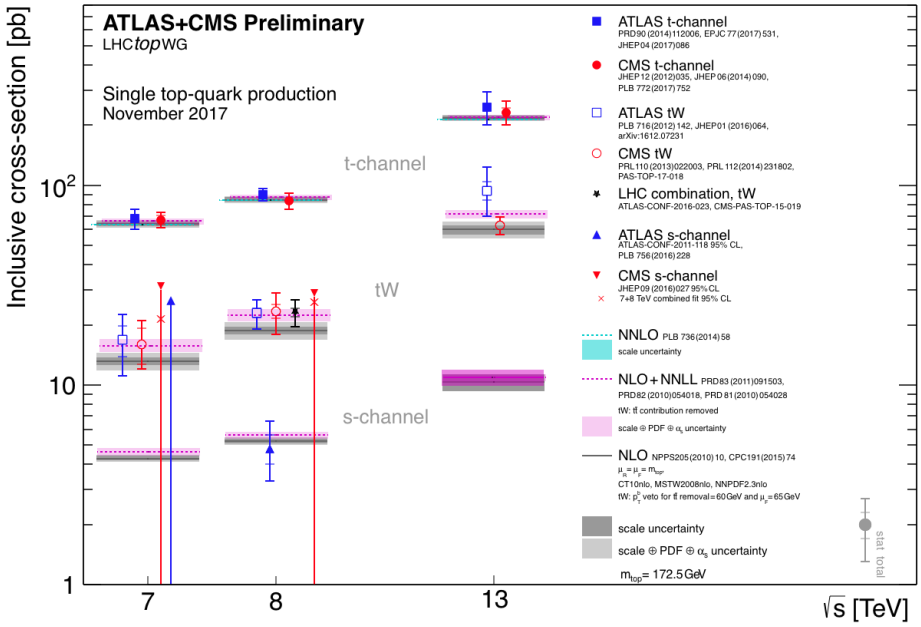

Figure 2.6.: Summary of ATLAS and CMS measurements of the single top production cross sections in various channels as a function of the centre of mass energy. The measurements are compared to theoretical calculations based on: NLO QCD, complemented with NNLL resummation and NNLO QCD (t-channel only) [29].

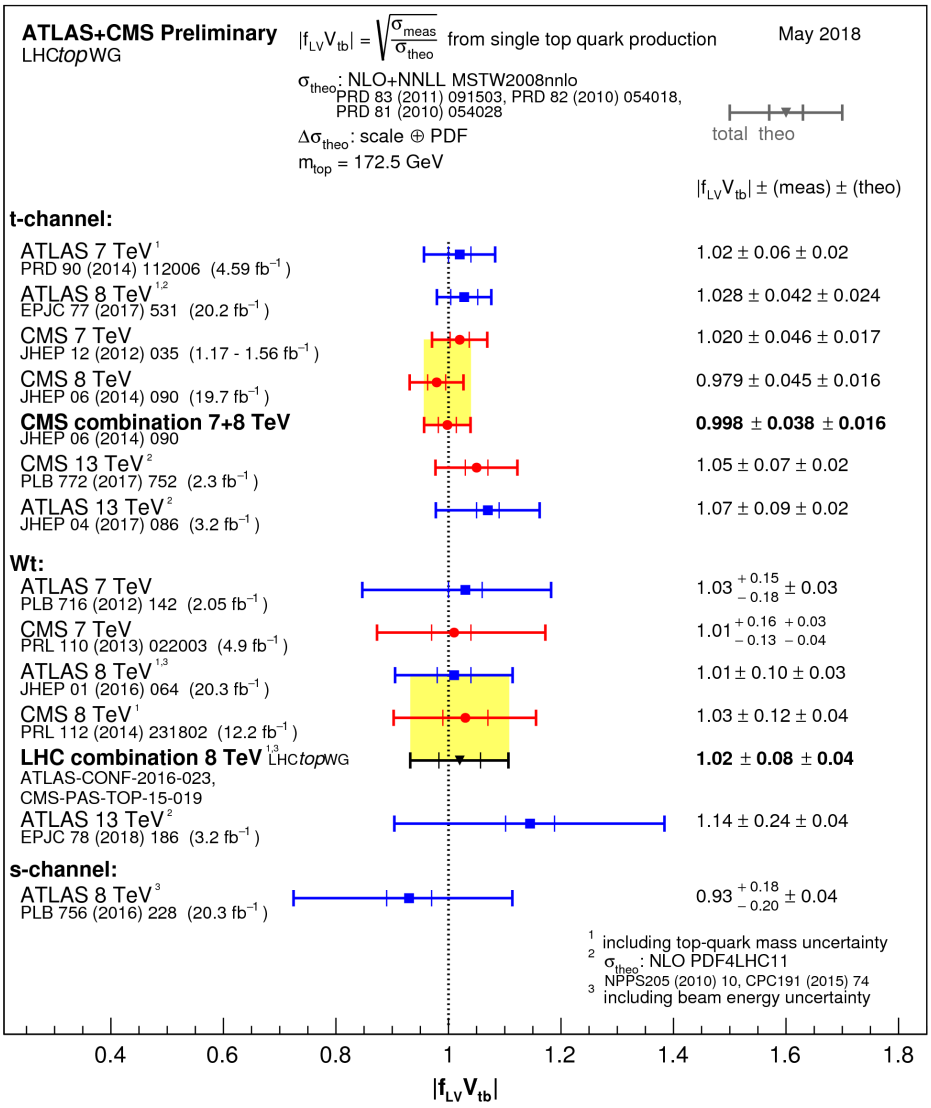

Figure 2.7.: Summary of the ATLAS and CMS extractions of the CKM matrix element V_{tb} from single top quark measurements. For each result, the contribution to the total uncertainty originating from the uncertainty on the theoretical prediction for the single top production cross section is shown along with the uncertainty originating from the experimental measurement of the cross section [29].

2.2.2. Top Quark Decay

As shown, the CKM matrix element V_{tb} is close to unity, therefore top quarks decay almost exclusively to a W boson and a b quark. Therefore, the different decay channels of top quark production are defined by decay channels of a W boson, which decays either leptonically (charged lepton and its corresponding neutrino) or hadronically (two quarks, $q\bar{q}$). The W boson decay branching ratios are summarised in Table 2.2. According to the W boson decays, three different decay channels exist for top quark pairs:

- *All hadronic* or *all jets* channel: when both W bosons decay hadronically. This channel has the largest branching ratio, but suffers from large background.
- *Lepton+jets* or *single lepton* channel: when one W boson decays leptonically and the other hadronically. This channel has small background compared to the branching ratio which is sufficiently high.
- *Dilepton* channel: when both W bosons decay leptonically. This channel has the smallest branching ratio but also very small backgrounds. The main challenge of this channel is the $t\bar{t}$ system reconstruction due to the two undetectable neutrinos which contribute to the missing transverse energy.

Process	Branching ratio [%]
$W \to qq'$	67.60 ± 0.27
$W \to e\bar{\nu}_e$	10.75 ± 0.13
$W \to \mu\bar{\nu}_\mu$	10.57 ± 0.15
$W \to \tau\bar{\nu}_\tau$	10.25 ± 0.20
$\tau \to e\bar{\nu}_e\nu_\tau$	17.83 ± 0.04
$\tau \to \mu\bar{\nu}_\mu\nu_\tau$	17.41 ± 0.04

Table 2.2.: The branching ratios of the W boson decays. Leptonically decaying τ leptons are considered to be part of the leptonic decay of the W boson. The values are taken from [8].

Figure 2.8 shows the $t\bar{t}$ decay channels with their corresponding branching ratios. The analysis presented in this thesis is performed in the $t\bar{t}$ dilepton channel including leptonic τ decays. At the final state, it is expected to have two leptons (electron or muon) with opposite charge and two b quarks.

2.2.3. Top Quark Properties

The properties of the top quark make it special. As mentioned above, the top quark is the heaviest elementary particle with too short lifetime to create any bound states. Hence, its properties are directly transferred to the decay products (charge, spin or polarisation). The top quark might play an important role in Higgs physics studies,

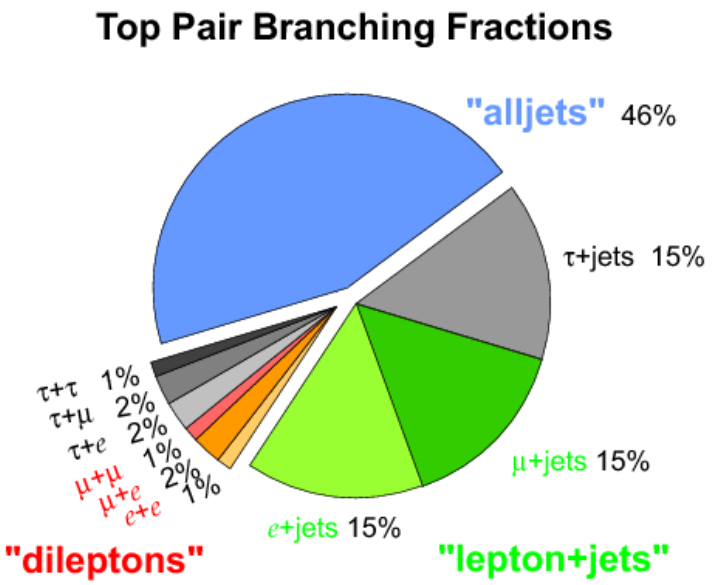

Figure 2.8.: Branching ratios of the different $t\bar{t}$ channels at Born level.

because of the Yukawa coupling to the Higgs field that is almost unity. In this section, several important top quark property measurements will be briefly described.

The Mass:
As the top quark has a mass close to the electroweak symmetry breaking scale, it may play an important role in beyond the SM (BSM) scenarios. Therefore it is important to perform precise measurements of the top quark mass. The most recent measurement is performed by the CMS experiment in the lepton+*jets* channel at a centre of mass energy of 13 TeV resulting: $m_t = 172.25 \pm 0.63$ (stat+syst) GeV [33]. The other LHC measurements are presented in Figure 2.9.

Charge:
The top quark is the electroweak isospin partner of the bottom quark and is expected to have an electric charge of $+2/3e$. The charge of the top quark was measured by the ATLAS [34] and CMS [35] experiments at a centre of mass energy of $\sqrt{s} = 7$ TeV. The charge of the top quark quoted by the ATLAS is: $Q_t = 0.64 \pm 0.02(\text{stat.}) \pm 0.08(\text{syst.})e$. This excludes models that propose a heavy quark with electric charge of $-4/3e$, instead of the SM top quark, with a significance of more than 8σ.

Charge Asymmetry:
In the SM, the charge asymmetry is produced by interference between the Born and the one-loop diagram of the $q\bar{q} \to t\bar{t}$ processes and $q\bar{q} \to t\bar{t}g$ with initial-state and final-state

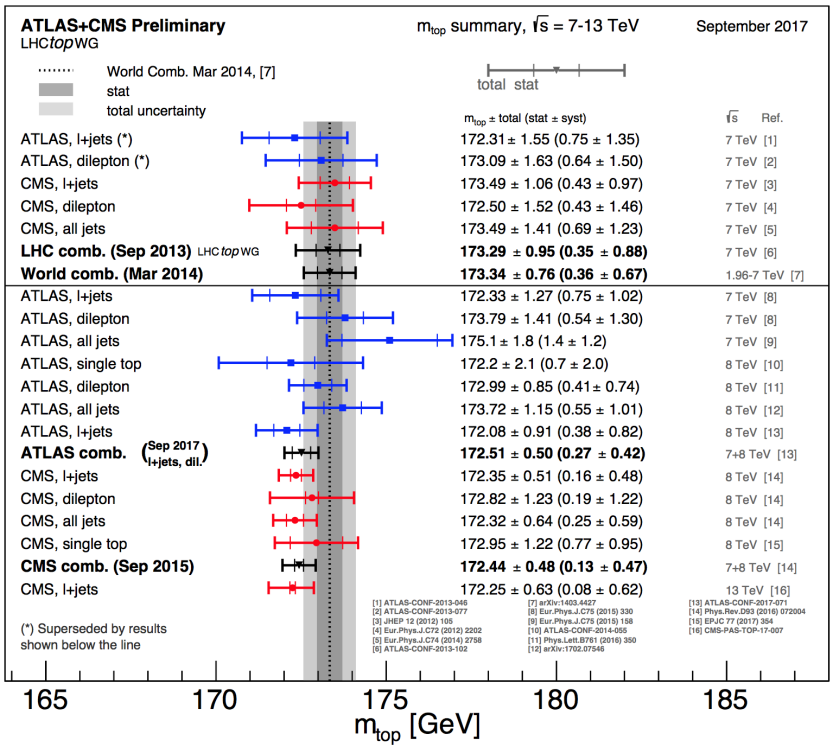

Figure 2.9.: Summary of the ATLAS and CMS direct m_t measurements. The results are compared with the LHC and Tevatron + LHC m_t combinations [29].

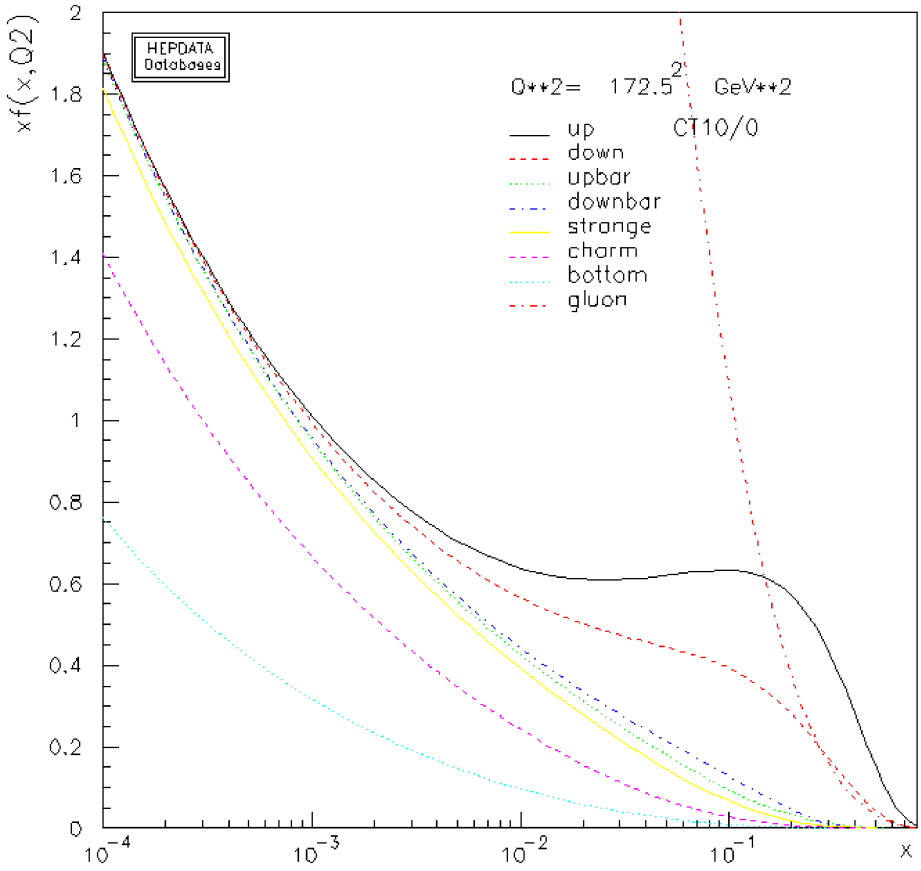

Figure 2.10.: Different parton distribution (PDFs) for protons at the scale $Q^2 = m_t^2$ with a top quark mass of $m_t = 172.5$ GeV based on the CT10 PDF [37,38].

radiation. The interference terms cause a difference of the top and anti-top rapidities y in case of production via $q\bar{q}$ annihilation [36]. In protons, valence quarks carry on average a larger fraction of the proton momentum than sea antiquarks (see Figure 2.10). The charge asymmetry transfers this difference to top and anti-top quarks, hence top anti-quarks produced through $q\bar{q}$ annihilation are more central than top quarks. An asymmetry can be calculated as:

$$A_C = \frac{N(|y_t| - |y_{\bar{t}}| > 0) - N(|y_t| - |y_{\bar{t}}| < 0)}{N(|y_t| - |y_{\bar{t}}| > 0) + N(|y_t| - |y_{\bar{t}}| < 0)}. \tag{2.17}$$

At the LHC the dominant process is gluon gluon fusion, so the charge asymmetry effect is expected to be small. The summary of LHC charge asymmetry measurements is presented in Figure 2.11.

Spin:
As the top quark decays before hadronising, the spin information is transfered to its decay products, so the spin of the top quark is determined through its decay products. The top quark pair is produced unpolarised at tree level but their spins are predicted to be correlated[10]. The spin correlation was observed by the ATLAS [39] and CMS [40] experiments at a centre of mass energy of $\sqrt{s} = 7$ TeV. In both cases the results are in good agreement with the SM.

After the top quark discovery large effort is made to measure its properties precisely. Studying the structure of the Wtb decay vertex through the measurement of the corresponding W boson polarisation (helicity) in $t\bar{t}$ decays is the main purpose of this thesis.

2.2.4. W boson polarisation

As already discussed in Section 2.1.1, the Wtb decay vertex has *vector* minus *axial vector* (V-A) structure as shown in Equation 2.7, which means that the vertex for weak charged currents only couples to left-handed particles or right-handed antiparticles. The full matrix element M for the top quark decay is:

$$iM = i|V_{tb}|\frac{g_W}{\sqrt{2}}\bar{b}\gamma^\mu P_L t W^-_\mu, \tag{2.18}$$

where P_L is the projection operator introduced in Section 2.1.1. The W boson from $t\bar{t}$ decays can have three polarisation states: Left-handed, longitudinal and right-handed. The helicity is defined as the projection of the spin $\vec{s}$ onto the momentum direction $\hat{p}$ ($h = \vec{s} \cdot \hat{p}$). The Figure 2.12 shows a schematic view of the three polarisation states. The corresponding fractions are calculated as the ratio of the relative decay width to the total width. Assuming the b quark has zero mass [11] and also due to the (V-A) structure of the Wtb vertex, the b quark is required to be left-handed. In the top quark rest frame, the W boson and the b quark are emitted back-to-back and therefore, due to angular momentum conservation, the W boson can then only either have longitudinal or left-handed helicity, depending on the orientation of the top quark spin. The right-handed W boson polarisation is not allowed at LO. The total decay width is calculated by applying *Fermi's golden rule*:

$$\Gamma = \frac{2\pi}{\hbar}\int |M|^2 d\phi, \tag{2.19}$$

where M is the full matrix element for the top-quark decay. Taking the initial and final states as well as the mass of the b quark and also $g_W^2 = 4\sqrt{2}G_F m_W^2$ into account, the decay width takes the form [41]:

$$\Gamma = \frac{G_F m_W^2 m_t}{8\sqrt{2}\pi}|V_{tb}|^2\sqrt{\lambda}\frac{(1-y^2)^2 + x^2(1-2x^2+y^2)}{x^2}, \tag{2.20}$$

[10] The lifetime of the top quark is much shorter than the spin decorrelation time. Also top quark pair production in QCD is parity invariant.

[11] This assumption is justified by the small b quark mass compared to the masses of the top quark and the W boson.

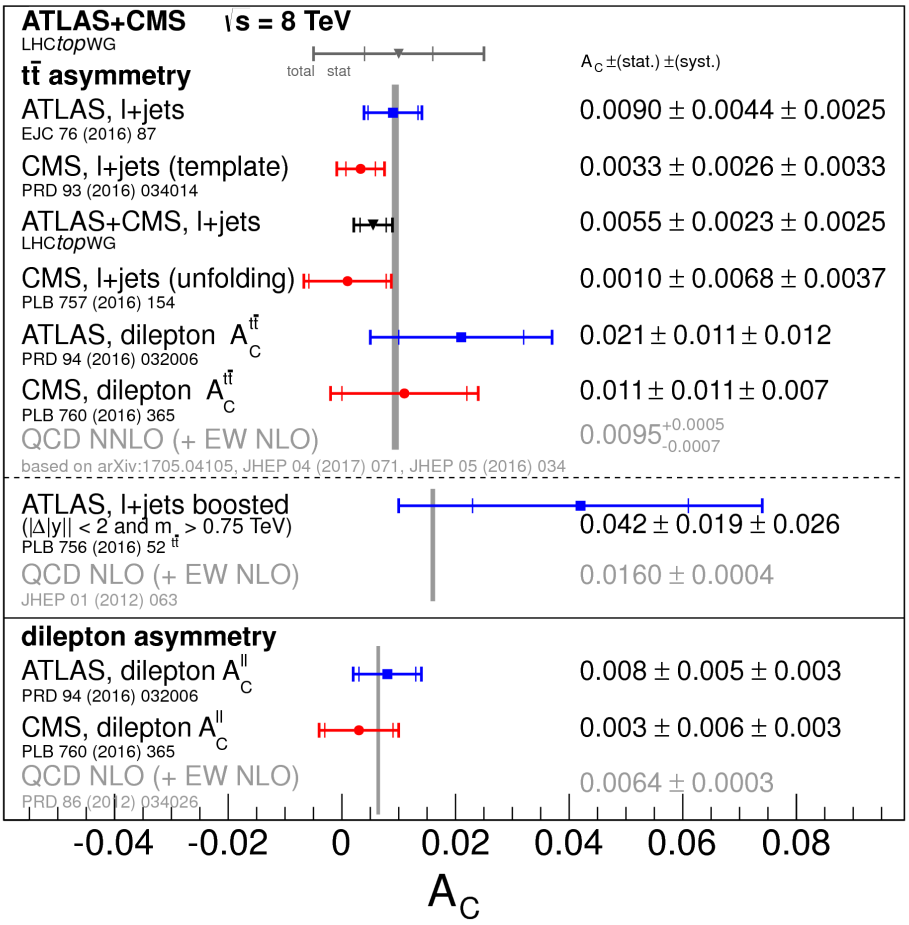

Figure 2.11.: Summary of the charge asymmetry measurements at ATLAS and CMS at 8 TeV showing both the inclusive measurements and the measurement using boosted events which is restricted to $M_{t\bar{t}} > 0.75$ TeV and $|\delta|y|| < 2$, compared to the respective theory predictions [29].

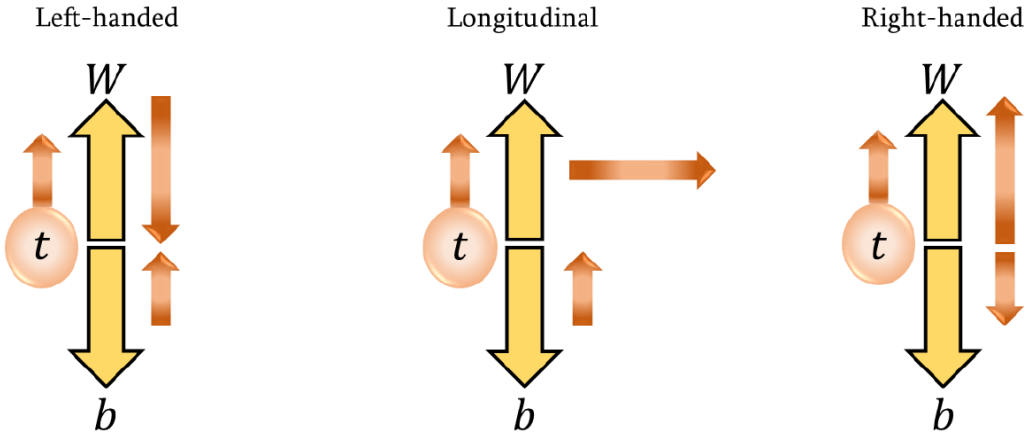

Figure 2.12.: Decay of the top quark into a W boson and a b quark in the top quark rest frame. The large yellow arrows represent the momentum of the particles and the thin brownish arrows the spin. The probability for the top-quark to decay into a right-handed W boson is suppressed by the ratio m_b^2/m_t^2.

where $x = m_W/m_t, y = m_b/m_t$ and $\lambda = 1 + x^4 + y^4 - x^2y^2 - 2x^2 - 2y^2$. At LO, the helicity fractions take the form:

$$\begin{aligned} F_L &= \frac{(1-y^2)^2 - x^2(1+y^2)}{(1-y^2)^2 + x^2(1-2x^2+y^2)} = \frac{1}{1+2x^2} + \dots \\ F_0 &= \frac{x^2(1-x^2+y^2+\sqrt{\lambda})}{(1-y^2)^2 + x^2(1-2x^2+y^2)} = \frac{2x^2}{1+2x^2} + \dots \\ F_R &= \frac{x^2(1-x^2+y^2-\sqrt{\lambda})}{(1-y^2)^2 + x^2(1-2x^2+y^2)} = y^2\frac{2x^2}{(1-x^2)^2(1+2x^2)} + \dots . \end{aligned} \tag{2.21}$$

As shown in Equation 2.21, the right handed contribution is proportional to y^2. The helicity fractions in cases with and without including b quark mass differ for F_L and F_0 in the order of 0.09% while it is smaller for F_R with a variation of 0.04%. Gluon radiation can also alter the helicity fractions. The radiative corrections to the normalised left handed and longitudinal helicity rates are sizable, $\mathcal{O}(\alpha_s) \approx 1 - 2\%$[12], respectively, while the effect is much smaller for right handed states $\approx 0.10\%$ [41]. The theory predictions for the W boson helicity fractions at NNLO QCD, including b quark mass, radiative corrections, and electroweak effects with the relative precision of $\mathcal{O}(1\ \%)$ are: $F_L = 0.311 \pm 0.005, F_0 = 0.687 \pm 0.005$ and $F_R = 0.0017 \pm 0.0001$ [42] for $m_t = 172.8 \pm 1.3$ GeV, $m_W = 80.401 \pm 0.43$ GeV and $m_b = 4.8$ GeV.
To incorporate effects from BSM physics into the Wtb vertex, the Lagrangian of this

[12]In this calculations is discussed $m_b \neq 0$ effects for the Born term and the α_s contributions.

vertex can be expressed using a minimum set of four anomalous couplings [43]

$$\mathcal{L}_{W_{tb}} = -\frac{g}{\sqrt{2}}\bar{b}\gamma^{\mu}(V_L P_L + V_R P_R)tW_{\mu}^{-} - \frac{g}{\sqrt{2}}\bar{b}\frac{i\sigma^{\mu\nu}q_{\nu}}{M_W}(g_L P_L + g_R P_R)tW_{\mu}^{-} + ..., \quad (2.22)$$

where V_L and V_R are left handed and right handed vector couplings and g_L and g_R are the left-handed and right-handed tensor couplings. In the SM, $V_L = V_{tb} \simeq 1$ and $V_R = g_L = g_R = 0$ at the tree level, due to the (V-A) structure of the Wtb vertex. The indirect limits have been set on V_R, g_L and g_R which are expressed in effective operators as [44]

$$\begin{aligned} V_L &= V_{tb} + C_{\phi q}^{3,33*}\frac{v^2}{\Lambda^2} \\ V_R &= \frac{1}{2}C_{\phi\phi}^{33}\frac{v^2}{\Lambda^2} \\ g_L &= \sqrt{2}C_{dW}^{33*}\frac{v^2}{\Lambda^2} \\ g_R &= \sqrt{2}C_{uW}^{33}\frac{v^2}{\Lambda^2} \end{aligned} \quad (2.23)$$

.

On the theoretical side, there have been a number of investigations on BSM physics contributions to the Wtb vertex, including two-Higgs doublet models (2HDM) [45], the minimal supersymmetric extension of the standard model (MSSM) [46], top-color assisted technicolor models (TC2) [47], and Little Higgs models [48]. In the 2HDM, the existence of five Higgs bosons is predicted, with two neutral scalars (h^0 and H^0), one pseudo scalar (A^0), and two charged Higgs bosons ($H^{\pm}$). In this model, the top quark decays to lighter charged Higgs bosons and a b quark: $t \to H^{+}b$. The MSSM assigns a bosonic (fermionic) super partner to every fermion (boson) in the SM, and predicts that the lightest superfermion masses are close to their SM partners. The one-loop corrections to the total width of $t \to Wb$ allow the top quark to decay to lighter supersymmetric particles. In the MSSM, the genuine supersymmetric corrections are SUSY electroweak (SUSY-EW) corrections. The TC2 model predicts heavy particles: three top pions (Π_t^0, $\Pi_t^{\pm}$) and a top-Higgs H_t^0. These particles can show up in loop corrections to the Wtb vertex. In all above described models, the Wtb vertex is modified which allows to measure W helicity fractions that are not predicted by the SM. However all models would only have small contributions of 1% or smaller [49]. The analysis presented in this thesis uses the model, to search for non-SM couplings.

Measurement of the W Boson Polarisation

In order to analyse the W boson polarisation the angular distribution ($\cos\theta^*$) of the charged lepton from the leptonic W decay is used:

$$\frac{1}{\Gamma}\frac{d\Gamma}{d\cos\theta^*} = \frac{3}{8}(1-\cos\theta^*)^2 F_L + \frac{3}{4}\sin^2\theta^* F_0 + \frac{3}{8}(1+\cos\theta^*)^2 F_R, \quad (2.24)$$

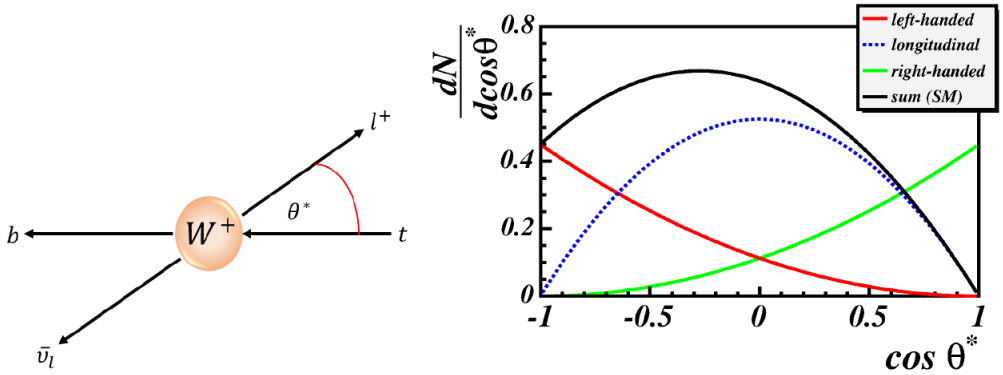

Figure 2.13.: The $\cos\theta^*$ helicity angle defined as the angle between the charged lepton and the negative direction of the b quark in the W boson rest frame (left) and the angular distribution of the charged lepton (right).

where θ^* is defined as the angle between the charged lepton and the negative direction of the b quark in the W boson rest frame as show in Figure 2.13 (left). Figure 2.13 (right) shows the distribution for the left-handed, right-handed and longitudinal distribution as well as the total SM distribution. The $textnormalcos\theta^*$ distribution gives a good separation power between the three helicity states. The sum of the fractions is equal to unity, $F_L + F_0 + F_R = 1$. There are two main approaches to measure the W boson helicity fractions:

- **Angular asymmetry:** The angular asymmetry defined as [50]:

$$A\pm = \frac{N(\cos\theta^* > z) - N(\cos\theta^* < z)}{N(\cos\theta^* > z) + N(\cos\theta^* < z)}, \tag{2.25}$$

  where $z = \pm(1 - 2^{\frac{2}{3}})$. The angular asymmetries can then be translated into the W boson helicity fractions as:

$$\begin{aligned} F_L &= \frac{1}{1-\beta} - \frac{A_+ - \beta A_-}{3\beta(1-\beta^2)}; \\ F_0 &= -\frac{1+\beta}{1-\beta} + \frac{A_+ - A_-}{3\beta(1-\beta)}; \\ F_R &= \frac{1}{1-\beta} + \frac{A_+ - \beta A_-}{3\beta(1-\beta^2)}, \end{aligned} \tag{2.26}$$

  where $\beta = 2^{\frac{1}{3}-1}$.

- **Template fit:** The template fit method exploits the shape of the angular distribution. This method is used for this analysis and will be described in Section 7.1.

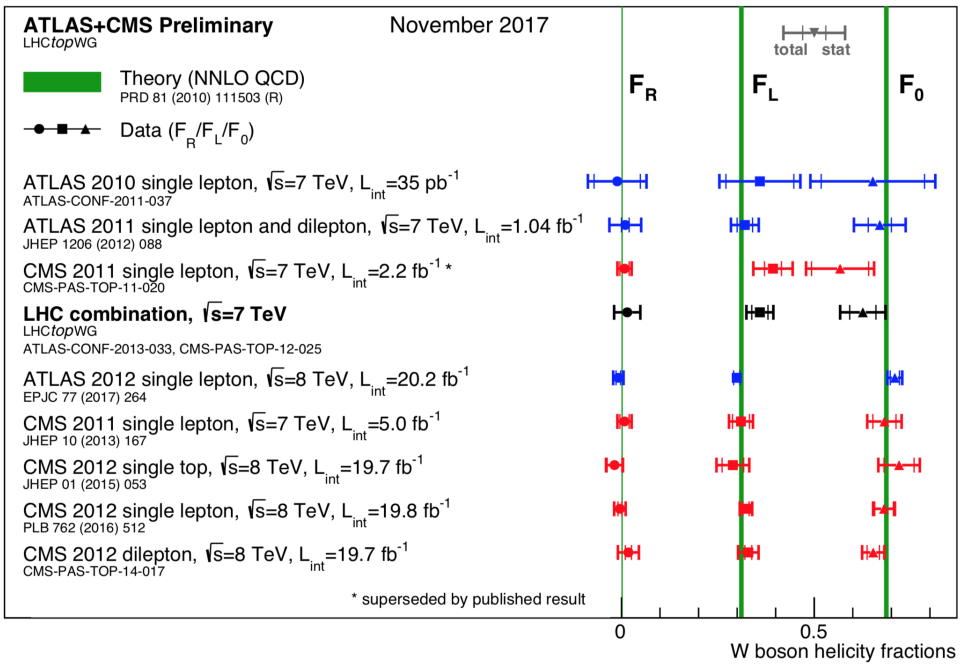

Figure 2.14.: The summary of the W boson polarisation measurements at LHC [29].

Finally, the polarisation of the W boson was studied by the CDF [51] and DØ [52] experiments at the Tevatron [53], also by ATLAS [54] and the CMS [55] experiments at the LHC [56], for different centre of mass energies and in different channels of the $t\bar{t}$ decays. The LHC results are summarised in Figure 2.14. All measured results are in good agreement with the SM. The most recent results will be discussed in Section 8.2 with the comparison to the results of the current analysis.

CHAPTER 3

Experimental Setup

The top quark is the heaviest elementary particle, so advanced experimental techniques are needed to detect and reconstruct top quark events. Only two hadron colliders were able to produce top quarks. The first one is the Tevatron at Fermilab near Chicago, a proton anti-proton ($p\bar{p}$) collider with a centre of mass energy of $\sqrt{s} = 1.96$ TeV (stopped operation in 2011) and the second one is the Large Hadron Collider (LHC) at CERN near Geneva, a proton proton (pp) collider with a centre of mass energy of $\sqrt{s} = 7$ TeV in 2011, $\sqrt{s} = 8$ TeV in 2012, $\sqrt{s} = 13$ TeV since 2015 and $\sqrt{s} = 14$ TeV is planned for 2020.
One of the most important factors for producing top quarks, apart from the centre of mass energy, is a high luminosity $\mathcal{L}$. The peak luminosity at $\sqrt{s} = 14$ TeV is $10^{34}\text{cm}^{-2}\text{s}^{-1}$. For the analysis presented in this thesis, data taken in 2012 with the ATLAS detector at a centre of mass energy of $\sqrt{s} = 8$ TeV and integrated luminosity of $\int \mathcal{L}dt = 20.2$ fb^{-1} is used. In this chapter, the LHC machine will be described briefly in Section 3.1. In Section 3.2, a brief description of the ATLAS detector and characteristics of data recorded during a Run1 by the ATLAS detector are presented.

3.1. The Large Hadron Collider (LHC)

Nowadays the Large Hadron Collider [57] is the most powerful two-ring-superconducting particle (pp and also Pb-Pb and pPb) accelerator and collider installed in the existing 26.7 km tunnel that was constructed between 1984 and 1989 for the CERN Large Electron-Positron collider (LEP) [58] machine. The LHC is installed approximately 100 m below the surface with a 1.4% incline. The LHC is the last element of the CERN particle acceleration system (shown on Figure 3.1). The proton bunches (consisting of about 10^{11}

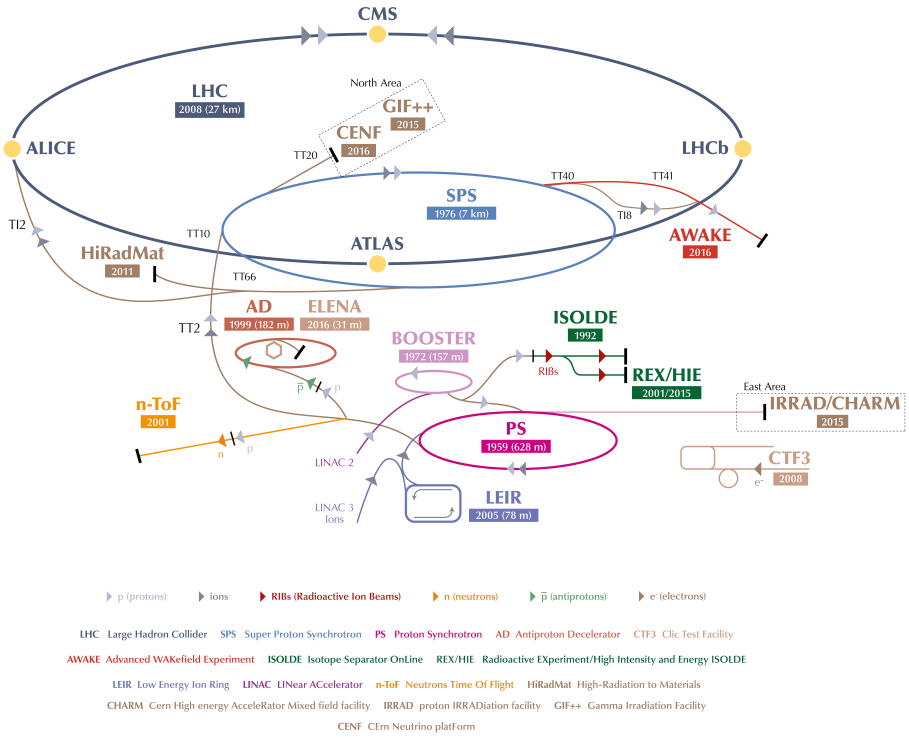

Figure 3.1.: CERN Accelerator Complex (© CERN).

protons)[1] are produced by hydrogen atoms and are accelerated up to 500 MeV by the injector chain Linac2. The next, in acceleration chain is the Proton Synchrotron Booster (PSB) up to 1.4 GeV the Proton Synchrotron (PS) up to 25 GeV the Super Proton Synchrotron (SPS) up to 450 GeV and the LHC to 7, 8, 13 or 14 TeV. The beams collide at four interaction points, where particle detectors are installed. The ATLAS [59] detector is located in point 1, the ALICE [60] detector in point 2, the CMS detector [61] in point 5, and the LHCb [62] detector in point 8.
The proton bunches are deflected by 1232 dipole magnets (in the curved LHC section) and focused by 392 quadrupole (in the straight sections) magnets made of superconducting Nb-Ti. These magnets operate at 1.9 K, using super-fluid He, and reach a magnetic field above 8 T. Furthermore in order to stabilise the beams and correct for small imperfections in the magnetic field, higher multipole order magnets are also used.
The ATLAS and CMS experiments are general-purpose detectors investigating a wide range of physics, such as: high precision measurements of Standard Model processes and couplings, and also searches for the Higgs boson and processes beyond the SM.
ALICE is a heavy-ion detector. The main physics program is to study strongly interacting matter and the quark-gluon plasma at extreme values of energy density and temperature in nucleus-nucleus collisions.
LHCb is a single-arm forward spectrometer and is dedicated to study heavy flavour physics. Its primary goal is to look for indirect evidence of new physics and CP violation in rare decays of beauty and charm hadrons.
Besides the main experiments briefly discussed above, there are three smaller special purpose experiments at the LHC: LHCf is [63] dedicated to the measurement of neutral particles emitted in the very forward region, TOTEM [64] measures the total pp cross section with luminosity independent method and studies elastic and diffractive scattering, and MoEDAL [65] directly search for the Magnetic Monopole and other highly ionizing Stable Massive Particles (SMPs).

Luminosity

Together with the beam energy, the luminosity is the most important performance parameter for particle colliders. The luminosity is a quantity that defines the ability of a collider to produce interactions (events) of a certain physics process. It is the proportionality factor between the event rate $\dot{N}$ and the cross section of the process of interest σ:

$$\dot{N} = \sigma \mathcal{L} \tag{3.1}$$

The luminosity of a ring collider like LHC is, defined as:

$$\mathcal{L} = \frac{N_1 N_2 n_b f}{A}, \tag{3.2}$$

[1] The design luminosity of $10^{34}\text{cm}^{-2}\text{s}^{-1}$ is reached by up to 2.808 bunches with a bunch crossing every 25 ns. Depending how well the beam is focused, this number corresponds to at least 20 inelastic collisions per bunch crossing on average.

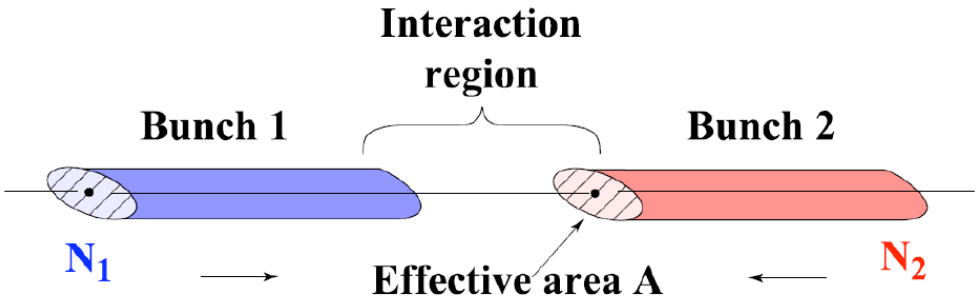

Figure 3.2.: The collision of two bunches with number of particles (N_1 and N_2). The hatched area shows the effective area A.

where N_1 and N_2 are the numbers of particles per bunch in beam 1 and 2, n_b is the number of bunches, f is the revolution frequency and A ($A = 4\pi\sigma_x\sigma_y$) is the effective beam overlap cross section given by the Gaussian width at the interaction point (schematic view in Figure 3.2). σ_x and σ_y can be determined using Van-der-Meer scans [66]. The geometric luminosity reduction factor F needs to be taken into account due to collisions with an offset or crossing angle at the interaction point. Also the beam emittance ϵ[2] is a function of the beam energy and is often specified by the normalised emittance ϵ_n for the accelerating beams and defined as: $\epsilon_n = \epsilon/\beta\gamma$, where γ is the Lorentz factor and $\beta = v/c \approx 1$ for the LHC. The beam width can be expressed by the *beta function* (β^*) and the emittance at the collision point as: $\sigma = \sqrt{\beta^*\epsilon}$. The luminosity can be expressed as:

$$\mathcal{L} = \frac{N_1 N_2 n_b f \gamma}{4\pi\epsilon_n\beta^*}F. \tag{3.3}$$

Since the bunch intensities and beam sizes of a collider vary over time, the number of events of a given process with cross section σ produced in the collisions can now be obtained by integrating over the time dependent luminosity:

$$N = \sigma \int \mathcal{L}dt, \tag{3.4}$$

where $\mathcal{L}dt$ is the *integrated luminosity*.
The summary of the parameters and peak performance of the LHC machine during 2010, 2011, and 2012 is shown in Table 3.1.

3.2. The ATLAS Detector

The ATLAS [59] (acronym for A Toroidal LHC ApparatuS) detector is one of the two largest general purpose detectors installed at the LHC. Physics studies require a detector which is able to measure the properties of the final state particles, allowing their identification. ATLAS is a set of cylindric sub-detectors, which covers almost the full

[2]Phase space volume of the colliding particle bunches.

Parameter	2010	2011	2012	Design value
Beam energy [TeV]	3.5	3.5	4	7
Bunch spacing [ns]	150	50	50	25
Number of bunches	368	1380	1374	2808
β^*[m]	3. 5	1.0	0.6	0.55
Average bunch intensity	1.2×10^{11}	1.5×10^{11}	1.0×10^{11}	1.15×10^{11}
Normalized emittance [μm rad]	2.4	2.0	2.5	3.75
Peak luminosity [$cm^{-2}s^{-1}$]	2.1×10^{32}	3.6×10^{33}	7.7×10^{33}	1.0×10^{34}

Table 3.1.: Performance related parameters overview [67, 68].

solid angle around the interaction point. The basic detector shape is completed by two end-caps in the bases of the cylinder and has a forward-backward symmetry with respect to the interaction point at the centre. The sub-detectors of the end-caps are disc shaped, centered around the beam pipe. The overall dimensions of a cylinder are 46 m in length and 25 m in diameter. The ATLAS detector weighs 7.000 tonnes and is located 100 m underground. A schematic representation of the ATLAS detector can be seen in Figure 3.3. The main sub-detector systems of ATLAS are:

- The magnetic system, which curves the charged particles and so their momenta can be measured.
- The tracking system, that identifies the passage of charged particles through the detector and measures their momenta.
- The calorimeter system, to measure the energy of the particles.
- The muon system, a dedicated tracking system to identify and measure the momenta of muons.

Integrated with the detector, there are two components:

- Trigger and Data Acquisition System, a specialized multi-level computing system, which selects physics events with distinguishing characteristics.
- The Software and Computing System.

Coordinate System

In the description of the ATLAS detector, a right-handed coordinate system is used. The nominal interaction point is defined as the origin of the coordinate system, while the beam direction (counter-clockwise running beam) defines the z-axis and the $x - y$ plane is transverse to the beam direction. The positive x-axis is defined as pointing from the interaction point to the centre of the LHC ring and the positive y-axis is defined as pointing upwards. Instead of a Cartesian coordinate system, a cylindrical one is more useful because of the symmetry of ATLAS detector. The azimuthal angle ϕ is defined

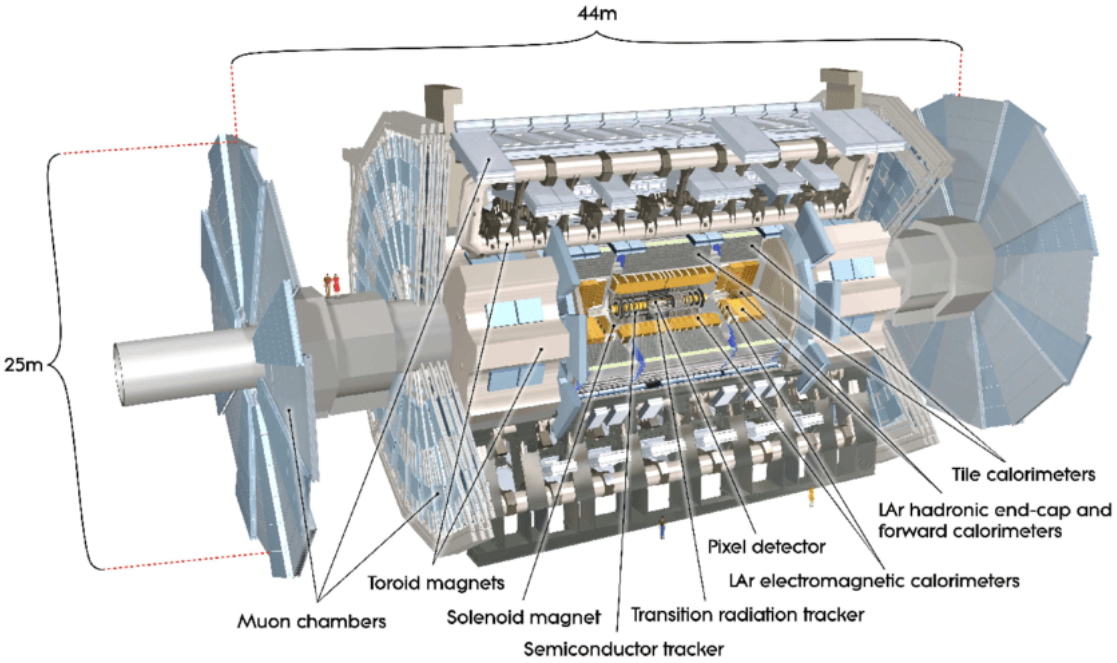

Figure 3.3.: The ATLAS detector with its sub-detectors and magnet systems (© CERN).

in the $x - y$ plane around the beam (z) axis and the polar angle θ is defined as the angle from beam (z)-axis. In the description of relativistic particles ($m << E$) , it is convenient to use *pseudorapidity* defined using the polar angle θ as:

$$\eta = -\ln[\tan\left(\frac{\theta}{2}\right)]. \tag{3.5}$$

The difference in pseudorapidity $\Delta\eta$ is invariant under a Lorentz transformation. For the same reason, the distance defined in the $\eta - \phi$ space is often used:

$$\Delta R = \sqrt{\Delta\eta - \Delta\phi}. \tag{3.6}$$

The transverse momentum (p_T) and the transverse energy (E_T) of the particle are defined in the $x - y$ plane as:

$$p_T = \sqrt{p_x^2 - p_y^2},\ E_T = E\sin(\theta). \tag{3.7}$$

3.2.1. Magnet System

The ATLAS magnet systems consists of four super conducting magnets, shown in Figure 3.4.

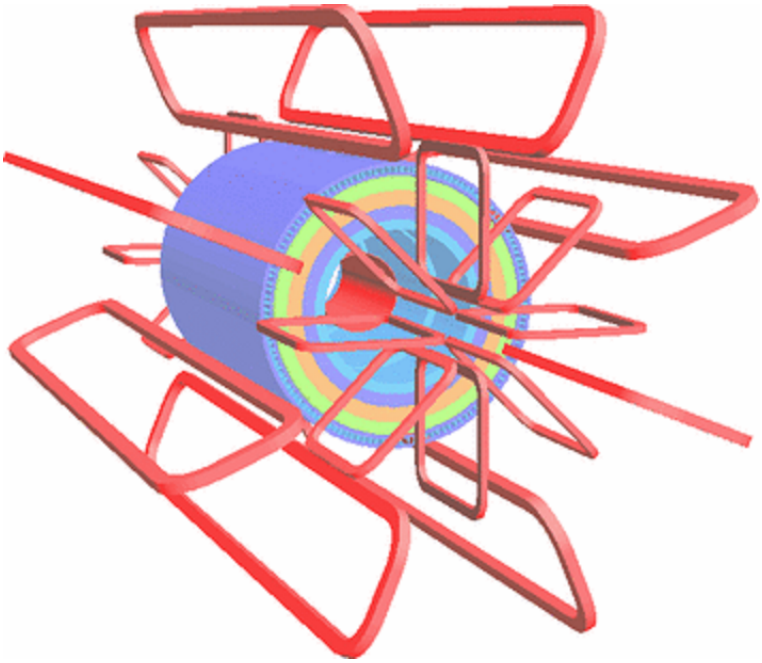

Figure 3.4.: The magnet system of the ATLAS experiment with central solenoid magnet and barrel and end-cap toroids (© CERN).

The Central Solenoid (CS)

The Central Solenoid (CS) creates a 2 T axial magnetic field in the region where the inner tracker (for details see Section 3.2.2) is installed. The dimensions of the solenoid magnet are: 5.3 m in length, 2.4 m inner diameter, and an outer diameter of 2.49 m.

The air-core Toroid

The air-core Barrel Toroid (BT) and two air-core End-Cap Toroids (ECT) provide a toroidal field configuration for the muon spectrometer (for details see Section 3.2.4). Each toroid is composed of eight super-conducting coils, aligned radially and symmetrically around the beam pipe. The end-cap toroids are rotated by 22.5^o in relation to the barrel toroid. In this way the magnetic fields overlap. This system provides a toroidal magnetic field of about 0.5 T for the muon detectors in the barrel region, and of about 1 T for the muon detectors at the end-caps. The barrel toroid is 25.3 m long and the inner diameter is 9.4 m, while the outer one is 20.1 m. The working point temperature of both magnet systems is 4.5 K and is cooled down with liquid helium.

3.2.2. The Inner Tracking System

The ATLAS inner tracking system is also named Inner Detector (ID) and is designed to measure the direction, momentum, and charge of electrically-charged particles produced

in each proton-proton collision. The ID is the closest to the interaction point and is composed of three subsystems: the pixel detector, the semiconductor tracker (SCT), and the transition radiation tracker (TRT), which have barrel and end-cap components, as shown in Figure 3.5. The trajectories of charged particles can be determined by their ionising effects on the material they pass through. The track curvature in a magnetic field can be used to determine a particle's momentum and charge. By reconstructing the tracks of the particles, their momentum and interaction vertices can be determined.

The Pixel Detector

The Pixel Detector is designed to provide a very high-precision set of measurements as close to the interaction point as possible. The system consists of three barrels at average radius of 50.5 mm, 88.5 mm, and 122.5 mm and three discs on each side of the barrel, which are installed perpendicular to the beam pipe. The overall barrel has 1.744 modules. The pixel detector covers the region defined by $|\eta| < 2.5$ and each module is a silicon wafer sectioned into pixels with a minimum size of $50 \times 400\ \mu m^2$ and contains 16 front-end chips (FE) bump-bonded to the sensor; the total number of readout channels, in three layers is in the barrel and three discs in each end-cap, $\sim$ 80.4 million. The accuracy of the single hit resolution is $10 \times 115\ \mu\text{m}^2$ ($R/\phi \times z$ for the barrel, $R/\phi \times R$ for discs).
The innermost layer is important for the identification of secondary vertices caused by heavy flavour decays. For improving the reconstruction of these vertices, an additional pixel layer was attached during the shutdown between 2012 and 2015. This layer is called *Insertable B-layer* (*IBL*) which is located at a distance of 25.7 mm to the beam pipe.

The Semi-Conductor Tracker (SCT)

The Semi-Conductor Tracker (SCT) system is designed to provide precision measurements of hits per track in the intermediate radial range, contributing to the measurement of momentum, impact parameter, and vertex position, as well as providing good pattern recognition. The SCT surrounds the Pixel detector, also covers the region defined by $|\eta| < 2.5$. It consists of four double layers of silicon microstrip detectors in the barrel and nine disks for each end-cap, which can give information of four space points for each track. The strips are joined in pairs with angles of 40 mrad in order to measure both $R - \phi$ coordinates. The resolution per module in the barrel is 17 μm and 580 μm, for $R-\phi$ and z directions respectively and 17 μm and 580 μm, for $R-\phi$ and R in the disks, respectively. The SCT has 4.088 modules and about 6.3 million readout channels.

The Transition Radiation Tracker (TRT)

The Transition Radiation Tracker (TRT) provides additional information of the particle type that flew through the detector, i.e. to distinguish electrons from pions. The TRT

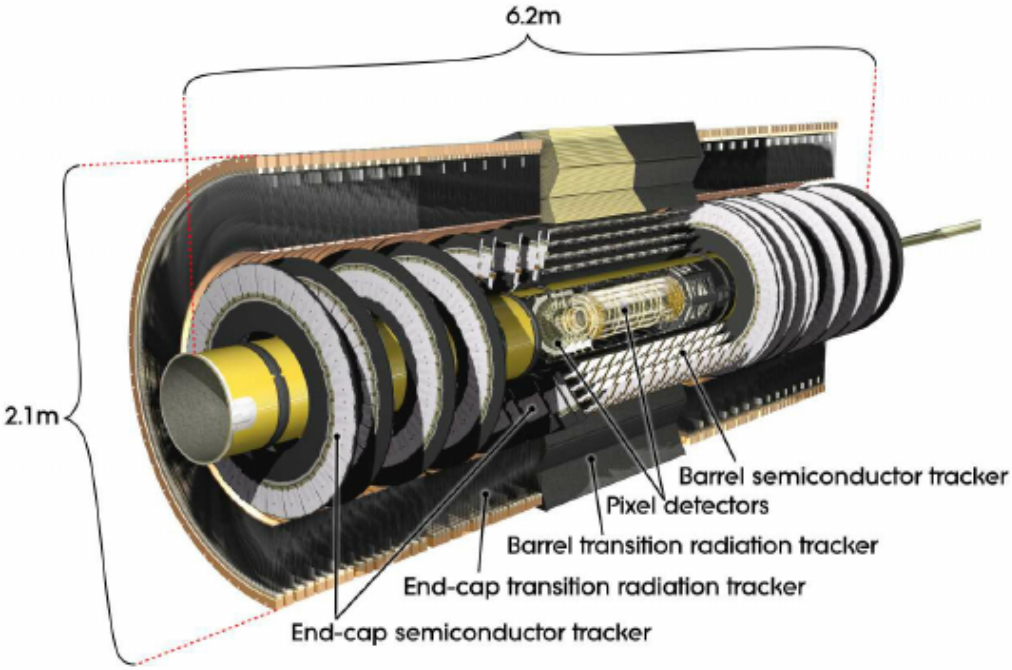

(a)

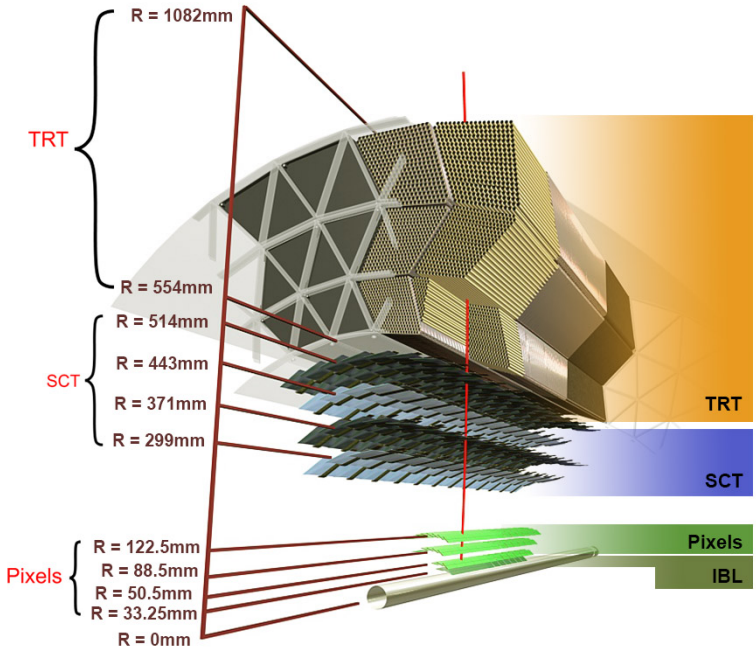

(b)

Figure 3.5.: The Inner Detector of the ATLAS experiment. a): Inner Detector with its different sub-detectors. b): The transverse section of the ID including the distances of the detector layers with respect to the beam line (© CERN).

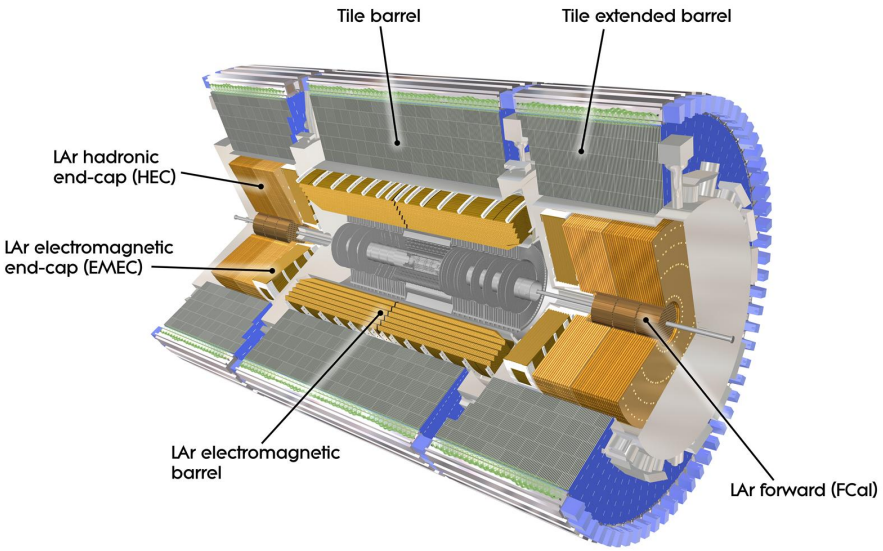

Figure 3.6.: The Calorimeter System of the ATLAS experiment (© CERN).

covers the region defined by $|\eta| < 2.0$ and consists of 4 mm diameter straw tubes filled with a $Xe/CO_2/O_2$ gaseous mixture. It provides a large number of hits (typically 36 per track) on $R - \phi$. The transverse momentum of charged tracks are grater than 0.5 GeV. The length of the straws (50.000) is 144 cm in the barrel region and the straws are parallel to the beam axis, while in the end-cap region, the 39 cm long straws (250.000) are arranged radially in wheels (18). The accuracy is of 130 μm per straw in $R - \phi$ direction. The total number of TRT readout channels is approximately 350.000.

3.2.3. The Calorimeter System

The calorimeter system is used to measure the energy of hadrons, electrons, and photons. For electron and photon identification the electromagnetic calorimeter (EM) is used, and the hadronic calorimeter is dedicate to the identification of hadrons. The calorimeter system of the ATLAS detector is of a type known as a sampling calorimeter which has alternately placed layers as structure of active and passive detector material. The energy deposits of particle showers induced by particle interaction with passive material are measured in the active material. An overview of the calorimeter system is shown in Figure 3.6. The calorimeter system provides containment for both electromagnetic and hadronic showers, i.e. only muons are able to reach the muon system. Hence, the calorimeters must be deep enough and its depth is an important design parameter. The total thickness of the EM calorimeter is > 22 radiation lengths (X_0) in the barrel and > 24 X_0 in the end-caps. For the hadronic calorimeters ≈ 9.7 interaction lengths (λ) of active calorimeter in the barrel and 10λ in the end-caps are satisfying requirements to

provide good resolution for high-energy jets.

The Electromagnetic (EM) Calorimeter

The Electromagnetic calorimeter is ideally suited for precision measurements of electrons and photons, because of its fine granularity over the η region matched to the inner detector. In order to satisfy the physics requirements for jet reconstruction and E_T^{miss} measurements the rest of the calorimeter is coarser. The EM calorimeter is divided into a barrel part ($|\eta| < 1.475$) and two end-cap components ($1.375 < |\eta| < 3.2$), placed in their own cryostat, and provides complete ϕ symmetry without azimuthal cracks. The EM calorimeter uses liquid argon (LAr) as an active material and lead as passive absorber material over its full coverage. The thickness of the lead has been optimised as a function of η in terms of EM calorimeter performance in energy resolution. The design resolution for the EM calorimeter is $\frac{\sigma_E}{E} = \frac{10\%}{\sqrt{E}} \oplus 0.7\%$ [3].

The Hadronic Calorimeter

The hadronic calorimeter of ATLAS consists of three different sub-detectors. They are the tile calorimeter (TileCal), the LAr hadronic end-cap calorimeter (HEC), and the LAr forward calorimeter (FCal).
The TileCal is placed directly outside the EM calorimeter. It consists of a barrel and two extended barrels covering the range of $|\eta| < 1.0$ and $0.8 < |\eta| < 1.7$, respectively. Steel is used as absorber and scintillating tiles as active material. The barrel and extended barrels are divided azimuthally into 64 modules and segmented in depth in three layers thickness of: 1.5, 4.1 and 1.8 λ for the barrel and 1.5, 2.6 and 3.3 λ for the extended barrel. Radially, the tile calorimeter extends from an inner radius of 2.28 m to an outer radius of 4.25 m.
The HEC consists of two independent wheels per end-cap, located directly behind the end-cap electromagnetic calorimeter and sharing the same LAr cryostats. The HEC extends out to $|\eta| = 3.2$. Copper plates are used as absorbing material, while LAr is used again as active material. The inner radius of the HEC is 0.475 m and the outer one is 2.03 m.
The FCal are located in each end-cap of ATLAS and are divided into three modules. The first one has copper as passive material, while the other two have tungsten. The active material is, once more, LAr. The designed resolution for the hadronic calorimeter is $\frac{\sigma_E}{E} = \frac{50\%}{\sqrt{E}} \oplus 3\%$ for the barrel and end-caps and $\frac{\sigma_E}{E} = \frac{100\%}{\sqrt{E}} \oplus 10\%$ [3]in the forward regions.

3.2.4. The Muon System (MS)

The last set of ATLAS sub-detectors is the muon spectrometer. Due to the construction of the previous systems, muons are the only charged particles expected to reach this detector. The overall layout of the MS is shown in Figure 3.7. The muon measurements

[3] The energy E is measured in GeV

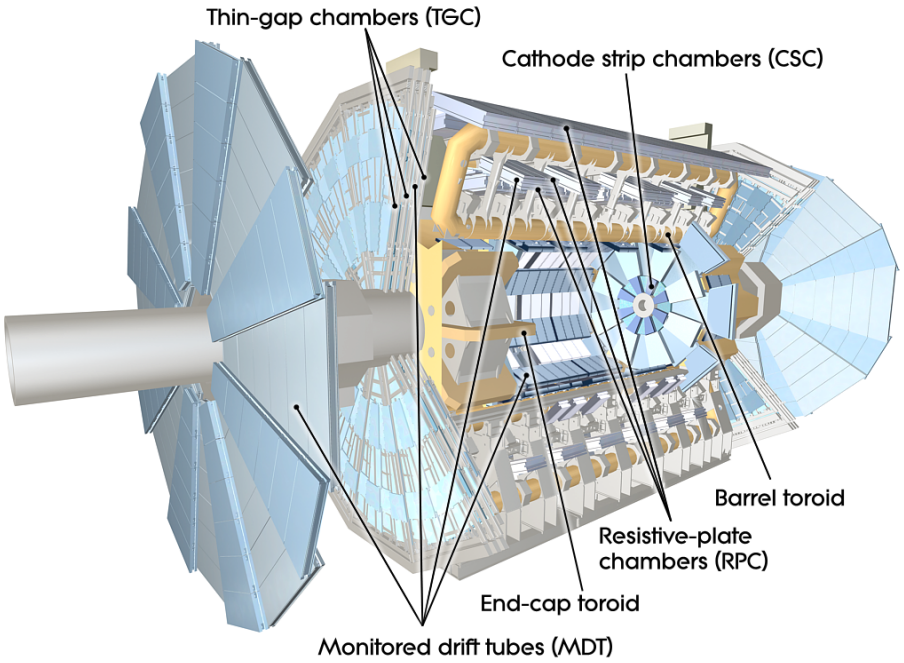

Figure 3.7.: The Muon System of the ATLAS experiment (© CERN).

are based on the magnetic deflection of muon tracks in the large superconducting air-core toroid magnets. The MS is instrumented with separate trigger and high-precision tracking chambers. The muons are bend by the magnetic field with the bending power[4] from 1.5 to 5.5 T, for the barrel toroid in the $|\eta| < 1.4$ region and by the two smaller end-cap toroids with the bending power from 1 to 7.5 T, in the $1.6 < |\eta| < 2.7$ regions. In the $1.4 < |\eta| < 1.6$ regions the magnetic field is provided by a combination of barrel and end-cap fields. The bending power is lower in such transistion regions. The field provided by this magnet configuration is mostly orthogonal to the muon trajectories, while minimising the degradation of resolution due to multiple scattering. In total, approximately 1800 Hall sensors take part in field monitoring which are distributed throughout the spectrometer volume.
In the barrel region, tracks are measured in chambers arranged in three cylindrical layers around the beam axis at a radius of approximately 5 m, 7 m, and 10 m. In the end-cap regions, the muon chambers with the shape of wheels are perpendicular to the beam axis and located at $|z| \approx 7.4$ m, 10.8 m, 14 m and 21.5 m from the interaction point. The Monitored Drift Tube chambers (MDTs) are used for a precision measurement of the track coordinates in the principal bending direction of the magnetic field. They

[4] bending power is characterised by $\int Bdl$, where B is the field component normal to the muon direction and the integral is computed along an infinite-momentum muon trajectory, between the innermost and outermost muon chamber planes.

cover the pseudorapidity range $|\eta| < 2.7$ (in the innermost end-cap layer their coverage is limited to $|\eta| < 2.0$). These chambers consist of three to eight layers of drift tubes filled with a gas mixture of 93 % Ar and 7% CO_2, at a pressure of 3 bar, which achieve an average resolution of 80 μm per tube.
The cathode strip chambers (CSC) are multiwire proportional chambers with cathodes segmented into strips in orthogonal directions. A higher granularity is used in the innermost plane over $2 < |\eta| < 2.7$. The coordinates are measured from the induced-charge distribution. The resolution of a chamber is 40 μm in the bending plane and about 5 mm in the transverse plane.
The trigger chambers cover the pseudorapidity range $|\eta| < 2.4$. In the barrel region, resistive plate chambers (RPC) are used while thin gap chambers (TGCs) are used in the end-cap regions. The trigger chambers provide bunch-crossing identification, well-defined p_{T} thresholds, and measure the muon coordinate in the direction orthogonal to the direction, determined by the precision-tracking chambers. The design resolution of the muon spectrometer is $\sigma_{p_T}/p_T = 10$ % at $p_{\mathrm{T}} = 1$ TeV.

3.2.5. The Trigger and Data Acquisition Systems

The ATLAS Trigger and data acquisition (TDAQ) systems were designed to reduce the event rate from about 1 GHz to $\sim$ 200 Hz. They are based on signatures of high p_T particles and missing transverse energy, since only the interesting events should be selected and stored. The ATLAS TDAQ system based on three levels of online event selection is presented in Figure 3.8. Each trigger level checks the decision made at the previous level and in case of necessity additional selection criteria are applied.
The Level1 trigger (LVL1) searches for signatures from high p_T particles and also selects events with large missing and total transverse energy. The LVL1 trigger is completely hardware based and takes decisions within 2.5 μs by looking into the calorimeter and the fast muon cambers (RPC and TGC) data. Meanwhile, the front-end electronics of the several sub-detectors keep the complete data in the pipeline memories. The data is then moved to the Readout Buffers (ROB) via the Readout Drivers (ROD). The event rate after LVL1 is about 75 kHz. For each event accepted by the LVL1 trigger Regions-of-Interest (RoIs) are defined which are used by the High-Level-Trigger (HLT).
The HLT is divided into two software-based trigger levels, the second level trigger (LVL2) and the Event Filter (EF). The LVL2 receives a list with RoI, which contains the positions of the objects selected by LVL1. In this way, the LVL2 only needs to access about 2% of the full event data in order to take its decision. After this level, which has a latency of 10 ms, the event rate is about 3.5 kHz.
Finally, the event information is then passed to the Sub-Farm Input (SFI), which provides the full data to the EF. This filter has a latency of 1 s and achieves an event rate of about 200 Hz. The selected events are then moved into the Sub-Farm Output (SFO) and stored to be analysed later.

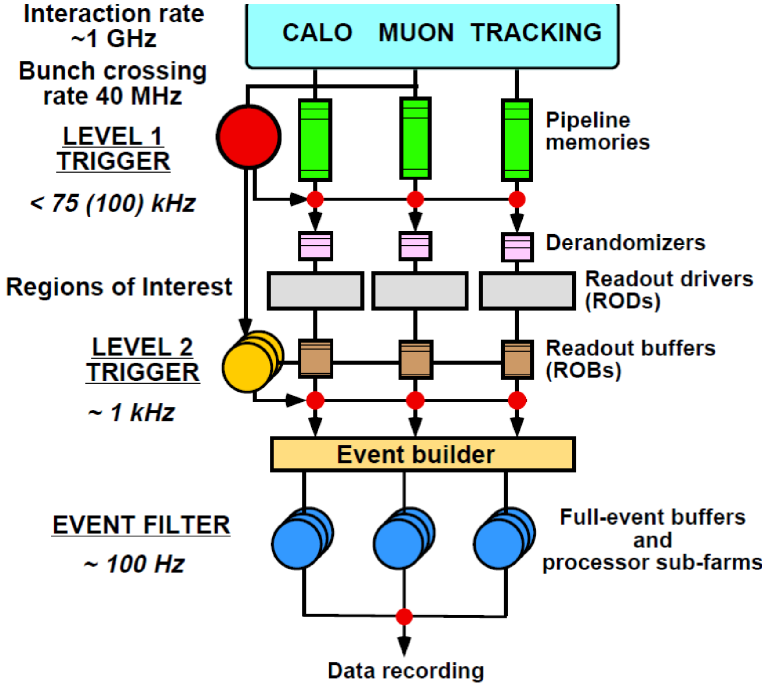

Figure 3.8.: Block diagram of the ATLAS TDAQ system (© CERN).

Performance of the ATLAS Experiment

During the Run I period of the LHC, the ATLAS experiment collected pp collision data at centre of mass energies of $\sqrt{s} = 7$ TeV and $\sqrt{s} = 8$ TeV. In 2011, the integrated luminosity recorded by the ATLAS detector ($\sqrt{s} = 7$ TeV) was 5.08 fb^{-1}(93 % of the total delivered by LHC) and in 2012 ($\sqrt{s} = 8$ TeV) the corresponding integrated luminosity was 21.3 fb^{-1} (93.4% of the total delivered by LHC). The recorded data must fulfill ATLAS good data quality (DQ) requirements. Figure 3.9 shows the cumulative luminosity versus time of good quality data taken during stable beams. For pp collisions at 7 and 8 TeV centre of mass energy, the integrated luminosity was 4.57 fb^{-1} (90 % of the total recorded by ATLAS) and 20.3 fb^{-1}(95 % of the total recorded by ATLAS), respectively. The monitoring of recorded events is performed online during data taking using automated systems, like the *Data Quality Monitoring Framework* [69]. At this stage, all possible parameters and conditions of the ATLAS detector are constantly inspected. The recorded events are calibrated and further checked offline by the detector subgroups and experts. Only events fulfilling all physics requirements are stored in the so-called *Good Run List*(GRL).
Overall, data corresponding to 20.2 fb^{-1} integrated luminosity are used for the presented analysis collected by the ATLAS detector between April and October 2012 with colliding proton beams at $\sqrt{s} = 8$ TeV centre of mass energy.

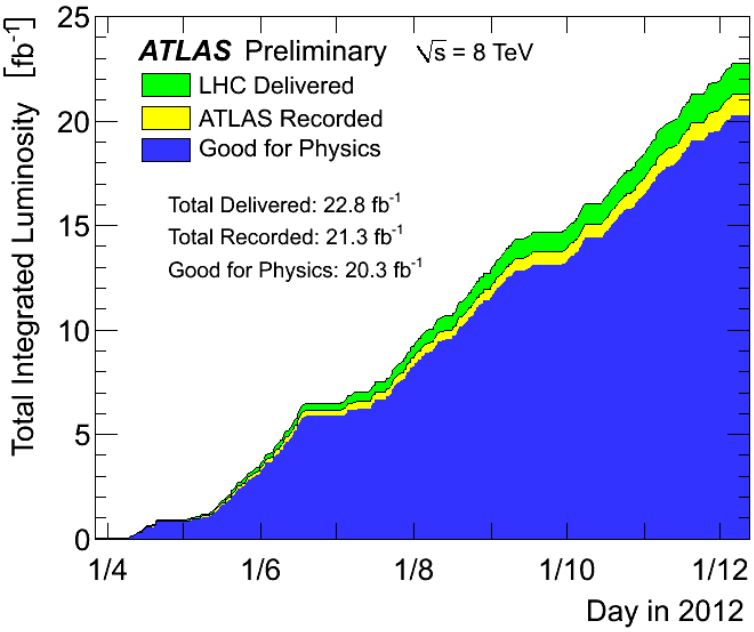

Figure 3.9.: Cumulative luminosity versus time delivered (green), recorded by ATLAS (yellow), and certified to be good quality data (blue) during stable beams for *pp* collisions at 7 and 8 TeV centre of mass energy in 2011 and 2012.

CHAPTER 4

Object Definition

The $t\bar{t}$ dilepton channel produces the following physics objects: electrons, muons, missing transverse energy, from the two neutrinos, and jets, in particular two b jets. In this chapter the identification and reconstruction of these objects are discussed.

4.1. Electrons

The electron candidates, in the ATLAS detector (*central region*), are reconstructed from energy deposits in the electromagnetic (EM) calorimeter matched to a track in the inner detector [70]. The reconstruction process includes three steps as follows.

- *Cluster reconstruction*: The EM clusters are reconstructed by seed clusters of longitudinal towers with a threshold above 2.5 GeV of the total cluster transverse energy using a *sliding-window algorithm* [71]. This algorithm is based on summing cells within a fixed-size rectangular window in the $\eta - \phi$ plane and the position is adjusted to maximise the contained transverse energy. The fact that the cluster size is fixed allows for a very precise cluster energy calibration.
- *Track association with the cluster*: The tracks with $p_T > 0.5$ GeV are extrapolated from their last measured point to the middle layer of the EM calorimeter. A track and a cluster are considered to be successfully matched if the distance between the track impact point and the EM cluster barycentre is $|\eta| < 0.05$. The effect of bremsstrahlung losses on the asimuthal distance is also taken into account with a track-cluster matching window of $\Delta\phi = 0.1$ on the side where the extrapolated track bends as it traverses the solenoidal magnetic field. An electron candidate is considered as reconstructed if at least one track is matched to the seed cluster. In case of multiple track matches to a cluster, tracks with hits in the pixel detector or

the SCT are given priority, and the match with the smallest $\triangle R = \sqrt{\Delta\eta^2 + \Delta\phi^2}$ distance is chosen. If the matched track does not exist, the cluster is classified as an unconverted photon candidate.

- *Reconstructed electron candidate*: After a successful track-cluster matching, the cluster sizes are optimised to take into account the overall energy distributions in the EM barrel cells size of 3×7 and in the EM endcaps cells size of 5×5 in $\eta - \phi$ space. The total reconstructed electron-candidate energy is determined from the sum of the estimated energy deposit in the material in front of the EM calorimeter, the measured energy deposit in the cluster (corrected for the estimated fraction of energy measured by the sampling calorimeter), the estimated energy deposit outside the cluster (lateral leakage), and the estimated energy deposit beyond the EM calorimeter (longitudinal leakage) [72].

Based on information from the final cluster and the track best matched to the original seed cluster the four-momentum of central electrons is computed.
Not all objects built by the electron reconstruction algorithms are signal electrons. Background objects include hadronic jets as well as background electrons from photon conversions, Dalitz decays and semileptonic heavy flavor hadron decays. It is necessary to reject as much background objects as possible and keeping the efficiency for signal electrons high. For this reason multivariate analysis (MVA) techniques are employed in this analysis. Out of the different MVA techniques, the likelihood (LH) technique was used. The electron LH makes use of signal and background probability density functions (PDFs) of the discriminating variables. For each object, a probability is calculated, whether it is signal or background. The signal and background probabilities for a given electron are combined into a discriminant $d_{\mathcal{L}}$ on which a cut is applied [70]:

$$d_{\mathcal{L}} = \frac{\mathcal{L}_s}{\mathcal{L}_s + \mathcal{L}_b};\ \mathcal{L}_s(\overrightarrow{x}) = \prod_{i=1}^{n} \mathrm{P}_{s,i}(x_i), \tag{4.1}$$

where $\overrightarrow{x}$ is the vector of variable values and $P_{s,i}(x_i)$ is the value of the signal probability density function of the i^{th} variable evaluated at x_i. In the same way, $P_{b,i}(x_i)$ refers to the background probability function.
Signal and background PDFs used for the electron LH identification are obtained from data. The variables measuring bremsstrahlung effects are included. Furthermore, additional variables with significant discriminating power but also a large overlap between signal and background that prevents explicit cuts can be included.
The electron candidates are characterised by LH selections as: LOOSE, MEDIUM and VERY TIGHT. The efficiencies of electrons in each case roughly match the electron efficiencies in the equivalent cut-based selections, but to have better rejection of light-flavor jets and conversions. In order to increase the electron signal efficiency, while keeping the rate of misidentified leptons low, the medium LH working point was used for the presented measurement.
In order to further reject hadronic jets mis-identified as electrons, isolation cuts are

required. The electron isolation in this analysis requires that the ratio of the sum of transverse momentum of the tracks with $p_T > 0.4$ GeV in a cone of size $\Delta R = 0.3$ around the electron track, to the p_{T} of the electron is less than 0.12 i.e. $\frac{p_T^{cone30}}{p_T} < 0.12$. The tracks considered in the sum must originate from the primary vertex associated to the electron track and pass the good quality track selection. In addition, the electron track longitudinal impact parameter with respect to the primary vertex, z_0, is required to be smaller than 2 mm.
As already mentioned above, central electrons are used for the present analysis, with $|\eta_{cluster}| < 2.47$, where $\eta_{cluster}$ is the pseudorapidity of the calorimeter cluster associated with the electron candidate. The calorimetry transition region between barrel and endcap, $1.37 < |\eta_{cluster}| < 1.52$, is excluded. Electron candidates are required to match the logical OR of the lowest unprescaled single electron trigger in 2012 data-taking, *EF_e24vhi_medium1*, and single electron *EF_ e60_ medium1* trigger applying a threshold on the cluster E_T at the Event Filter (EF), trigger stage of 24 and 60 GeV, respectively. In case of transverse energy of electron candidate is more than 60 GeV ($E_T > 60$ GeV), the two triggers are combined with a logical OR to improve the trigger efficiency.
In order to measure identification and reconstruction efficiency, a clean and unbiased sample of electrons is required. The *tag-and-probe* method is used to derive the electron efficiencies from $Z \to ee$ and $J/\Psi \to ee$ events in data and MC samples. In both cases, strict selection criteria are applied to one of the two decay electrons (called "tag") and the second electron candidate ("probe") is used for the efficiency measurement. The number of matched and probed leptons in a sample is used to calculate the efficiencies in data (ϵ_{data}) and MC (ϵ_{MC}) samples to derive scale factors (SF) according to $SF = \epsilon_{data}/\epsilon_{MC}$. SFs are typically a few percent different from unity. The reconstruction and identification efficiency of electrons parametrised as a function of E_T and η is given in Figure 4.1.

4.2. Muons

The muon identification is performed according to several reconstruction criteria, according to the available information from the inner detector (ID), the muon spectrometer (MS), and the calorimeter systems. These reconstruction criteria lead to different muon "types" [73].

1. *Stand-Alone (SA) muons*: The muon trajectory is reconstructed only in the MS. SA muons are mainly used to extend the acceptance to the range $2.5 < |\eta| < 2.7$ which is not covered by the ID;

2. *Combined (CB) muons*: This is the main type of reconstructed muons, where track reconstruction is performed independently in the ID and MS. These tracks are later combined into one combined track. CB candidates have the highest muon purity;

3. *Segment-tagged (ST) muons*: A track in the ID is classified as a muon if, once extrapolated to the MS, it is associated with at least one local track segment in

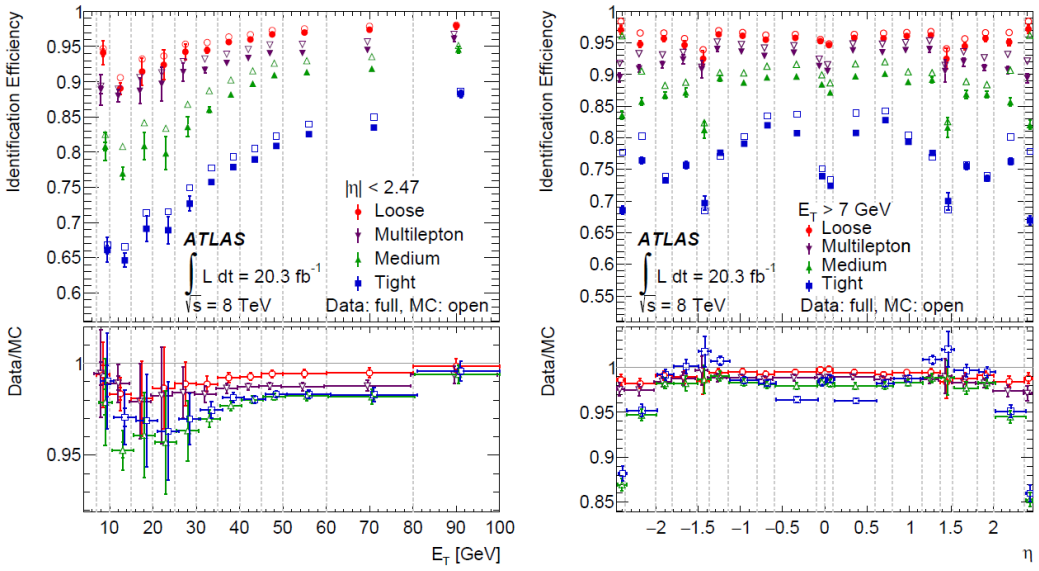

Figure 4.1.: Identification efficiency in data as a function of E_T (left), η (right) and the number for loose LH, medium LH and very tight LH selections, compared to MC expectation for electrons from $Z \to ee$ decay. The lower panel shows the data-to-MC efficiency ratios. The data efficiency is derived from the measured data-to-MC efficiency ratios and the MC prediction for electrons from $Z \to ee$ decays [70].

the MDT or CSC chambers;

4. *Calorimeter-tagged (CaloTag) muons*: A track in the ID is identified as a muon if it is associated to an energy deposit in the calorimeter compatible with a minimum ionising particle. This type has the lowest purity of all the muon types but it recovers acceptance regions with no MS coverage.

For the present analysis CB muons are used. In addition to combined track information (from ID and MS), the muon candidates are required to have pseudorapidity being limited by the ID acceptance, $|\eta| < 2.5$. These include requirements of hit patterns in the Pixel, SCT and TRT detectors which are:

- Number of pixel hits + number of crossed dead pixel sensors > 0.
- Number of SCT hits + number of crossed dead SCT sensors ≥ 5
- Number of pixel holes + number of SCT holes < 3
- Denote n = nTRTHits + nTRTOutliers. For $0.1 < |\eta| < 1.9$: n > 5 and nTRTOutliers/n < 0.9

The transverse momentum must fulfill the requirement: $p_T > 25$ GeV and in addition, the muon track longitudinal impact parameter with respect to the primary vertex, z_0, is required to be smaller than 2 mm.
The muon objects are required to match the logical OR of two single muon triggers during the 2012 data taking, *EF_mu24i_tight* and *EF_mu36_tight*. The triggers apply a threshold on the p_T at the EF trigger stage of 24 and 36 GeV, respectively. Separation by the distance $\Delta R > 0.4$ from any selected jet is also required, for muons.
The muons are required to satisfy p_{T} dependent and track based isolation criteria denoted as *mini-isolation* [74]. This isolation has good performance under high pile-up conditions and in boosted top quark topologies, where the separation between the muon and a b-tagged jet scales as $m_{top}/p_{T,top}$. The *mini-isolation* is defined as scalar sum of the transverse momentum p_T of the tracks in a cone of $\Delta R < 10$ GeV$/p_{\mathrm{T}}^{\mu}$ around the muon track, which have a $p_{\mathrm{T}}^{track} > 1$ GeV. The *mini-isolation* is required to be less than 5% of the muon p_T.
The reconstruction, identification, and trigger efficiencies of muons differ between data and simulation. The *tag-and-probe* method is used to derive the muon efficiencies from $Z \to \mu\mu$ events and corresponding SFs are applied to MC simulation to bring it in agreement with the data efficiency. SFs are typically a few percent different from unity. The reconstruction efficiency of muons parametrised as a function of p_T and η is given in Figure 4.2.

4.3. Jets

Jets are key ingredients of many high-energy physics measurements at the LHC as they are the dominant feature of high-energy pp interactions. A jet is a composite object

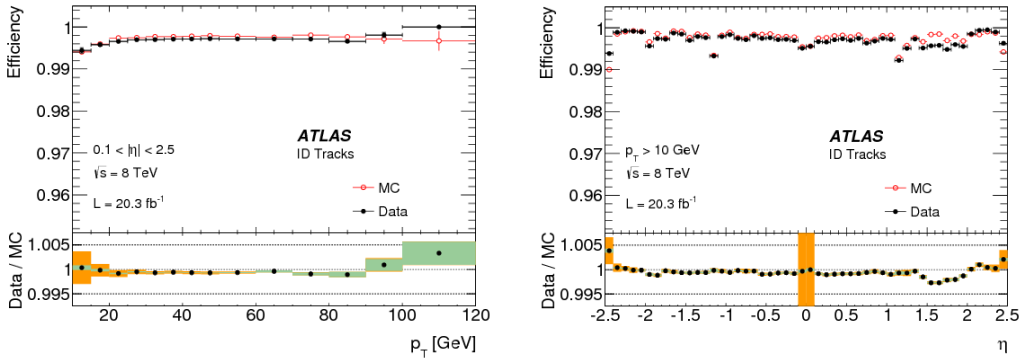

Figure 4.2.: ID muon reconstruction efficiency as a function of p_T (left) , η (right) measured in $Z \to \mu\mu$ events for muons with $p_T > 10$ GeV [73].

of collimated sprays of particles and resulting from fragmentation of hard scattered partons. The kinematic properties of the jet reflect those of an initiating parton. The most widely accepted jet definition for hadron collider experiments involves a clustering of calorimeter cells in a metric of $\eta - \phi$, which has the virtue of taking into account the Lorentz boost of jet systems. The properties that should be satisfied by a jet definition are [75]:

1. Simple to implement in an experimental analysis;
2. Simple to implement in the theoretical calculation;
3. Defined at any order of perturbation theory;
4. Yields finite cross sections at any order of perturbation theory;
5. Yields a cross section that is relatively insensitive to hadronisation.

This analysis uses jets reconstructed by first clustering energy deposits into *topo-clusters* (calorimeter jets) [76] and then clustering these using the $anti - k_t$ [77] algorithm with distance parameter $R = 0.4$. The reconstruction is done using the *FastJet* [78] software package. The *topo-clusters* formation algorithm starts from a seed cell with signal-to-noise ratio above a threshold of $S/N = 4$. Cells neighbouring the seed (or the cluster being formed) that have a signal-to-noise ratio of $S/N \geq 2$ are included iteratively. Finally, all calorimeter cells neighbouring the formed *topo-clusters* are added. The *topo-clusters* algorithm efficiently suppresses the calorimeter noise.
The next stage is calibration of the *topo-clusters*. At first the *topo-clusters* are calibrated at the EM scale to measure energy deposited in the calorimeter via the particles producing electromagnetic showers[1]. A second *topo-cluster* built on previous EM scale collection is calibrated using the local cluster weighting (LCW) [79, 80] method. In the

[1]For the calibration test-beam data using electrons were used.

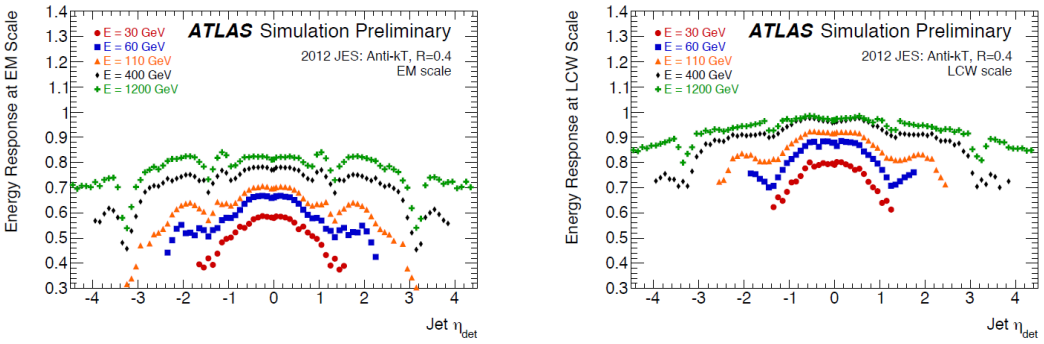

Figure 4.3.: Energy response as a function of η_{det} (the η of the jet relative to the geometric centre of the detector) for EM (left) and LCW (right) scale $anti-k_t$, $R = 0.4$ jets before calibration [81].

LCW method, clusters are classified as electromagnetic or hadronic by considering the non-compensating nature of the ATLAS calorimeters. Secondly, the energy falling outside clustered cells is estimated from how isolated the cluster is, and finally the amount of energy falling in inactive areas of the detector is estimated from the position and energy deposited in each layer of the calorimeter [76]. The jets are calibrated using energy and pesudo-rapidity η dependent calibration factors[2] and corrected for pileup effects. The LCW method improves the resolution compared to the EM scale, as shown in Figure 4.3. The next step after calibration is to apply a jet finding algorithm. The $anti-k_t$ inclusive jet finding algorithm which belongs to a class of sequential recombination jet algorithms is used. The algorithm repeatedly calculates the distance d_{ij} between two clusters i and j and the distance d_{iB} between cluster i and the beam direction (B). In case the distance is smallest between the clusters i and j , they are combined (four momentum recombination scheme is used) while if the distance is the smallest between i and B the object i is assigned as jet and removed from the list of clusters. The distances are defined as:

$$d_{ij} = min\ (k_{ti}^{2p},\ k_{tj}^{2p})\frac{\Delta_{ij}^2}{R^2};\ d_{iB} = k_{ti}^{2p}{}^{3} \tag{4.2}$$

where $\Delta_{ij}^2 = (y_i - y_j)^2 + (\phi_i - \phi_j)^2$ and k_{ti}, y_i, ϕ_i are the transverse momentum, rapidity and azimuth of cluster i, respectively. For the anti$-k_t$ jet-clustering algorithm the parameter p is equal to -1 ($p = -1$) . The key feature of the algorithm is that the soft particles do not modify the shape of the jet, while hard particles do. The resulting shape of hard jets using the $anti-k_t$ algorithm is circular with a radius R and the softer jets have more complex shapes as shown in Figure 4.4. The jets reconstructed using the $anti-k_t$ algorithm satisfy all requirements listed above. As discussed above jet energy calibrations can be performed using EM scale (EM+JES) and LCW calibration (LCW+JES) including jet calibration using in-situ techniques, which is applied to jets

[2]The calibration factors derived from Monte Carlo simulations of charged and neutral pions.
[3]d_{iB} is a distance to the beam.

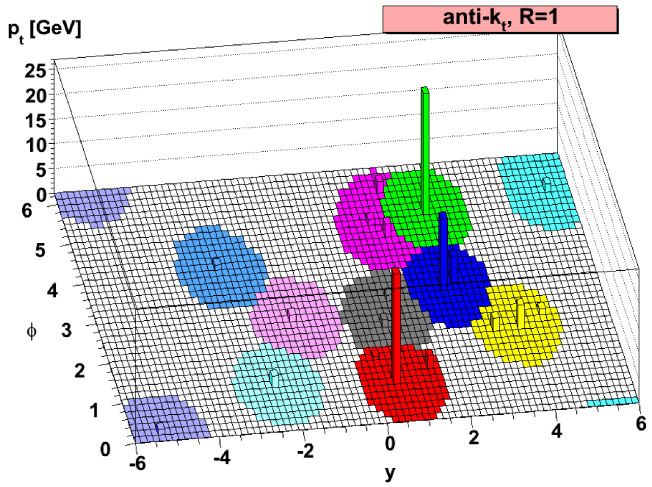

Figure 4.4.: A sample parton-level event, together with many random soft emissions, clustered with the $anti - k_t$ algorithm [77].

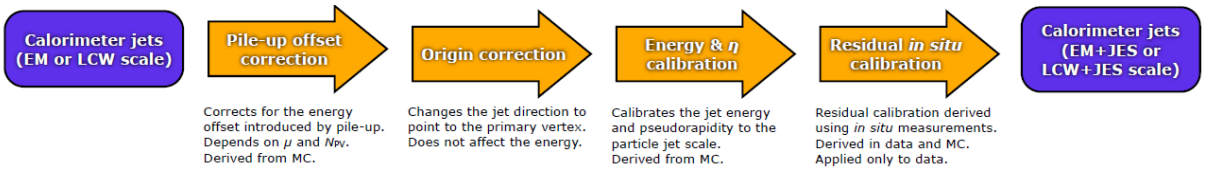

Figure 4.5.: Overview of the ATLAS jet calibration scheme [82].

reconstructed only in data [81]. Figure 4.5 shows schematically the jet calibration chain.

Jet Cleaning

After reconstruction and energy calibration, jets are required to have $p_T > 25$ GeV and $|\eta| < 2.5$. In order to avoid double counting of electrons, if a reconstructed jet is within $\Delta R < 0.2$ of a selected electron, the jet is discarded. Also in case of an electron being within $\Delta R < 0.4$ to remaining jets, the electron is removed.

The Jet Vertex Fraction

In order to further reduce multiple proton-proton interaction effects from the same bunch crossing (*in-time* pile-up) and next and/or previous bunch crossings (*out-of-time* pile-up) the *Jet Vertex Fraction* (JVF) variable is used to identify the origin vertex of a given jet [83]. The JVF is defined for each primary vertex (PV). For a given jet labeled jet$_i$,

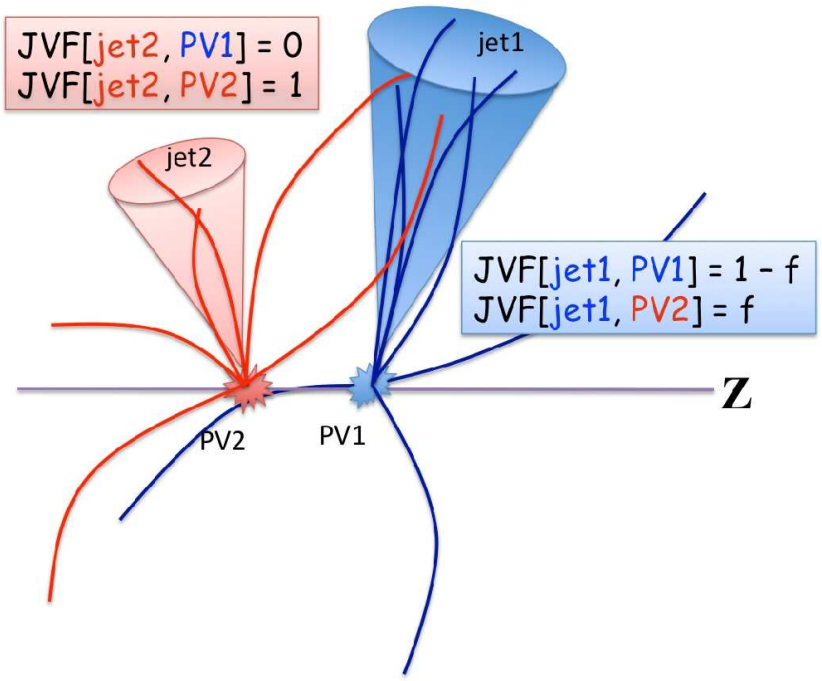

Figure 4.6.: Schematic representation of the JVF principle.

its JVF with respect to the primary vertex PV_j is given by:

$$JVF(jet_i, PV_j) = \frac{\sum_k p_T(track_k^{jet_i}, PV_j)}{\sum_n \sum_l p_T(track_l^{jet_i}, PV_n)}, \tag{4.3}$$

where k runs over all tracks originating from PV_j matched to jet_i, n over all primary vertices in the event, and l runs over all tracks originating from PV_n matched to jet_i. Only tracks with $p_T > 500$ MeV are considered in the JVF calculation. The JVF is defined with respect to the event hard-scatter vertex, selected as the primary vertex with the highest $\sum_{tracks} p_T^2$. JVF may be thus interpreted as an estimate of the fraction of energy in the jet that can be associated with the hard-scatter interaction. The principle of the JVF variable is shown schematically in Figure 4.6. Figure 4.7 shows the discriminating power of the JVF distribution between hard-scatter and pile-up jets with $p_T^{jet} > 20$ GeV in a $Z(\rightarrow ee) +$ jets sample. A value of -1 is assigned to calorimeter jets which do not have associated tracks. The value of JVF $= -1$ is assigned to calorimeter jets which do not have associated tracks; JVF $= 0$ indicates that all associated tracks originate from pile-up vertices; $0 <$ JVF < 1 indicates that some associated tracks originate from the hard-scatter vertex, while others come from pile-up and JVF $= 1$ indicates that all associated tracks come from the hard-scatter. For this analyses as in all ATLAS 8 TeV analysis, for all jets with $p_T < 50$ GeV and $|\eta| < 2.4$ $|\mathrm{JVF}| \geq 0.5$ is required. This value well rejects pile-up jets and have a high rate of hard-scatter jet selection.

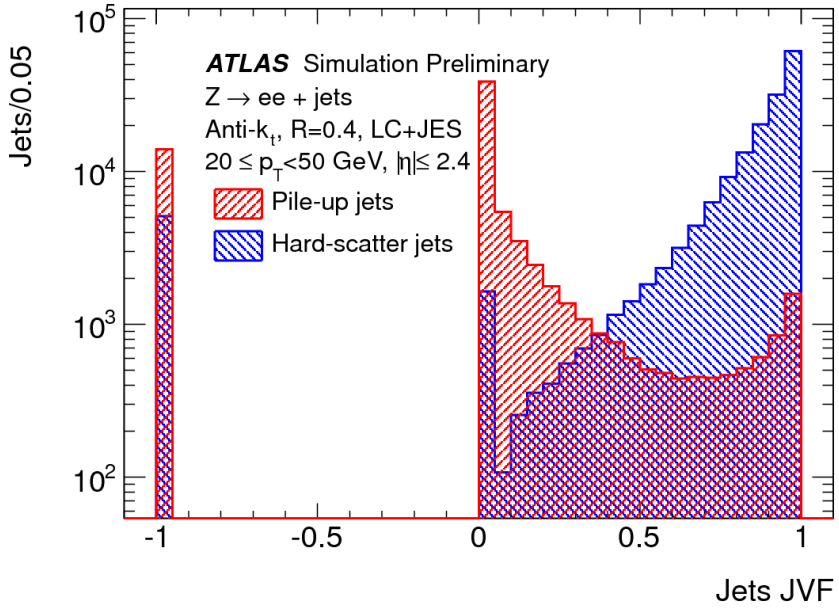

Figure 4.7.: JVF distribution for hard-scatter (blue) and pile-up (red) in simulated Z+jets events [83].

4.3.1. *b*-tagged Jets

The identification of jets containing b hadrons is an important tool used in a spectrum of measurements comprising the Large Hadron Collider (LHC) physics programme. As already mentioned in Section 2.2, the top quark almost exclusively decays into a W boson and a b quark. In the presented analysis, two jets originating from b quarks at the final state are expected. For the jet classification, coming from b, c or light flavour (u, d, s) quarks, their mean lifetime is used. Due to the long lifetime of b hadrons ($c\tau \approx 0.5$ mm [8]) displaced secondary decay vertices of these b hadrons can be reconstructed as shown in Figure 4.8. In addition, the b hadron decays into charged leptons (electron or muon) with high branching fraction ($\approx 10\%$ for each in total 20% [8]). Also b hadrons have high mass.

Several algorithms to identify jets containing b hadrons have been developed and used in ATLAS: *SV1* [77] based on the inclusive secondary vertex reconstruction, *IP3D* [77] uses longitudinal and the transverse impact parameter, *JetFitter* [84] is a decay chain reconstruction algorithm based on the topological structure of b and c hadron decays inside the jet. Based on the results from these algorithms, the most discriminating variables are combined in artificial neural networks. The most commonly used in ATLAS is the *MV1* [77] algorithm. For each b-tagging algorithm a set of operating points are defined, based on the inclusive b-tag efficiency in a simulated sample of $t\bar{t}$ events. Figure 4.9 shows the expected performance of the various b-tagging algorithms (*JetFitterCombNN* combines the output of *IP3D* and *JetFitter* in a neural network and *JetFitterCombNNc* neural networks are explicitly trained to separate c-tag jets and b-tag jets) for a given

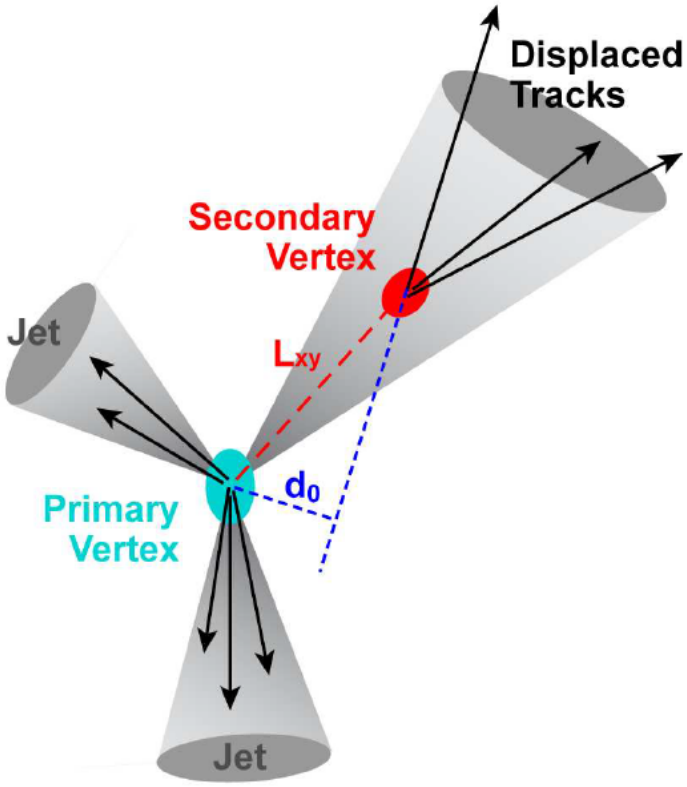

Figure 4.8.: Secondary vertex reconstruction. L_{xy} is the distance of the secondary vertex from the primary vertex in the plane orthogonal to the proton beam direction. The impact parameter of a track is marked as d_0.

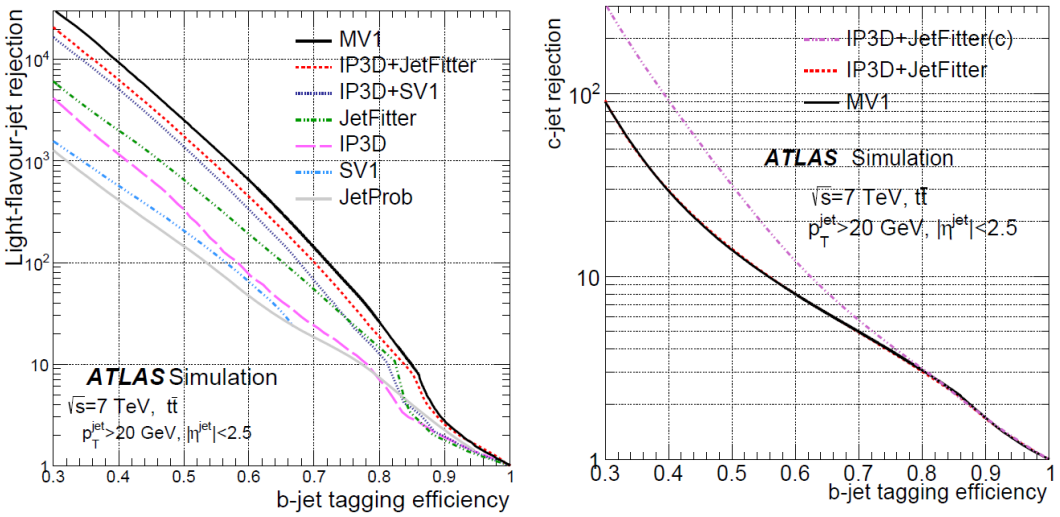

Figure 4.9.: Light-jet rejection (left) and c-tag jet rejection (right) as a function of the b-tag efficiency for the b-tagging algorithms, based on simulated $t\bar{t}$ events [77].

b-tag operating point. The best performance for light jet rejection is shown by *MV1*, so this algorithm is used for the present analysis with an operating point of 70%, which corresponds to light and c-tag jet rejection factors of $\sim$ 130 and 5, respectively. In order to take possible differences between the Monte Carlo simulation and real data into account, the b-tagging algorithms needs to be calibrated in data. The calibration results are presented as scale factors defined as the ratio of the tagging efficiency in data and in simulation $SF = \frac{\epsilon_{data}}{\epsilon_{sim}}$. In order to derive the b-tagging efficiency from data a, combinatorial likelihood approach is applied to dileptonic $t\bar{t}$ events [85]. The c-tagging efficiency is measured using a sample of jets containing D^* mesons, by comparing the yield of D^* mesons before and after the tagging requirement. The mis-tag rate is defined as the fraction of jets originating from light flavour which are tagged by a b-tagging algorithm. The mis-tag rate is measured in an inclusive jet sample, using the negative tag method [86]. For the *MV1* algorithm at operating point 70%, the b-tag efficiencies are in good agreement between the data and simulation (SF $\approx$ 1) with a total uncertainty of 2–8%. The scale factors for the c-tag jet calibration are consistent with unity with uncertainties varying between 8– 15% and the mis-tag rate scale factors are larger than unity with the uncertainties varying 15–43%. The corresponding plots are shown on Figure 4.10.

4.4. Missing Transverse Momentum

The total transverse momentum of the colliding protons is zero before the collision and so the transverse momentum of final state particles needs to be zero as well due to the transverse momentum conservation. The momentum imbalance in the transverse plane

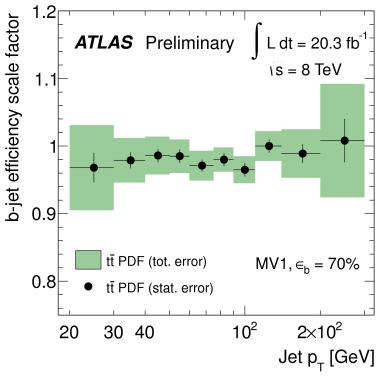

(a)

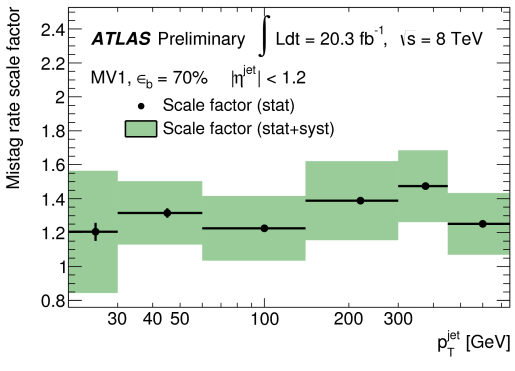

(b)

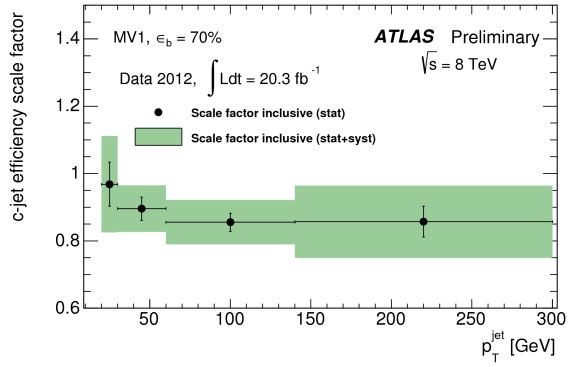

(c)

Figure 4.10.: SFs for the b (a)), c (b)) and mis-tag (c)) rate as a function of jet p_T [85, 86].

to the beam axis may be an indication of the presence of undetectable particles, such as neutrinos or new weakly-interacting particles. This imbalance is obtained from the negative vector sum of the momenta of all particles. The magnitude of the missing transverse momentum is denoted as E_T^{miss}. In order to measure E_T^{miss} precisely, it is required to minimize the impact of a limited detector coverage, finite detector resolution, the presence of dead regions and different sources of noise that can produce fake E_T^{miss} [87]. In the reconstruction of E_T^{miss} [88], energy deposits in the calorimeters and muons reconstructed in the muon spectrometer are used. Tracks are added to recover the contribution from low-p_{T} particles which are missed in the calorimeters. Also physics objects are required to be fully reconstructed and calibrated. Calorimeter energy deposits are associated with a reconstructed and identified high-p_{T} parent object in a specific order: electrons, photons, hadronically decaying τ leptons, jets and muons, also deposits which are not associated to any of these objects are also taken into account in the so called "soft term". Missing energy can be expressed as:

$$E_{x,(y)}^{miss} = E_{x,(y)}^{miss,e} + E_{x,(y)}^{miss,\gamma} + E_{x,(y)}^{miss,\tau} + E_{x,(y)}^{miss,\mathrm{jets}} + E_{x,(y)}^{miss,\mathrm{SoftTerm}} + E_{x,(y)}^{miss,\mu}. \tag{4.4}$$

Each term in Equation 4.4 is calculated as the negative sum of the calibrated reconstructed objects and projected onto the x and y directions. Electron, Muon, and Jet selection and calibration were already described in Sections 4.1, 4.2 and 4.3, respectively. The photons are reconstructed from cells in clusters associated with photons in the EM calorimeter, required to have $p_{\mathrm{T}} > 10$ GeV and calibrated at the electromagnetic scale. Hadronically decaying τ leptons are seeded by calorimeter jets and fulfill the requirements $p_{\mathrm{T}} > 10$ GeV and $|\eta| < 2.5$. The τ-jets are calibrated with the local cluster weighting. The SoftTerm includes contributions both from jets with $p_{\mathrm{T}} < 20$ GeV and from unassociated *topo-clusters*/tracks. This term is calculated from *topo-clusters* and tracks not associated to high-p_{T} objects, the *topo-clusters* being calibrated using the LCW technique and removing any overlap between tracks and *topo-clusters*.
All terms in Equation 4.4 are affected by pile-up. The most affected terms are the jets and SoftTerm, because the pile-up largely produces hadronic energy and they are reconstructed from larger regions in the calorimeters. Several methods [89] were developed to suppress such contributions. The total magnitude of E_T^{miss} is given by:

$$E_T^{miss} = \sqrt{(E_x^{miss})^2 + (E_x^{miss})^2}. \tag{4.5}$$

In the $t\bar{t}$ dilepton decays, real E_T^{miss} is expected from two neutrinos from W bosons decay.

CHAPTER 5

Modelling of Physics Processes

The analysis presented in this thesis is a measurement of W boson helicity fractions in $t\bar{t}$ decays when both W bosons decay leptonically. In order to perform the physics measurements, simulated and measured events are compared.
The dataset used in this analysis corresponds to data recorded by the ATLAS experiment in 2012 with a centre of mass energy of $\sqrt{s} = 8$ TeV. The performance of the ATLAS detector during Run I was already described in Section 3.2. The concepts of the ATLAS event simulation is discussed in Section 5.1, and the modelling of the signal and background processes are described in Sections 5.2 and 5.3, respectively.

5.1. The ATLAS Event Simulation

The ATLAS simulation chain consists of four steps. Monte Carlo (MC) event generators are used to provide a model of high-energy physics collisions as complete as possible. The description of the physics process starts from very short distance scales up to the typical scale of hadron formation and decay. According to the factorisation theorem [21], the event generation is divided into different stages, corresponding to different kinematic regimes (a schematic view is shown in Figure 5.1):

- *Hard Interaction (Scattering)*: in general, it is the basic piece of the event simulation, which can be calculated at fixed order perturbation theory in the coupling constants. At this stage, computations are based on matrix elements, which are provided by matrix-element (ME) generators.

- *Parton Showers (PS)*: QCD evolution connects the hard scale of coloured parton creation with the hadronisation scale where the transition to colourless hadrons occurs.

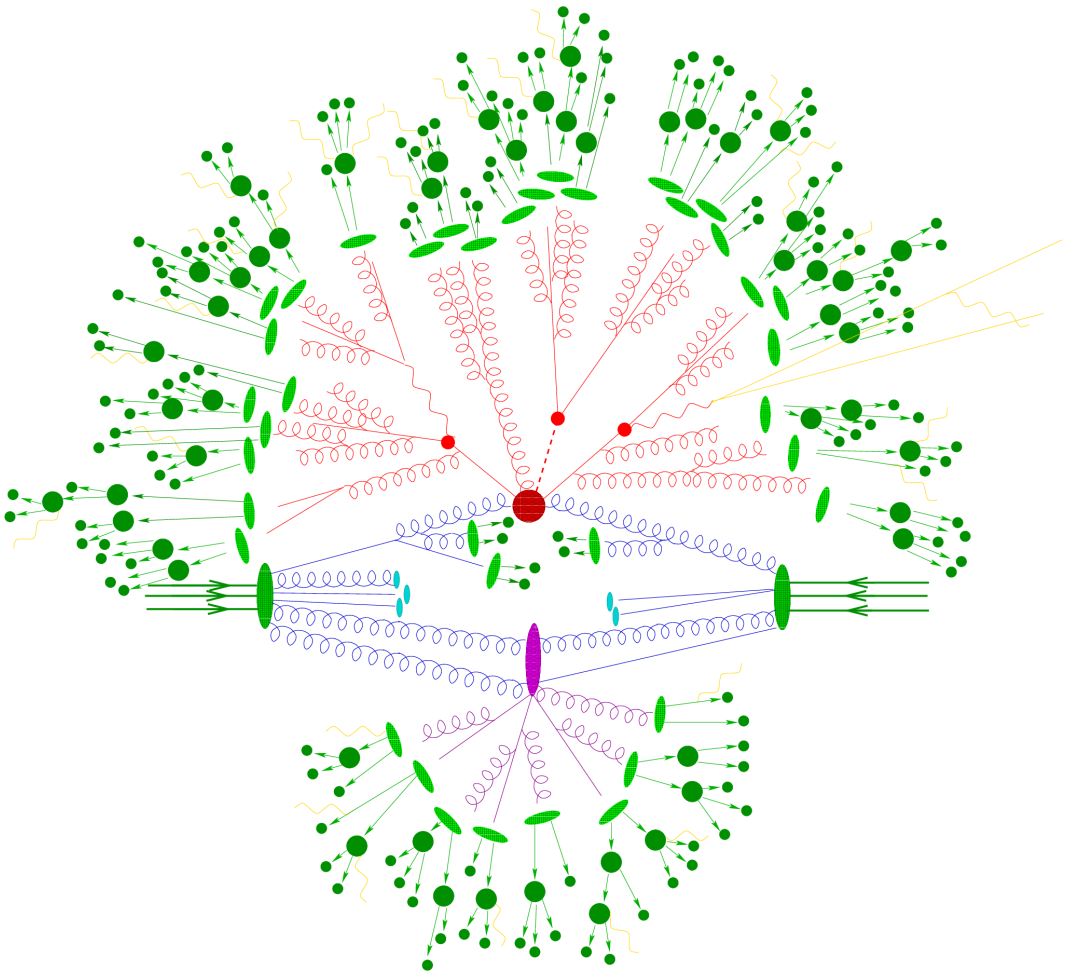

Figure 5.1.: The representation of a pp collision by an event generator. The hard interaction is illustrated by the big red blob. Additional hard QCD radiation is produced (red) and a secondary interaction takes place (purple blob) before the final state partons hadronise (light green blobs) and hadrons decay (dark green blobs). Photon radiation occurs at any stage (yellow).

- *Hadronisation*: QCD partons are transformed into primary hadrons, applying purely phenomenological fragmentation models. The string fragmentation [90] and cluster fragmentation [91] models are mainly used nowadays. Finally, the primary hadrons are decayed into particles that can be observed in detectors.
- *Underlying Event*: generally accompanies of hadron collisions, where remnants of the incoming hadrons produce secondary hard or semi-hard interactions. For such effects, the QCD factorisation theorem is not valid and also no complete first principles theory is available. For the description, phenomenological models with a set of parameters to be adjusted by using comparisons with data are used.
- *QED Bremsstrahlung*: photon radiation which can occur at any stage of the process.

In order to provide a realistic estimate of the detector response to collision events, MC generators are used together with a detector simulation taking into account geometry and material specifications of the ATLAS detector. The interaction of the particles with the ATLAS detector relies on the Geant4 [91] particle simulation toolkit. It includes a detailed detector description, but is time consuming. For the case, when huge MC statistics are required, the ATLAS collaboration uses a so called "fast simulation" where the detector response is parametrised. For the current analysis, the fast simulated samples use the ATLFAST-II simulation, which uses the parameterised calorimeter simulation FastCaloSim [92].
The digitisation step converts energy deposited by the core simulation into currents and voltages for comparison to the read-out system [93].
As mentioned above, at different stages of event generation, phenomenological models are used. Each of these models presents several free parameters which need to be optimised in order to reach a reasonable description of the experimental data. This optimisation process is known as tuning, and the resulting parameter sets are referred to as MC generator tunes.
The final step is reconstruction which is identical for the ATLAS recorded and simulated data and will be discussed in Chapter 6.
For the W boson helicity measurement in the dilepton channel, both signal and background processes are estimated from MC simulation and normalised to their theoretical cross sections. For this process, the backgrounds arise mainly from the production of a Z boson in association with jets (Z+jets) and single top quark events, mainly from Wt associated production. Small contributions arise from diboson (WW, WZ, ZZ) production and misidentified leptons. In the following, the signal and background processes will be described. The generation parameters of MC samples used for this analysis can be seen in Table 5.1.

5.2. Signal Process

The $t\bar{t}$ sample is generated using Powheg NLO generator [103–105] with the CT10 [37,38] Parton Distribution Functions (PDF) set assuming a top quark mass of 172.5 GeV. It

Sample	Generator	PDF	Shower	Normalisation
$t\bar{t}$ + jets	PowHeg	CT10	Pythia 6.425	NNLO+NNLL [94–96]
Z + jets	Alpgen	CTEQ6L1	Pythia 6.426	NLO [97]
W + jets	Alpgen	CTEQ6L1	Pythia 6.426	NLO [98]
Single top (s-channel, Wt)	PowHeg	CT10	Pythia 6.426	aNNLO [99–101]
Single top (t-channel)	PowHeg	CT10	Pythia 6.427	aNNLO [99–101]
Diboson	Sherpa	CT10	Sherpa	NLO [102]

Table 5.1.: The basic generator parameters used to simulate signal and background processes.

is interfaced to Pythia 6.425 [106] to model the showering and hadronisation, with the CTEQ61L [107] set of PDFs and Perugia2011C [108] underlying event tune.
The sample is normalised to the theoretical calculation performed at next-to-next-to leading order (NNLO) in QCD that includes resummation of next-to-next-to-leading logarithmic (NNLL) soft gluon terms with top++2.0 [25, 26, 28] yielding 253^{+15}_{-16} pb for 8 TeV. Effects due to PDF variations, choice of α_S, and the input top quark mass are taken as systematic uncertainties. The PDF and αs uncertainties are calculated using the PDF4LHC prescription [109] with the MSTW2008 68% CL NNLO [110, 111], CT10 NNLO [38, 112] and NNPDF2.35fFFN [113] PDF sets, added in quadrature to the scale uncertainty.
Unlike "multi-leg"[1] generators, Powheg is expected to describe the jet multiplicity properly only for $t\bar{t}$ accompanied by up to one jet. Nevertheless, this generator, when interfaced with Pythia, provides a good description of the jet multiplicity in data up to much higher jet multiplicities. In combination with the parton shower modelled with Pythia, it also reproduces the heavy flavour fractions of $t\bar{t}$ production [114]. The estimation of systematic uncertainties in the modelling of signal events is based on alternative generators and generator parameters. Such alternative MC generators for the current analysis are MC@NLO [115] and HERWIG [116] using JIMMY [117] for the parton shower. Further information about the alternative MC samples and the evaluation of signal modelling systematic uncertainties is provided in Section 7.2.5.

5.3. Background Processes

5.3.1. Z/W+jets

Z+jets production can be reconstructed as dilepton $t\bar{t}$ events as a final state is expected with two leptons with opposite charge (in case of the Z boson decaying leptonically) and jets. Other Z+jets channels can not mimic signal events, only with the exception if they include so called *Misidentified* (*misID*) or *fake* leptons. In case of W+jets, a contribution is only possible in case of *fake* lepton candidate. Details about *fake* lepton backgrounds will be discussed in Section 5.3.4.
The MC Samples of W/Z+jets events at 8 TeV are generated using the Alpgen v2.14 [118]

[1] Multi-leg generators use matrix elements with a variable number of final state partons.

leading-order (LO) generator and the CTEQ6L1 [107] PDF set. Parton shower and fragmentation are modeled with Pythia 6.425 [106]. To avoid double counting of partonic configurations generated by both the matrix-element calculation and the parton shower evolution, a parton-jet matching scheme called "MLM matching" [119] is employed.
The Z/W+jets background is generated with up to five additional partons separated in different parton flavour and is normalised to the inclusive NNLO theoretical cross section [120].

Z+jets corrections

The $Z(\rightarrow ll)$+jets cross section is measured as a function of the p_{T} of the recoiling Z boson, reconstructed from the momenta of the two leptons. The result is presented in Figure 5.2 for the inclusive $Z+ \geq 1$ jet selection, normalised to the inclusive $Z(\rightarrow ll)$ cross section. As a result the Alpgen generator (not only but Alpgen is the one used for this analysis) predicts a harder spectrum of Z boson transverse momentum ($p_T(Z)$) than in data. In order to correct this difference studies are performed for data and for simulated samples at $\sqrt{s} = 8$ TeV in a Z+jets dominated region. The correction factors w_Z were derived bin-by-bin from this comparison, as shown in Figure 5.3, as the ratio:

$$w_Z = \frac{Z(data)}{Z(MC)} = \frac{N_{data} - N_{other(MC)}}{N_{Z(MC)}}, \tag{5.1}$$

where N_{data} and $N_{other(MC)}$ are the number of observed events and expected background events from other sources, respectively, and $N_{Z(MC)}$ is the Z+jets MC prediction, calculated in each bin of the $p_T(Z)$ distribution. As a cross-check, these correction factors were derived from the exclusive two jet-bin with no b-tags, Z_{light}+jets (jets originating from light flavour quarks) and Z_{HF}+jets (jets originating from heavy flavour quarks) samples separately, also ee and $\mu\mu$ channels were studied separately. In all cases the weights were consistent.
The prediction of heavy flavour jets produced with a Z boson is another known issue of the Alpgen+Pythia generator. The fraction of additional jets originating from heavy-flavour quarks in association with the Z boson varies significantly with jet and b-tagged jet multiplicity. Z_{HF} and Z_{light} normalisation corrections can be derived by solving the following system of equations in at least 2 jets which are no b-tagged jets ($\geq$ 2j, $0b$) and at least 2 jets with exactly 1 b-tagged jet ($\geq$ 2j, $1b$) :

$$\begin{aligned} x * N_{Z_{HF}}^{2j,0b} + y * N_{Z_{light}}^{2j,0b} &= N_{data}^{2j0b} - N_{other}^{2j0b}, \\ x * N_{Z_{HF}}^{2j,1b} + y * N_{Z_{light}}^{2j,1b} &= N_{data}^{2j1b} - N_{other}^{2j1b}, \end{aligned} \tag{5.2}$$

where x and y are the scale factors for the number of Z_{HF} and Z_{light} jets, respectively. Correction factors of $x = 1.50$ for Z_{HF} and $y = 0.94$ for Z_{light} contributions were obtained.

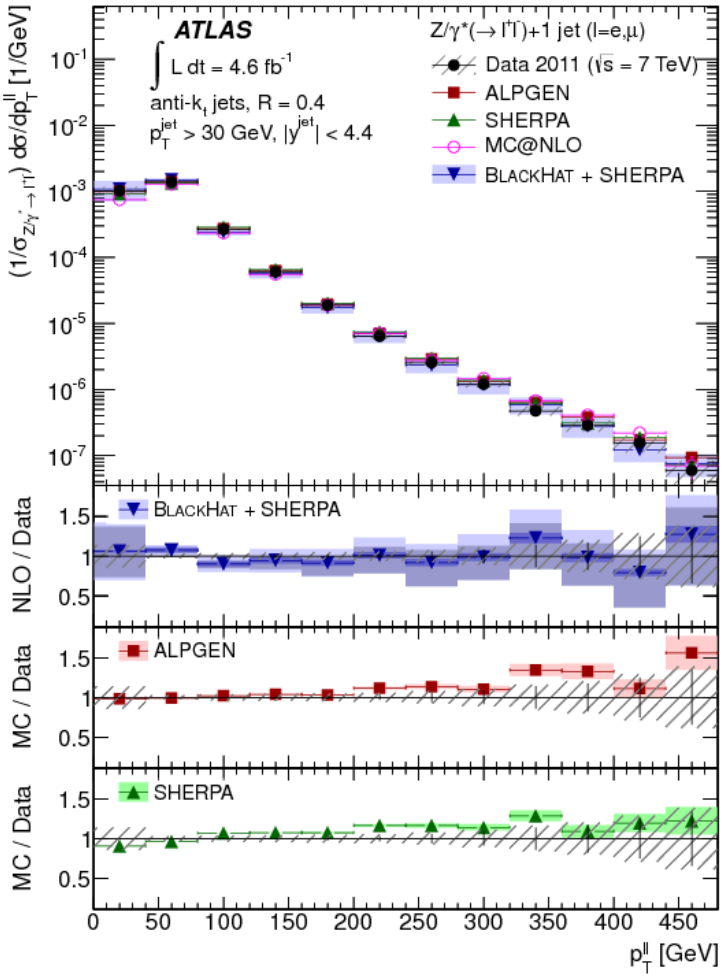

Figure 5.2.: Measured cross section for $Z(\rightarrow ll)$+jets as a function of the transverse momentum of the Z boson candidate, p_T^{ll}, in events with at least one jet in the final state [121].

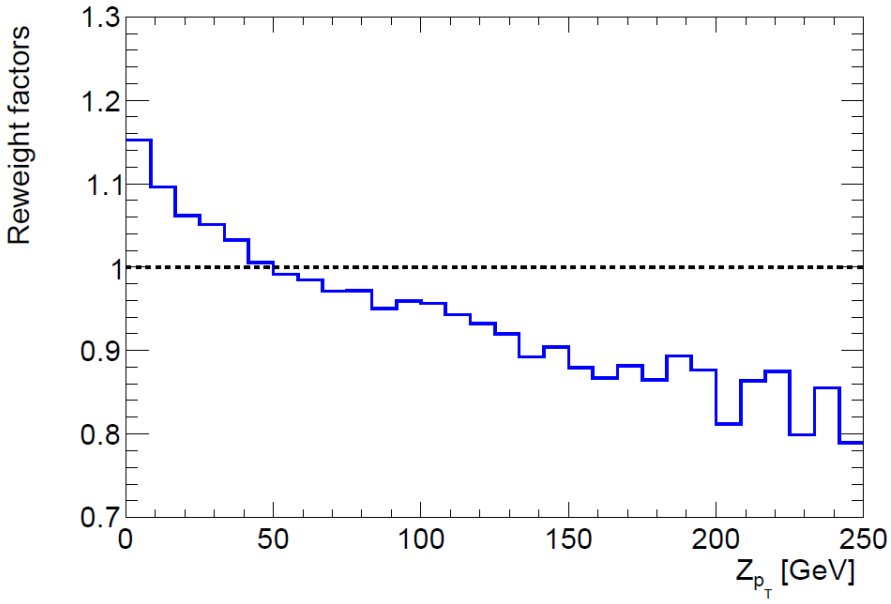

Figure 5.3.: Derived correction factors using Equation 5.1 per $p_T(Z)$ bin in a Z+jets dominated region using Alpgen+Pythia Z+jets prediction at $\sqrt{s} = 8$ TeV.

5.3.2. Single Top Processes

Samples of single top quark backgrounds corresponding to the s-channel, t-channel, and Wt production mechanisms are generated with Powheg [103–105] using the CT10 PDF set [112]. In the case of the Wt-channel, the nominal sample uses the *diagram removal* approach to handle the diagrams interfering with $t\bar{t}$ production starting at NLO [122]. All samples are interfaced to Pythia 6.425 [106] with the CTEQ61L set of parton distribution functions and Perugia2011C underlying event tune.

5.3.3. Diboson Processes

The diboson, $WW/WZ/ZZ$+jets, samples are generated using Sherpa with up to three additional partons in the hard process and are normalised to their NLO theoretical cross sections [123]. Heavy flavour quarks (b and c quarks) are treated as massive in the generation of all diboson samples.

5.3.4. Fake Lepton Background

The *mis-identified* lepton background (*fake*) originates from different types of sources depending on the lepton flavour. The electron fakes consist of non-prompt electrons, electrons from photon conversions, and mis-identified jets with a high fraction of their energy deposited in the EM calorimeter. The muon fakes consist of non-prompt muons, such as those from semileptonic B or C-hadron decays.

Two alternative methods were studied in the dilepton channel:

1. In $t\bar{t}$ dilepton events, the region with same-sign leptons is expected to be dominated by fakes, their contribution is estimated from this region, assuming that an approximately equal number of fakes is expected in the same-sign (SS) as in the opposite-sign (OS) dilepton region. The contribution was derived as follows:

$$fakes = Data(SS) - MC(SS). \tag{5.3}$$

2. For the current analysis the *fake* lepton background is estimated by using MC events containing only one true lepton that pass the dilepton event selection and by requiring the second lepton to fail the truth matching cut i.e. matching criteria between the reconstructed lepton and the leptons in the truth record of the MC simulation is not fulfilled.

Inclusive yields of fakes in the SS method and fakes in MC differ only by 5%. Figure 5.4 presents the individual contribution of each MC sample and *fakes* from the SS method, in the 2 jet inclusive region. The shape agreement in H_T between the two methods indicates that fakes estimated from MC would be a reasonable approach. The small difference in shape between the H_T distributions obtained by the two methods is considered to be a shape uncertainty on the *fake* background estimate.

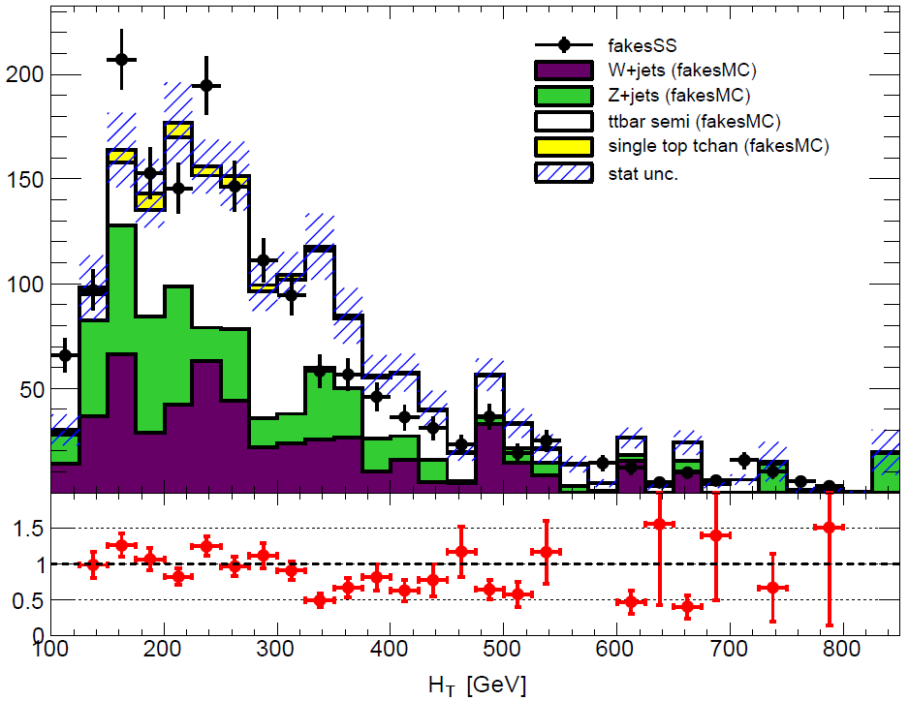

Figure 5.4.: H_T distribution, comparing fakes estimated from the SS dilepton selection and MC prediction. Z+jets corrections are also applied in the *fake* lepton background contribution.

CHAPTER 6

Event Selection

This analysis is based on data collected by the ATLAS experiment in pp collisions at a centre of mass energy of $\sqrt{s} = 8$ TeV between April and October 2012. The corresponding integrated luminosity is $\int \mathcal{L} dt = 20.20$ fb^{-1}. Only events collected using a single electron or muon trigger under stable beam conditions and for which all detector subsystems were fully operational are considered. In this chapter, the characteristics of the event selection in the dilepton final state topology of the $t\bar{t}$ system is discussed.

6.1. Event Selection

The dilepton final state topology of the $t\bar{t}$ system is characterised by two high-p_{T} leptons (electrons or muons), with opposite sign electric charge (OS), at least two high-p_{T} jets, and missing transverse energy due to the undetected two neutrinos. For all dilepton channels, an event selection is performed using the following criteria:

- The events are required to pass a single lepton (electron or muon) trigger.
- Rejecting non-collision background is required, that means having at least one reconstructed vertex with at least five associated tracks.
- Events with exactly two good leptons (electron or muon) with opposite charge are selected, with good lepton definition as presented in Sections 4.1 and 4.2.
- The selected lepton (elector or muon) is required to be matched with a high-level trigger lepton with the matching criteria $\Delta R < 0.15$.
- Events are discarded if any jet with $p_{\mathrm{T}} > 20$ GeV is independently identified as out-of-time activity from a previous pp collision or as calorimeter noise [124].

- The cut applied for the missing transverse energy is $E_T^{miss} > 30$ GeV in ee and $\mu\mu$ channels. The scalar sum of the transverse energy of leptons and jets, H_T, is calculated in the $e\mu$ channel and $H_T > 130$ GeV is required.
- Cuts on the mass of the dilepton system $m_{ll} > 15$ GeV are applied in order to reduce the Z+jets background, $|m_{ll} - m_Z| > 10$ GeV, where $m_Z = 91$ GeV.
- At least two good jets are required for the event to be selected, using the jet definition introduced in Section 4.3.
- At least one selected jet is required to be b-tagged with the MV1 tagger at 70% working point, as it is described in Section 4.3.1.

In addition, the leading and sub-leading leptons should have $p_{\mathrm{T}} > 25$ GeV and be in the η range $|\eta| < 2.5$. Leading and sub-leading jets should also have $p_{\mathrm{T}} > 25$ GeV and be in the η range $|\eta| < 2.5$. The selected events are categorised in $1b$-tag exclusive (number of b-tagged jets $= 1$) and $2b$-tag inclusive (number of b-tagged jets ≥ 2) categories. Event yields for all three (ee, $\mu\mu$ and $e\mu$) channels and both b-tag regions are shown in Table 6.1. Figures 6.1 - 6.6 show data/prediction comparisons after event selection in all three dilepton (ee, $\mu\mu$ and $e\mu$) channels and for both (1 exclusive and 2 inclusive) b-tag regions. The figures for data/prediction comparisons for sub-leading leptons and jets are presented in Appendix A.

6.2. Event Reconstruction

In order to measure helicity fractions, a full reconstruction of the $t\bar{t}$ system is needed, to build the observable $\cos\theta^*$ defined as in Equation 2.24. Reconstructing the $t\bar{t}$ kinematics in the dilepton channel is challenging due to the two neutrinos in the final state, making the system under-constrained. Hence, assumptions are mandatory to perform the $t\bar{t}$ reconstruction in this channel. The mostly used methods for $t\bar{t}$ reconstruction are:

- Kinematic Method (KIN) [125, 126]: A system of equations is solved numerically.
- Matrix Element method (ME) [52, 127]: The probability distribution is calculated based on $gg \to t\bar{t}$ leading-order matrix elements.
- Neutrino Weighting method (NW) [128]: Making a hypothesis about possible combination of the neutrino's pseudo-rapidities (η_1, η_2), the full neutrino momenta can be determined.
- method (MT2) [129]: In order to get the transverse momentum of the two neutrinos, the method uses the information extracted from the kinematic variable M_{T2} [130] of the event, where M_{T2} is defined as:
  $M_{T2} \equiv \min_{\vec{k}_T^{(1)}+\vec{k}_T^{(2)}=E_T^{miss}}[\max\{M_T(\vec{p}_T^{(1)},\ \vec{k}_T^{(1)}),\ M_T(\vec{p}_T^{(2)},\ \vec{k}_T^{(2)})\}]$,
  where M_T is the transverse mass for two unresolved particles and $\vec{p}_T^{(i)}$ is the transverse momentum of the visible final state particles in the detector (charged leptons

Sample	=1 b-tag	≥ 2 b-tags
$t\bar{t}$	6014± 402	4703± 315
Z + jets	905± 307	115± 39
Single top	395± 26	142± 10
Diboson	40± 13	3± 1
Fakes	10± 5	1± 0
Total expected	7363± 748	4964± 365
Data	7733	4789

Sample	=1 b-tag	≥ 2 b-tags
$t\bar{t}$	6797± 455	5405± 362
Z + jets	1065± 362	128± 44
Single top	428± 28	156± 10
Diboson	46± 16	4± 1
Fakes	2± 1	0± 0
Total expected	8337± 862	5653± 417
Data	8729	5637

Sample	=1 b-tag	≥ 2 b-tags
$t\bar{t}$	15512± 993	13877± 8670
Z + jets	83 ± 28	9 ± 2
Single top	733± 49	393± 16
Diboson	29± 10	3± 1
Fakes	10± 5	0± 0
Total expected	16370± 1085	14284± 889
Data	16857	14218

Table 6.1.: Event yields in the ee (top left), $\mu\mu$ (top right), and $e\mu$ channels (bottom) for 1 exclusive and 2 inclusive b-tag regions after event selection. Errors on the Monte Carlo yields come from the uncertainties in the normalisation of each sample.

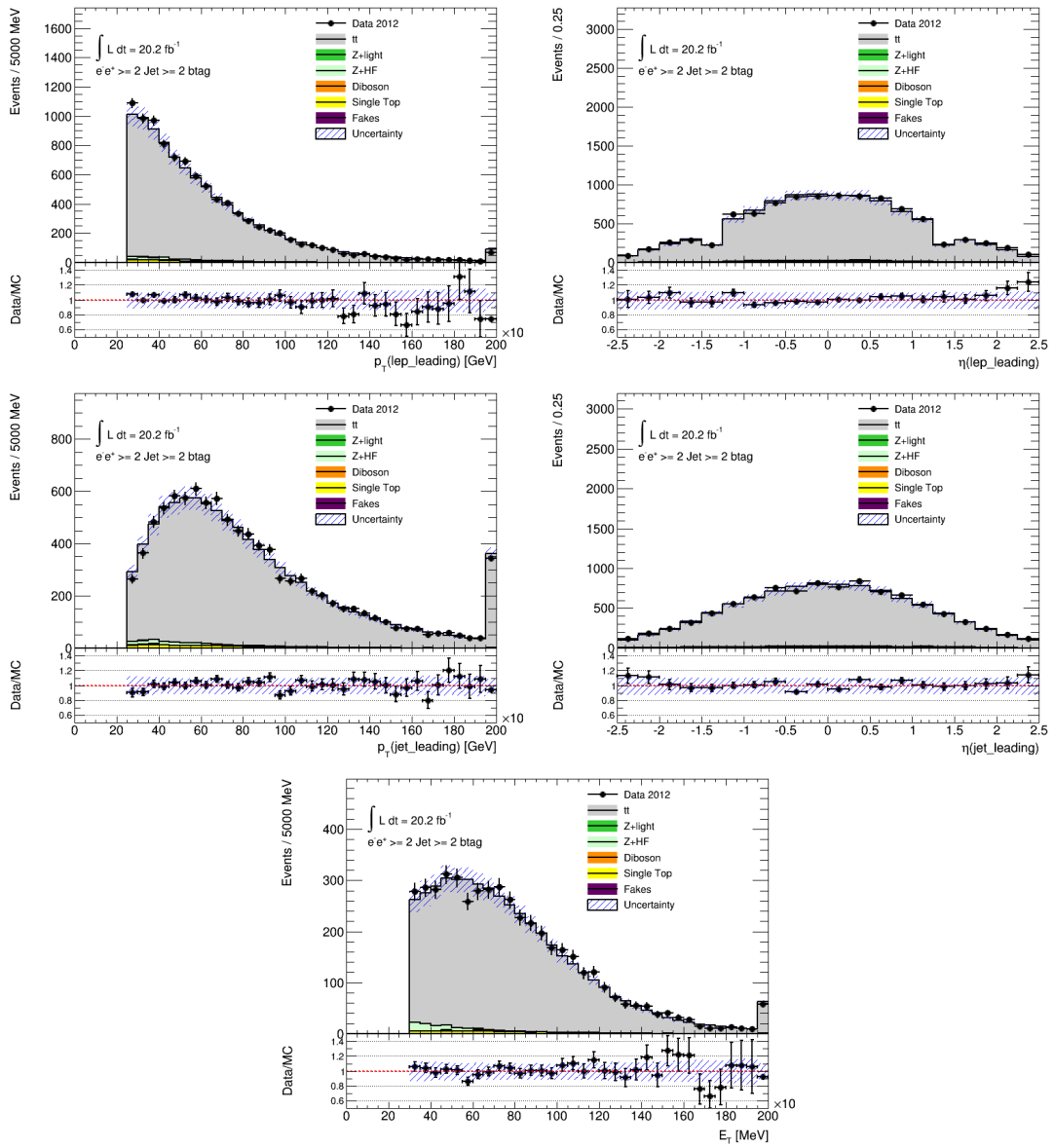

Figure 6.1.: Plots showing data/MC agreement after event selection for the reconstructed objects (lepton, jets, E_T^{miss}) in the 2 inclusive b-tag, ee region. Statistical and background normalisation uncertainties are included.

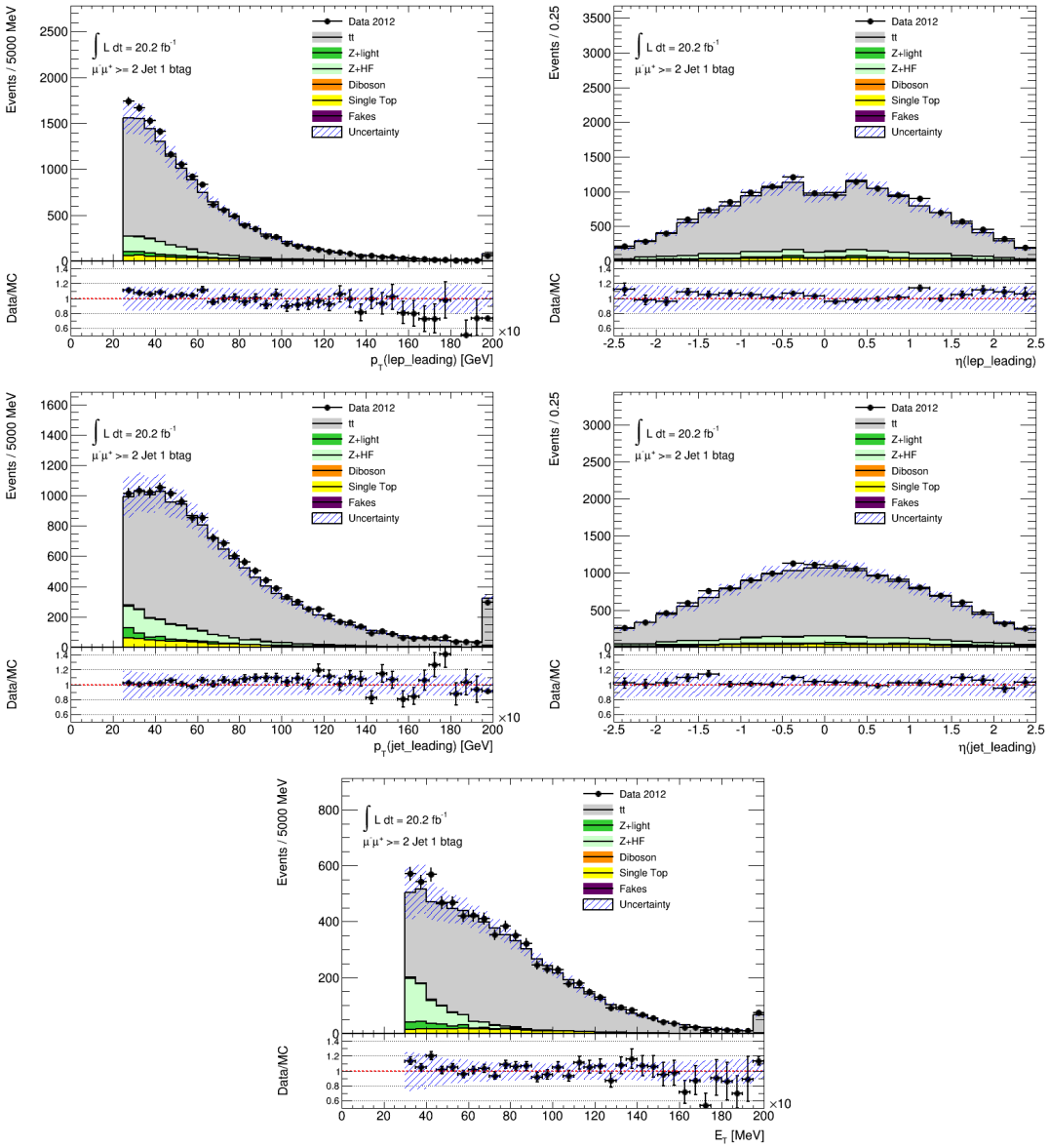

Figure 6.2.: Plots showing data/MC agreement after event selection for the reconstructed objects (lepton, jets, E_T^{miss}) in the 1 exclusive b-tag, $\mu\mu$ region. Statistical and background normalisation uncertainties are included.

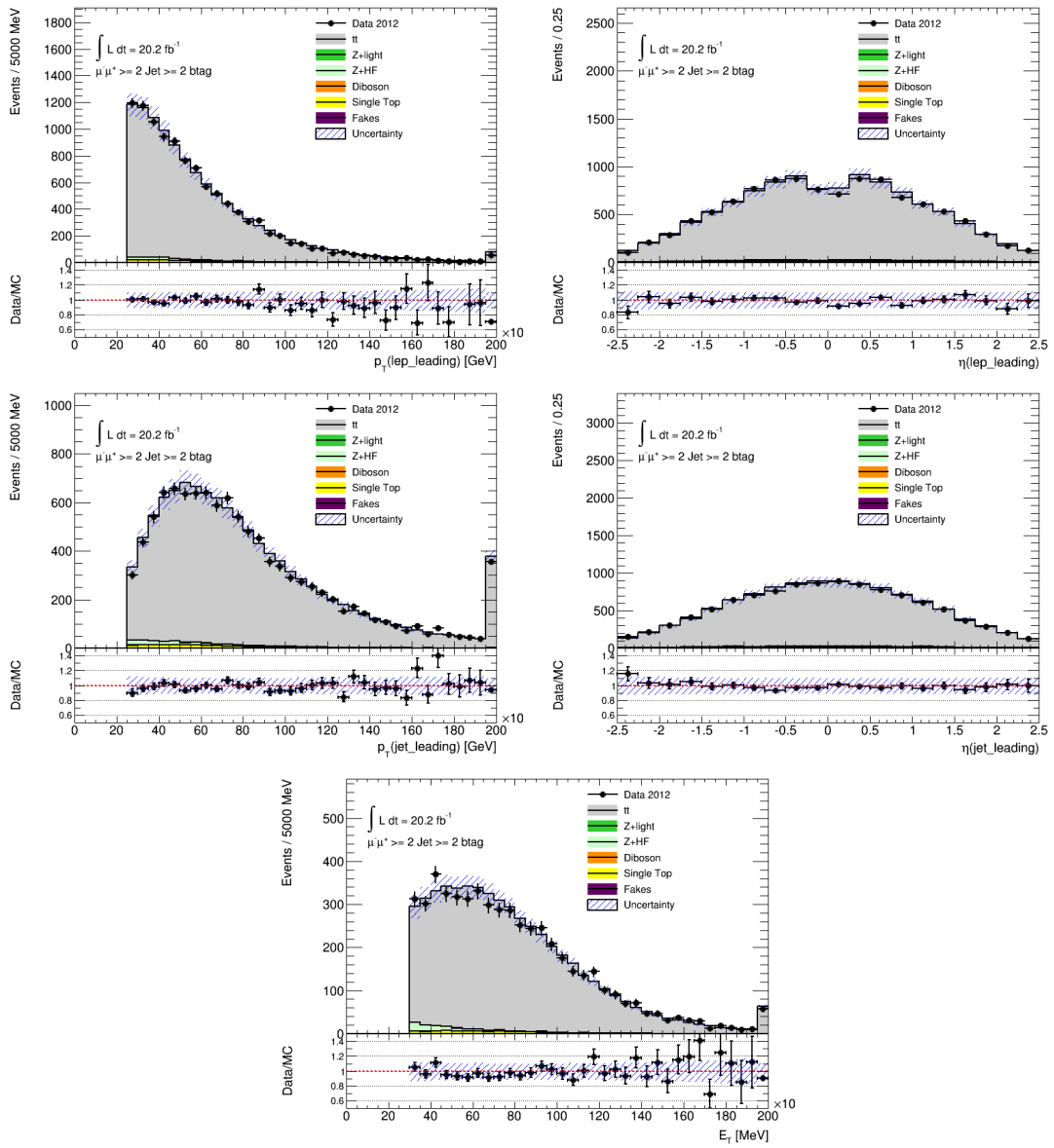

Figure 6.3.: Plots showing data/MC agreement after event selection for the reconstructed objects (lepton, jets, E_T^{miss}) in the 2 inclusive b-tag, $\mu\mu$ region. Statistical and background normalisation uncertainties are included.

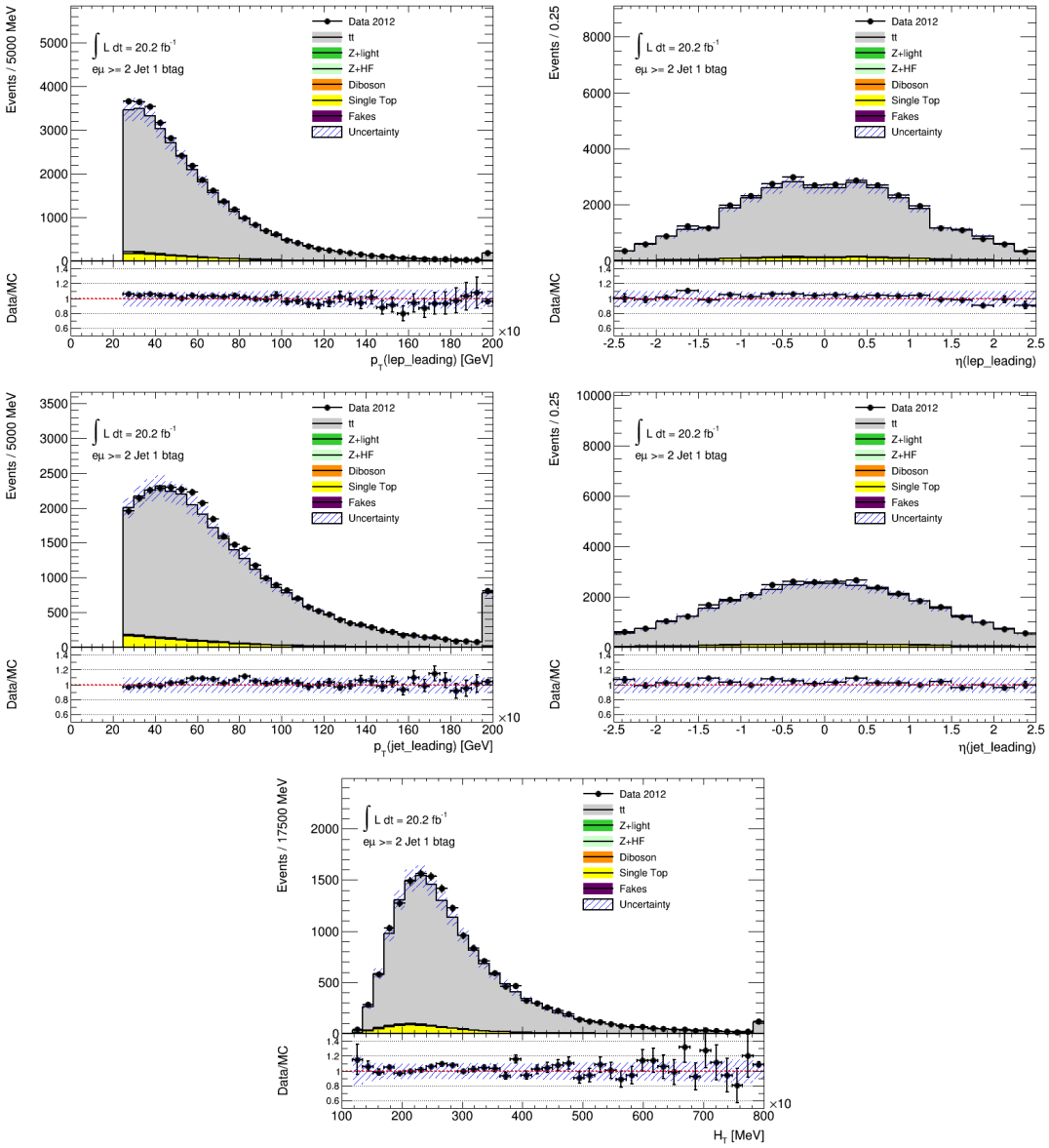

Figure 6.4.: Plots showing data/MC agreement after event selection for the reconstructed objects (lepton, jets, E_T^{miss}) in the 1 exclusive b-tag, $e\mu$ region. Statistical and background normalisation uncertainties are included.

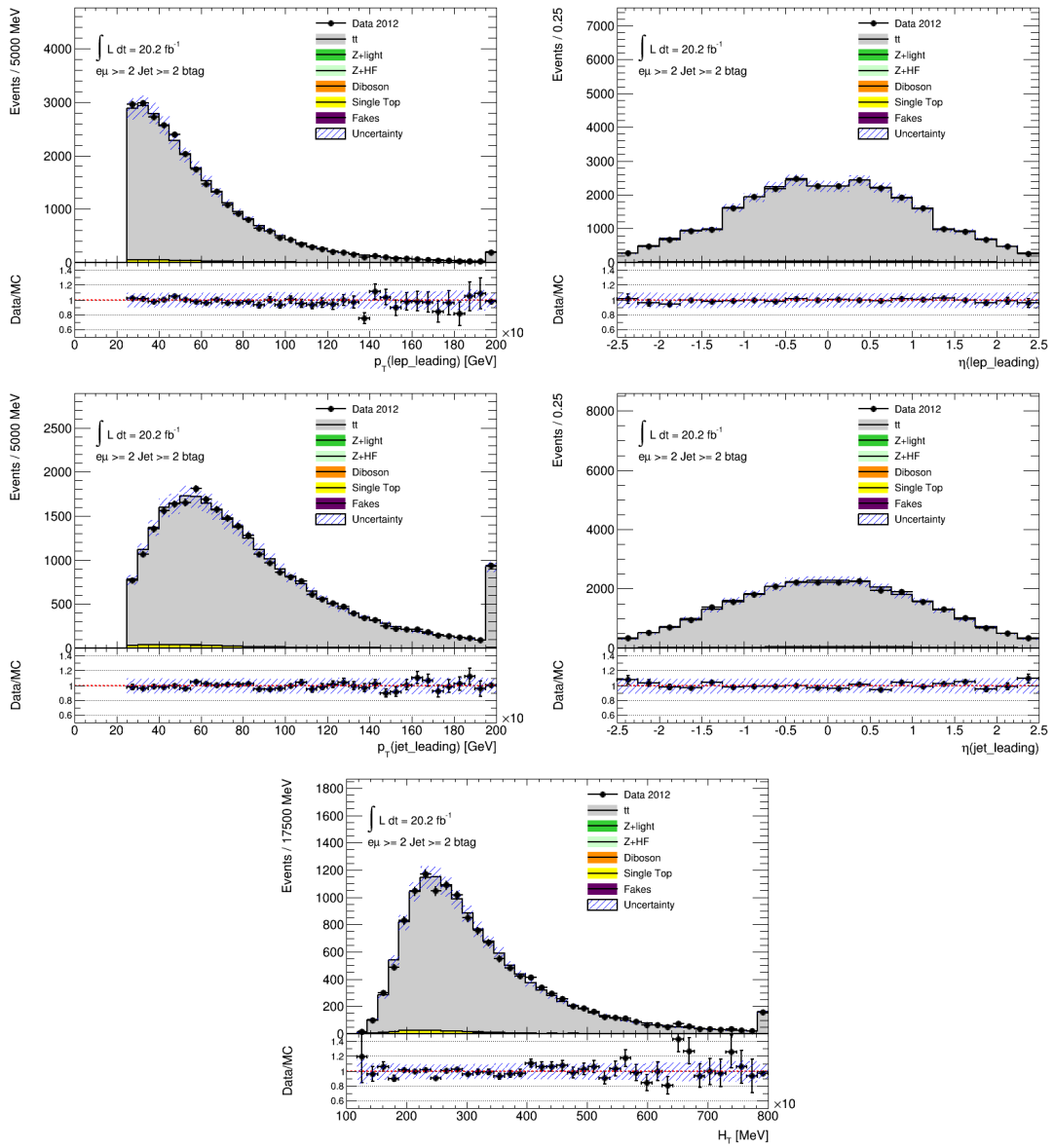

Figure 6.5.: Plots showing data/MC agreement after event selection for the reconstructed objects (lepton, jets, E_T^{miss}) in the 2 inclusive b-tag, $e\mu$ region. Statistical and background normalisation uncertainties are included.

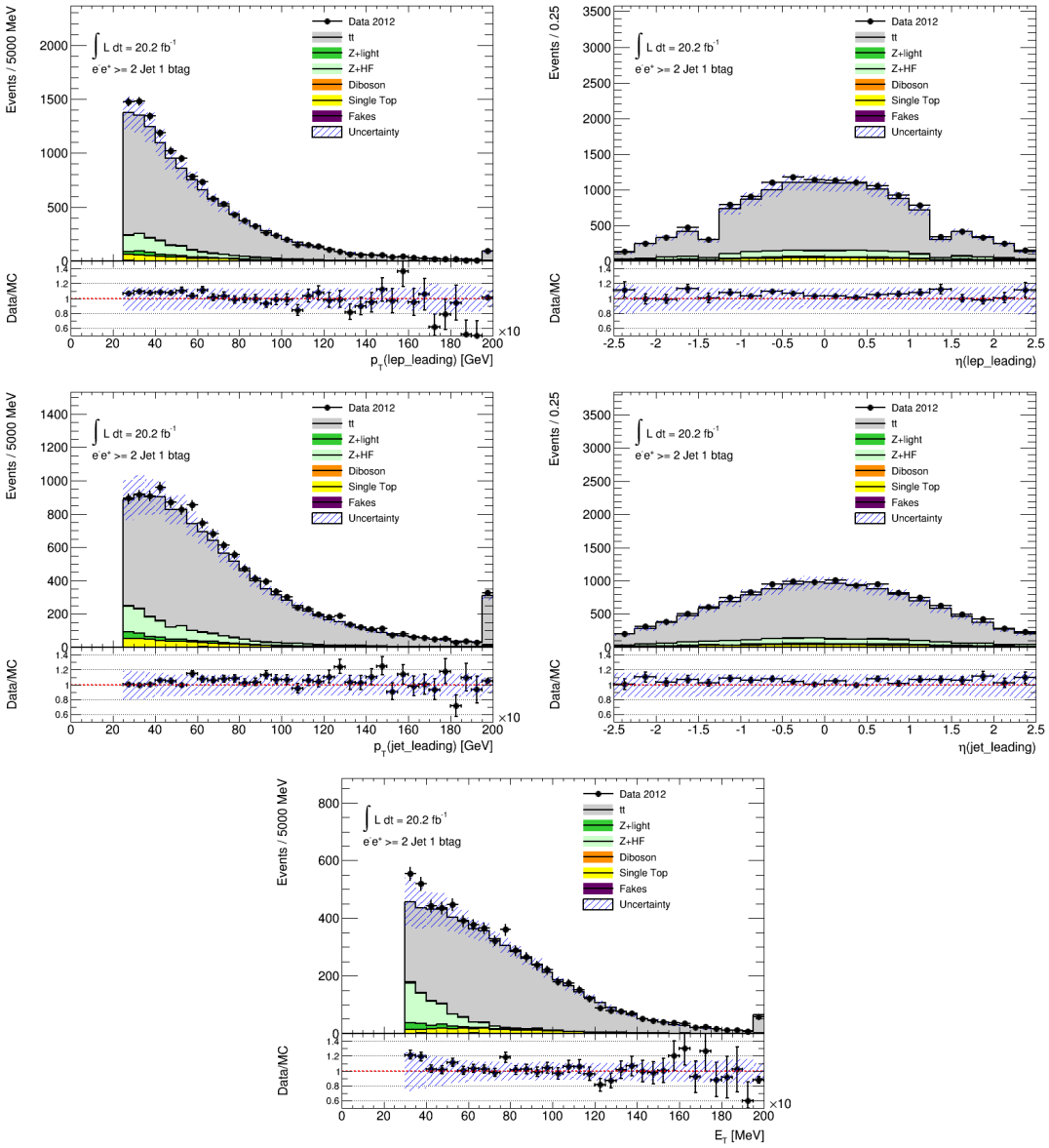

Figure 6.6.: Plots showing data/MC agreement after event selection for the reconstructed objects (lepton, jets, E_T^{miss}) in the 1 exclusive b-tag, ee region. Stat+bkg.norm uncertainties are included.

and jets) and $\vec{k}_T^{(i)}$ is the transverse momentum of the neutrinos.

KIN method is used for this analysis.
In order to reconstruct the $t\bar{t}$ kinematics in the dilepton final state all the momenta of two charged leptons, two neutrinos and two b-tag jets are needed, in total[1] 24 vector components. The $t\bar{t}$ dilepton process can be represented as:

$$pp \to t\bar{t} + X \to W^+ b W^- \bar{b} + X \to l^+ \bar{\nu} b l^- \bar{\nu} \bar{b} + X. \tag{6.1}$$

From these 24 vector components two leptons, two b-tag jets (in total 16 vector components) and the sum of the momenta of the two neutrinos in the x and y directions are measured. The unknowns can be reduced with additional constraints by the fixing neutrino, W boson, and top quark masses. The masses of neutrino, W and t are assumed to be: $m_\nu = 0$ GeV, $m_W = 80.4$ GeV and $m_t = 172.5$ GeV. Assuming the process given in Equation 6.1, the following kinematic constraints can be set:

$$\begin{aligned}
p_b + p_{W^+} &= p_t, \\
p_{\bar{b}} + p_{W^-} &= p_{\bar{t}}, \\
p_{l^+} + p_\nu &= p_{W^+}, \\
p_{l^-} + p_{\bar{\nu}} &= p_{W^-}, \\
p_{\nu_x} + p_{\bar{\nu}_x} &= E_x^{miss}, \\
p_{\nu_y} + p_{\bar{\nu}_y} &= E_y^{miss}.
\end{aligned} \tag{6.2}$$

The above set of equations 6.2 can be solved and the four-vectors of t and $\bar{t}$ will be determined. However, there still are ambiguities that need to be determined. The set of equations 6.2 is equivalent to a polynomial of fourth order hence, there can be up to four real solutions. In the simplest case, at the final state there are two leptons and two b-tagged jets, hence there is a twofold ambiguity to assign the lepton and b-tag jet to the proper top quark. Furthermore, as discussed in Section 6.1, selected events are required to have more than two jets which increases this ambiguity even more. Finally, one also needs to address the fact that the measured quantities entering the equations are subject to experimental uncertainties.

6.2.1. Kinematic method (KIN)

The KIN method was used for top mass reconstruction and other studies by CDF [125,126]. In order to find the solution of the kinematic equations the numerical Newton-Raphson method [131] is used in the selected events with more than two reconstructed jets. The two jets with the highest value of b-tag weight (as determined by MV1 b-tagging algorithm) are used for reconstruction. An alternative way is to use two jets with the highest transverse energy (E_T) but selecting by b-tag weight improves the

[1] 6(particles) × 4(vector components) = 24 vector components.

efficiency of choosing the correct jets, from about 54% to 69%. The experimental uncertainties on the measured objects are taken into account by smearing the phase-space of the measured jet transverse momenta p_T and E_T^{miss} according to their resolution. For each point in this space the procedure described below is applied to find a solution for the t and $\bar{t}$ four-vectors. The resolution functions are determined in a similar way as the transfer functions used in KLfitter [132]. As smearing of the lepton p_T does not change the reconstruction efficiency, lepton momenta are not smeared. In case of the four kinematically possible solutions, the KIN method takes the solution which leads to the lowest effective mass of the $t\bar{t}$ system. The reason for this is that the partonic $t\bar{t}$ cross-section is a decreasing function of the partonic energy $\hat{s} \simeq m(t\bar{t})$ (except very close to the $m(t\bar{t})$ boundary), therefore, it is more probable to have events with smaller $m_{t\bar{t}}$. The numerical algorithm to find the solution actually stops after finding two solutions. This is mostly for efficiency reasons, since it is known that most of the time there are two solutions and the probability that four real solutions exist is very small (a few percent). In consequence, we would gain very little and the effectiveness of the method would be decreased (longer processing time).
The twofold ambiguity in the lepton and b-tag jet assignment is resolved in the following way. For a given lepton-jet pairing (lep1-jet1, lep2-jet2), the kinematic solution with the lowest $m(t\bar{t})$ is taken. The smearing is performed and the reconstruction of the $t\bar{t}$ kinematics for a given pairing is tried, number of N_{smear} times. There could be no solution found given the "smeared" jets and E_T^{miss} . Therefore, for a given event, it is possible to end up with less reconstructed trials (N_{smear}^{reco}) that were originally tried (N_{smear}) . For the second lepton-jet pairing possibility (lep1-jet2, lep2-jet1), the previously described procedure is repeated and a different number of reconstructed trials is obtained. The correct pairing is chosen to be the one that has more reconstructed trials, i.e. the one that maximises the ratio: $N_{smear}^{reco}/N_{smear}$. If the initial set of particles (the unsmeared set), does not lead to a solvable system of equations, the first smeared set that leads to a solution is taken for the measurement. In the present analysis N_{smear} is chosen[2] to be equal to 500. This number was chosen after optimisation studies and as a result for 98% of the selected events of the $t\bar{t}$ system can be reconstructed.

6.2.2. Performance of Kinematic method

Reconstructed events are categorized in 1b-tag exclusive and 2b-tag inclusive regions. In order to check the $t\bar{t}$ event reconstruction performance, a comparison of reconstructed object properties with truth level objects (information recorded by the MC generator) is needed. For both, t and $\bar{t}$, 20% of reconstructed events satisfy $\Delta R(t^{truth}, t^{reco}) < 0.3$ in 2 b-tag inclusive region and 13 % in 1b-tag exclusive region.
It was also checked how the method solves the twofold ambiguity of lepton-jet pairing using the following definitions:

- Count events when the b-tag jet was assigned to the correct lepton. For jets the matching criterion $\Delta R(b_{jet}^{truth},\ b_{jet}^{reco}) < 0.3$ between reconstructed b-tag jet and

[2] $N_{smear} = 500$ for presented analysis.

	2 inclusive b-tag [%]	1 exclusive b-tag [%]
Both b-tag jets correctly matched	76	49
Both b-tag jets wrongly assigned	14	28
At least one b-tag jet is not correctly matched	10	23

Table 6.2.: Summary of fractions of correctly matched jets in %, after event reconstruction.

generated b quark is used (the same for the reconstructed $\bar{b}$).

- Count events when the b-tag jet was wrongly assigned to the lepton using the matching criterion $\Delta R(\bar{b}_{jet}^{truth}, b_{jet}^{reco}) < 0.3$ between reconstructed b-tag jet and generated b quark (the same for the reconstructed $\bar{b}$).
- Count events when there is at least one b-tag jet that does not match to truth level b or $\bar{b}$ quark.

Table 6.2 summarises fractions of correctly matched jets after event reconstruction in both, 2b-tag inclusive and 1b-tag exclusive regions. Figure 6.7 presents a comparison of some properties between reconstructed top quarks and top quarks at generated level, in Figure 6.8, the observable of the analysis cosθ^* at generated and reconstructed levels is compared.

6.2.3. Data and Prediction Comparison after Reconstruction

After full reconstruction of the $t\bar{t}$ system, a data/prediction comparison of reconstructed objects is performed. Event yields for all three (ee, $\mu\mu$ and $e\mu$) channels and 2b-tag inclusive and 1b-tag exclusive regions are shown in Table 6.3. Data/prediction comparisons for reconstructed objects (p_T and η of the neutrino and the top quark, also p_T and mass of the $t\bar{t}$ system), are also shown in Figures 6.9 - 6.14 and cosθ^* distributions are shown in Figure 6.15. Good agreement between data and prediction is observed. Additional figures are presented in Appendix B.

6.2.4. Acceptance effects

The acceptance effects caused by event selection and reconstruction modify the cosθ^* distribution. The $cos\theta^*$ distribution in the full phase space (before applying any selection) and the corresponding distributions after $t\bar{t}$ system reconstruction at generated and reconstructed levels are compared. Due to the isolation requirements the high cosθ^* values are cut, while the p_T selection affect low cosθ^* values. The total effect is shown in Figure 6.16.

6.2.5. Correlations Between Positive and Negative Leptonic Measurements

Since there are two simultaneous measurements being performed per event (the angles from positive and negative W bosons) decays, the correlation between the two angles

Sample	=1 b-tag	≥ 2 b-tags
$t\bar{t}$	5296± 339	4594± 294
Z + jets	637± 216	77± 26
Single top	246± 17	78± 5
Diboson	20± 7	1± 0
Fakes	5± 2	1± 0
Total expected	6204± 580.9	4749.9± 325.5
Data	6518	4789

Sample	=1 b-tag	≥ 2 b-tags
$t\bar{t}$	5997± 384	5273± 337
Z + jets	723± 246	85± 29
Single top	267± 18	91± 6
Diboson	22± 7	2± 1
Fakes	1± 0	0± 0
Total expected	7009± 655	5450± 373
Data	7260	5371

Sample	=1 b-tag	≥ 2 b-tags
$t\bar{t}$	15512± 993	13589± 8670
Z + jets	83 ± 28	7 ± 2
Single top	733± 49	239± 16
Diboson	29± 10	1± 1
Fakes	10± 5	0± 0
Total expected	16370± 1085	13837± 889
Data	16857	13763

Table 6.3.: Event yields in the ee (top left), $\mu\mu$ (top right), and $e\mu$ channels (bottom) for 1 exclusive and 2 inclusive b-tag regions after event reconstruction. Errors on the Monte Carlo yields come from the uncertainties in the normalisation of each sample.

needs to be quantified. Even though they are, in principle, uncorrelated as the decays themselves are independent, a non-zero correlation could be introduced through the reconstruction. In the case of non-negligible correlation, it would be incorrect to evaluate the uncertainties in the different channels independently, and the correlation would need to be correctly accounted for. In the case of negligible correlation, the two channels can be treated and evaluated fully independently.
To estimate the correlation, two-dimensional plots (one angle per axis) are produced and the correlation factor ($= -1$ for perfect anti-correlation, $= +1$ for perfect correlation, $= 0$ for completely uncorrelated) is calculated. The correlation plot is shown in Figure 6.17. The correlation factor is evaluated for all dilepton channels with exactly one b-tag and for at least two b-tags passing the nominal selection.
The correlation factor is calculated to be $+0.085$ for the $1b$-tag exclusive region and $+0.062$ in the $2b$-tag inclusive region. The correlation is considered to be negligible, and the measurements are considered to be independent for the rest of this analysis.

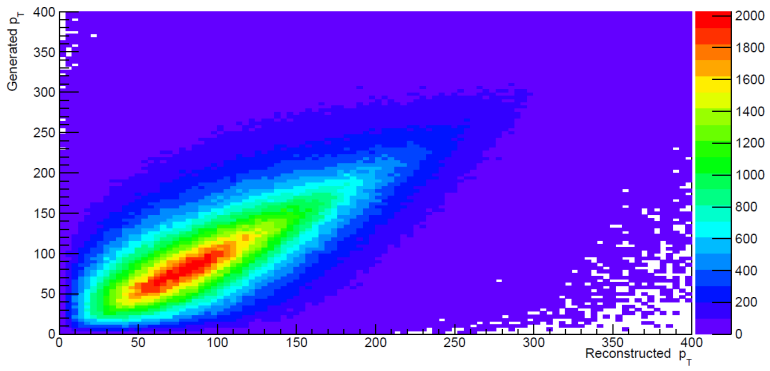

(a)

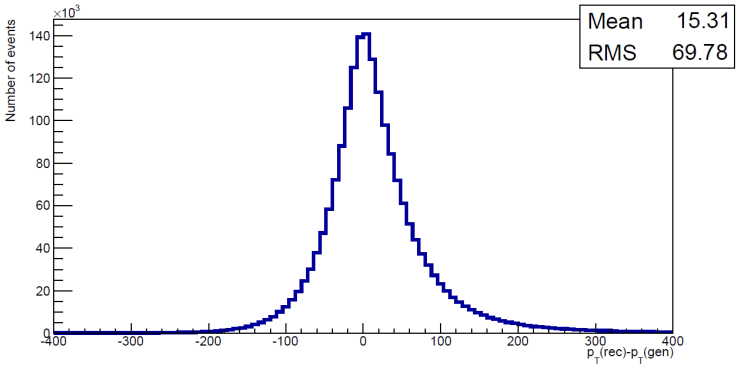

(b)

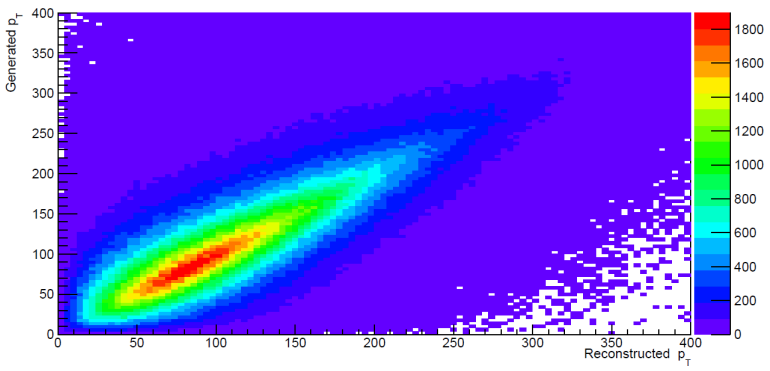

(c)

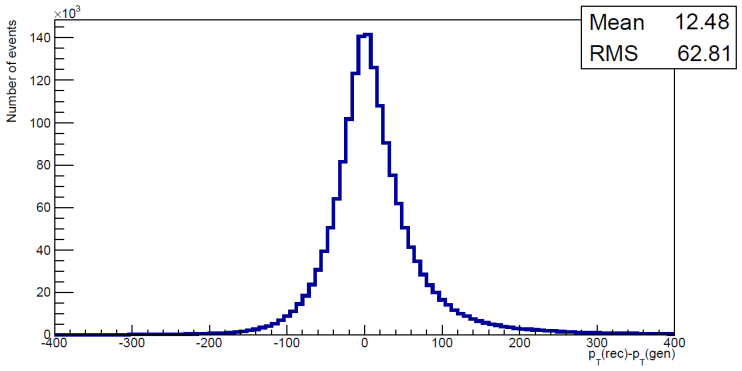

(d)

Figure 6.7.: A comparison of the generated and reconstructed p_T^t (both p_T^t and $p_T^{\bar{t}}$ are included in the plots) distribution in 1b-tag exclusive (a) and b)) and 2b-tag inclusive regions (c) and d)). The correlation factor in the1b-tag exclusive region is 63% and 76% in 2b-tag inclusive region.

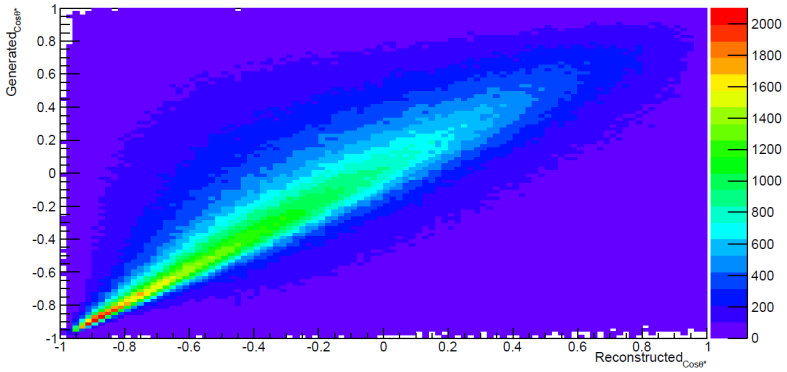

(a)

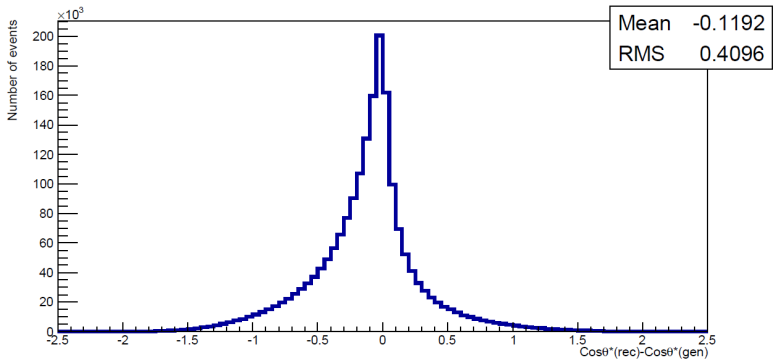

(b)

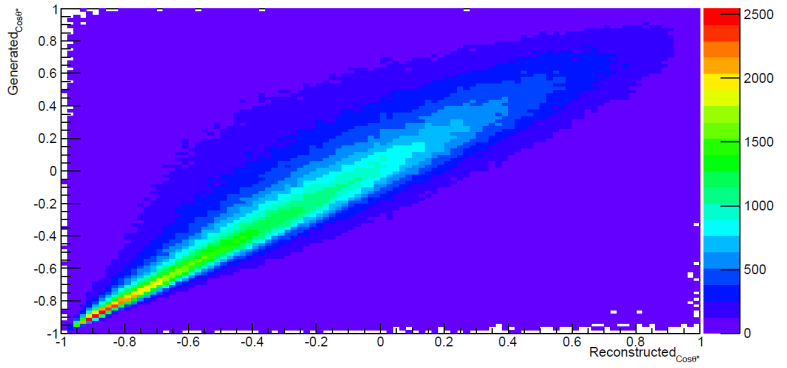

(c)

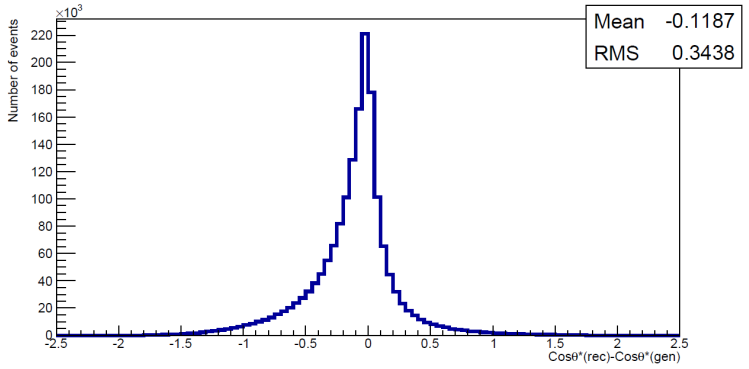

(d)

Figure 6.8.: A comparison of the generated and reconstructed cosθ^* distribution in 1b-tag exclusive (a) and b)) 2b-tag inclusive regions (c) and d) . The correlation factor in the 1b-tag exclusive region is 60% and 74% in 2b-tag inclusive region.

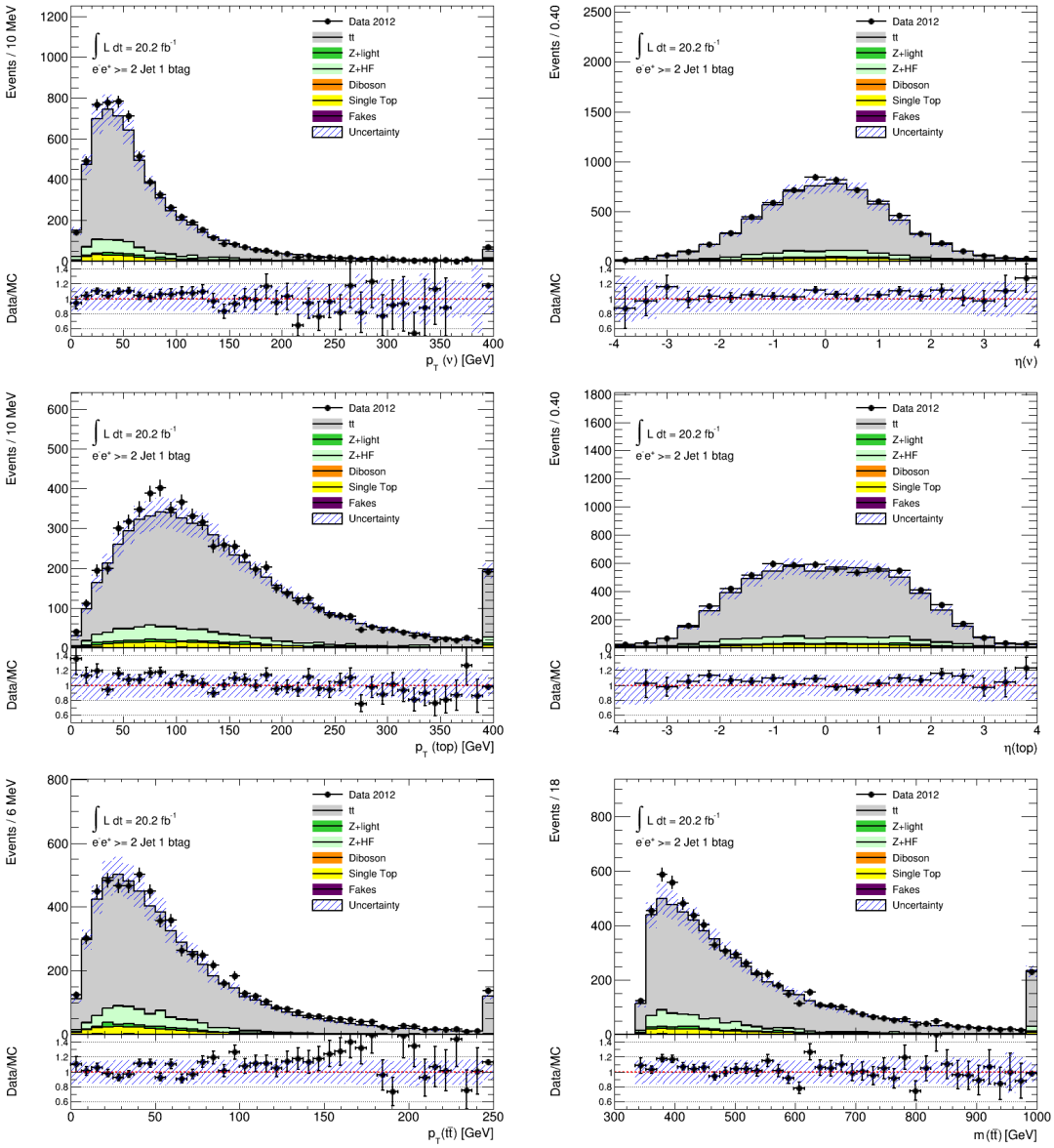

Figure 6.9.: Plots showing data/MC agreement after event reconstruction for the reconstructed objects (ν, t, and $t\bar{t}$) in the 1 exclusive b-tag, ee region. Statistical and background normalisation uncertainties are included.

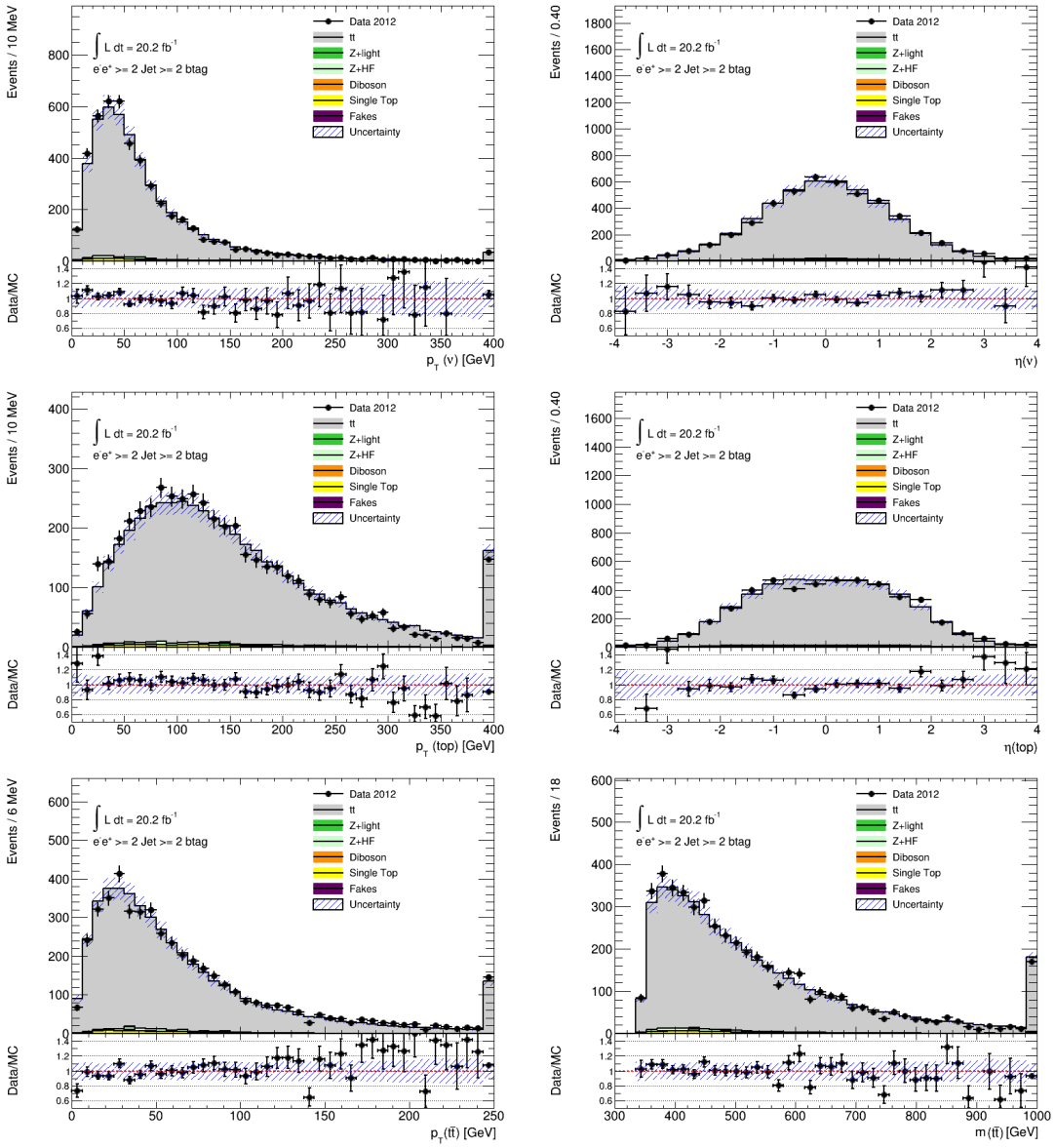

Figure 6.10.: Plots showing data/MC agreement after event reconstruction for the reconstructed objects (ν, t, and $t\bar{t}$) in the 2 inclusive b-tag, ee region. Statistical and background normalisation uncertainties are included.

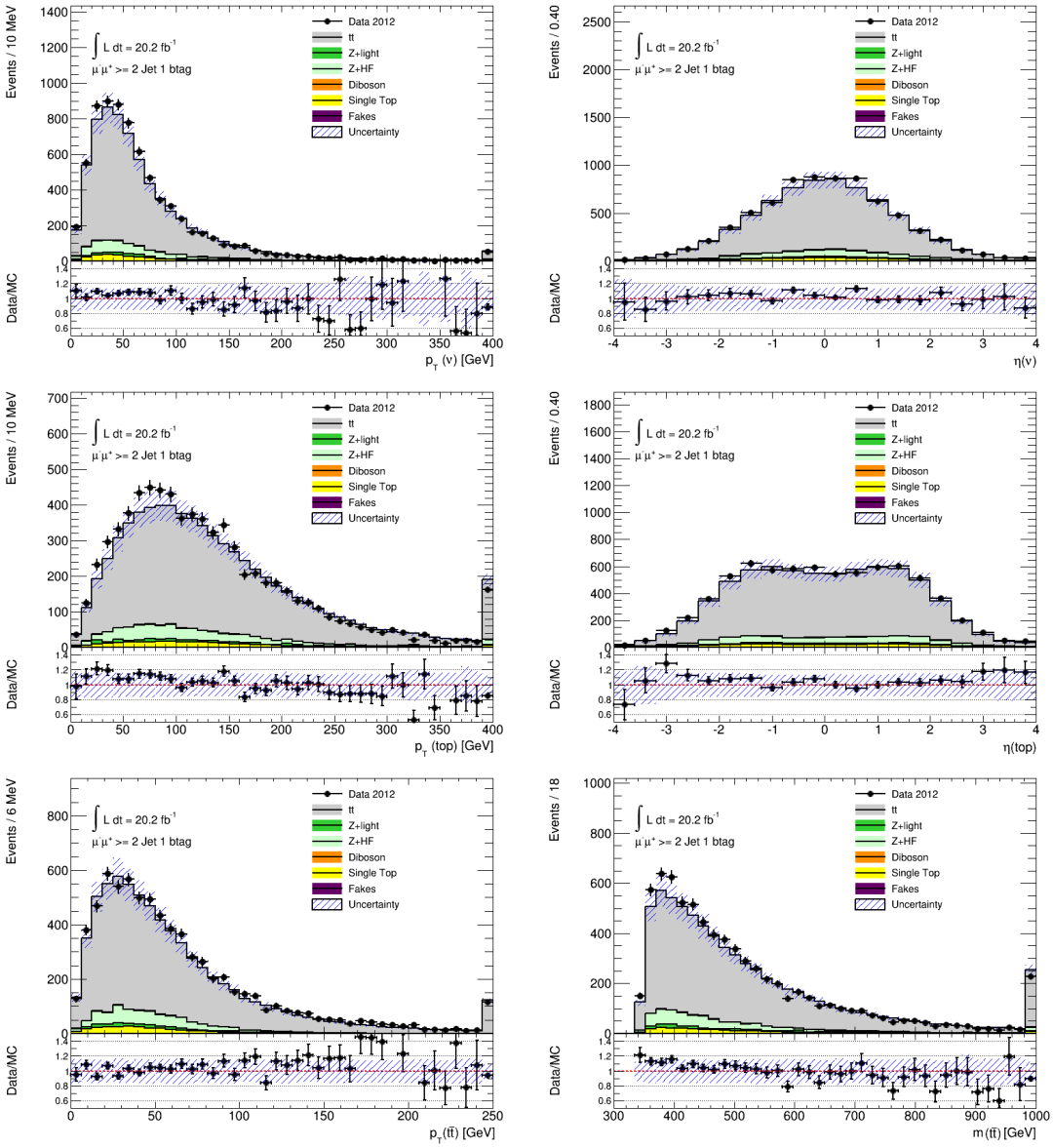

Figure 6.11.: Plots showing data/MC agreement after event reconstruction for the reconstructed objects (ν, t, and $t\bar{t}$) in the 1 exclusive b-tag, $\mu\mu$ region. Statistical and background normalisation uncertainties are included.

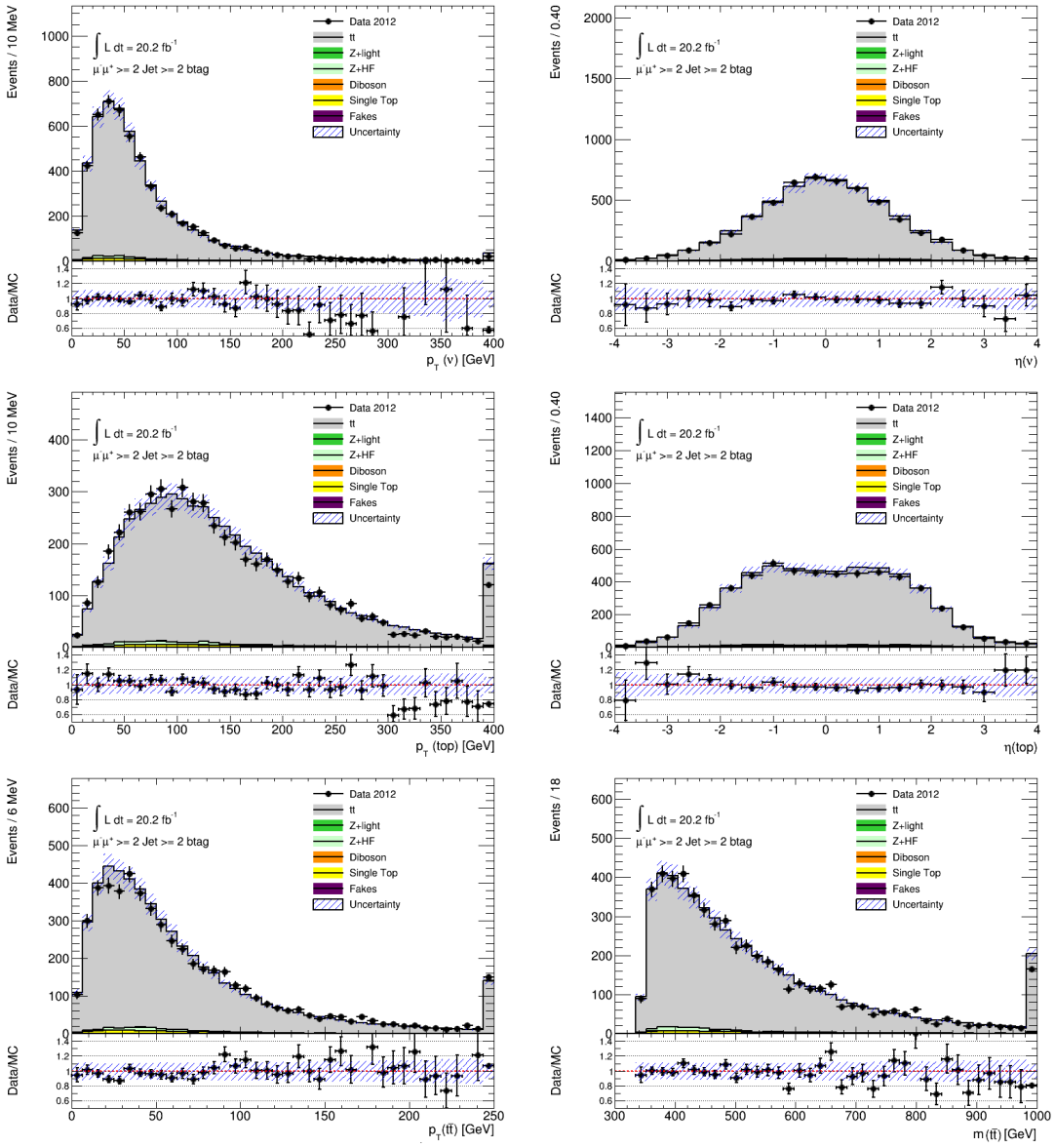

Figure 6.12.: Plots showing data/MC agreement after event reconstruction for the reconstructed objects (ν, t, and $t\bar{t}$) in the 2 inclusive b-tag, $\mu\mu$ region. Statistical and background normalisation uncertainties are included.

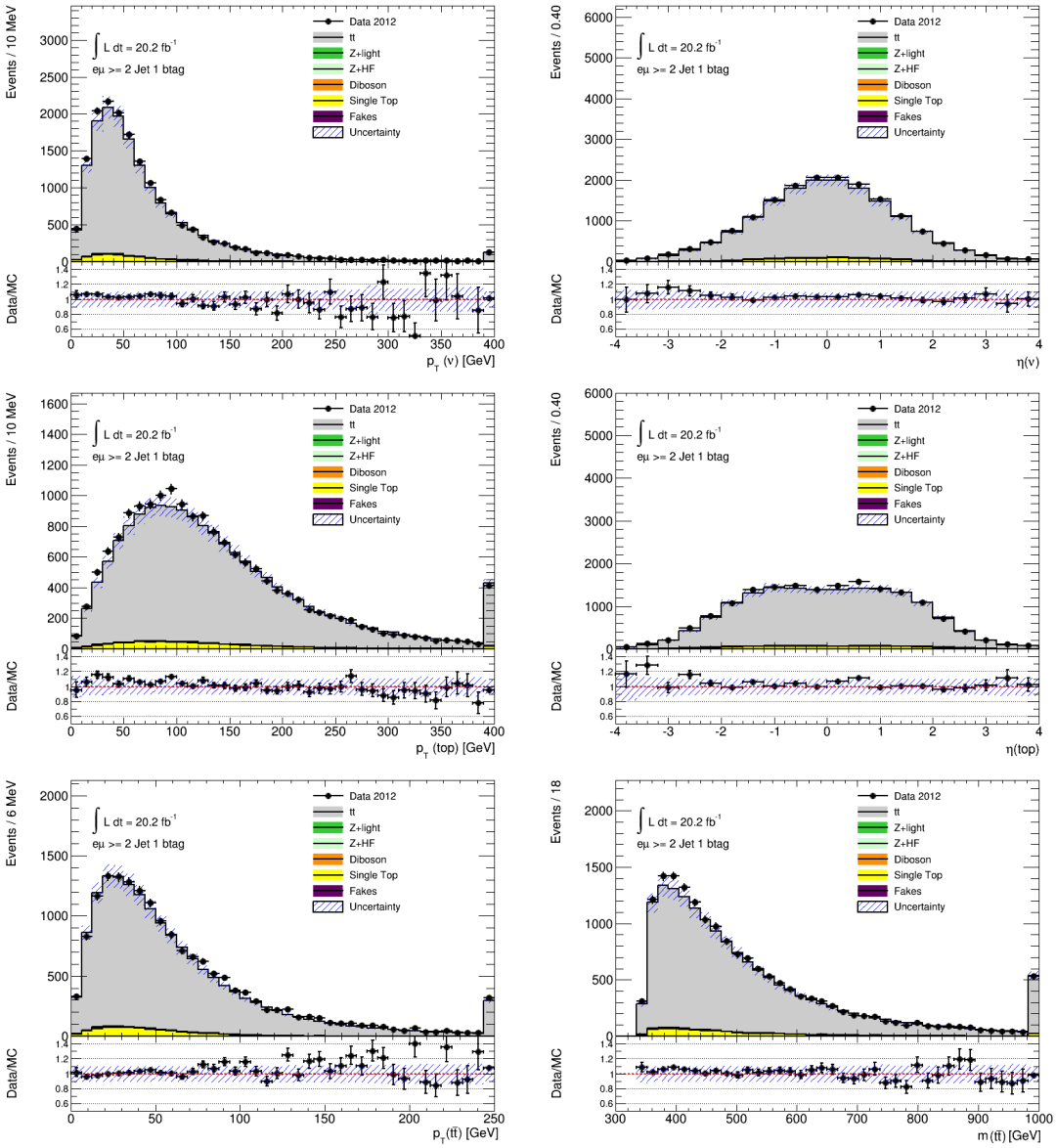

Figure 6.13.: Plots showing data/MC agreement after event reconstruction for the reconstructed objects (ν, t, and $t\bar{t}$) in the 1 exclusive b-tag, $e\mu$ region. Statistical and background normalisation uncertainties are included.

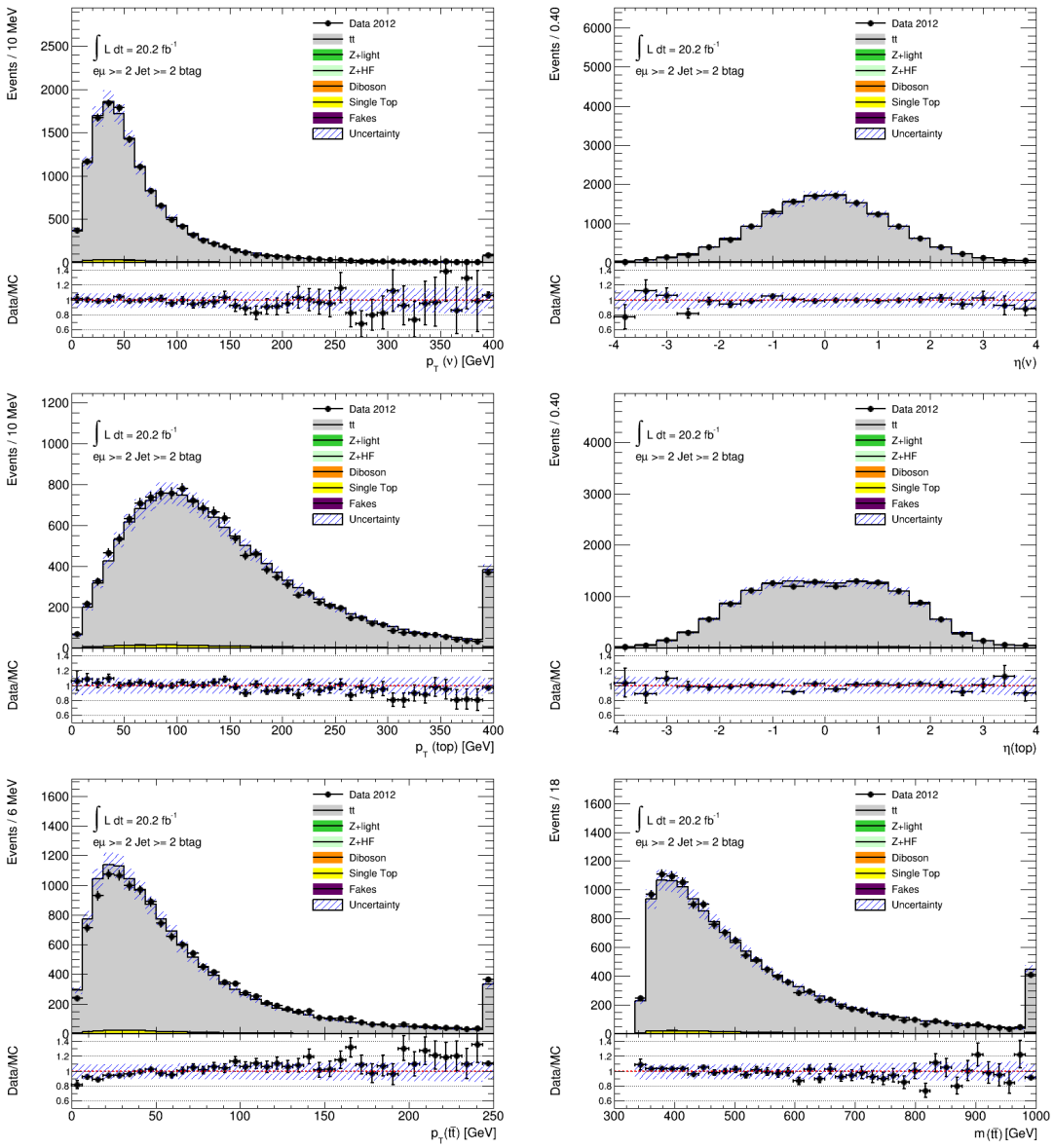

Figure 6.14.: Plots showing data/MC agreement after event reconstruction for the reconstructed objects (ν, t, and $t\bar{t}$) in the 2 inclusive b-tag, $e\mu$ region. Statistical and background normalisation uncertainties are included.

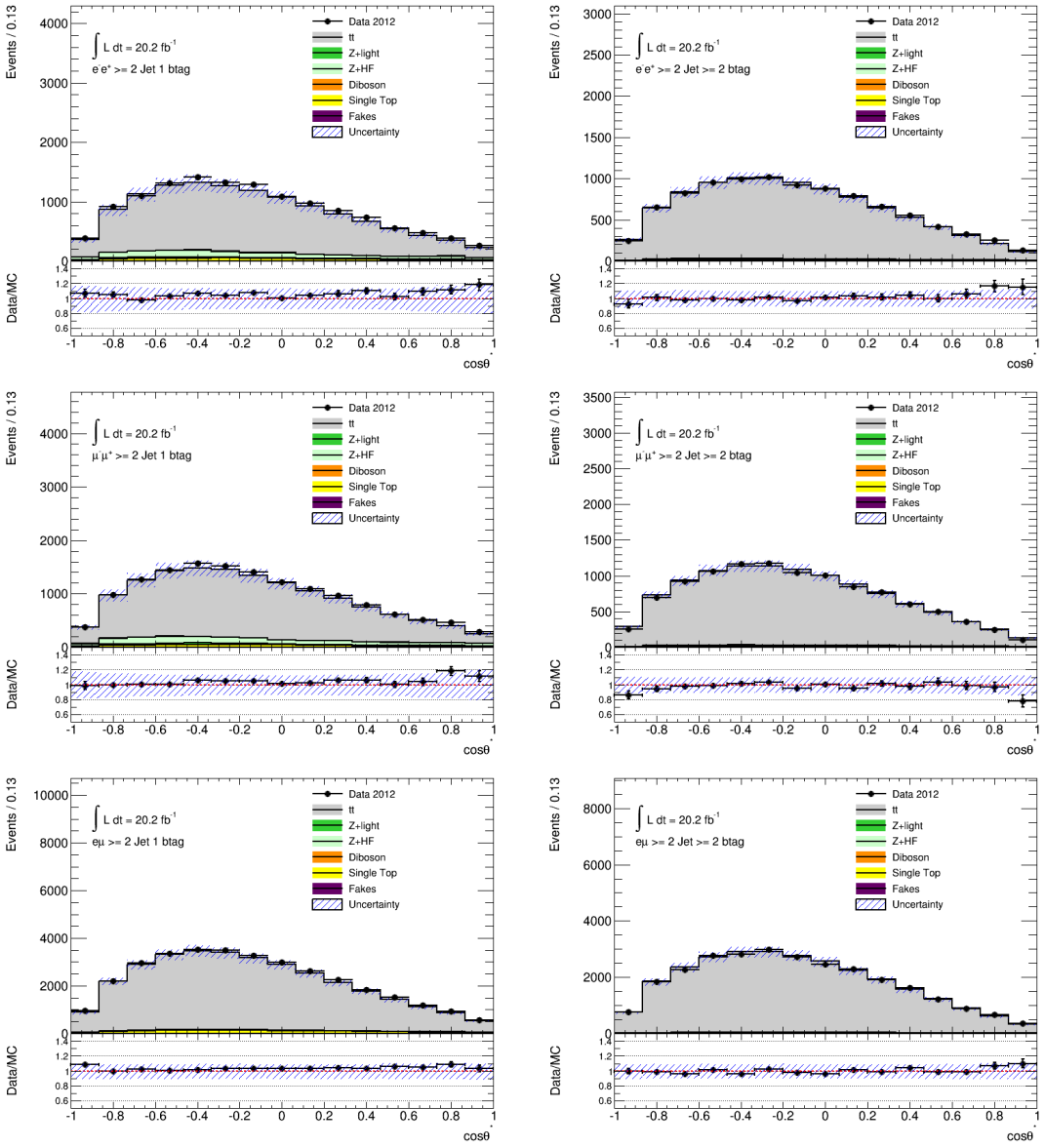

Figure 6.15.: Plots showing data/MC agreement after $t\bar{t}$ system reconstruction for ee, $\mu\mu$ and $e\mu$ channels in the 1 exclusive b-tag (left) and 2 inclusive b-tag (right) regions, for the observable cosθ^*. Statistical and background normalisation uncertainties are included.

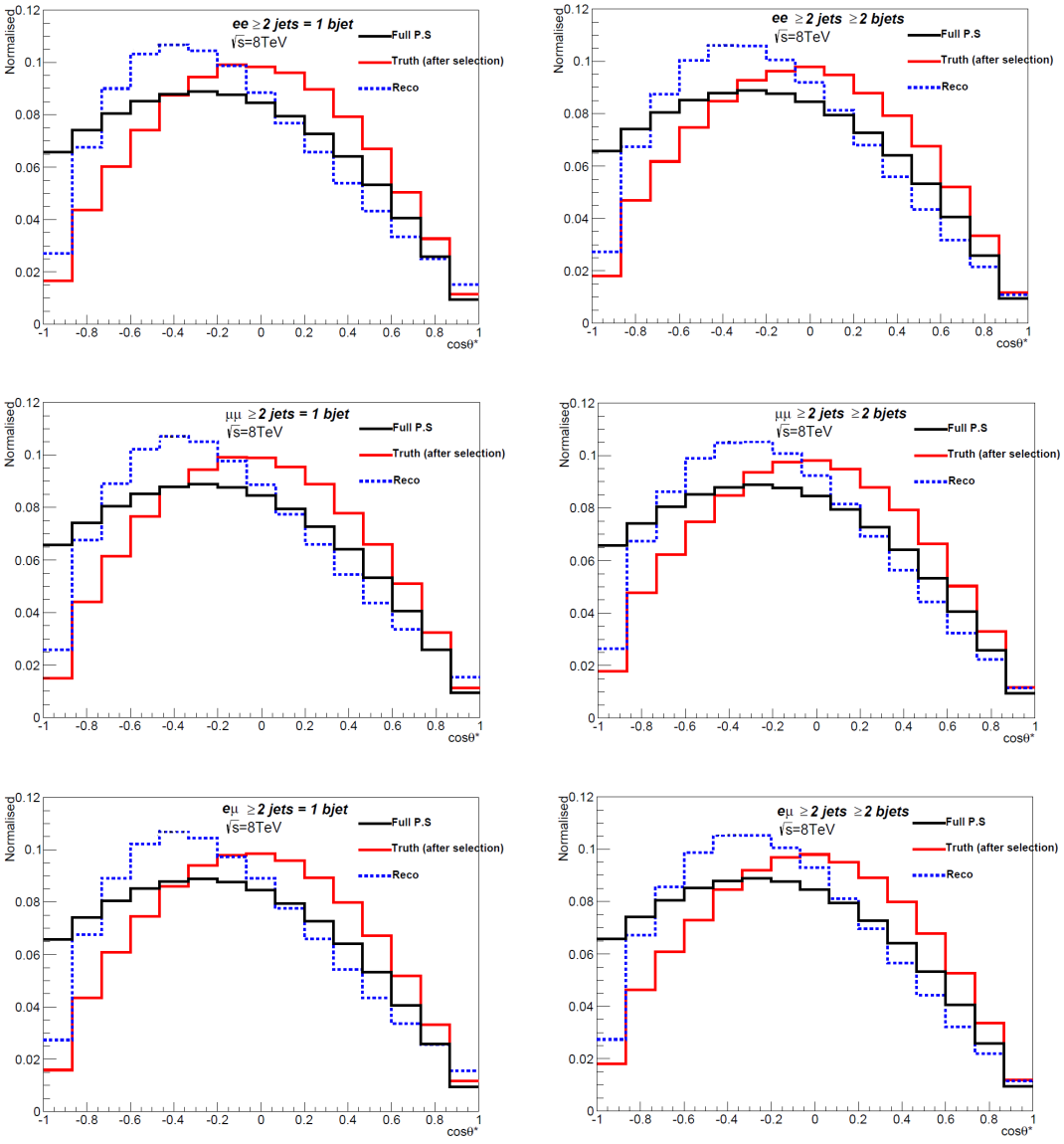

Figure 6.16.: The cosθ^* distributions for the full phase space and after acceptance effects on the generated and reconstructed level, in the dilepton channels split by lepton flavor (ee, $\mu\mu$ and $e\mu$) and b-tag regions (one exclusive, two inclusive).

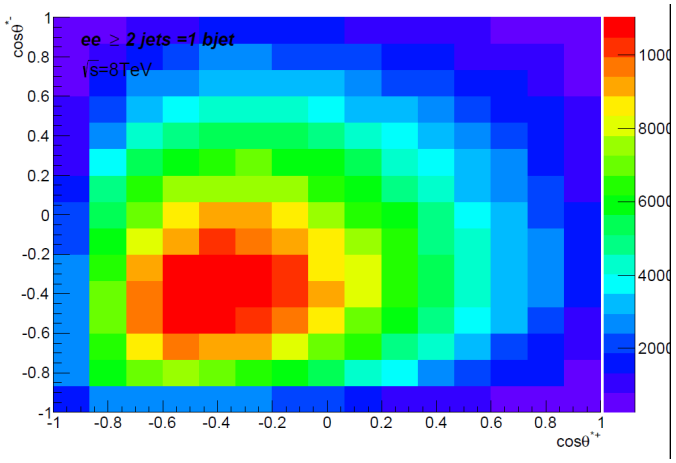

(a)

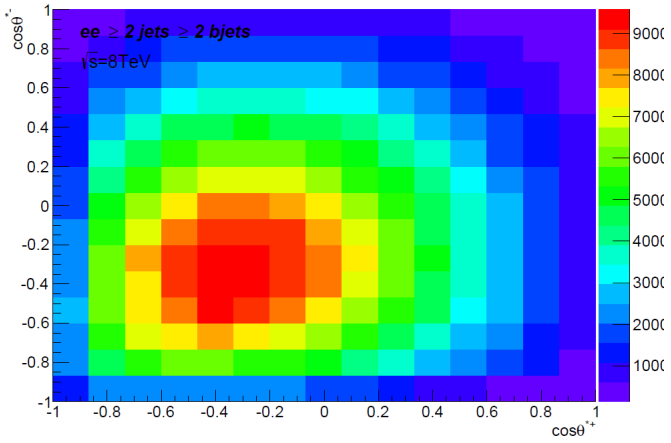

(b)

Figure 6.17.: Two-dimensional distributions of the reconstructed $\cos\theta^*$ from positively and negatively charged leptons in all dilepton channels with exactly one b-tag (a) and two or more than two b-tags (b) passing the nominal selection.

CHAPTER 7

Analysis Strategy and Uncertainty Evaluation

For the measurement of the W boson helicity fractions, the angular distribution of the charged lepton (electron or muon) in the rest frame of the W boson is used. After the reconstruction of the $t\bar{t}$ system a binned likelihood template fit is performed, as it is discussed in Section 7.1. Statistical uncertainties as well as uncertainties caused by object reconstruction and $t\bar{t}$ signal modelling effects are discussed in Section 7.2.

7.1. Template Fitting

The W boson helicity fractions are obtained by comparing the shape of real data and simulated distributions using a binned likelihood template fit method. The production of pure helicity templates using a reweighting method is discussed in Section 7.1.1 and the likelihood fit itself in Section 7.1.2. The combination procedure used for all dilepton channels is introduced in Section 7.1.3 and finally the closure tests on the fitting method discussed in Section 7.1.4.

7.1.1. Template Reweighting

Since there is currently no next-to-leading order (NLO) simulation $t\bar{t}$ sample capable of generating pure W boson helicity states in $t\bar{t}$ production, the three required signal templates are produced by re-weighting the NLO POWHEG $t\bar{t}$ sample at generated (truth) level.

- The signal sample is generated with the POWHEG MC generator as already discussed in Section 5.2. In order to define standard model helicity fractions from the signal ($t\bar{t}$) sample F_i^{Powheg}, the $\cos\theta^*$ distribution for the full phase from this sample is fitted with the function given in equation 2.24 of the angular distribution.

- The truth weights are needed to be applied on $\cos\theta^*$ angular distribution to prepare pure helicity templates. These weights are calculated after full $t\bar{t}$ event reconstruction at generated level, for the left-handed, right-handed, and longitudinal helicity states in each event, separately for the W^+ and W^- bosons using:

$$W_i(\cos\theta^*) = \frac{w_i(\cos\theta^*)}{w_0(\cos\theta^*) + w_L(\cos\theta^*) + w_R(\cos\theta^*)} \tag{7.1}$$

  where $i = 0$, L, R and the components $w_i(\cos\theta^*)$ are defined as:

$$\begin{aligned} w_0(\cos\theta^*) &= \frac{3}{4}(1-\cos^2\theta^*)F_0^{\text{Powheg}}, \\ w_L(\cos\theta^*) &= \frac{3}{8}(1-\cos\theta^*)^2 F_L^{\text{Powheg}}, \\ w_R(\cos\theta^*) &= \frac{3}{8}(1+\cos\theta^*)^2 F_R^{\text{Powheg}}, \end{aligned} \tag{7.2}$$

  where for F_0, F_L and F_R the values derived from the full phase space fit are used.

- Finally, these weights are applied to the reconstructed $\cos\theta^*$ distribution.

Template Distributions

In order to measure the W boson helicity fractions, three reweighted signal and three background templates are used. The background templates correspond to: Z+jets and single top quark events as dominant backgrounds and the remaining background, which is the sum of diboson and fake leptons background. Figure 7.1 displays the reweighted signal templates and Figure 7.2 displays the background templates for the ee, $\mu\mu$ and $e\mu$ channels in 1b-tag exclusive and 2b-tag inclusive regions for fully reconstructed $t\bar{t}$ events. As discussed in Section 6.2.4 acceptance effects distort the full $\cos\theta^*$ distribution as pure helicity templates. The spikes on the remaining background in ee and $\mu\mu$ channels and on Z+jets in the $e\mu$ channel is caused by a leak of MC statistics in the 2b-tag inclusive region.

7.1.2. Likelihood Fit

A binned likelihood fit is performed using the signal and background templates mentioned above. The fit procedure is based on the ROOT Minuit package [133, 134]. The number of expected events in the fit corresponds to the sum of all template normalisations:

$$n_{\text{exp}} = n_0 + n_{\text{L}} + n_{\text{R}} + n_{\text{Z+jet}} + n_{\text{SingleTop}} + n_{\text{Rem.Bkg.}}, \tag{7.3}$$

Then it is compared to the data distribution via the likelihood function, assuming Poisson statistics for the number of events in each bin:

$$\mathscr{L} = \prod_{i=1}^{N_{\text{bins}}} \text{Poisson}(n_{\text{data},i}, n_{\text{exp},i}) \prod_{j=1}^{N_{\text{bkg}}} \frac{1}{\sqrt{2\pi}\sigma_{\text{bkg.j}}} e^{\frac{-(n_{\text{bkg.j}}-\hat{n}_{\text{bkg.j}})^2}{2\sigma^2_{\text{bkg.j}}}}, \tag{7.4}$$

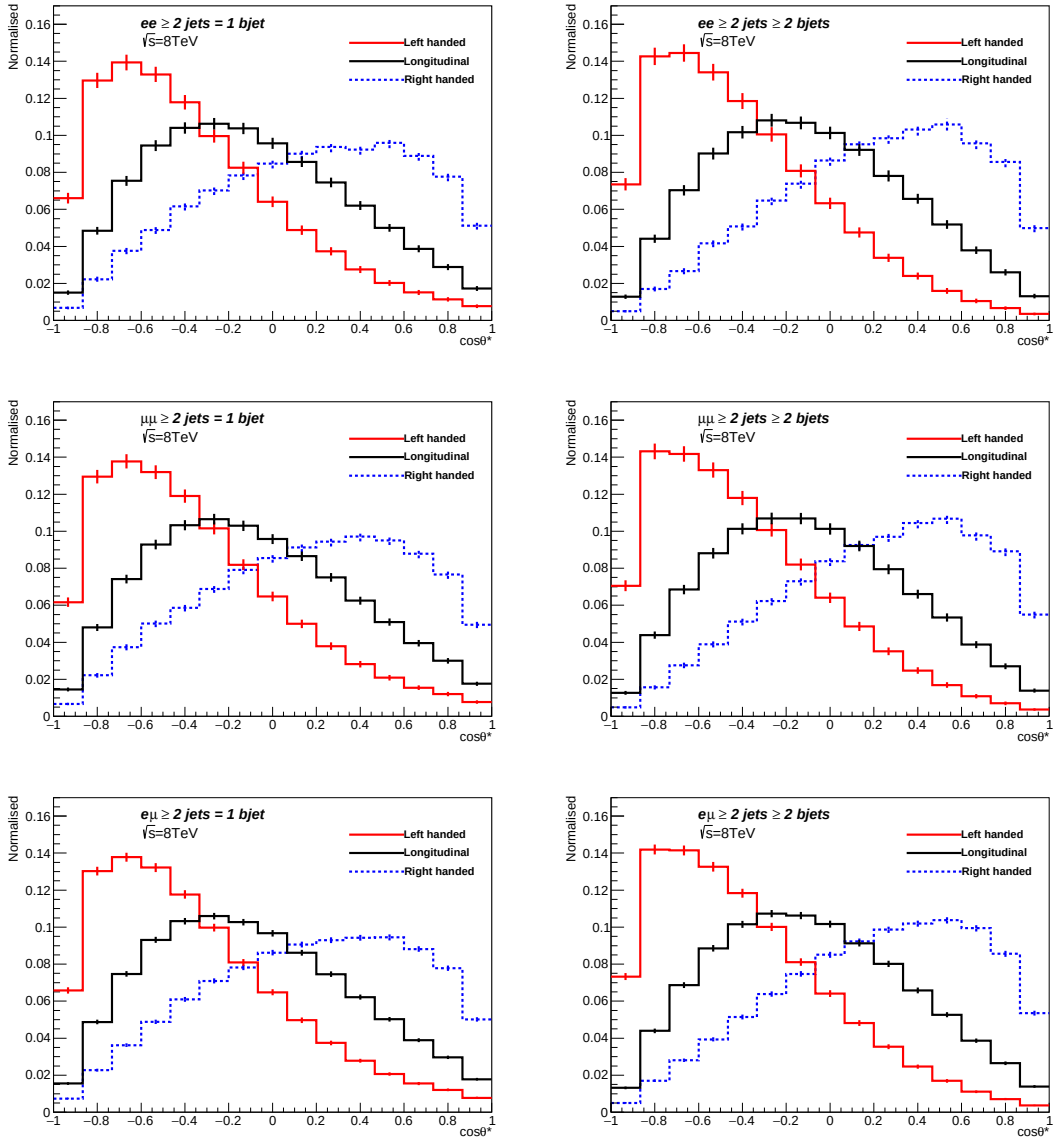

Figure 7.1.: Reconstructed signal templates for ee, $\mu\mu$, and $e\mu$ channels in 1 exclusive and 2 inclusive b-tag regions.

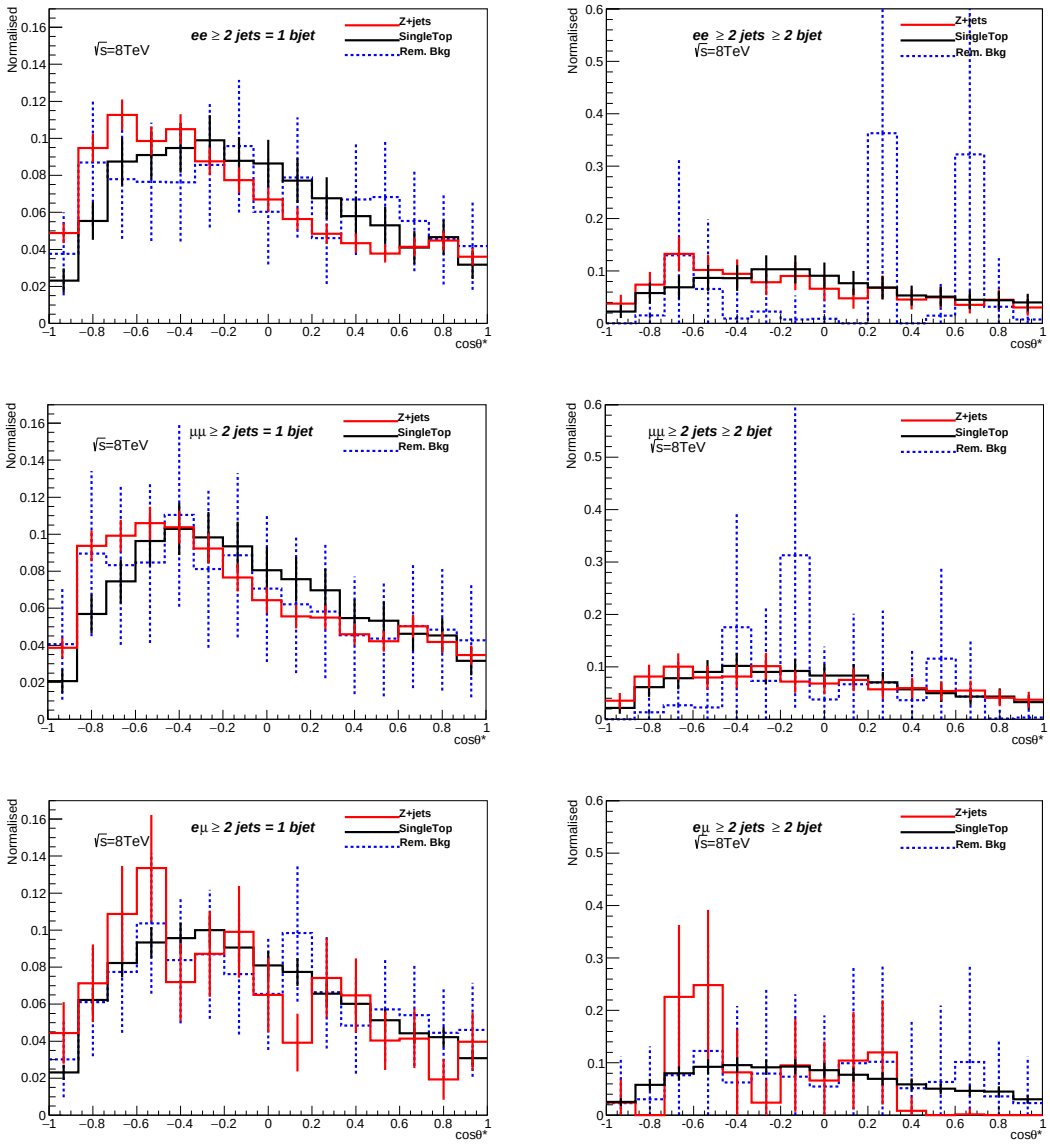

Figure 7.2.: Reconstructed background templates for ee, $\mu\mu$, and $e\mu$ channels in 1 exclusive and 2 inclusive b-tag regions.

Fit Parameter	Relative Width of Gaussian Prior
n_0	-
n_L	-
n_R	-
n_{Z+jets}	0.35
n_{stop}	0.068
$n_{Rem.\ Bkg.}$	0.43

Table 7.1.: List of all free parameters in the bin-by-bin likelihood fit as well as the relative widths (width/normalisation) of the Gaussian priors assumed in the fit with floating backgrounds. Rem.bkg contains Fake leptons and dibosons with the relative width of Gaussian prior of 0.50 and 0.35, respectively. For total Rem.bkg, the value varies a bit for different dilepton channels.

where the background normalisation uncertainties are constrained by Gaussian priors, and $\sigma_{\text{bkg.}}$ is the background normalisation uncertainty for a given background. All free parameters in Equation 7.3 are common across all lepton and b-tagged regions (e.g. the same $n_{\text{Z+light}}$ parameter is common across all signal regions).
An overall normalisation uncertainty of 35% is applied to Z+jets and diboson contributions. For electroweak single top quark production, an uncertainty of 6.8% is assumed. A summary of all the free parameters in the fit and their uncertainties are given in Table 7.1. For most backgrounds, the normalisations are taken from theory calculations (explained in Section 5.3), except the normalisation for fake leptons which is 50% (see Section 5.3.4 for details). These background normalisations and uncertainties is shown in Table 6.3.
The normalisation for each helicity template is allowed to float unconstrained in the fit. In the extraction of production-level helicity fractions, the reconstruction efficiency per helicity state is required, as the analysis has different sensitivity to each helicity state. These efficiencies, ϵ_i^{sel}, are calculated using the nominal $t\bar{t}$ sample and are shown in Table 7.2. Given that the total $t\bar{t}$ cross-section cancels in the calculation of the helicity fractions (Equation 2.21), the quantities N_i are defined to translate the post-fit normalisation, $n_{\text{i, templ.}}$, into experimentally independent quantities using these efficiencies. The relationship is given by:

$$n_{\text{i, templ.}} = \epsilon_i^{\text{sel}} \cdot N_i \quad \text{for i= 0, L, R,} \tag{7.5}$$

where again, the $n_{\text{i, templ.}}$ are the parameters in the likelihood fit. Using N_i allows the final helicity fractions to be expressed with the simple ratio:

$$F_{\text{i}} = \frac{N_i}{N_0 + N_L + N_R}, \text{ for i= 0, L, R.} \tag{7.6}$$

Selection eff.	ee	$\mu\mu$	$e\mu$
1 Exclusive b tag			
ϵ_0	0.004	0.005	0.012
ϵ_L	0.003	0.003	0.008
ϵ_R	0.004	0.005	0.013
2 Inclusive b tags			
ϵ_0	0.003	0.004	0.010
ϵ_L	0.002	0.003	0.007
ϵ_R	0.004	0.004	0.011

Table 7.2.: Selection efficiencies in the 1 exclusive and 2 inclusive b-tag regions in the ee, $\mu\mu$, and $e\mu$ channels.

7.1.3. Combination of Dilepton Channels

In order to obtain the most precise measurement of the W boson helicity fractions in the dilepton channel, a combination of the orthogonal dilepton channels in the 2 inclusive b-tag region (3 channel combination $ee + \mu\mu + e\mu$) and in the 1 exclusive +2 inclusive b-tag regions ($2 \times 3 = 6$ channel combination $ee + \mu\mu + e\mu$) is performed. The channels are combined via a simultaneous likelihood fit. The combination of signal templates for each W helicity state is performed using extended distributions which are obtained by concatenating the bins of the individual helicity fraction distributions. Each background contribution is fitted separately. The selection efficiencies for the combined templates are adjusted accordingly. For uncertainty studies the combination of all dilepton channels is used separately for only 2 inclusive b-tag region and combined 1 exclusive and 2 inclusive b-tag regions.

7.1.4. Ensemble Tests

Ensemble tests are performed for the estimation of systematic and expected statistical uncertainties. *Pseudo-data* distributions are obtained from MC simulation and scaled to the actual data statistics. Ensembles (*pseudo-experiments*) are obtained by fluctuating each bin of the pseudo-data distribution according to Poisson statistics. For the template fit, 5.000 sets of pseudo experiments are generated. The mean values of N_0, N_L and N_R are used to calculate the specific W boson helicity fractions for each pseudo-data distribution. The differences between the fractions obtained from the nominal distribution and the fractions obtained from each systematic variation are considered. For systematics with up and down variations, the calculated systematic shifts are added in quadrature according to whether they affect the helicity fractions positively or negatively. For one sided sources of systematic uncertainty (e.g. jet energy resolution, signal modelling systematics), the single variation is symmetrised and taken as both the positive and negative effect. All positive (negative) contributions are then summed in quadrature.

7.1.5. Method Validation

It is necessary to make sure that the fit does not cause any bias. For this reason the method is validated by performing linearity tests and creating pull distributions. The pull for parameter N is defined as:

$$\text{Pull} = \frac{N_j - N_{nom}}{\sigma_{N_j}}, \tag{7.7}$$

where N_{nom} is the nominal value, N_j the fitted value and σ_{N_j} the uncertainty of the fit. The variety of nominal values N_{nom} for each fraction is set. The longitudinal W helicity fraction is varied between 0.4 and 1.0 by steps of 0.1, while the iteration steps for left-handed and right-handed fractions are 0.05, also enforcing the condition that the sum of the three fractions equals unity. For each value of N_{nom} the pull distribution is obtained and the mean and standard deviation values are compared to the expectations of zero and unity, respectively. No significant deviations from the expectations are observed. The complete set of pull distributions corresponding to the three ($ee + \mu\mu + e\mu$ in 2b-tag inclusive) and six ($ee + \mu\mu + e\mu$ in 2b-tag inclusive +1b-tag exclusive) channels combination are presented in Figures 7.3 and 7.4.
To test the linearity of the method, ensemble tests are performed on pseudo-data distributions. The W-helicity fractions are calculated from the mean of the distributions:

$$F_{\text{i}} = \frac{< N_i >}{< N_0 > + < N_L > + < N_R >} \text{ for } i = 0, \text{L, R.} \tag{7.8}$$

The result for the fractions are plotted dependent on their input values and fitted with linear functions. The slope of the fit is expected to be one and the offset is expected to be zero for an unbiased estimator. The linearity test results for the three channel combination ($ee + \mu\mu + e\mu$ in 2b-tag inclusive) and the fully combined region (1 exclusive +2 inclusive b-tag, $ee + \mu\mu + e\mu$) are shown in Figures 7.5 and 7.6. No significant deviations from the expectations are observed.

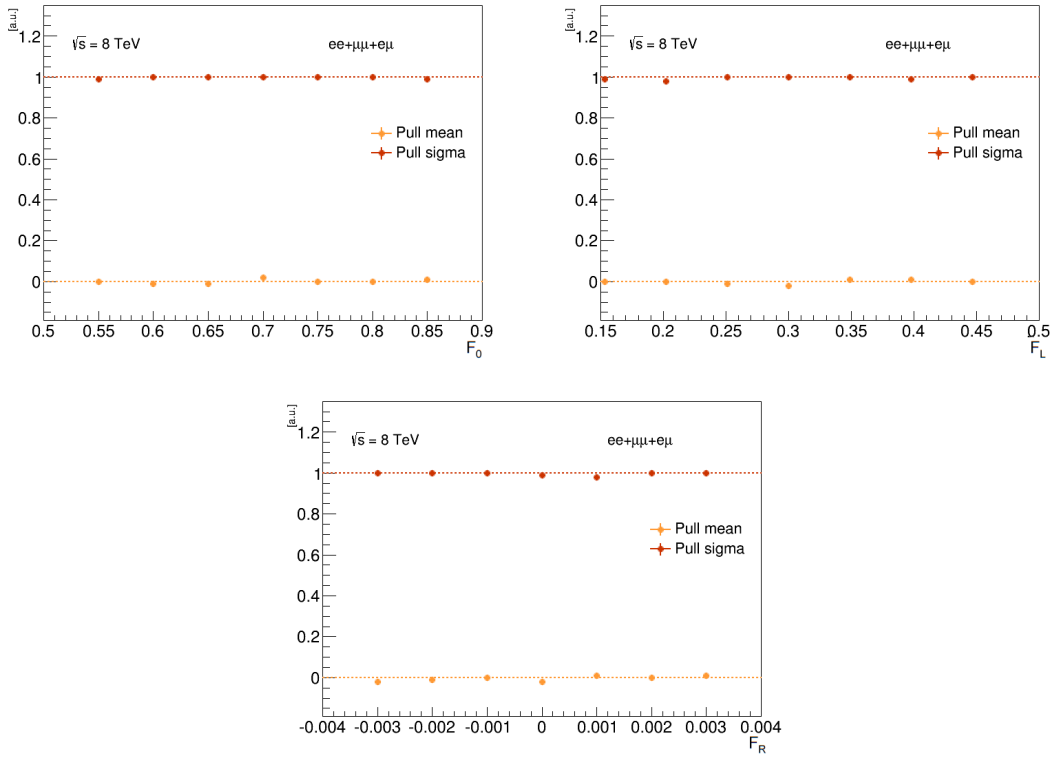

Figure 7.3.: Plots showing the pull distributions summary for F_0, F_L, and F_R in the $ee + \mu\mu + e\mu$, two inclusive b-tag tag region. 5000 sets of pseudo-data were fit to perform the test. Good closure is seen for all helicity fractions and no bias is observed. The (unphysical) negative F_R values are within expected statistical uncertainties.

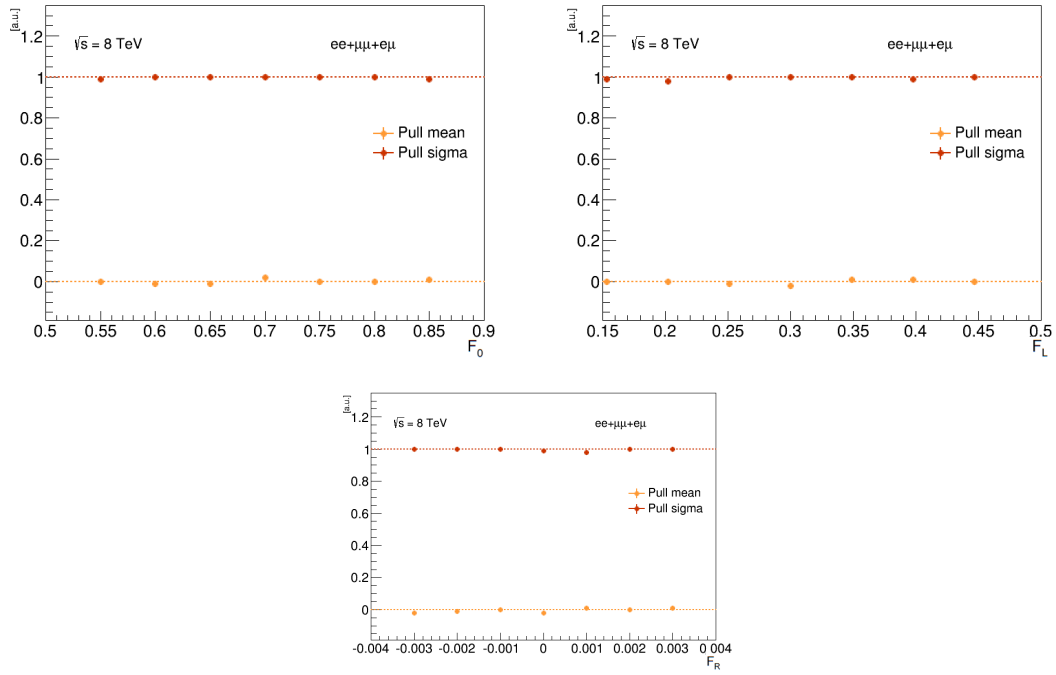

Figure 7.4.: Plots showing the pull distributions summary for F_0, F_L, and F_R in the $ee + \mu\mu + e\mu$, one exclusive + two inclusive b-tag tag region. 5000 sets of pseudo-data were fit to perform the test. Good closure is seen for all helicity fractions and no bias is observed. The (unphysical) negative F_R values are within expected statistical uncertainties.

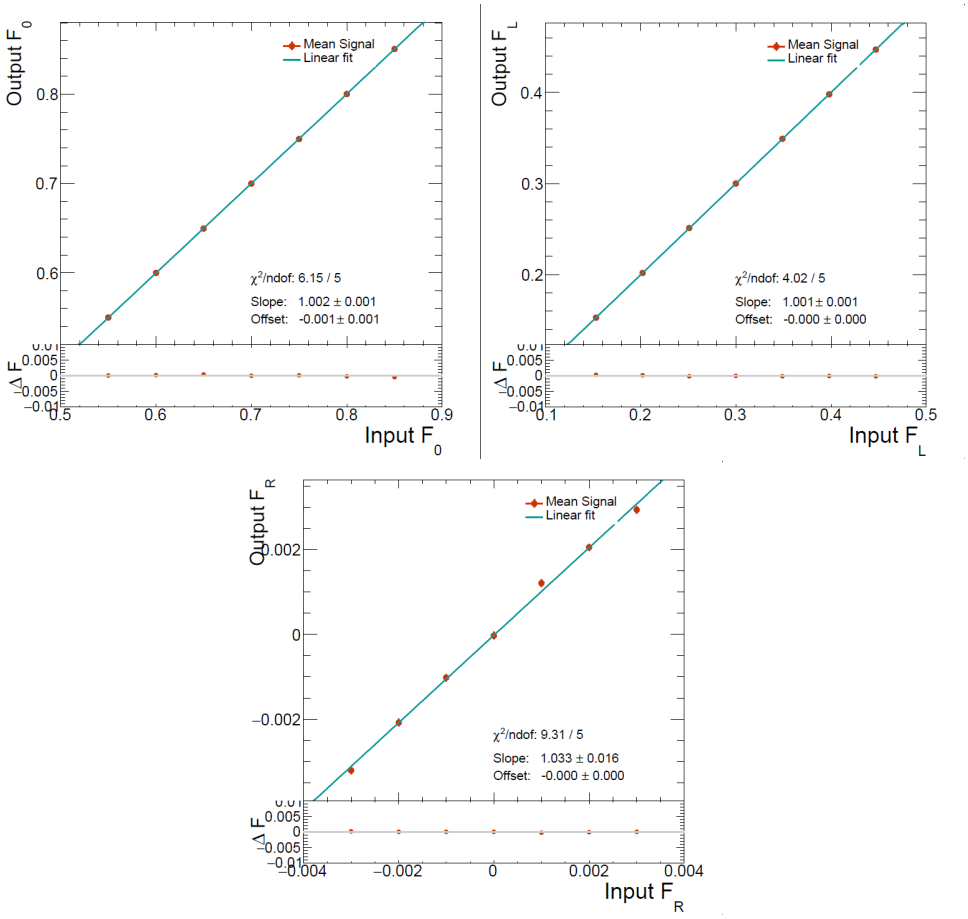

Figure 7.5.: Linearity checks for F_0, F_L, and F_R in the $ee+\mu\mu+e\mu$ in two inclusive b-tag region. 5000 sets of pseudo-data were fit to perform the test. Reasonable closure is seen for all helicity fractions and no bias is observed.

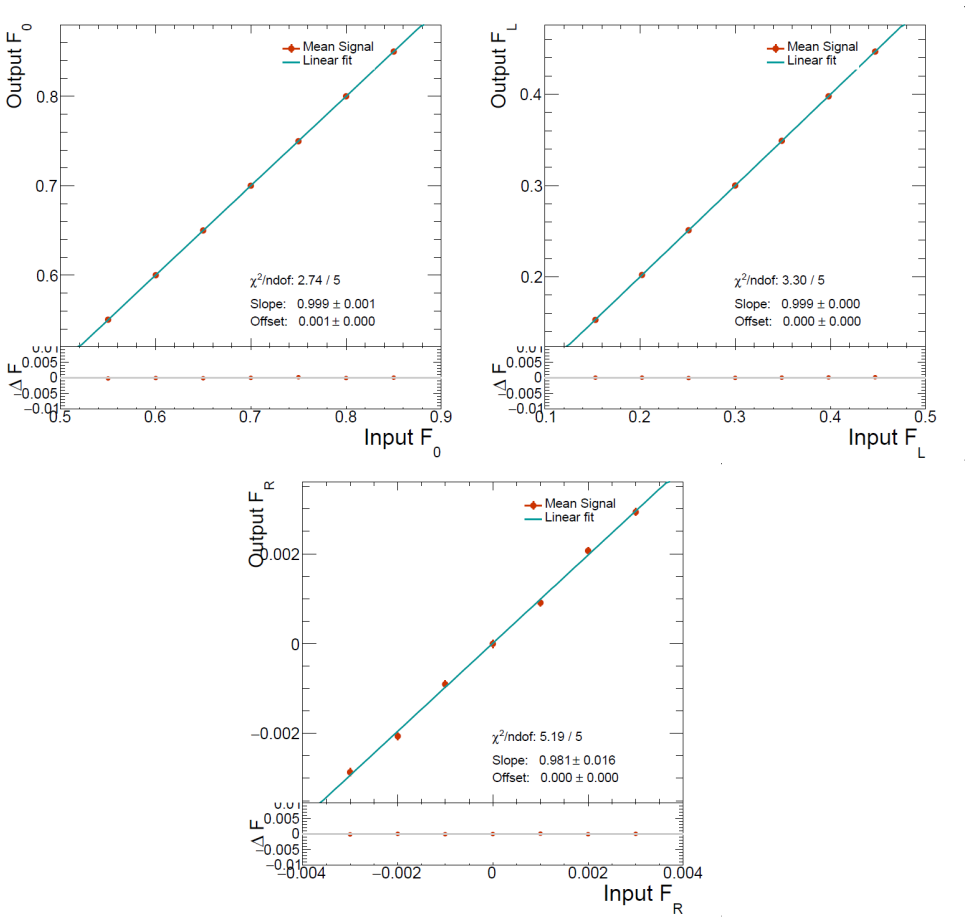

Figure 7.6.: Linearity checks for F_0, F_L and F_R in the $ee + \mu\mu + e\mu$ in one exclusive + two inclusive b-tag region. 5000 sets of pseudo-data were fit to perform the test. Good closure is seen for all helicity fractions and no bias is observed.

7.2. Evaluation of Expected Statistical and Systematic Uncertainties

The limited statistics of data and MC samples and the modelling of the physics processes and detector effects play an important role in precision measurements of W boson helicity fractions in the dilepton channel. In this section, the evaluation of statistical and systematic uncertainties will be discussed.

7.2.1. Evaluation of Expected Statistical Uncertainties

The expected statistical uncertainties are obtained from fits to the pseudo-data distributions, where Minuit provides the fitted number of events and the corresponding statistical uncertainties. Since the helicity fractions are obtained from the fitted number of events, the uncertainty propagation has been considered accordingly. Table 7.3 summarises the statistical uncertainty expectation obtained in each channel from ensemble test fits. The normalisations of the background contributions were kept fixed during these tests in order to estimate the absolute statistical uncertainties. All three dilepton channels (ee, $\mu\mu$ and

Channel		2incl. b-tag	1excl.+2incl. b tag
ee	σ_{F_0}	0.032	0.026
	σ_{F_L}	0.022	0.017
	σ_{F_R}	0.014	0.012
$\mu\mu$	σ_{F_0}	0.029	0.023
	σ_{F_L}	0.020	0.015
	σ_{F_R}	0.013	0.010
$e\mu$	σ_{F_0}	0.018	0.014
	σ_{F_L}	0.012	0.009
	σ_{F_R}	0.008	0.006

Table 7.3.: Absolute statistical uncertainty expectations of the helicity fractions fitted in $ee, \mu\mu$, and $e\mu$ channels in the 2 inclusive b-tag and the combined 1 exclusive +2 inclusive b-tag. The background normalisation uncertainties were kept fixed in the fit.

$e\mu$ in the 2b-tag inclusive region) are combined. Increasing the statistics, the combined sensitivities show better results, as expected. The six-channel combination including one b-tag exclusive provides the lowest expected statistical uncertainty. The corresponding helicity fraction distributions are shown in Figures 7.7 and 7.8,assuming SM values. The background normalisations could be treated either as fixed to their Monte Carlo predictions in the fit or be allowed to float within their theoretical uncertainties according to a Gaussian prior. In the latter scenario, the width of the obtained helicity fraction distributions of fitting 5000 pseudo-experiments yields the expected statistical + background normalisation uncertainties discussed in Section 5.3. On the other hand, in the former

scenario, the width of the helicity distributions gives the absolute expected statistical uncertainty as mentioned before. The results of this comparison are summarised in Table 7.4. In general, the test shows stability against the different background normalisation treatments in the fit with respect to the expected statistical uncertainties (statistical + background normalisation) for fixed (floating) treatments. Due to the smaller systematic uncertainties, the floating background normalisation treatment is chosen as the default method in this analysis.

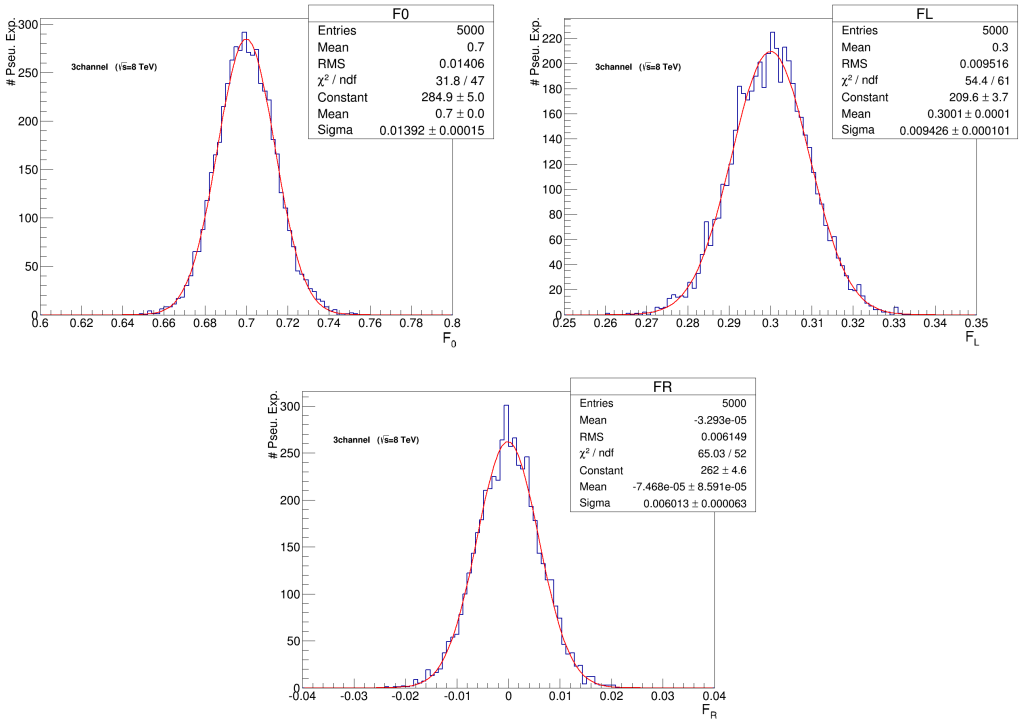

Figure 7.7.: The helicity fraction distributions obtained by pseudo-experiments: $ee + \mu\mu + e\mu$ channel in 2 incl b-tag.

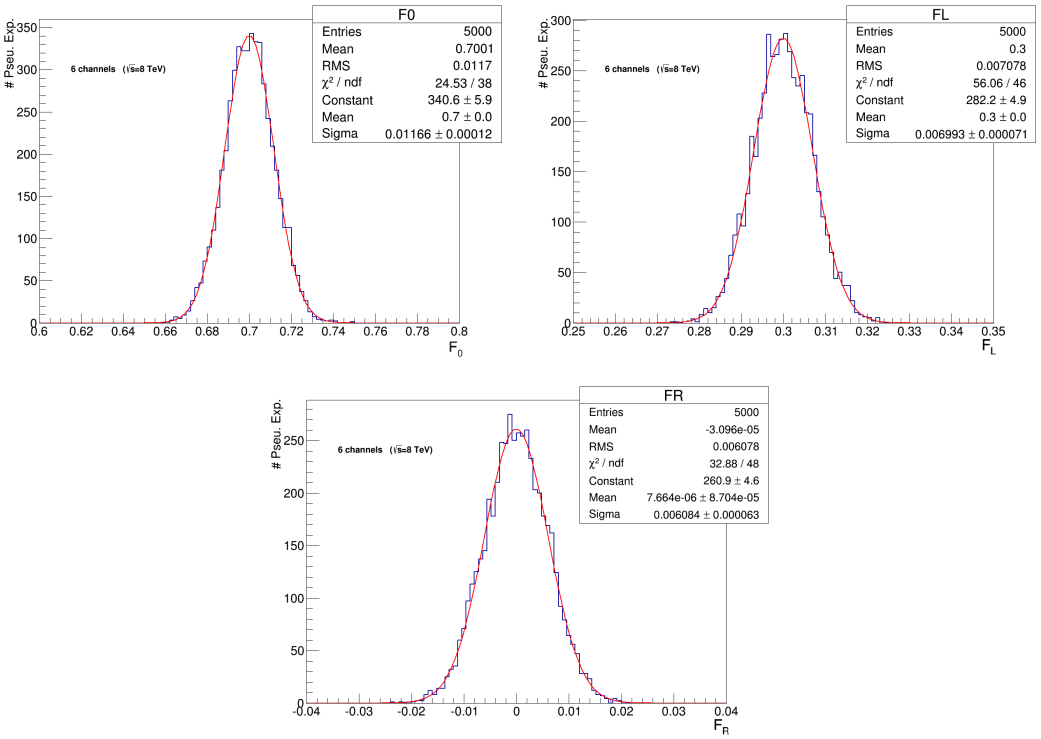

Figure 7.8.: The helicity fraction distributions obtained by pseudo-experiments: $ee + \mu\mu + e\mu$ channel in 2 incl. + 1 excl b-tag.

Background norm. unc. mode		2incl. b-tag	1excl+2incl b-tag
combination of ee, $\mu\mu$ and $e\mu$ channels			
Fixed	σ_{F_0}	0.014	0.011
	σ_{F_L}	0.009	0.007
	σ_{F_R}	0.006	0.006
Floating	σ_{F_0}	0.014	0.012
	σ_{F_L}	0.010	0.007
	σ_{F_R}	0.006	0.006

Table 7.4.: Expected statistical (statistical + backgrounds) uncertainty of the helicity fractions fitted using all three channels combined in 2 inclusive b-tag and the combined 1 excl. +2 incl. b-tag using fixed (floating) background normalisation treatment. The fit results are compared when the background normalisations are fixed to their Monte Carlo predictions and when they are allowed to float within their theoretical uncertainties according to Gaussian priors.

7.2.2. Systematic Uncertainties

Estimating systematic uncertainties is critical in most top quark properties studies. These uncertainties can be related to both, physics processes under study and/or modelling of the detector. In the following section sources of systematics will be discussed as listed in Table 7.5. Each source can have a normalisation and (or) a shape effect on the signal/background distribution.

Systematic uncertainty	Type	Components
Luminosity	N	1
Physics Objects		
Electron	SN	5
Muon	SN	6
E_T^{miss}	SN	2
Jet energy scale	SN	26
Jet vertex fraction	SN	1
Jet energy resolution	SN	11
Jet reconstruction efficiency	SN	1
b tagging efficiency	SN	6
c tagging efficiency	SN	4
Light jet tagging efficiency	SN	12
Background Model		
Z+jets normalisation	SN	1
Single top cross section	N	1
Single top model	SN	1
Fake background	SN	1
Diboson+jets normalisation	N	1
Signal Model		
$t\bar{t}$ Radiation	SN	2
$t\bar{t}$ MC Generator	SN	1
$t\bar{t}$ Showering & Hadronisation	SN	1
$t\bar{t}$ PDF	SN	3
Top mass	SN	1
Method related Template Statistics	SN	1

Table 7.5.: List of systematic uncertainties considered. "N" represents uncertainties only affecting the normalisation for all processes and channels, whereas "S" denotes systematic uncertainties that are considered as shape-only in all processes and channels. "SN" means that the uncertainty affects both shape and normalisation. Some of the systematic uncertainties are split into several different components for a more accurate treatment (number indicated in the column labeled as "Components").

Some sources of systematic variations are not considered in the total systematic uncertainty calculation, because these systematic effects are very small. The systematic sources are considered if:

a) The difference between the total yield of the varied $\cos\theta^*$ distribution and the total nominal yield is larger than the total nominal Monte Carlo statistical uncertainty;

b) The difference in yield between the nominal sample and a variation is larger than the nominal MC uncertainty in two or more bins.

When the difference between the nominal $\cos\theta^*$ distribution and a given systematic variation is smaller than the statistical uncertainty on the Monte Carlo yield of the nominal sample, that systematic variation is removed from consideration when calculating the total systematic error. The following sections describe each of the systematic uncertainties considered in the analysis. Further discussion comparing variation yields with respect to the nominal Monte Carlo statistical uncertainty as well as the effect of systematic uncertainties on the shape of the templates can be found in Appendix C.

Luminosity

The luminosity estimate has an uncertainty of 1.9% [135] in $\sqrt{s} = 8$ TeV analyses. This uncertainty constrains the background normalisation and is hence included in the statistical + background normalisation uncertainty. The impact of the luminosity is fully correlated between the three signal contributions. Therefore the effect is negligible ($< 10^{-6}$) in the calculation of the W helicity fractions.

7.2.3. Physics Objects

From the object reconstruction discussed in this section arises several systematic uncertainties.

Leptons

The uncertainties associated with leptons can originate from several sources:

- Lepton reconstruction and identification efficiency,
- Lepton trigger efficiency,
- Lepton momentum and energy scales,
- Lepton momentum and energy resolutions.

The total number of uncertainties associated with electrons is six and for muons five. As discussed in Sections 4.1 and 4.2, the measured efficiencies of reconstruction, trigger, and identification differ between real and simulated data. The scale factors (SF) are derived using tag-and-probe techniques on the $Z \to l^+l^-$ ($l = e,\ \mu$) process in data and

applied on simulated samples to correct the simulation for these discrepancies.
The accuracy of the lepton momentum scale and resolution in simulation is checked using reconstructed distributions of the $Z \to l^+l^-$ and $J/\psi \to l^+l^-$ masses. In the case of electrons, E/p studies using $W \to e\nu$ events are also used, where p is the combined measurement of the track momentum in the inner detector and E is the energy in the calorimeter. Small discrepancies are observed between data and simulation, and corrections for the lepton energy scale and resolution in the latter are implemented using the tools provided by the combined performance groups. In the case of muons, the momentum scale and resolution corrections are applied to the simulation. These uncertainties in the muon spectrometer and the tracking systems are considered, and varied separately.
For the present analysis, the shape of the pseudo data distributions for nominal and systematic variations for electrons and muons are presented in Appendix C.1.1 and C.1.2. A total of five components for electron and six for muon, three for each (e, μ) (which originate from scale factor calculations) are taken into account in the total systematic uncertainty calculation.

Jet Reconstruction Efficiency

The jet reconstruction efficiency is overestimated in MC simulations [76]. This effect is taken into account by the evaluation of an additional systematic uncertainty. Reconstructed jets are removed in MC samples randomly to match the efficiency in data. Online jets with $p_{\mathrm{T}} < 30$ GeV are affected, of which 0.2 % are dropped [76]. The analysis is then repeated with the reduced set of jets and the difference to the nominal selection is quoted as uncertainty.

Jet Vertex Fraction Efficiency

All jets used in the analysis must satisfy the requirement $|\mathrm{JVF}| > 0.5$. The per-jet efficiency to satisfy the jet vertex fraction requirement is measured in $Z(\to l^+l^-) + 1$-jet events in data and simulation, selecting separately events enriched in hard-scatter jets and events enriched in jets from other proton interactions in the same bunch crossing (pileup). The corresponding uncertainty is evaluated in the analysis by changing the nominal JVF cut value by 0.1 up and down and repeating the analysis using the modified cut value.
For the present analysis, the shape of the pseudo data distributions for nominal and systematic variated JVF value is presented in Appendix C.1.3.

Jet Energy Scale

The jet energy scale (JES) and its uncertainty have been derived combining information from test-beam data, LHC collision data and simulation [76, 136–139]. The jet energy scale calibration is described in Section 4.3. In order to derive the uncertainties of the JES dijet, $Z, \gamma + jets$ and multi-jet events depending on p_{T} and η of the jet are used.

The jet energy scale uncertainty is split into 26 uncorrelated sources and these sources are treated independently in this analysis in the following way:

- in-situ-techniques: In total 15 components: detector description (3), statistics (4), physics modelling (4) and mixed detector plus modelling (4). These uncertainties are evaluated from different *in-situ* techniques and in each category, the components are ordered by their effect, beginning with the largest. Figure 7.9 shows the jet response ratio of the data to the Monte Carlo simulation as a function of p_{T} for three *in-situ* techniques.

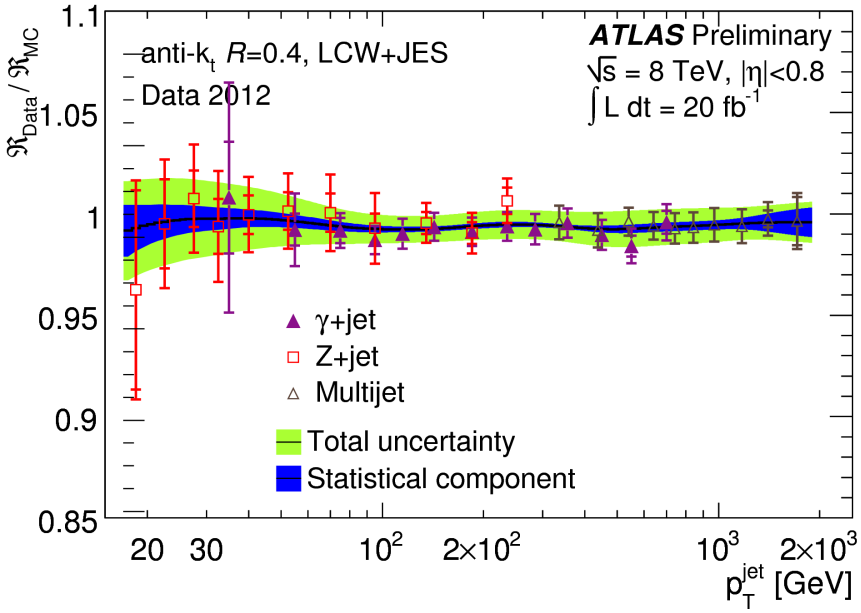

Figure 7.9.: Jet response ratio of the data to the Monte Carlo simulation as a function of p_{T} for three *in-situ* techniques combined to determine the *in-situ* energy scale correction: Z+jet (squares), γ+jet (full triangles) and multijet (empty triangles). The error bars indicate the statistical and the total uncertainties (adding in quadrature statistical and systematic uncertainties). The results are shown for anti$-k_t$ jets with radius parameter of $R = 0.4$ calibrated with the LCW+JES scheme. The result of the combination of the *in-situ* techniques is shown as the dark line. The outer band indicates the total uncertainty resulting from the combination of *in-situ* techniques, while the inner dark band shows the fraction purely from statistical uncertainties [81].

- η-intercalibration: In total 2 components. The dijet events are employed to apply an η-intercalibration in which the average η for forward jets ($0.8 < |\eta| < 4.5$) is equalised to the p_{T} of balancing jets in the central region ($|\eta| < 0.8$). The aim of this intercalibration is to remove any residual pseudorapidity difference in the jet

response following the MC calibration.

- pile-up: In total 5 components. The uncertainties on the pile-up corrections occur because of mis-modelling of the number of primary vertices and average interactions per bunch crossing.
- jet flavour composition and response: In total 2 components. The difference in calorimeter response for different jet flavour types (gluon, or light jets) is taken as uncertainty.
- b-JES: Only one component. The uncertainty on the jet response difference in the calorimeter for b-tag jets and other quark jets.
- High-p_{T} jets: Only one component. For jets with $p_{\mathrm{T}} > 1$ TeV, the JES uncertainties are taken from single-particle response measurements due to the limited statistics.

The same jet calibration procedure is also used in fast simulation samples (see Section 5.1) using a dedicated set of JES factors for the calibration in energy and $|\eta|$. While comparing full and fast simulations it is observed that the calibration factors are different. This difference is included as an additional fast simulation specific systematic since the *in-situ* methods are not used to validate fast simulation. The size of this uncertainty compared to other systematic uncertainties is much smaller than the other uncertainties for jets with the parameter $R = 0.4$ as demonstrated in Figure 7.10 where the additional fast simulation uncertainty is at most 1% at 20 GeV while η decreases with increasing p_{T}. For the present analysis, the shape of the pseudo data distributions for nominal and

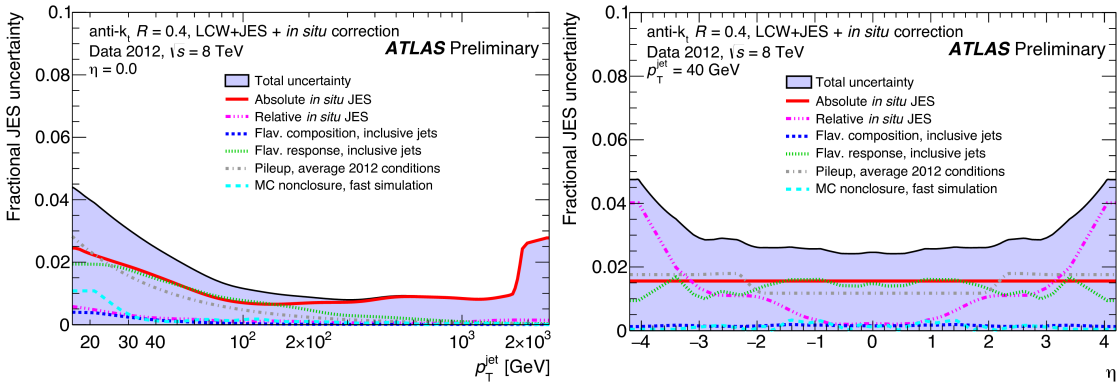

Figure 7.10.: Total uncertainty on the calibration of anti$-k_t$, $R = 0.4$ jets in fast simulation as a function of p_{T} and η. "Absolute *in-situ* JES" refers to the uncertainty arising from Z, γ+jets and multi-jet measurements, while "Relative *in-situ* JES" refers to the uncertainty arising from the dijet η-intercalibration. "MC non-closure, fast simulation" refers to the additional non-closure observed in fast simulation when comparing to full simulation [81].

systematic variations for JES are presented in Appendix C.1.4. From the 26 components of the total systematic uncertainty calculation, only the first component of physics modelling is taken into account[1].

Jet Energy Resolution

The jet energy resolution has been measured separately for data and simulation using two *in-situ* techniques. The expected fractional p_{T} resolution for a given jet was measured as a function of its p_{T} and rapidity. For the majority of the jet p_{T} spectrum, the width of the balance between jets and well measured photons or reconstructed, leptonically Z bosons is used to measure the detector resolution. Additionally, the balance between dijet events can be used to extend these measurements to higher p_{T} and $|\eta|$. For very low-p_{T} jets, there is a significant contribution to the jet energy resolution from pile-up particles and electronic noise [81]. The effect of the total jet energy resolution is parameterised as the sum of three terms:

$$\frac{\sigma_{p_{\mathrm{T}}}}{p_T} = \frac{N}{p_T} \oplus \frac{S}{\sqrt{p_T}} \oplus C, \tag{7.9}$$

where N parameterises the effect of electronic and pile-up noise, S parameterises stochastic effects which are caused by the sampling nature of the calorimeters, and C is a p_{T} independent constant term. The correlation matrix as a function of p_{T} and $|\eta|$ is built in order to account for correlations between the measurements at different $|\eta|$. All correlations between the p_{T} and $|\eta|$ regions covered by the *in-situ* studies can be described. To estimate the total systematic effect of the jet energy resolution, eleven orthogonal nuisance parameters are used[2].
For the present analysis, the shape of the pseudo data distributions for nominal and systematic variations for JER are presented in Appendix C.1.5. The JER systematic effect is very small and it is not included in the total systematic uncertainty calculation, described in Section 7.2.2.

Heavy- and Light- Flavour Tagging

The effects of uncertainties have been evaluated in efficiencies for the heavy flavour identification of jets using the b tagging algorithm. These efficiencies are measured from data and are jet flavour dependent. Efficiencies for b-tag and c-tag quarks in the simulation have to be corrected by the factors which are p_{T}-dependent. The scale factors and their uncertainties are applied to each jet in the simulation by taking into account its flavour and p_{T}. A total of six independent sources of uncertainty affecting the b tagging efficiency and four affecting the c tagging efficiency are considered. Each of these uncertainties corresponds to a resulting eigenvector after diagonalising the matrix

[1] The procedure how to treat the systematic sources i.e which to neglect and which to take into account is described in Section 7.2.2.

[2] An eigenvector reduction is performed which results in a maximum of twelve additional nuisance parameters.

containing the information of total uncertainty per p_{T} bin and the bin-to-bin correlations. In the case of light-flavour jets, the corrections also depend on jet η. A total of twelve uncertainties are considered for the efficiency of light jet tagging which depend on jet p_{T} and η regions. These systematic uncertainties are taken as uncorrelated between b-tag jets, c-tag jets, and light flavour jets. A per-jet weighting procedure is applied to simulated events to propagate the calibration of b tagging and the related uncertainties. For the present analysis the shape of the pseudo data distributions for nominal and systematic variations for heavy and light-favour tagging are presented in Appendix C.1.6. All components are included in the calculation of the total systematic uncertainty.

Missing Transverse Momentum Uncertainty

Two different types of uncertainties affect the E_T^{miss}: uncertainties of the objects used to calculate the E_T^{miss} and the uncertainties on the *SoftTerm* (see Section 4.4 for more details). The object related uncertainties are included in the fit. The *SoftTerm* component possesses up and down variation. The shape of the pseudo data distributions for the nominal and the systematic *SoftTerm* variation is presented in Appendix C.1.7. Overall this uncertainty is neglected in the calculation of the total systematic uncertainty for this analysis.

7.2.4. Uncertainties on the Background Estimates

Z+jets Modelling

The Z+jets process is the dominant background for ee and $\mu\mu$ channels. An overall normalisation uncertainty of 35% is applied to the Z+jets contribution. The overall uncertainty takes into account 5% uncertainty on the theoretical NNLO QCD cross section and 24% uncertainty on the extrapolation to higher jet multiplicities [123]. Additionally, the full size $Z_{p_{\mathrm{T}}}$ correction ($Z_{p_{\mathrm{T}}}$ re-weighting and HF corrections described in Section 5.3.1) is taken as a shape-only systematic and is included in the fit.

Electroweak Background Modelling

An uncertainty of $\pm 6.8\%$ is assumed for the theoretical cross sections of the single top quark production [99, 100] in the dilepton channel, corresponding to the theoretical uncertainty on Wt-channel production, the only one contributing to this final state. An uncertainty on the single top background shape is assessed by comparing Wt-channel MC samples generated with different schemes (diagram removal vs diagram subtraction) to take into account Wt and $t\bar{t}$ diagram interference. The change in the fitted helicity fractions due to the change of single top sample was found to be negligible ($(\mathcal{O}(10^{-5})$) for all fractions and has been subsequently dropped from further discussions on the total systematic uncertainty. Additionally, a PROTOS t-channel single top sample with anomalous Wtb couplings was used in place of the nominal t-channel single top sample to assess the impact on the extracted helicity fractions. The observed effect was also observed to be negligible ($\mathcal{O}(10^{-4})$) and dropped from further consideration.

Remaining Background

The remaining background consists of two background components: dibosons and fake leptons.

- **Dibosons:** The uncertainty on the diboson background rate includes the uncertainty on the inclusive diboson NNLO cross section of ±5% [123] added in quadrature to the uncertainty of 24% due to the extrapolation to the high jet multiplicity regions.

- **Fake leptons:** Since the fake lepton background was estimated using both simulation and real data, 50% normalisation uncertainty is applied to the fake lepton yield across all fitting regions to cover the maximum difference between the two methods (detailed description in Section 5.3.4).

7.2.5. Signal Modelling

The following sections describe uncertainties in the shapes of the signal modelling which have a strong affect on the $\cos\theta^*$ distribution.

Initial and Final State Radiation

For the uncertainty estimation due to QCD initial- and final-state radiation (ISR/FSR) modelling, samples generated with POWHEG-BOX interfaced to Pythia are used, with the varied values for the factorisation scale (μ is varied from 0.5 to 2). The parameter responsible for high p_{T} radiation damping is h_{damp} in the POWHEG-BOX generator ($h_{damp} = m_t$ for $\mu = 2$ and $h_{damp} = 2m_t$ for $\mu = 0.5$), and the transverse momentum scale of space-like parton shower evolution in Pythia. These variations span the ranges compatible with the results of measurements of $t\bar{t}$ production in association with jets. For the total radiation uncertainty, the one with the largest effect on the measured helicity fractions, is taken and it is symmetrised.
For the present analysis, the shape of the pseudo-data distributions for nominal and systematic variations for ISR/FSR are presented in Figure 7.11.

MC Generator Uncertainty

An uncertainty due to the MC generator choice for the hard process is evaluated by comparing events produced by POWHEG-BOX and MC@NLO, both interfaced to Herwig for showering and hadronisation. The full difference is taken as systematic uncertainty. The shape of the $\cos\theta^*$ distributions for each MC generator is shown in Figure 7.12.

Parton Shower and Hadronization

An uncertainty due to the choice of the parton shower and hadronisation model is derived by comparing events produced by POWHEG interfaced with Pythia or Herwig. Effects

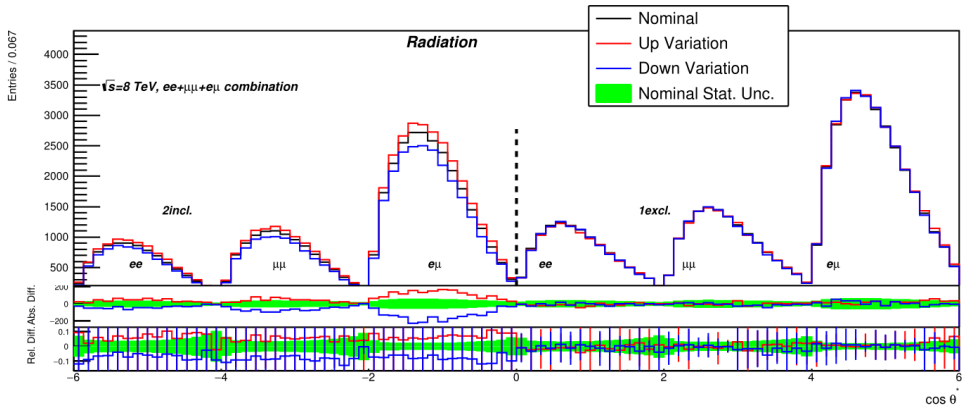

Figure 7.11.: Generated pseudo-data for the ee, $\mu\mu$ and $e\mu$ combination for systematic variations of ISR/FSR radiation and the nominal $t\bar{t}$ sample. The bottom plot shows the absolute and relative differences between the variations and the nominal sample in comparison to the statistical uncertainty of the nominal sample.

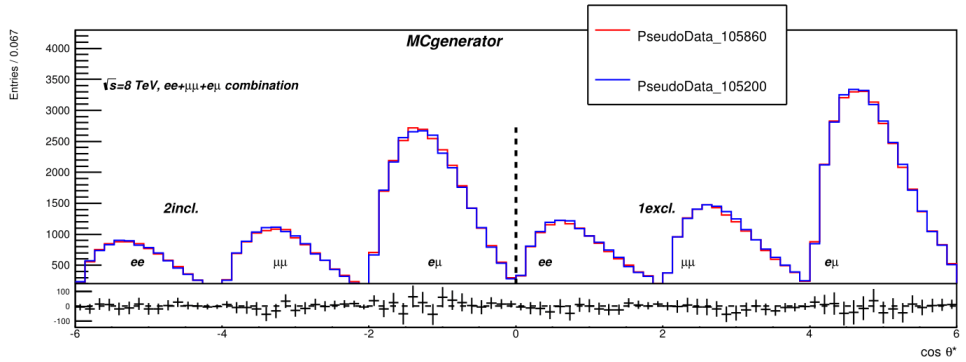

Figure 7.12.: Generated pseudo-data for the ee, $\mu\mu$ and $e\mu$ combination for systematic variations of the matrix element generator. The bottom plot shows the relative difference between the variations.

on the shapes are compared, symmetrised and applied to the shapes predicted by the default model. The full difference is taken as the systematic uncertainty.
The shape of the $\cos\theta^*$ distributions for each shower model is shown in Figure 7.13.

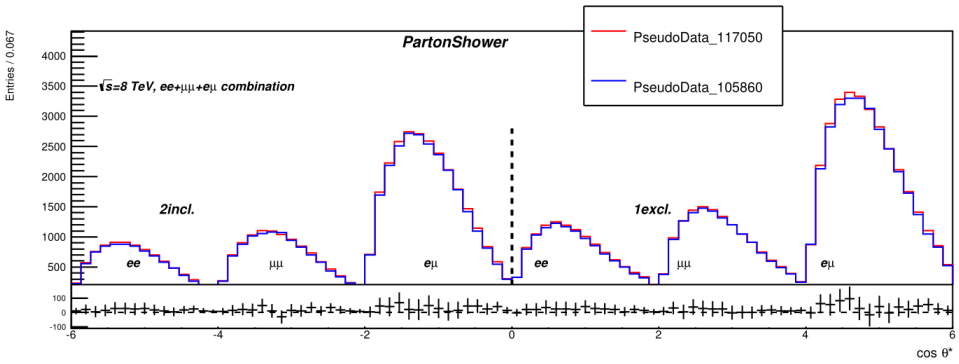

Figure 7.13.: Generated pseudo-data for the ee, $\mu\mu$ and $e\mu$ combination for systematic variations of the parton shower model. The bottom plot shows the relative difference between the variations.

Top quark mass

The signal templates are generated with a top quark mass of $m_{top} = 172.5$ GeV. In the reconstruction, also the top quark mass has been fixed to this value. The uncertainty due to the usage of this fixed mass is evaluated. This is done using pseudo data with different input top masses for the signal process. The obtained helicity fractions are plotted dependent on the corresponding top quark mass and are fitted with a linear curve. The uncertainties in the measurement of the W boson helicity fractions are obtained from the slope multiplied by the uncertainty in the current Tevatron combination, $174.34 \pm 0.37(\text{stat.}) \pm 0.52(\text{syst.})$ [140]. Figure 7.14 shows W boson helicity fractions obtained as a function of the top quark mass.

PDF

The PDF uncertainty on the $t\bar{t}$ signal is evaluated using an aMC@NLO [141] $t\bar{t}$ sample following the recommendation of the PDF4LHC [109] working group. It takes into account the differences between three PDF sets: CT10 NLO [112], MSTW2008 68% CL NLO [110,111] and NNPDF 2.3 NLO [113]. The final PDF uncertainty is a combination of:

a) the intra-PDF uncertainty, which evaluates the changes due to the variation of different PDF parameters within a single PDF error set and

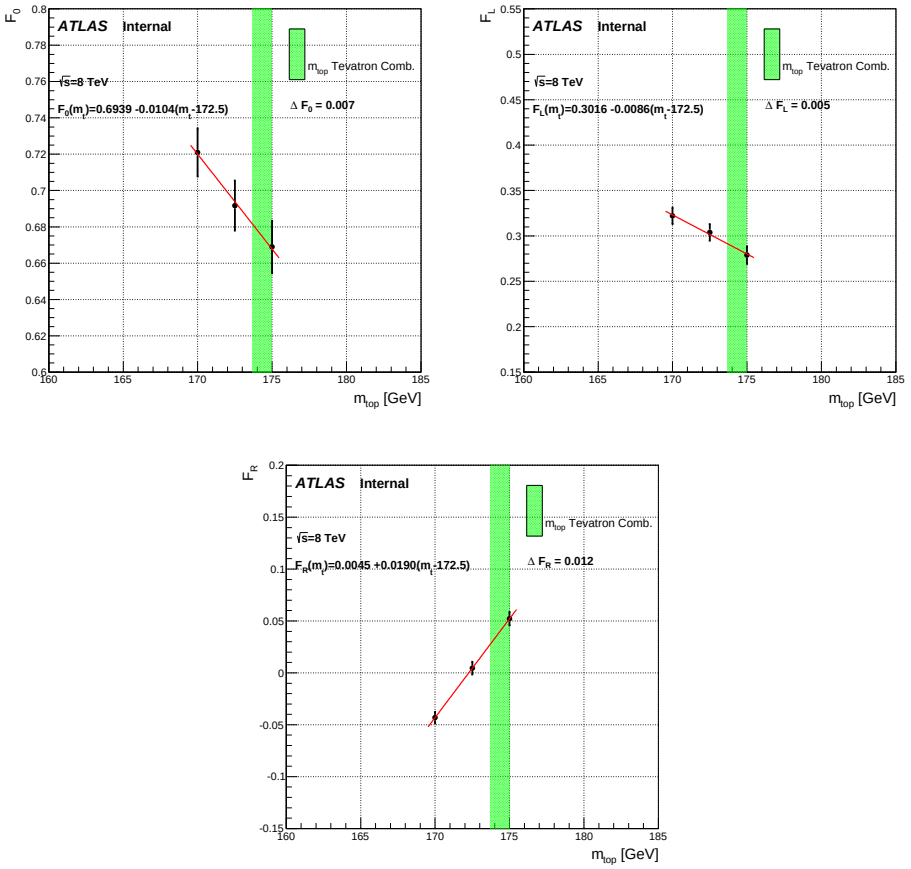

Figure 7.14.: Plots showing the helicity fractions w.r.t. different top quark mass points obtained in the $ee + \mu\mu + e\mu$ 2 inclusive b-tag region. 5000 sets of pseudo-data were fit to perform the test.

b) the inter-PDF uncertainty, which evaluates differences between different PDF sets.

The evaluation methods used for CT10, MSTW, and NNPDF are symmetric Hessian, asymmetric Hessian, and sample standard deviation, respectively. Half the width of the combination of the three estimates is taken as systematic uncertainty. The corresponding plots are shown in Figure 7.15

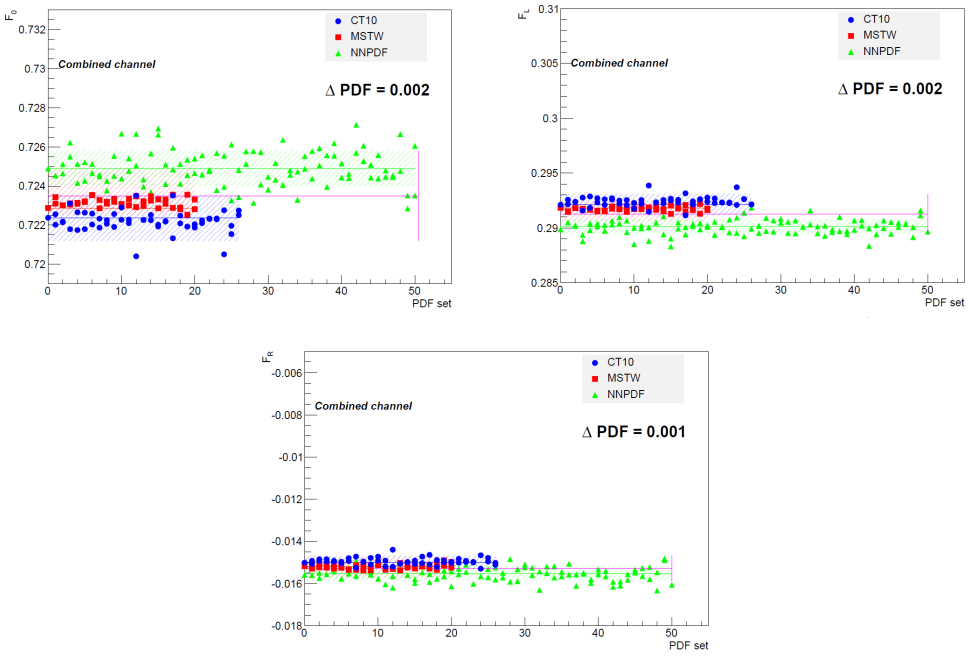

Figure 7.15.: Plots showing the helicity fractions w.r.t. different PDF sets obtained in the $ee + \mu\mu + e\mu$ 2 inclusive b-tag region. 5000 sets of pseudo-data were fit to perform the test.

7.2.6. Method Related Uncertainties

Template statistics

Ensemble tests are performed in order to account for possible fluctuations in the templates. In these ensemble tests, the template distributions are fluctuated within their sample statistics while the pseudo data distribution is not changed. The uncertainty that arises due to this limited template statistics for each W boson helicity fraction is the width of the distribution for a given fraction. The width of the distributions are taken as a measure uncertainty value. The result is comparable to the statistical uncertainty. Due to the reweighting method, signal templates have the largest uncertainties. The uncertainty contribution due to the signal and each background template statistics are shown in Table 7.6.

Template	2incl b-tag			1excl+2incl b-tag		
	F_0	F_L	F_R	F_0	F_L	F_R
Signal ($t\bar{t}$)	0.008	0.004	0.004	0.007	0.004	0.004
Single Top	0.002	0.001	0.001	0.002	0.002	0.001
Z+jets	0.004	0.001	0.003	0.005	0.002	0.003
Rem. backgrounds	0.002	0.001	0.002	0.002	0.001	0.001
Total	0.009	0.004	0.005	0.008	0.004	0.004

Table 7.6.: The uncertainty in measuring the W boson helicity fractions due to limited MC template statistics.

7.2.7. Summary of systematic uncertainties

The systematic uncertainties which are considered in the total uncertainty calculation must fulfill certain conditions (see Section 7.2.2). The estimated uncertainties in the W boson helicity fractions measurement for $2b$-tag inclusive and $1b$-tag exclusive $+2b$-tag inclusive regions for $ee+\mu\mu+e\mu$ dilepton channels combination are summarised in Tables 7.7-7.9. On the tables, the numbers in parentheses in the N_{syst} column refer to the number of variations with corresponding templates deviating by more than two bins w.r.t. the nominal template. Systematic variations are grouped by their plus/minus behaviour. Single-sided sources of systematic error are symmetrised. For the radiation uncertainty, the larger of the two variations is taken as the total uncertainty and symmetrised. When the difference between the up and down total systematic uncertainty is less than 0.015, the magnitude of the larger uncertainty is taken as the total symmetrised uncertainty. The systematic uncertainties dominated are by the signal modelling sources.

		F_0	
Systematic uncertainty	N_{syst}	$ee + \mu\mu + e\mu$ 2incl	$ee + \mu\mu + e\mu$ 1excl+2incl
Reconstructed Objects			
Muon	6(3)	+0.0006 -0.0001	+0.0028 -0.0011
Electron	5(3)	+0.0003 -0.0002	+0.0021 -0.0016
JES	26(1)	+0.0025 -0.0078	+0.0020 -0.0080
JVF	1(1)	0.0034 0.0003	0.0121 0.0113
b-tagging	3(3)	+0.0016 -0.0015	+0.0117 -0.0125
Sum of Reco Objects	-	+0.0045 -0.0079	+0.0173 -0.0187
Modelling			
Radiation	radLo radHi	+0.0068 -0.0068	+0.0248 -0.0248
Parton Shower & Hadronisation	1(1)	+0.0148 -0.0148	+0.0206 -0.0206
ME Generator	1(1)	+0.0116 -0.0116	+0.0157 -0.0157
PDF	3(3)	+0.0020 -0.0020	0.0021 0.0021
Top Quark Mass	3(3)	+0.0066 -0.0066	+0.0101 -0.0101
Sum of Modelling	-	+0.0212 -0.0212	+0.0372 -0.0372
Method Uncertainty			
Template Statistics	3(3)	+0.009 -0.009	+0.008 -0.008
Total Syst.	-	+0.0234 -0.0242	+0.0417 - 0.0423
Stat. + Bkg.	-	0.0141	0.0116

Table 7.7.: Summary of systematic and statistical uncertainties in the two inclusive b-tag and one exclusive + two inclusive b-tag combined ee, $\mu\mu$ and $e\mu$ channel measurements of F_0.

		F_L	
Systematic uncertainty	N_{syst}	$ee + \mu\mu + e\mu$ 2incl	$ee + \mu\mu + e\mu$ 1excl+2incl
Reconstructed Objects			
Muon	6(3)	+0.0004 -0.0000	+0.0003 -0.0004
Electron	5(3)	+0.0004 -0.0003	+0.0017 -0.0015
JES	26(1)	+0.0035 -0.0019	+0.0030 -0.0035
JER	1(1)	+0.0031 -0.0031	+0.0021 -0.0021
JVF	1(1)	0.0018 0.0001	0.0047 0.0025
b-tagging	3(3)	+0.0010 -0.0012	+0.0062 -0.0065
Sum of Reco Objects	-	+0.0041 -0.0023	+0.0071 -0.0075
Modelling			
Radiation	radLo radHi	+0.0037 -0.0037	+0.0083 -0.0083
Parton Shower & Hadronisation	1(1)	+0.0050 -0.0050	+0.0071 -0.0061
ME Generator	1(1)	+0.0038 -0.0.038	+0.0058 -0.0058
PDF	3(3)	+0.0020 -0.0020	0.0021 0.0021
Top Quark Mass	3(3)	+0.0053 -0.0053	+0.0049 -0.0049
Sum of Modelling	-	+0.0092 -0.0092	+0.0133 -0.0133
Method Uncertainty			
Template Statistics	3(3)	+0.004 -0.004	+0.004 -0.004
Total Syst.	-	+0.0108 -0.0103	+0.0156 -0.0158
Stat. + Bkg.	-	0.0095	0.0071

Table 7.8.: Summary of systematic and statistical uncertainties in the two inclusive b-tag and one exclusive + two inclusive b-tag combined ee, $\mu\mu$ and $e\mu$ channel measurements of F_L.

		F_R	
Systematic uncertainty	N_{syst}	$ee + \mu\mu + e\mu$ 2incl	$ee + \mu\mu + e\mu$ 1excl+2incl
Reconstructed Objects			
Muon	6(3)	+0.0004 -0.0000	+0.0000 -0.0006
Electron	5(3)	+0.0003 -0.0001	+0.0004 -0.0003
JES	26(1)	+0.0061 -0.0097	+0.0049 -0.0115
JVF	1(1)	0.0016 0.0005	0.0074 0.0088
b-tagging	3(3)	+0.0010 -0.0009	+0.0055 -0.0059
Sum of Reco Objects	-	+0.0064 -0.0097	+0.0104 -0.0156
Modelling			
Radiation	radLo radHi	+0.0057 -0.0057	+0.0172 -0.0172
Parton Showe & Hadronisation	1(1)	+0.0099 -0.0099	+0.0146 -0.0146
ME Generator	1(1)	+0.0078 -0.0078	+0.0101 -0.0101
PDF	3(3)	0.0010 0.0010	0.0010 0.0010
Top Quark Mass	3(3)	+0.0121 -0.0121	+0.0150 -0.0150
Sum of Modelling	-	+0.0184 -0.0184	+0.0289 -0.0289
Method Uncertainty			
Template Statistics	3(3)	+0.005 -0.005	+0.004 -0.004
Total Syst.	-	+0.0200 -0.0213	+0.0309 -0.0330
Stat. + Bkg.	-	0.0060	0.0061

Table 7.9.: Summary of systematic and statistical uncertainties in the two inclusive b-tag and one exclusive + two inclusive b-tag combined ee, $\mu\mu$ and $e\mu$ channel measurements of F_R.

CHAPTER 8

Results

The template fitting method described in Section 7.1 was applied to the full 2012 dataset and collected with the ATLAS detector at a centre of mass energy of $\sqrt{s} = 8$ TeV in order to measure the W boson helicity fractions in $t\bar{t}$ dileptonic events. The amount of the integrated luminosity of the data set is $\int \mathcal{L}dt = 20.2$ fb^{-1}. These measurements have been performed in combined dilepton channels (ee, $\mu\mu$ and $e\mu$) and studied separately in two inclusive b-tag region as well as with a combination to the one exclusive b-tag region. The total systematic uncertainty is calculated by symmetrising all up (down) variations and summing the contributions in quadrature. For modelling systematics, except for radiation uncertainty, the full difference between the two samples is taken and symmetrised, while for the radiation, the maximum difference w.r.t the nominal sample is taken and symmetrised. The summary of systematic and statistical errors is presented in Tables 7.7-7.9. Figure 8.1 shows the final template fits along with the associated statistical error for the combined $ee+\mu\mu+e\mu$ measurement in the two inclusive b-tag region. Three signal and three background templates are used in the fit and each background component is allowed to float separately within its uncertainty. The uncertainty band in the data-to-fit ratio corresponds to the total, systematic and statistical uncertainties in the fit result. Figure 8.2 shows the final template fit for the combined measurement of one exclusive and two inclusive b-tag regions in all three dileptonic channels. The best-fit result is in good agreement with the data distribution, as shown in both graphical represantations.

The measured W boson helicity fractions obtained using the dileptonic $t\bar{t}$ events with $\geq$2 b-tags are given in Table 8.1.

By construction, the individual fractions sum up to one. The F_0 value is positively correlated with F_L (ρ_{F_0,F_L}= +0.11) and anti-correlated with F_R (ρ_{F_0,F_R}= -0.16), also F_L and F_R are positively correlated (ρ_{F_L,F_R}= +0.52). The quoted values correspond to the

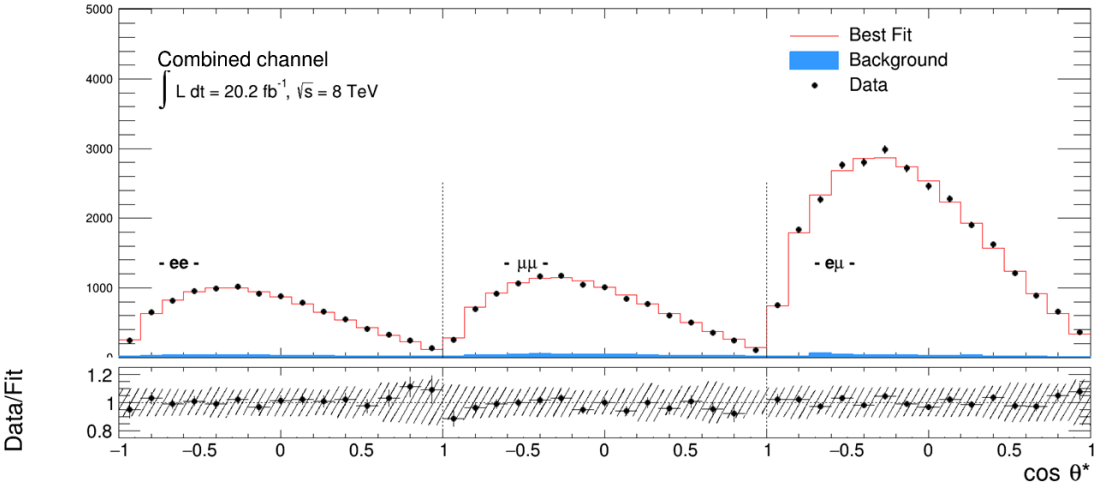

Figure 8.1.: Fit results and statistical errors for the combined $ee + \mu\mu + e\mu$ channel in two inclusive b-tag region.

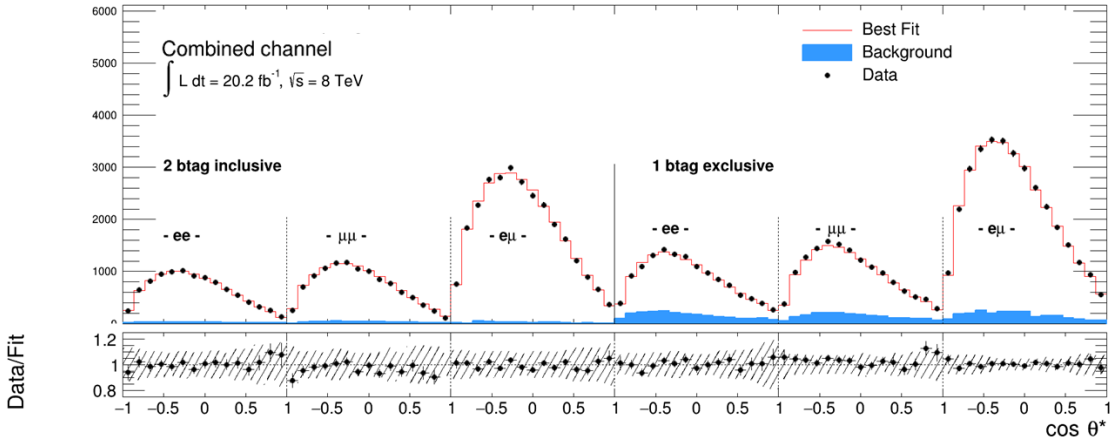

Figure 8.2.: Fit results and statistical errors for the combined $ee + \mu\mu + e\mu$ channel in one exclusive + two inclusive b-tag region.

total correlation coefficient, considering both statistical and systematic uncertainties. These results are consistent with the SM predictions given at NNLO accuracy [142]. The W boson helicity fractions also obtained using $t\bar{t}$ events with 1 b-tag and $\geq 2b$-tags are given in Table 8.2. In the combination of 1 b-tag and $\geq 2b$-tag regions, despite improving the statistical error and several sources of systematic error, the total systematic uncertainty is found to be larger than in the two inclusive b-tag measurement.
In the case of the $\geq$2b-tags, the dominant systematic uncertainty contributions come from the modelling of $t\bar{t}$ events (initial and final state radiation, parton showering and

($\geq$2 b-tags)
$F_0 = 0.695 \pm 0.014$ (stat.+bkg) $^{+0.023}_{-0.024}$ (syst.)
$F_L = 0.291 \pm 0.009$ (stat.+bkg) $^{+0.011}_{-0.010}$ (syst.)
$F_R = 0.012 \pm 0.006$ (stat.+bkg) $^{+0.020}_{-0.021}$ (syst.)

Table 8.1.: Measured W helicity fractions in two inclusive b-tag region, $ee + \mu\mu + e\mu$ channels.

hadronisation, and Monte Carlo generator choice for the matrix element) and the limited statistics in the MC templates, all of which directly affects the object kinematics.

1 Excl. + 2 Incl., $ee + \mu\mu + e\mu$ Combination
$F_0 = 0.686 \pm 0.012$ (stat.+bkg) $^{+0.042}_{-0.042}$ (syst.)
$F_L = 0.293 \pm 0.007$ (stat.+bkg) $^{+0.016}_{-0.016}$ (syst.)
$F_R = 0.020 \pm 0.006$ (stat.+bkg) $^{+0.033}_{-0.033}$ (syst.)

Table 8.2.: Measured W helicity fractions in one exclusive + two inclusive b-tag regions, $ee + \mu\mu + e\mu$ channels.

8.1. Constraints on Wtb Vertex

The final fitted helicity fractions can be used to constrain anomalous couplings related to the production of $t\bar{t}$ introduced in Section 2.2.3. Any deviation of F_0, F_L, and F_R from the Standard Model prediction could be caused by new physics contributing to the Wtb vertex, and so the final fitted helicity fractions can be used to constrain any such anomalous couplings of new interactions associated with the top quark that may exist at higher energies. The Wtb vertex parametrisation in terms of an effective Lagrangian has already been introduced in Equation 2.22. The observables F_L and F_0 are similarly sensitive to g_{R}, while the dependence of F_R on this coupling is smaller. On the other hand, the measurement of F_R sets the strongest constraint on the g_{L} and V_{R} couplings [50, 143]. As an example, Figure 8.3 shows the influence on the left-handed W boson helicity fraction F_L of the anomalous couplings.

Limits on anomalous couplings (V_{R}, g_{L}, and g_{R}) are obtained from the measurement of the W boson helicity fractions in the two inclusive b-tags region by utilising the dependence of the fractions on the couplings. The `EFTfitter` tool [144] is used to extract limits on the anomalous couplings. This tool has been developed for interpreting sets of measurements in such models using a Bayesian ansatz by calculating the posterior probabilities of the corresponding free parameters numerically. For simplicity, all couplings are assumed to be real. The limit setting makes use of the measured helicity fractions F_0

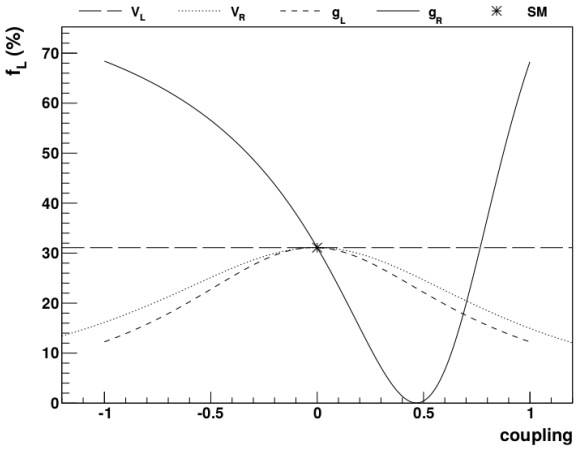

Figure 8.3.: Dependence of the fraction of longitudinally polarised W bosons on the anomalous couplings V_{R}, g_{L}, and g_{R} as implemented in the `EFTfitter` tool [144].

and F_L as well as their total uncertainties. The third fraction, F_R, is considered via the constraint of $\sum F_i = 1$. As the correct correlation between the uncertainties is crucial for the limit setting, the total covariance matrix was derived and provided as input for `EFTfitter`.
The covariance matrix for each systematic uncertainty component, k, can be expressed as:

$$C_{syst,k} = \begin{pmatrix} \sigma^2_{F_0} & cF_0F_L & cF_0F_R \\ cF_0F_L & \sigma^2_{F_L} & cF_LF_R \\ cF_0F_R & cF_LF_R & \sigma^2_{F_R} \end{pmatrix}, \tag{8.1}$$

where σ_{F_i} is the uncertainty on each helicity fraction, F_i, for a given systematic component. It is assumed that each systematic source is correlated across the different helicity fractions, so the off-diagonal terms can be written as:

$$cF_iF_j = \sigma_{F_i}\sigma_{F_j}. \tag{8.2}$$

The signs of the components σ_{F_i} contain information about the effect on a given fraction, whether the variation effect is positive or negative. For each systematic uncertainty, the overall normalisation is $F_0 + F_L + F_R = 1$ but such that there is at least one positive uncertainty and at least one negative uncertainty.
Once all components of the matrices are calculated, e.g. by using the numbers, resulted from each systematic source, available in Appendix D, the full covariance matrix C can be constructed as the sum of the statistical covariance matrix (C_{stat}) and the direct total

sum of all systematic matrices[1], expressed as:

$$C = C_{stat} + \sum_k C_{syst,k}. \tag{8.3}$$

For the fully combined measurement ($ee+\mu\mu+e\mu$, 1 exclusive b-tag + 2 inclusive b-tag), the summed systematic matrix is given by

$$C_{\text{syst}} = \begin{pmatrix} 0.00299 & -0.00088 & -0.00174 \\ -0.00088 & 0.00051 & 0.00063 \\ -0.00174 & 0.00063 & 0.00115 \end{pmatrix}. \tag{8.4}$$

The statistical covariance matrix, C_{stat}, is obtained directly from the fit. The total covariance matrix, $C_{\text{stat + syst}}$ is given by

$$C_{\text{stat + syst}} = \begin{pmatrix} 0.00312 & -0.00080 & -0.00167 \\ -0.00080 & 0.00056 & 0.00067 \\ -0.00167 & 0.00067 & 0.00158 \end{pmatrix}. \tag{8.5}$$

The total covariance matrix is used as input to the EFT fit which places limits on anomalous Wtb couplings. Moreover, the fit takes the correlation coefficients between the fractions as input. In order to translate the covariance matrix, C, into the correlation matrix, S, we define first the diagional matrix D where

$$D = \sqrt{\text{diag}(C)} \tag{8.6}$$

i.e. D is the square root of the diagonal matrix obtained from C. Then, S is obtained via

$$S = D^{-1}CD^{-1}. \tag{8.7}$$

The off-diagonal elements of S are the correlation coefficients ρ with the values of:

$$\begin{aligned} \rho(F_0, F_L) &= -0.61, \\ \rho(F_0, F_R) &= -0.75, \\ \rho(F_L, F_R) &= 0.71. \end{aligned} \tag{8.8}$$

The sensitivity of anomalous Wtb limits derived using the 6-channel combination can be compared with the limits derived from any other region given the central values obtained from the template fit and the correlation coefficients obtained from the above procedure. The two inclusive b-tag region correlation coefficients are calculated to be

$$\begin{aligned} \rho(F_0, F_L) &= 0.11, \\ \rho(F_0, F_R) &= -0.16, \\ \rho(F_L, F_R) &= 0.52. \end{aligned} \tag{8.9}$$

Results showing the 68% and 95% posterior integrals for g_{L} and g_{R} (while fixing $V_L = 1$, $V_R = 0$) are shown in Figure 8.4, as well as the 68% and 95% posterior integrals for g_{R}

[1] Assuming each systematic uncertainty component is uncorrelated from all others.

and V_{R}, while fixing the other parameters to their SM values.
In Figure 8.5, the one-dimensional limits for each anomalous coupling are shown (for all other couplings fixed to their SM expectation). The 95% CL intervals for the anomalous couplings are also summarised in Table 8.3.

Coupling	95 % CL limit
V_{R}	$[-0.21, 0.30]$
g_{L}	$[-0.16, 0.13]$
g_{R}	$[0.03, 0.08], [0.74, 0.76]$

Table 8.3.: Limits for the anomalous coulings V_{R}, g_{L}, and g_{R} at 95 % CL. The limits were derived using the measured W boson helicity fractions (combination of $ee + \mu\mu + e\mu$ in the $2b$-tag incl. channel).

The results are in good agreement with the SM expectations.

8.2. Discussion of the Results

The results of the W boson helicity fractions measurement in the $t\bar{t}$ dilepton events at a centre of mass energy of $\sqrt{s} = 8$ TeV ($\int \mathcal{L}dt = 20.2$ fb^{-1}) with the ATLAS experiment are presented in Table 8.1. The dominant uncertainties correspond to systematic sources of $t\bar{t}$ modelling. These $t\bar{t}$ modelling systematic sources have more impact on the longitudinal F_0 and right-handed F_R helicity fractions than on the left-handed F_L fraction. Overall the results are in good agreement with the SM predictions.
The most precise measurement of the W boson helicity fractions was performed by the ATLAS experiment at a centre of mass energy of $\sqrt{s} = 8$ TeV($\int \mathcal{L}dt = 20.2$ fb^{-1}) in $t\bar{t}$ events in the lepton+jets final state [145, 146]. The results of the ATLAS and CMS collaborations are summarised on Table 8.4, for top quark pair production.
The W polarisation fractions have also been measured in single top quark production at a centre of mass energy of $\sqrt{s} = 8$ TeV by the CMS experiment. The results are shown in Table 8.5.
The best fit values for g_L and g_R anomalous tensor couplings are -0.017 and -0.008, respectively, while V_L and V_R vector couplings are assumed to be 1 and 0 [149].
The Wtb vertex was probed by the ATLAS experiment in single top quark production at $\sqrt{s} = 8$ TeV. The 95% confidence level limit was set on the g_R coupling resulting in $g_R \in [-0.18, 0.06]$ [150].
The limits on anomalous couplings were set by the ATLAS experiment in $t\bar{t}$ lepton+jets and dilepton events at $\sqrt{s} = 8$ TeV. The results for the dilepton channel are presented in Table 8.3 and for the single lepton channel in Table 8.6.
The large g_R values would only be possible if the single top quark cross section was much larger than observed, therefore this region is already excluded [31, 32, 151]. The results presented in this thesis are consistent with the other $\sqrt{s} = 8$ TeV measurements and they are also in agreement with the SM expectations.

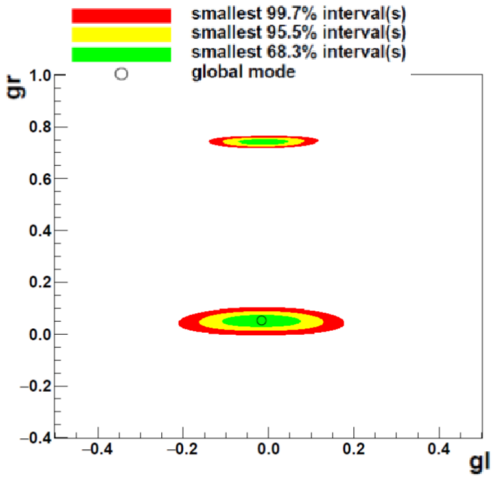

(a)

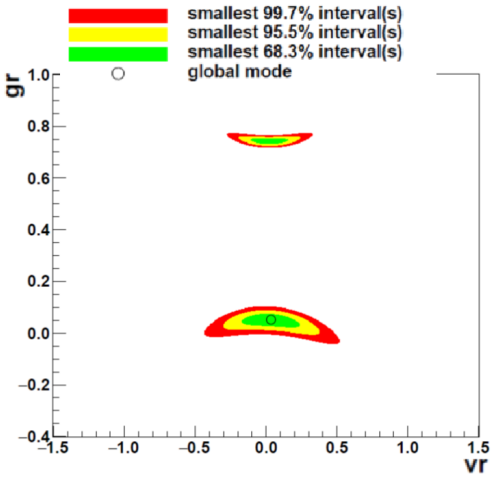

(b)

Figure 8.4.: a): Allowed regions at 68.3%, 95.5% and 99.7 % confidence level (CL) for the Wtb anomalous couplings g_{L} and g_{R}. The other couplings are fixed to their SM expectation ($V_L = 1$, $V_R = 0$). b): Corresponding limits on V_{R} and g_{R} for the other couplings fixed to their SM expectation. The limits were obtained using a combination of $ee, \mu\mu$ and $e\mu$ in the 2 b-tag inclusive region.

ATLAS experiment $t\bar{t}$ events at lepton+jets final state [145]
F_0 = 0.709 ± 0.012 (stat.+bkg) ± 0.015 (syst.)
F_L = 0.299 ± 0.008 (stat.+bkg) ± 0.013 (syst.)
F_R = -0.008 ± 0.006 (stat.+bkg) ± 0.012 (syst.)
CMS experiment $t\bar{t}$ events at lepton+jets final state [147]
F_0 = 0.681 ± 0.012 (stat.+bkg) ± 0.023 (syst.)
F_L = 0.323 ± 0.008 (stat.+bkg) ± 0.014 (syst.)
F_R = -0.004 ± 0.005 (stat.+bkg) ± 0.014 (syst.)
CMS experiment $t\bar{t}$ events at dilepton final state [148]
F_0 = 0.653 ± 0.016 (stat.+bkg) ± 0.024 (syst.)
F_L = 0.329 ± 0.009 (stat.+bkg) ± 0.025 (syst.)
F_R = 0.018 ± 0.008 (stat.+bkg) ± 0.026 (syst.)

Table 8.4.: The summary of the W helicity fractions measurement in $t\bar{t}$ events with a centre of mass energy of $\sqrt{s} = 8$ TeV at LHC.

F_0 = 0.720 ± 0.039 (stat.+bkg) ± 0.037 (syst.)
F_L = 0.298 ± 0.028 (stat.+bkg) ± 0.032 (syst.)
F_R = -0.018 ± 0.019 (stat.+bkg) ± 0.011 (syst.)

Table 8.5.: The summary of the W helicity fractions measurement in single top quark events with a centre of mass energy of $\sqrt{s} = 8$ TeV at the CMS experiment [149].

Coupling	95 % CL limit
V_{R}	$[-0.24, 0.31]$
g_{L}	$[-0.14, 0.11]$
g_{R}	$[-0.02, 0.06], [0.74, 0.78]$

Table 8.6.: Limits for the anomalous coulings V_{R}, g_{L}, and g_{R} at 95 % CL. The limits were derived using the measured W boson helicity fractions in lepton+jets in the 2b-tag incl. channel [147].

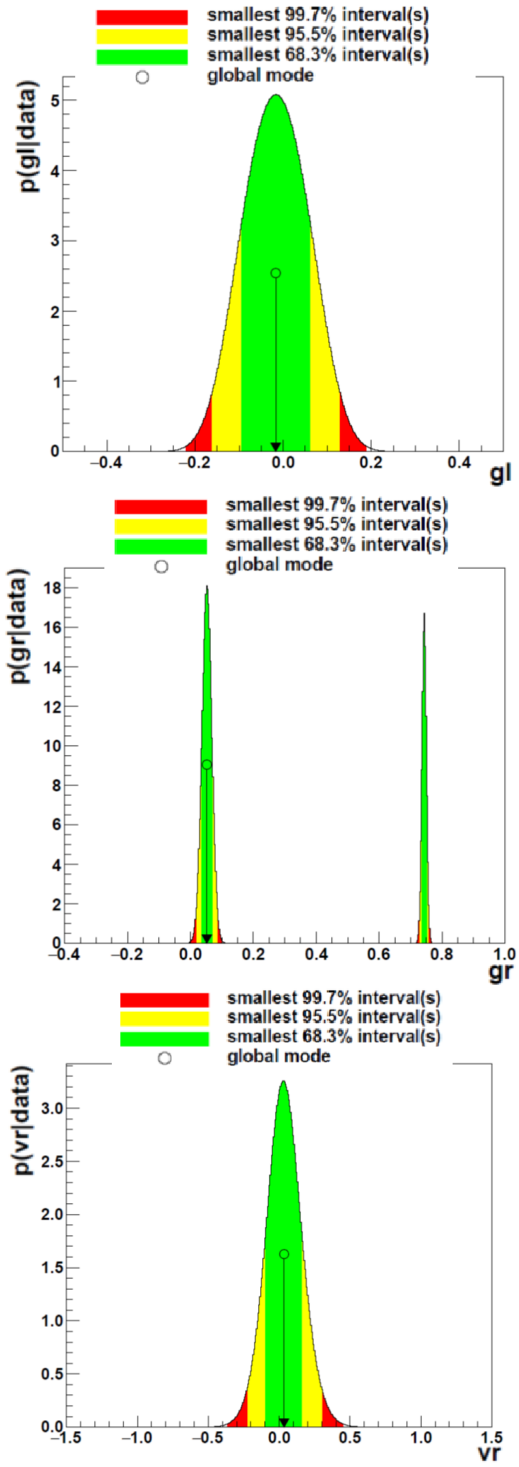

Figure 8.5.: Limits on V_R, g_{L} and g_{R} while fixing the other anomalous couplings to their SM values. The limits were obtained using a combination of $ee, \mu\mu$ and $e\mu$ in the 2 b-tag inclusive region.

CHAPTER 9

Summary and Conclusions

The W boson polarisation in top quark decays was analysed in this thesis. The measurements were based on data recorded by the ATLAS detector during 2012, with corresponding integrated luminosity of $\int \mathcal{L}dt = 20.2\text{fb}^{-1}$ at a centre of mass energy of $\sqrt{s} = 8$ TeV. The W boson helicity fractions were measured in the dilepton channel, characterised by the presence of two high-p_{T} leptons with opposite electric charge, missing transverse energy, and at least two high-p_{T} jets with at least one b-tagged jet. The background is composed of the production of Z-bosons with additional jets, single top quark production, background due to misidentified leptons, and diboson production. The studies were performed in the two b-tag inclusive region and also in combination with the one b-tag exclusive region.

The events were reconstructed using a kinematic method, which solves a kinematic equation system numerically. b-tagging information was used to improve the event reconstruction. Furthermore, the top-quark, W boson and neutrino masses were fixed.

In order to measure the W boson helicity fractions, the angular distribution of the charged lepton, $\cos\theta^*$, was used. This variable is defined as the angle between the charged lepton and the negative direction of the b-quark in the rest frame of the W boson. The W boson helicity fractions were measured using a template method. The shape of data and simulated distributions of the analysers are compared via a binned likelihood template fit approach, in order to measure the helicity fractions. Dedicated $t\bar{t}$ signal templates for longitudinal, left- and right- handed helicity states are produced by reweighting the simulated SM $t\bar{t}$ events at truth level. To account for the background processes, three templates for Z+jets background, single top quark production and the remaining background, combining misidentified and diboson backgrounds, are considered. The normalisation of the background processes are used to constrain the fit, while the normalisation of each signal template is considered as a free parameter. The likelihood fit provides good separation power between the three polarisation states.

The results obtained from the combined dilepton channels $ee + \mu\mu + e\mu$ with two b-tags are found to be:

$$
\begin{aligned}
F_0 &= 0.695 \pm 0.014\ \text{(stat.+bkg)}\ ^{+0.023}_{-0.024}\ \text{(syst.)},\\
F_L &= 0.291 \pm 0.009\ \text{(stat.+bkg)}\ ^{+0.011}_{-0.010}\ \text{(syst.)},\\
F_R &= 0.012 \pm 0.006\ \text{(stat.+bkg)}\ ^{+0.020}_{-0.021}\ \text{(syst.)}.
\end{aligned}
$$

The results are in good agreement with the NNLO prediction of the Standard Model within the uncertainties.
Using the measured W boson helicity fractions, limits were set on the anomalous couplings of the Wtb vertex. No deviation from the Standard Model prediction was observed. The dominant uncertainties come from systematics, especially from $t\bar{t}$ modelling for the present analysis. The precision could be improved by combining the results with the single lepton channel, also with the CMS results, presented on Table 8.4. Also the sensitivity on anomalous Wtb couplings could be increased by combining results with the single top quark measurements. The future measurements of the W boson polarisation will be performed at higher energies at the LHC.

Bibliography

[1] S. L. Glashow, *Partial Symmetries of Weak Interactions*, Nucl. Phys. **22** (1961) 579.

[2] A. Salam, *Weak and Electromagnetic Interactions*, Conf. Proc. **C680519** (1968) 367.

[3] S. Weinberg, *A Model of Leptons*, Phys. Rev. Lett. **19** (1967) 1264.

[4] G. Zweig, *An SU(3) model for strong interaction symmetry and its breaking. Version 2*, in: D. Lichtenberg and S. P. Rosen, editors, *Developments in the Quark Theory of Hadrons. VOL. 1. 1964 - 1978*, 1964 22–101.

[5] F. Halzen and A. D. Martin, *Quarks and Leptons: An Introductory Course in Modern Particle Physics*, John Wiley & Sons, (1984), ISBN 0471887412, 9780471887416.

[6] D. J. Gross and F. Wilczek, *Asymptotically Free Gauge Theories. I*, Phys. Rev. **D8** (1973) 3633.

[7] M. Thomson, *Modern Particle Physics*, Cambridge University Press, Cambridge, (September 2013).

[8] The Particle Data Group Collaboration, M. Tanabashi *et al.*, *Review of Particle Physics (RPP)*, Phys. Rev. **D98(3)** (2018) 030001.

[9] N. Cabibbo, *Unitary Symmetry and Leptonic Decays*, Phys. Rev. Lett. **10** (1963) 531.

[10] M. Kobayashi and T. Maskawa, *CP Violation in the Renormalizable Theory of Weak Interaction*, Prog. Theor. Phys. **49** (1973) 652.

[11] P. W. Higgs, *Broken symmetries, massless particles and gauge fields*, Phys. Lett. **12** (1964) 132.

[12] P. W. Higgs, *Broken Symmetries and the Masses of Gauge Bosons*, Phys. Rev. Lett. **13** (1964) 508.

[13] G. S. Guralnik, C. R. Hagen, and T. W. Kibble, *Global Conservation Laws and Massless Particles*, Phys. Rev. Lett. **13** (1964) 585.

[14] F. Englert and R. Brout, *Broken Symmetry and the Mass of Gauge Vector Mesons*, Phys. Rev. Lett. **13** (1964) 321.

[15] ATLAS and CMS Collaborations, *Combined Measurement of the Higgs Boson Mass in pp Collisions at $\sqrt{s} = 7$ and 8 TeV with the ATLAS and CMS Experiments*, Phys. Rev. Lett. **114** (2015) 191803.

[16] B. Pontecorvo, *Mesonium and anti-mesonium*, Sov. Phys. JETP **6** (1957) 429, [Zh. Eksp. Teor. Fiz.33,549(1957)].

[17] Z. Maki, M. Nakagawa, and S. Sakata, *Remarks on the unified model of elementary particles*, Prog. Theor. Phys. **28** (1962) 870, [34(1962)].

[18] CDF Collaboration, *Observation of top quark production in $\bar{p}p$ collisions*, Phys. Rev. Lett. **74** (1995) 2626.

[19] DØ Collaboration, *Observation of top quark*, Phys. Rev. Lett. **74** (1995) 2632.

[20] The ATLAS, CDF, CMS, DØ Collaboration, *First combination of Tevatron and LHC measurements of the top-quark mass*, ATLAS-CONF-2014-008, CDF-NOTE-11071, CMS-PAS-TOP-13-014, D0-NOTE-6416, FERMILAB-TM-2582-E (2014).

[21] J. C. Collins, D. E. Soper, and G. F. Sterman, *Factorization of Hard Processes in QCD*, Adv. Ser. Direct. High Energy Phys. **5** (1989) 1.

[22] S. Moch and P. Uwer, *Theoretical status and prospects for top-quark pair production at hadron colliders*, Phys. Rev. **D78** (2008) 034003.

[23] M. Czakon and A. Mitov, *NNLO corrections to top-pair production at hadron colliders: the all-fermionic scattering channels*, JHEP **12** (2012) 054.

[24] M. Czakon and A. Mitov, *NNLO corrections to top pair production at hadron colliders: the quark-gluon reaction*, JHEP **01** (2013) 080.

[25] M. Cacciari et al., *Top-pair production at hadron colliders with next-to-next-to-leading logarithmic soft-gluon resummation*, Phys. Lett. **B710** (2012) 612.

[26] P. Barnreuther, M. Czakon, and A. Mitov, *Percent Level Precision Physics at the Tevatron: First Genuine NNLO QCD Corrections to $q\bar{q} \to t\bar{t} + X$*, Phys. Rev. Lett. **109** (2012) 132001.

[27] ATLAS and CMS Collaborations, *Combination of ATLAS and CMS top quark pair cross section measurements in the eμ final state using proton–proton collisions at* $\sqrt{s} = 8$ *TeV*, ATLAS-CONF-2014-054, (2014).

[28] M. Czakon and A. Mitov, *Top++: A Program for the Calculation of the Top-Pair Cross-Section at Hadron Colliders*, Comput. Phys. Commun. **185** (2014) 2930.

[29] ATLAS and CMS Collaborations, https://twiki.cern.ch/twiki/bin/view/LHCPhysics/LHCTopWGSummaryPlots, May, 2018.

[30] ATLAS Collaboration, *Comprehensive measurements of t-channel single top-quark production cross sections at* $\sqrt{s} = 7$ *TeV with the ATLAS detector*, Phys. Rev. **D90** (2014) 112006.

[31] ATLAS Collaboration, *Measurement of the production cross-section of a single top quark in association with a W boson at* 8 *TeV with the ATLAS experiment*, JHEP **01** (2016) 064.

[32] ATLAS Collaboration, *Search for s-channel single top-quark production in proton–proton collisions at* $\sqrt{s} = 8$ *TeV with the ATLAS detector*, Phys. Lett. **B740** (2015) 118.

[33] A. Castro, *Recent Top Quark Mass Measurements from CMS in 10th International Workshop on Top Quark Physics (TOP2017) Braga, Portugal, September 17-22, 2017.*

[34] ATLAS Collaboration, *Measurement of the top quark charge in pp collisions at* $\sqrt{s} = 7$ *TeV with the ATLAS detector*, JHEP **11** (2013) 031.

[35] CMS Collaboration, *Constraints on the Top-Quark Charge from Top-Pair Events*, Tech. Rep. CMS-PAS-TOP-11-031, CERN, Geneva, (2012).

[36] J. H. Kuhn and G. Rodrigo, *Charge asymmetry of heavy quarks at hadron colliders*, Phys. Rev. **D59** (1999) 054017.

[37] Lai, Hung-Liang et al., *New parton distributions for collider physics*, Phys. Rev. **D82** (2010) 074024.

[38] J. Gao et al., *CT10 next-to-next-to-leading order global analysis of QCD*, Phys. Rev. **D89(3)** (2014) 033009.

[39] ATLAS Collaboration, *Observation of spin correlation in* $t\bar{t}$ *events from pp collisions at* $\sqrt{s} = 7$ *TeV using the ATLAS detector*, Phys. Rev. Lett. **108** (2012) 212001.

[40] CMS Collaboration, *Measurements of* $t\bar{t}$ *spin correlations and top-quark polarization using dilepton final states in pp collisions at* $\sqrt{s} = 7$ *TeV*, Phys. Rev. Lett. **112(18)** (2014) 182001.

[41] M. Fischer, S. Groote, J. G. Körner, and M. C. Mauser, *Longitudinal, transverse-plus and transverse-minus W bosons in unpolarized top quark decays at $O(\alpha_s)$*, Phys. Rev. **D63** (2001) 031501.

[42] A. Czarnecki, J. G. Korner, and J. H. Piclum, *Helicity fractions of W bosons from top quark decays at NNLO in QCD*, Phys. Rev. **D81** (2010) 111503.

[43] J. A. Aguilar-Saavedra and J. Bernabeu, *W polarisation beyond helicity fractions in top quark decays*, Nucl. Phys. **B840** (2010) 349.

[44] J. A. Aguilar-Saavedra, *A Minimal set of top anomalous couplings*, Nucl. Phys. **B812** (2009) 181.

[45] W. Bernreuther, P. Gonzalez, and M. Wiebusch, *The Top Quark Decay Vertex in Standard Model Extensions*, Eur. Phys. J. **C60** (2009) 197.

[46] S. P. Martin, *A Supersymmetry primer*, Adv. Ser. Direct. High Energy Phys.18,1 (1998) 1.

[47] C. T. Hill, *Topcolor assisted technicolor*, Phys. Lett. **B345** (1995) 483.

[48] T. Han et al., *Phenomenology of the little Higgs model*, Phys. Rev. **D67** (2003) 095004.

[49] S. M. Etesami, M. Khatiri Yanehsari, and M. Mohammadi Najafabadi, *The effects of standard model extensions on W-boson helicity ratios in top quark decay*, Int. J. Theor. Phys. **51** (2012) 3694.

[50] J. A. Aguilar-Saavedra et al., *Probing anomalous Wtb couplings in top pair decays*, Eur. Phys. J. **C50** (2007) 519.

[51] CDF Collaboration, *Measurement of W-boson polarization in top-quark decay using the full CDF Run II data set*, Phys. Rev. **D87** (2013) 031104.

[52] D$\emptyset$ Collaboration, *Measurement of the W boson helicity in top quark decays using* 5.4 fb^{-1} *of $p\overline{p}$ collision data*, Phys. Rev. **D83** (2011) 032009.

[53] CDF and D$\emptyset$ Collaborations, *Combination of CDF and D$\emptyset$ measurements of the W boson helicity in top quark decays*, Phys. Rev. **D85** (2012) 071106.

[54] ATLAS Collaboration, *Measurement of the W boson polarization in top quark decays with the ATLAS detector*, JHEP **06** (2012) 088.

[55] CMS Collaboration, *Measurement of the W-boson helicity in top-quark decays from $t\bar{t}$ production in lepton+jets events in pp collisions at $\sqrt{s} = 7$ TeV*, JHEP **10** (2013) 167.

[56] ATLAS and CMS Collaborations, *Combination of the ATLAS and CMS measurements of the W-boson polarization in top-quark decays*, ATLAS-CONF-2013-033, (2013).

[57] L. Evans and P. Bryant, *LHC Machine*, JINST **3** (2008) S08001.

[58] *LEP design report*, CERN, Geneva, (1984).

[59] ATLAS Collaboration, *The ATLAS Experiment at the CERN Large Hadron Collider*, JINST **3** (2008) S08003.

[60] ALICE Collaboration, *The ALICE experiment at the CERN LHC*, JINST **3** (2008) S08002.

[61] CMS Collaboration, *The CMS Experiment at the CERN LHC*, JINST **3** (2008) S08004.

[62] LHCb Collaboration, *The LHCb Detector at the LHC*, JINST **3** (2008) S08005.

[63] LHCf Collaboration, *The LHCf detector at the CERN Large Hadron Collider*, JINST **3** (2008) S08006.

[64] TOTEM Collaboration, *The TOTEM experiment at the CERN Large Hadron Collider*, JINST **3** (2008) S08007.

[65] Pinfold, James et al., *Technical Design Report of the MoEDAL Experiment*, Tech. Rep. CERN-LHCC-2009-006. MoEDAL-TDR-001, (2009).

[66] S. van der Meer, *Calibration of the effective beam height in the ISR*, Tech. Rep. CERN-ISR-PO-68-31. ISR-PO-68-31, CERN, Geneva, (1968).

[67] D. Fournier, *Performance of the LHC, ATLAS and CMS in 2011*, EPJ Web Conf. **28** (2012) 01003.

[68] M. Lamont, *Status of the LHC*, Journal of Physics: Conference Series **455(1)** (2013) 012001.

[69] A Corso-Radu et al., *Data Quality Monitoring Framework for the ATLAS experiment: Performance achieved with colliding beams at the LHC*, Journal of Physics: Conference Series **331(2)** (2011) 022027.

[70] ATLAS Collaboration, *Electron efficiency measurements with the ATLAS detector using 2012 LHC proton–proton collision data*, Eur. Phys. J. **C77** (2017) 195.

[71] Lampl, W. et al., *Calorimeter Clustering Algorithms: Description and Performance*, Tech. Rep. ATL-LARG-PUB-2008-002. ATL-COM-LARG-2008-003, CERN, Geneva, (2008).

[72] The ATLAS Collaboration, *Expected performance of the ATLAS experiment: detector, trigger and physics*, arXiv:0901.0512 [hep-ex].

[73] ATLAS Collaboration, *Measurement of the muon reconstruction performance of the ATLAS detector using 2011 and 2012 LHC proton–proton collision data*, Eur. Phys. J. **C74** (2014) 3130.

[74] K. Rehermann and B. Tweedie, *Efficient Identification of Boosted Semileptonic Top Quarks at the LHC*, JHEP **03** (2011) 059.

[75] J. E. Huth *et al.*, *Toward a standardization of jet definitions*, in: *1990 DPF Summer Study on High-energy Physics: Research Directions for the Decade (Snowmass 90) Snowmass, Colorado, June 25-July 13, 1990*, (1990), 1990 0134–136.

[76] ATLAS Collaboration, *Jet energy measurement with the ATLAS detector in proton–proton collisions at* $\sqrt{s} = 7$ *TeV*, Eur. Phys. J. **C73** (2013) 2304.

[77] ATLAS Collaboration, *Performance of b-jet identification in the ATLAS experiment*, JINST **11** (2016) P04008.

[78] M. Cacciari, G. P. Salam, and G. Soyez, *FastJet User Manual*, Eur. Phys. J. **C72** (2012) 1896.

[79] C. Cojocaru *et al.*, *Hadronic calibration of the ATLAS liquid argon end-cap calorimeter in the pseudorapidity region* $1.6 < |\eta| < 1.8$ *in beam tests*, Nucl. Instrum. Methods Phys. Res., A **531** (2004) 481.

[80] T. Barillari *et al.*, *Local Hadronic Calibration*, Tech. Rep. ATL-LARG-PUB-2009-001-2. ATL-COM-LARG-2008-006. ATL-LARG-PUB-2009-001, CERN, Geneva, (2008).

[81] ATLAS Collaboration, *Monte Carlo Calibration and Combination of In-situ Measurements of Jet Energy Scale, Jet Energy Resolution and Jet Mass in ATLAS*, ATLAS-CONF-2015-037, (2015).

[82] ATLAS Collaboration, *Jet energy measurement and its systematic uncertainty in proton–proton collisions at* $\sqrt{s} = 7$ *TeV with the ATLAS detector*, Eur. Phys. J. **C75** (2015) 17.

[83] ATLAS Collaboration, *Pile-up subtraction and suppression for jets in ATLAS*, ATLAS-CONF-2013-083, (2013).

[84] G. Piacquadio and C. Weiser, *A new inclusive secondary vertex algorithm for b-jet tagging in ATLAS*, Journal of Physics: Conference Series **119(3)** (2008) 032032.

[85] ATLAS collaboration, *Calibration of b-tagging using dileptonic top pair events in a combinatorial likelihood approach with the ATLAS experiment*, Tech. Rep. ATLAS-CONF-2014-004, CERN, Geneva, (2014).

[86] ATLAS collaboration, *Calibration of the performance of b-tagging for c and light-flavour jets in the 2012 ATLAS data*, Tech. Rep. ATLAS-CONF-2014-046, CERN, Geneva, (2014).

[87] ATLAS Collaboration, *Performance of Missing Transverse Momentum Reconstruction in ATLAS studied in Proton–Proton Collisions recorded in 2012 at* $\sqrt{s} = 8$ *TeV*, ATLAS-CONF-2013-082, (2013).

[88] ATLAS Collaboration, *Performance of missing transverse momentum reconstruction in proton–proton collisions at* $\sqrt{s} = 7$ *TeV with ATLAS*, Eur. Phys. J. **C72** (2012) 1844.

[89] ATLAS Collaboration, *Performance of Missing Transverse Momentum Reconstruction in ATLAS with 2011 Proton–Proton Collisions at* $\sqrt{s} = 7$ *TeV*, ATLAS-CONF-2012-101, (2012).

[90] B. R. Webber, *A QCD Model for Jet Fragmentation Including Soft Gluon Interference*, Nucl. Phys. **B238** (1984) 492.

[91] GEANT4 Collaboration, *GEANT4: A Simulation toolkit*, Nucl. Instrum. Meth. **A506** (2003) 250.

[92] ATLAS Collaboration, *The ATLAS calorimeter simulation FastCaloSim*, J. Phys. Conf. Ser. **331** (2011) 032053.

[93] ATLAS Collaboration, *The ATLAS Simulation Infrastructure*, Eur. Phys. J. **C70** (2010) 823.

[94] P. Nason, *A New method for combining NLO QCD with shower Monte Carlo algorithms.*, JHEP **11** (2004) 040.

[95] S. Frixione, P. Nason and C. Oleari, *Matching NLO QCD computations with Parton Shower simulations: the POWHEG method.*, JHEP **11** (2007) 070.

[96] S. Alioli et al., *A general framework for implementing NLO calculations in shower Monte Carlo programs: the POWHEG BOX.*, JHEP **06** (2010) 043.

[97] K. Melnikov and F. Petriello, *Electroweak gauge boson production at hadron colliders through* $O(\alpha_s^2)$, Phys. Rev. **D74** (2006) 114017.

[98] A. Juste et al., *Measurement of the charge asymmetry in top quark pair production in pp collision data at* $\sqrt{s} = 8$ *TeV using the ATLAS detector.*, Tech. Rep. ATL-COM-PHYS-2014-087, CERN, Geneva, (2014).

[99] N. Kidonakis, *Next-to-next-to-leading-order collinear and soft gluon corrections for tchannel single top quark production*, Phys. Rev. **D83** (2011) 091503.

[100] CDF Collaboration, *Two-loop soft anomalous dimensions for single top quark associated production with a W or H*, Phys. Rev. **D82** (2010) 054018.

[101] CDF Collaboration, *NNLL resummation for s-channel single top quark production*, Phys. Rev. **D81** (2010) 054028.

[102] J. Campbell and R. Ellis, *An update on vector boson pair production at hadron colliders*, Phys. Rev. **D60** (1999) 113006.

[103] P. Nason, *A New method for combining NLO QCD with shower Monte Carlo algorithms*, JHEP **11** (2004) 040.

[104] S. Frixione, P. Nason, and C. Oleari, *Matching NLO QCD computations with Parton Shower simulations: the POWHEG method*, JHEP **11** (2007) 070.

[105] S. Alioli et al., *A general framework for implementing NLO calculations in shower Monte Carlo programs: the POWHEG BOX*, JHEP **06** (2010) 043.

[106] T. Sjostrand, S. Mrenna, and P. Z. Skands, *PYTHIA 6.4 Physics and Manual*, JHEP **05** (2006) 026.

[107] Nadolsky, Pavel M. et al., *Implications of CTEQ global analysis for collider observables*, Phys. Rev. **D78** (2008) 013004.

[108] P. Z. Skands, *Tuning Monte Carlo Generators: The Perugia Tunes*, Phys. Rev. **D82** (2010) 074018.

[109] M. Botje *et al.*, *The PDF4LHC Working Group Interim Recommendations.*

[110] A. D. Martin, W. J. Stirling, R. S. Thorne, and G. Watt, *Parton distributions for the LHC*, Eur. Phys. J. **C63** (2009) 189.

[111] A. D. Martin, W. J. Stirling, R. S. Thorne, and G. Watt, *Uncertainties on alpha(S) in global PDF analyses and implications for predicted hadronic cross sections*, Eur. Phys. J. **C64** (2009) 653.

[112] H.-L. Lai et al., *New parton distributions for collider physics* **82** (2010) 074024.

[113] R. D. Ball *et al.*, *Parton distributions with LHC data*, Nucl. Phys. **B867** (2013) 244.

[114] ATLAS Collaboration, *Search for the Standard Model Higgs boson produced in association with top quarks and decaying into $b\bar{b}$ in pp collisions at $\sqrt{s} = 8$ TeV with the ATLAS detector*, Eur. Phys. J. **C75** (2015) 349.

[115] S. Frixione, P. Nason, and B. R. Webber, *Matching NLO QCD and parton showers in heavy flavor production*, JHEP **08** (2003) 007.

[116] Corcella, G. et al., *HERWIG 6: An Event generator for hadron emission reactions with interfering gluons (including supersymmetric processes)*, JHEP **01** (2001) 010.

[117] J. Butterworth, J. Forshaw, and M. Seymour, *Multiparton interactions in photoproduction at HERA* **72** (1996) 637.

[118] M. L. Mangano, M. Moretti, F. Piccinini, R. Pittau, and A. D. Polosa, *ALPGEN, a generator for hard multiparton processes in hadronic collisions*, JHEP **07** (2003) 001.

[119] M. L. Mangano, M. Moretti, and R. Pittau, *Multijet matrix elements and shower evolution in hadronic collisions: $Wb\bar{b}$ + n jets as a case study*, Nucl. Phys. **B632** (2002) 343.

[120] K. Melnikov and F. Petriello, *Electroweak gauge boson production at hadron colliders through O(alpha(s)**2)*, Phys. Rev. **D74** (2006) 114017.

[121] ATLAS Collaboration, *Measurement of the production cross section of jets in association with a Z boson in pp collisions at $\sqrt{s} = 7$ TeV with the ATLAS detector*, JHEP **07** (2013) 032.

[122] S. Frixione et al., *Single-top production in MC@NLO*, JHEP **03** (2006) 092.

[123] J. M. Campbell and R. K. Ellis, *An Update on vector boson pair production at hadron colliders*, Phys. Rev. **D60** (1999) 113006.

[124] ATLAS Collaboration, *Selection of jets produced in proton-proton collisions with the ATLAS detector using 2011 data*, Tech. Rep. ATLAS-CONF-2012-020, CERN, Geneva, (2012).

[125] CDF Collaboration, *W boson polarisation measurement in the $t\bar{t}$ dilepton channel using the CDF II Detector.*, Phys. Lett **D73** (2013) 112006.

[126] CDF Collaboration, *Measurement of the top quark mass using template methods on dilepton events in p anti-p collisions at $\sqrt{s} = 1.96$ TeV*, Phys. Rev **D03** (2006) 052.

[127] ATLAS Collaboration, *Measurement of the charge asymmetry in dileptonic decay of top quark pairs in pp collisions at $\sqrt{s}$ = 7 TeV using the ATLAS detector*, Tech. Rep. ATLAS-CONF-2012-057, CERN, Geneva, (2012).

[128] DØ Collaboration, *Measurement of the top quark mass using dilepton events*, Phys. Rev. Lett. **80** (1998) 2063.

[129] D. Guadagnoli and C. B. Park, *M_{T2}-reconstructed invisible momenta as spin analizers, and an application to top polarization*, JHEP **01** (2014) 030.

[130] A. Barr, C. Lester, and P. Stephens, *m(T2): The Truth behind the glamour*, J. Phys. **G29** (2003) 2343.

[131] W. Press et al., *Numerical Recipes: The Art of Scientific Computing (3rd ed.)*, Cambridge University Press, New York, (2007).

[132] J. Erdmann et al., *A likelihood-based reconstruction algorithm for top-quark pairs and the KLFitter framework*, Nucl. Instrum. Meth. **A748** (2014) 18.

[133] F. James and M. Roos, *MINUIT: a system for function minimization and analysis of the parameter errors and corrections*, Comput. Phys. Commun. **10(CERN-DD-75-20)** (1975) 343.

[134] R. Brun and F. Rademakers, *ROOT: An object oriented data analysis framework*, Nucl. Instrum. Meth. **A389** (1997) 81.

[135] ATLAS Collaboration, *Luminosity determination in pp collisions at* $\sqrt{s} = 8$ *TeV using the ATLAS detector at the LHC*, Eur. Phys. J. **C76** (2016) 653.

[136] ATLAS Collaboration, *In-situ jet energy scale and jet shape corrections for multiple interactions in the first ATLAS data at the LHC*, ATLAS-CONF-2011-030, (2011).

[137] ATLAS Collaboration, *In-situ pseudorapidity intercalibration for evaluation of jet energy scale uncertainty using dijet events in proton–proton collisions at* $\sqrt{s} = 7$ *TeV*, ATLAS-CONF-2011-014, (2011).

[138] ATLAS Collaboration, *Jet Energy Resolution and Selection Efficiency Relative to Track Jets from In-situ Techniques with the ATLAS Detector Using Proton–Proton Collisions at a Center of Mass Energy* $\sqrt{s} = 7$ *TeV*, ATLAS-CONF-2010-054, (2010).

[139] ATLAS Collaboration, *In-situ pseudorapidity intercalibration to evaluate jet energy scale uncertainty and calorimeter performance in the forward region*, ATLAS-CONF-2010-055, (2010).

[140] CDF and DØ Collaboration, Tevatron Electroweak Working Group, *Combination of CDF and DØ results on the mass of the top quark using up to 9.7* fb^{-1} *at the Tevatron*, FERMILAB-CONF-14-227-E-TD, TEVEWWG-top2014-01, CDF-Note-11105, D0-Note-6444 (2014).

[141] J. Alwall et al., *The automated computation of tree-level and next-to-leading order differential cross sections, and their matching to parton shower simulations*, JHEP **1407** (2014) 079.

[142] A. Czarnecki *et al.*, *Helicity fractions of W bosons from top quark decays at NNLO in QCD*, Phys. Rev **D81** (2010) 111503.

[143] F. Bach and T. Ohl, *Anomalous Top Couplings at Hadron Colliders Revisited*, Phys. Rev. **D86** (2012) 114026.

[144] N. Castro et al., *EFTfitter—A tool for interpreting measurements in the context of effective field theories*, Eur. Phys. J. **C76(8)** (2016) 432.

[145] ATLAS Collaboration, *Measurement of the W boson polarisation in $t\bar{t}$ events from pp collisions at $\sqrt{s} = 8$ TeV in the lepton+jets channel with ATLAS*, Eur. Phys. J. **C77** (2017) 264.

[146] M. J. Kareem, *Measurement of the W boson helicity fractions in $t\bar{t}$ events at $\sqrt{s} = 8$ TeV in the lepton+jets channel with the ATLAS detector*, Ph.D. thesis, II.Physik-UniGö-Diss-2017-01, Göttingen University, (2017).

[147] CMS Collaboration, *Measurement of the W boson helicity fractions in the decays of top quark pairs to lepton + jets final states produced in pp collisions at $\sqrt{s} =$ 8TeV*, Phys. Lett. **B762** (2016) 512.

[148] CMS Collaboration, *Measurement of the W boson helicity using $t\bar{t}$ events in the dilepton final state at sqrt(s) = 8 TeV*, Tech. Rep. CMS-PAS-TOP-14-017, CERN, Geneva, (2015).

[149] CMS Collaboration, *Measurement of the W boson helicity in events with a single reconstructed top quark in pp collisions at $\sqrt{s} = 8$ TeV*, JHEP **01** (2015) 053.

[150] ATLAS Collaboration, *Probing the Wtb vertex structure in t-channel single-top-quark production and decay in pp collisions at $\sqrt{s} = 8$ TeV with the ATLAS detector*, JHEP **04** (2017) 124.

[151] ATLAS Collaboration, *Fiducial, total and differential cross-section measurements of t-channel single top-quark production in pp collisions at* 8 *TeV using data collected by the ATLAS detector*, Eur. Phys. J. **C77** (2017) 531.

Appendices

APPENDIX A

Control Plots After Event Selection

This appendix contains figures that show data/prediction comparisons for sub-leading leptons and jets, after event selection in all three dilepton (ee, $\mu\mu$, and $e\mu$) channels, for both (1 exclusive and 2 inclusive) b-tag regions.

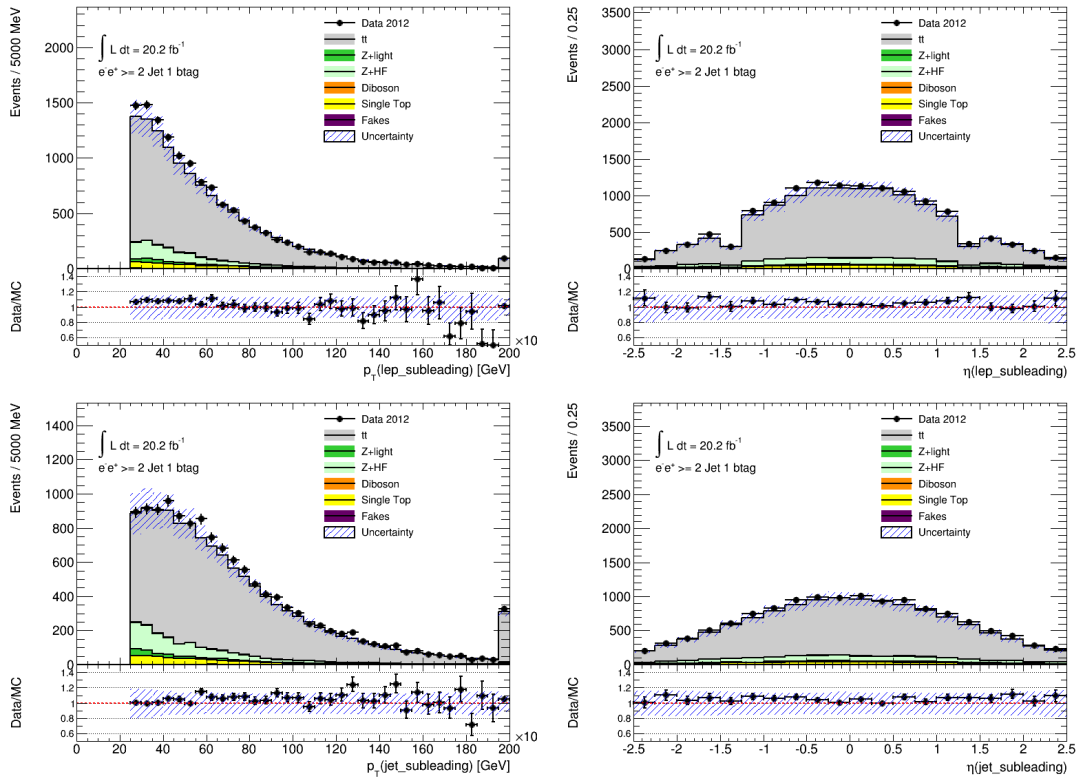

Figure A.1.: Plots showing data/MC agreement after event selection for the reconstructed objects (lepton, jets, E_T^{miss}) in the 1 exclusive b-tag, ee region. Stat+bkg.norm uncertainties are included.

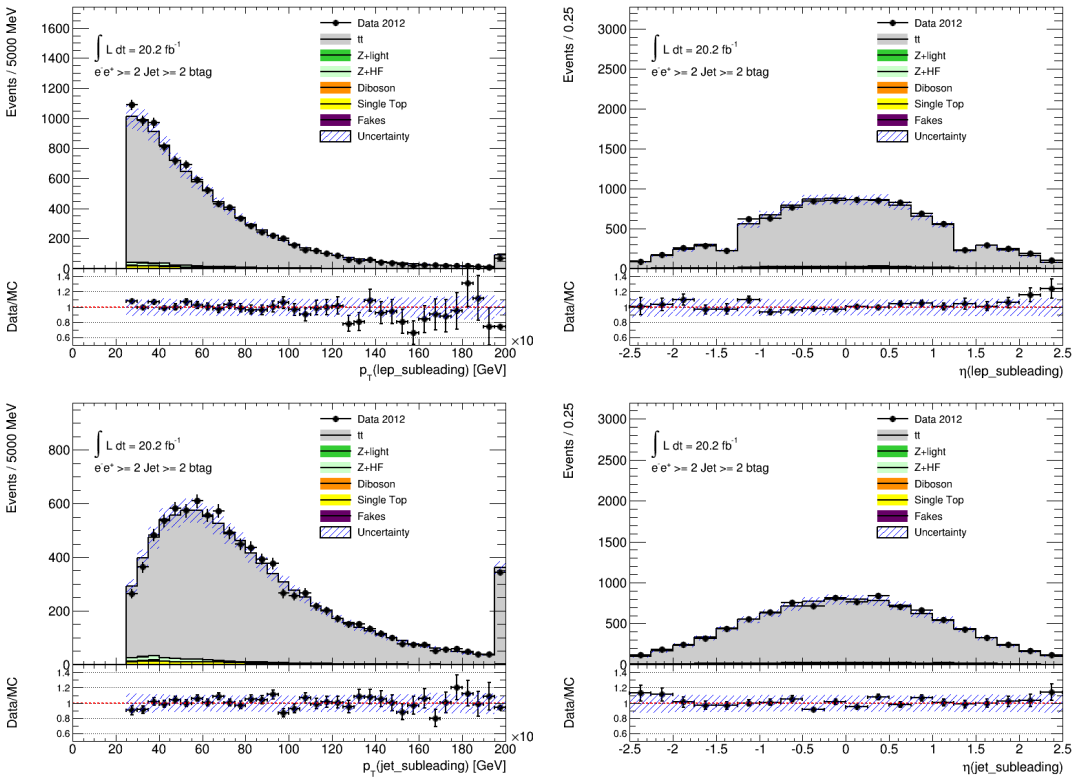

Figure A.2.: Plots showing data/MC agreement after event selection for the reconstructed objects (lepton, jets, E_T^{miss}) in the 2 inclusive b-tag, ee region. Statistical and background normalisation uncertainties are included.

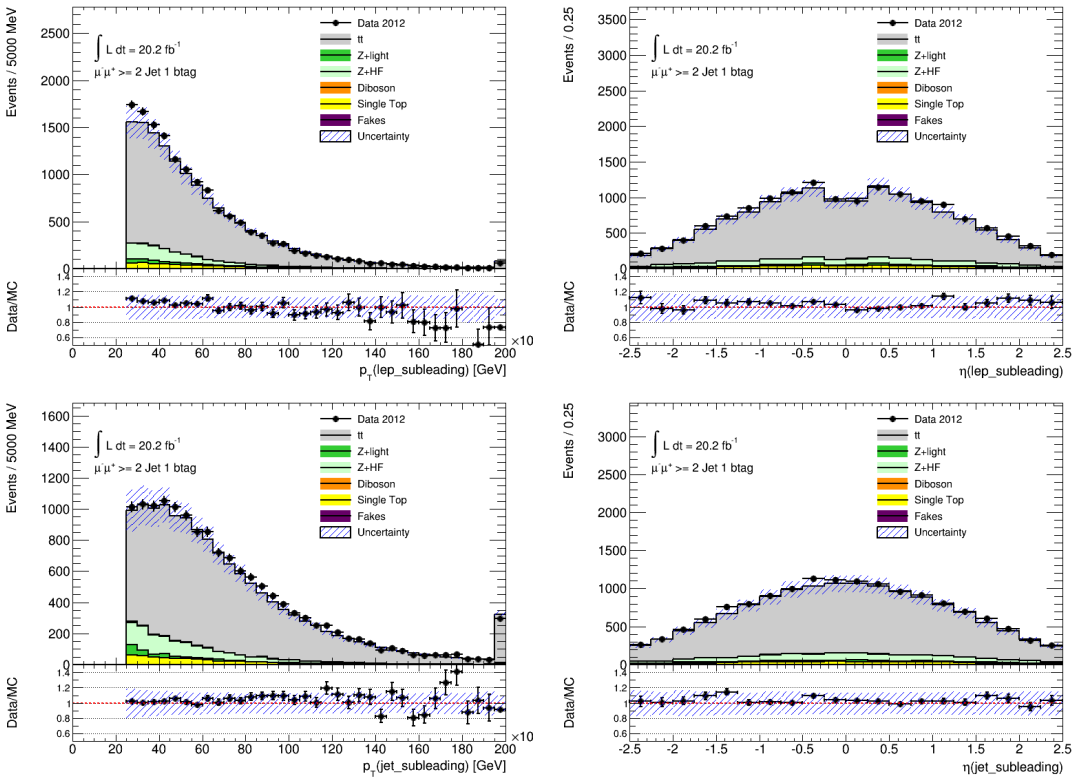

Figure A.3.: Plots showing data/MC agreement after event selection for the reconstructed objects (lepton, jets, E_T^{miss}) in the 1 exclusive b-tag, $\mu\mu$ region. Statistical and background normalisation uncertainties are included.

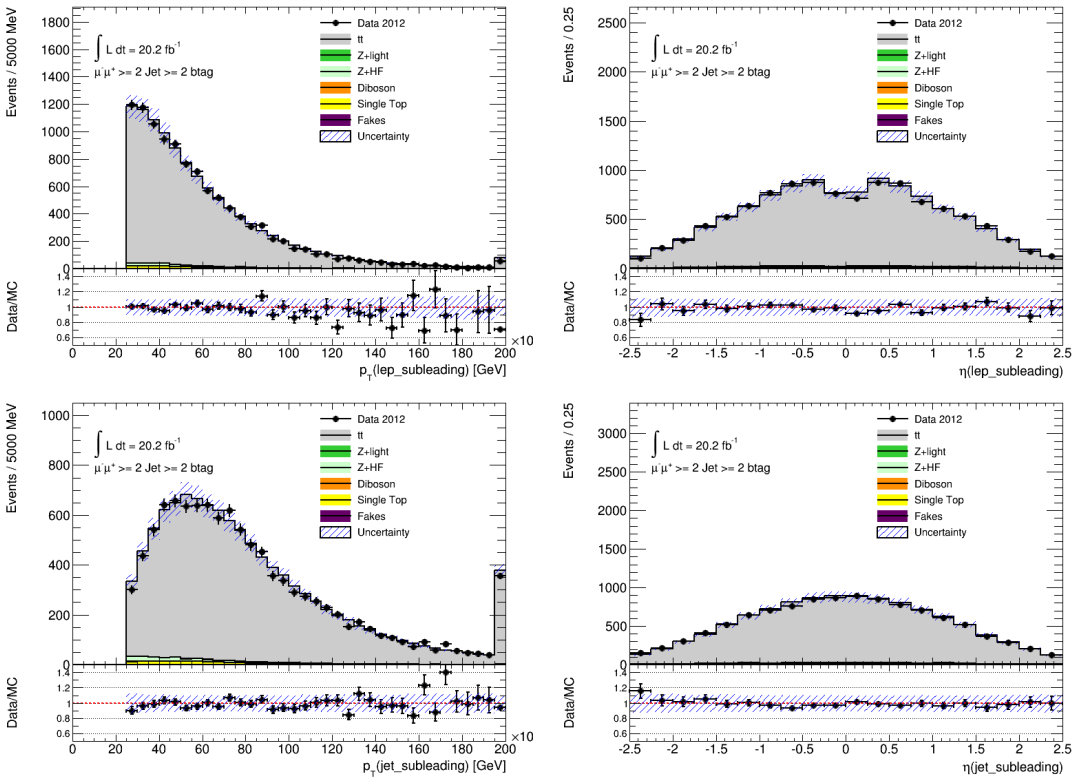

Figure A.4.: Plots showing data/MC agreement after event selection for the reconstructed objects (lepton, jets, E_T^{miss}) in the 2 inclusive b-tag, $\mu\mu$ region. Statistical and background normalisation uncertainties are included.

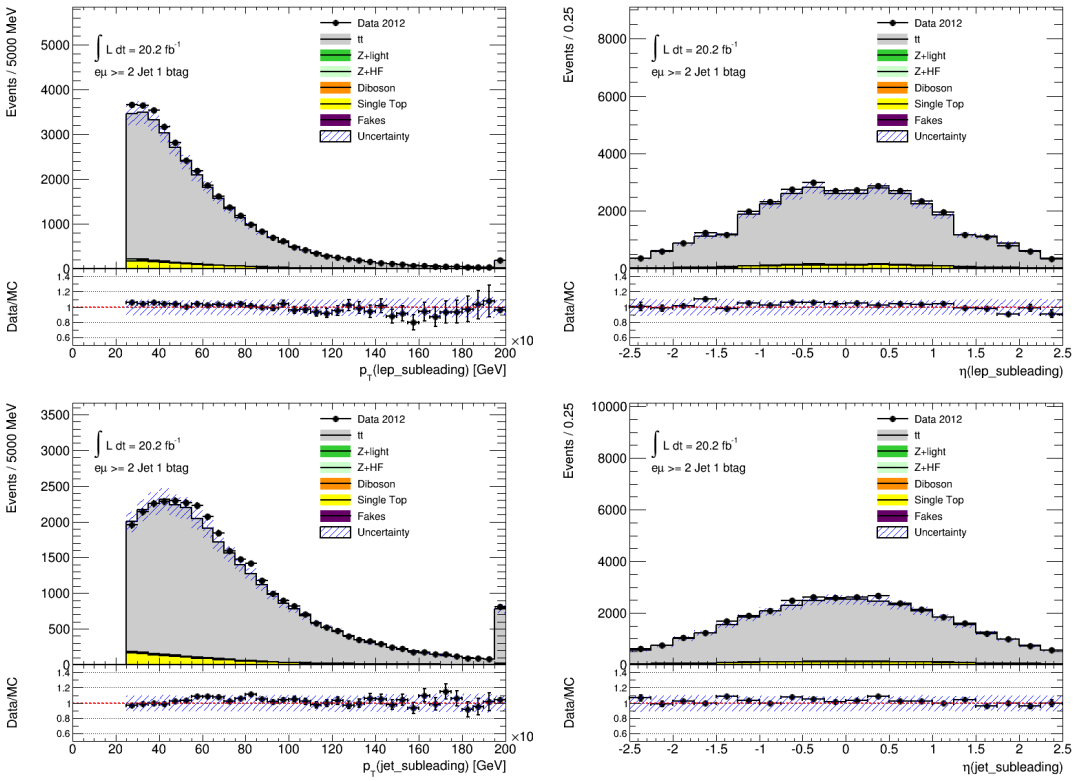

Figure A.5.: Plots showing data/MC agreement after event selection for the reconstructed objects (lepton, jets, E_T^{miss}) in the 1 exclusive b-tag, $e\mu$ region. Statistical and background normalisation uncertainties are included.

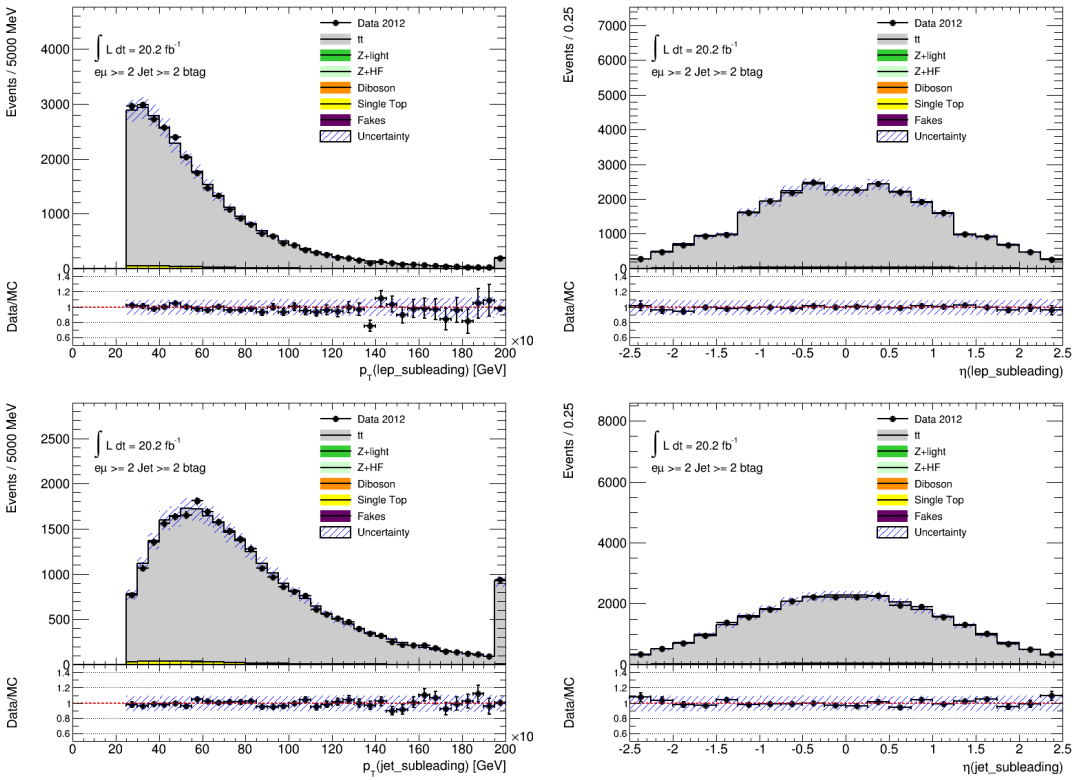

Figure A.6.: Plots showing data/MC agreement after event selection for the reconstructed objects (lepton, jets, E_T^{miss}) in the 2 inclusive b-tag, $e\mu$ region. Statistical and background normalisation uncertainties are included.

APPENDIX B

Control Plots After Event Reconstruction

This appendix contains figures that show data/prediction comparisons after event reconstruction in all three dilepton (ee, $\mu\mu$, and $e\mu$) channels and for both (1 exclusive and 2 inclusive) b-tag regions. Figure B.7 shows the ratio $N^{reco}_{smear}/N_{smear}$ for given events, where N_{smear} is number of total smears and N^{reco}_{smear} is the number of reconstructions for this event discussed in Section 6.2.1. As the distribution is flat, a cut on this value was not set.

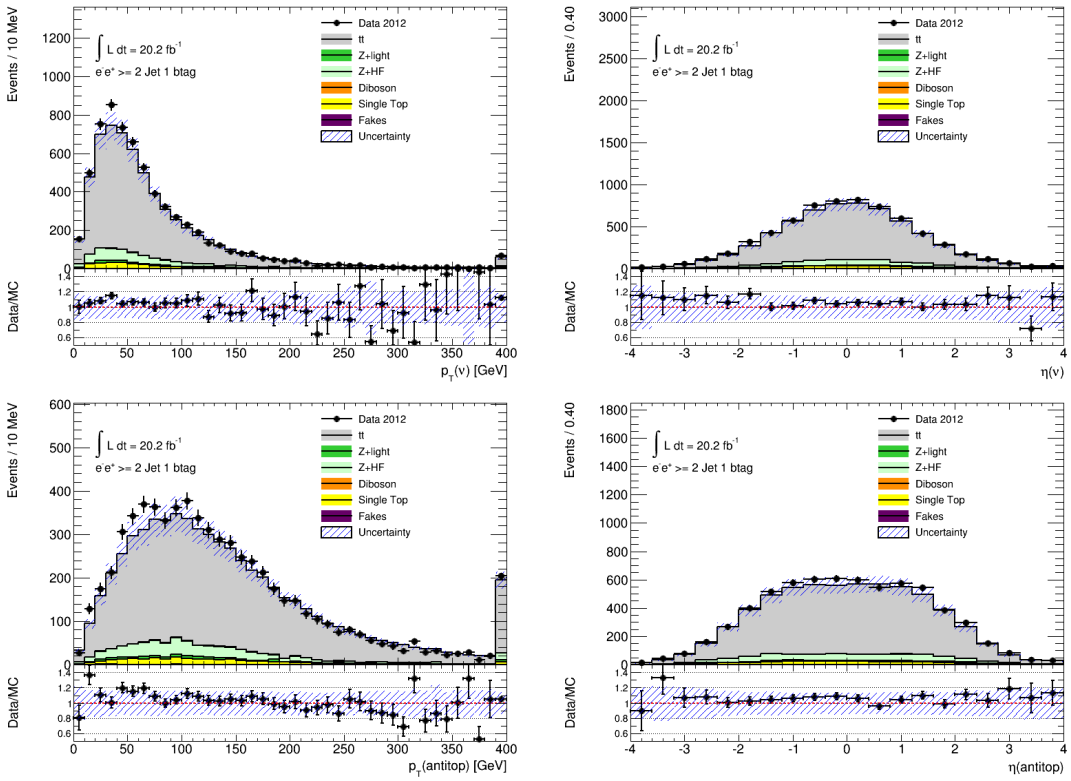

Figure B.1.: Plots showing data/MC agreement after event reconstruction for the reconstructed objects ($\bar{\nu}$ and $\bar{t}$) in the 1 exclusive b-tag, ee region. Stat+bkg.norm uncertainties are included.

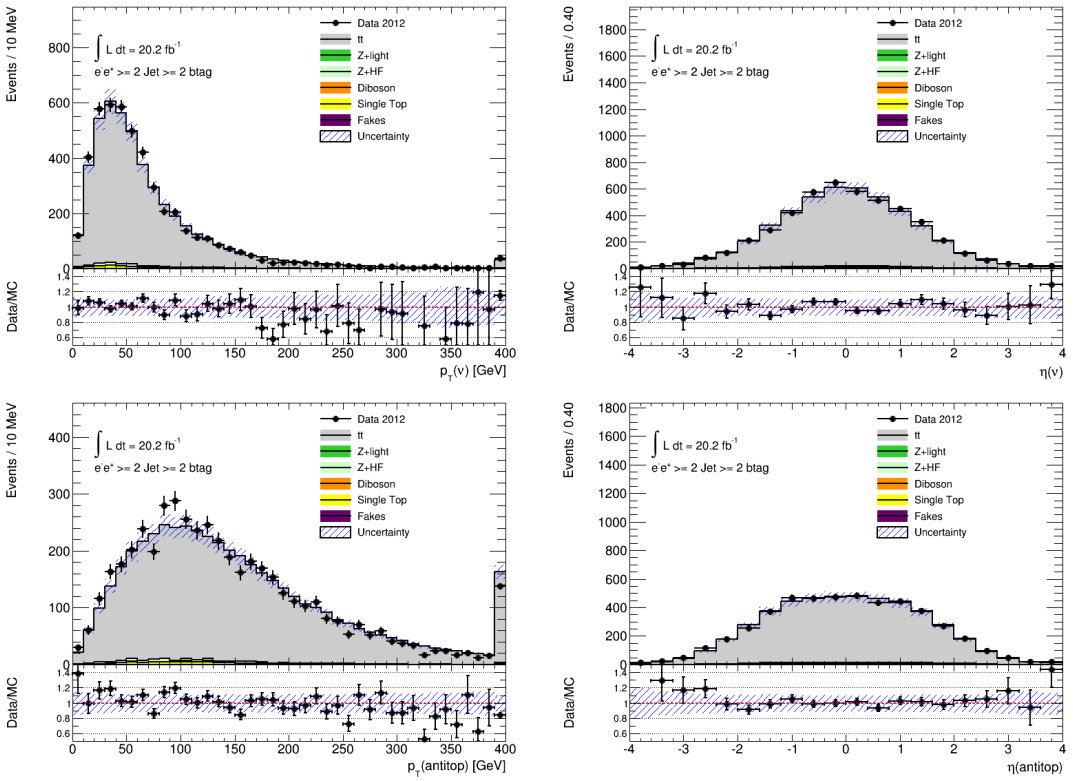

Figure B.2.: Plots showing data/MC agreement after event reconstruction for the reconstructed objects ($\bar{\nu}$ and $\bar{t}$) in the 2 inclusive b-tag, ee region. Statistical and background normalisation uncertainties are included.

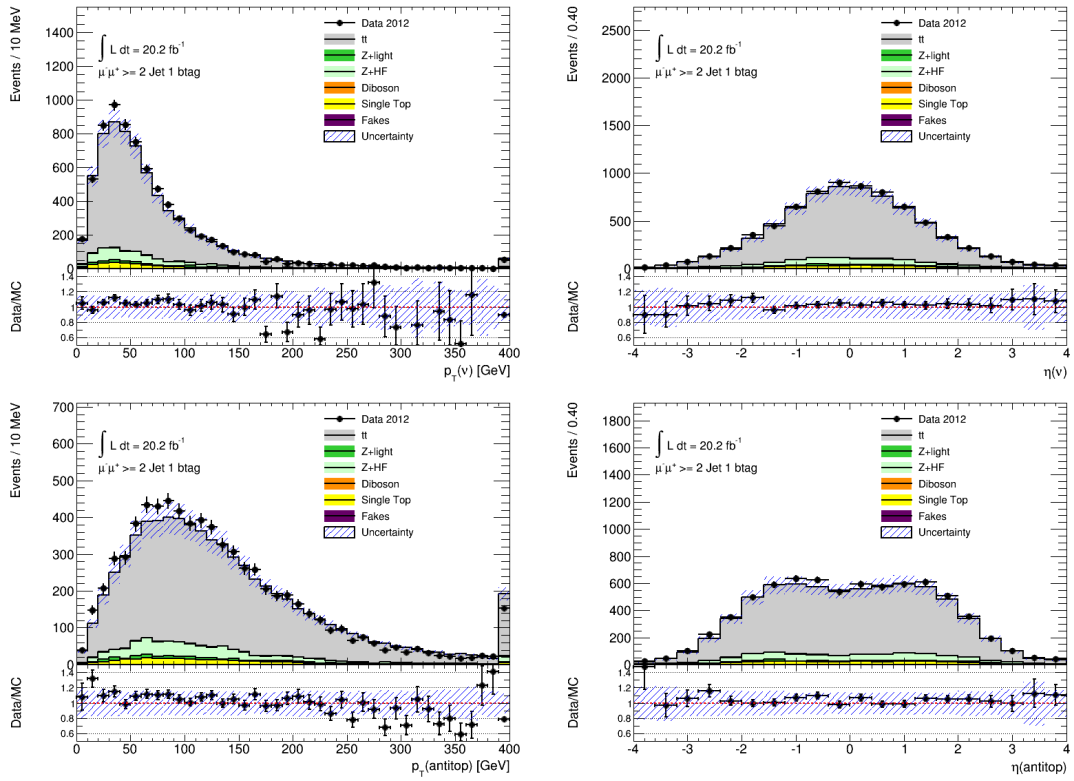

Figure B.3.: Plots showing data/MC agreement after event reconstruction for the reconstructed objects ($\bar{\nu}$ and $\bar{t}$) in the 1 exclusive b-tag, $e\mu$ region. Statistical and background normalisation uncertainties are included.

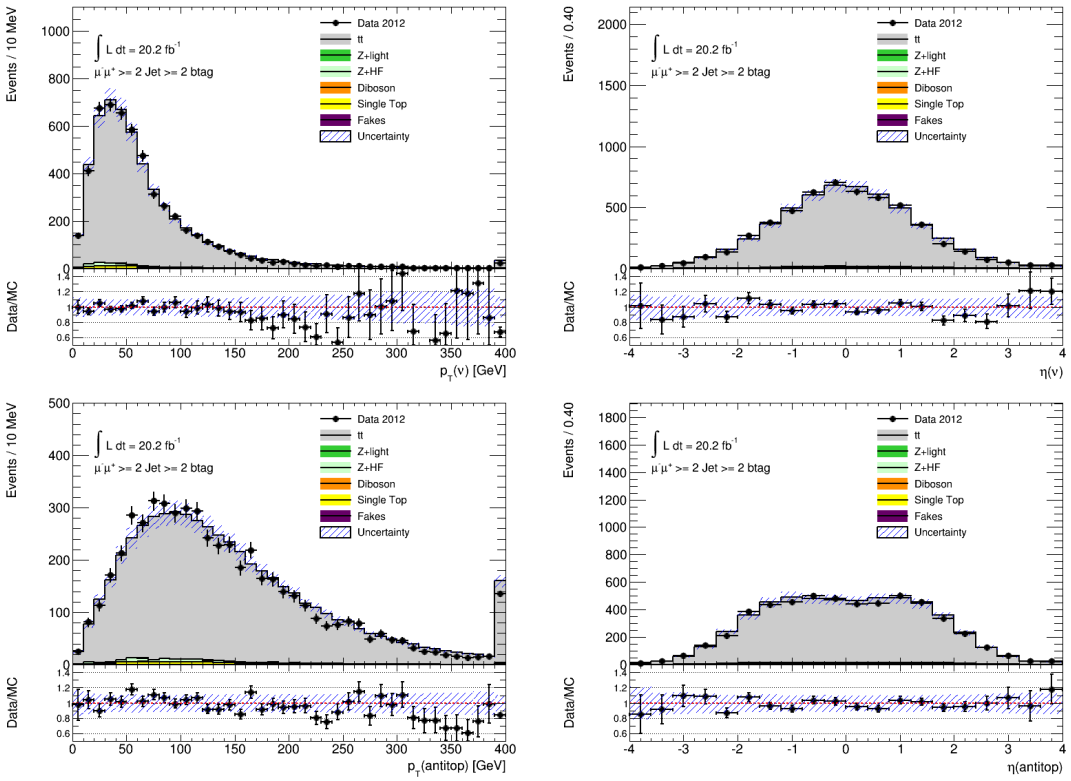

Figure B.4.: Plots showing data/MC agreement after event reconstruction for the reconstructed objects ($\bar{\nu}$ and $\bar{t}$) in the 2 inclusive b-tag, $\mu\mu$ region. Statistical and background normalisation uncertainties are included.

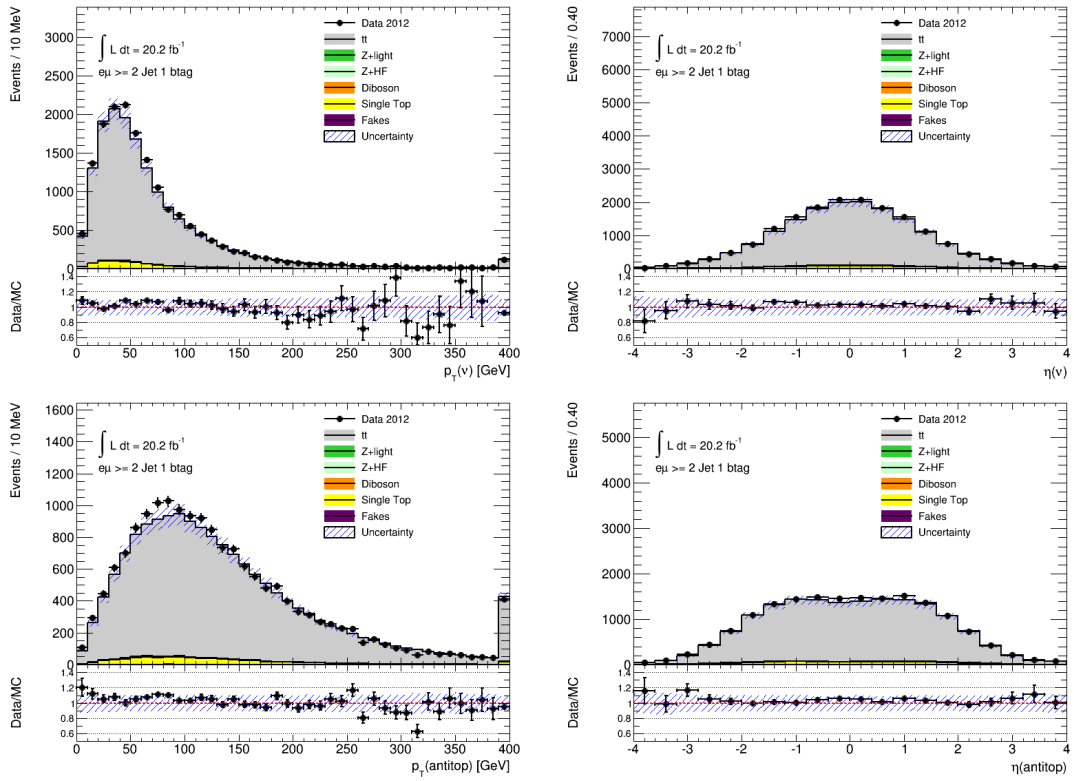

Figure B.5.: Plots showing data/MC agreement after event reconstruction for the reconstructed objects ($\bar{\nu}$ and $\bar{t}$) in the 1 exclusive b-tag, $e\mu$ region. Statistical and background normalisation uncertainties are included.

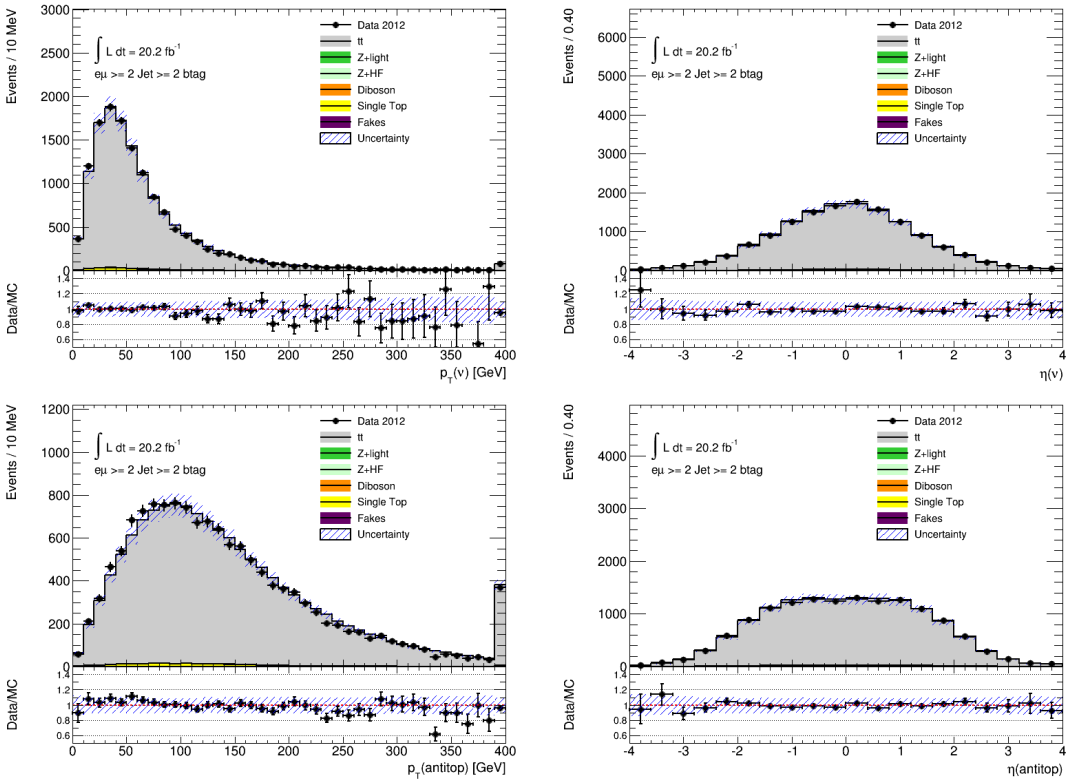

Figure B.6.: Plots showing data/MC agreement after event reconstruction for the reconstructed objects ($\bar{\nu}$ and $\bar{t}$) in the 2 inclusive b-tag, $e\mu$ region. Statistical and background normalisation uncertainties are included.

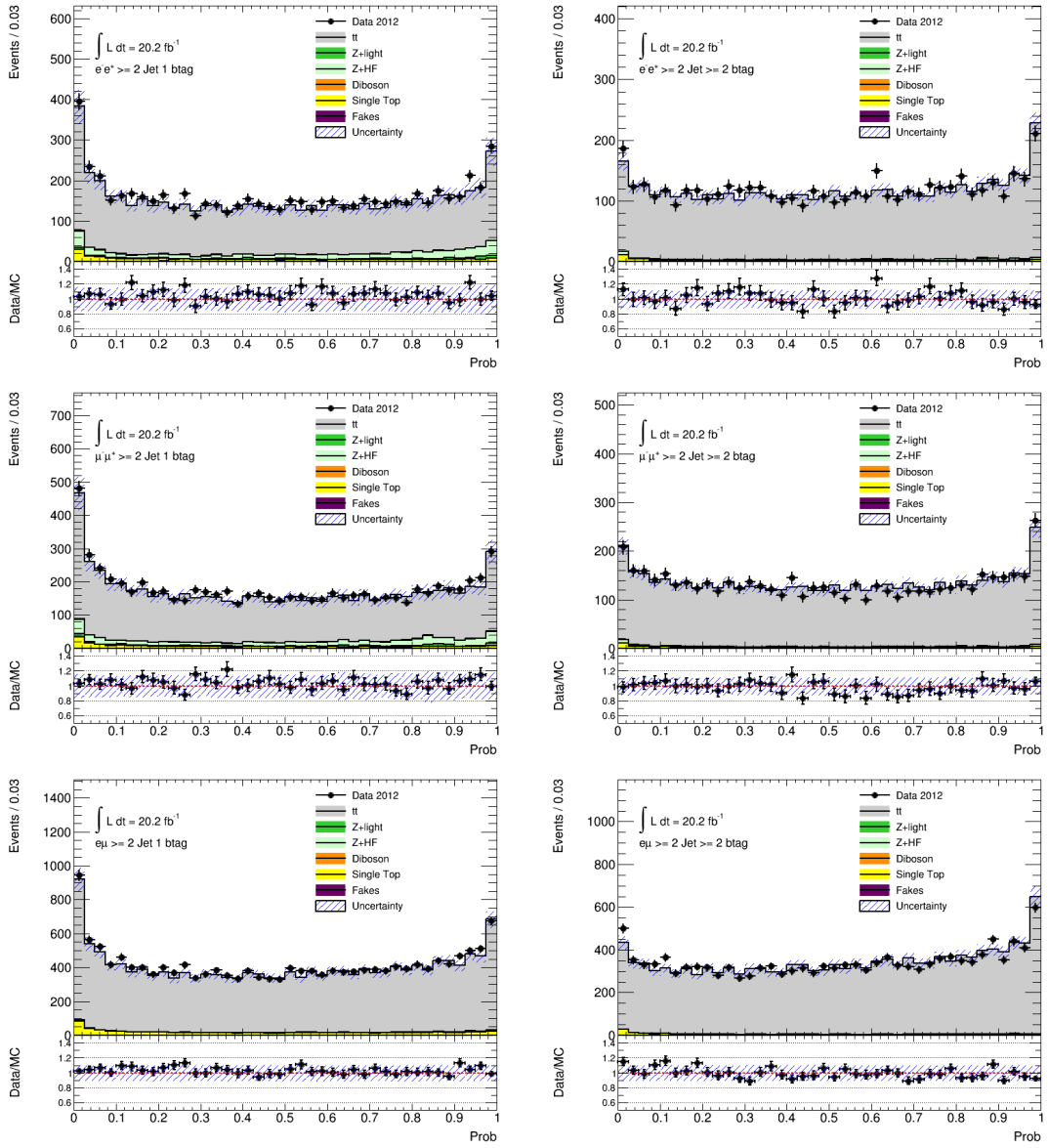

Figure B.7.: Plots showing data/MC agreement after $t\bar{t}$ system reconstruction for ee, $\mu\mu$ and $e\mu$ channels in the 1 exclusive b-tag (left) and 2 inclusive b-tag (right) regions, for value Prob= $N_{reco}^{smear}/N_{smear}$. Statistical and background normalisation uncertainties are included.

APPENDIX C

Pseudo-Data from Systematic Variations + Comparison to Statistical Uncertainty

This appendix contains plots showing the templates created after running selection and reconstruction on systematic variations of the $t\bar{t}$ signal. Differences between variations and the nominal sample are overlaid with the Monte Carlo statistical uncertainty of the nominal sample (green band in relative difference plots). When the differences between the nominal $\cos\theta^*$ distribution and a given systematic variation is smaller than the statistical uncertainty on the Monte Carlo yield of the nominal sample, that systematic variation is removed from consideration when calculating the total systematic error. A variation is kept if a) the difference between the total yield of the varied $\cos\theta^*$ distribution and the total nominal yield is larger than the total nominal Monte Carlo statistical uncertainty and/or b) if the difference in yield between the nominal sample and a variation is larger than the nominal MC uncertainty in two or more bins. The identification of significant systematics was performed via a script, but the plots here can be used to check the results by eye. Additionally, the six channel plots allow for comparisons of the differing effect of a given systematic in ee, $\mu\mu$ and $e\mu$, 1excl/2incl regions. Here, the absolute and relative difference is shown with error bars. The list of the kept systematics is as follows:

- ELE_TRIGGER, ELE_ID: Electron trigger and identification;
- MUON_TRIGGER, MUON_ID, MUON_RECO: Muon trigger, identification and reconstruction;
- JVF : Jet vertex fraction;
- jes_EffectiveNP_Modelling1: Jet energy scale modelling;

- BTAG_btag (6) , BTAG_ctag (4), BTAG_mistag (16);
- Parton Shower;
- MC Generator;
- ISR/FSR $t\bar{t}$ Radiation;
- Top quark mass.

C.1. Detector Systematics

C.1.1. Electron Systematics

The plot name definitions:

- ees: electron energy scale.
- ELE_ID: electron identification.
- ELE_RECO: electron reconstruction.
- ELE_TRIGGER: electron trigger.
- err: electron energy response.

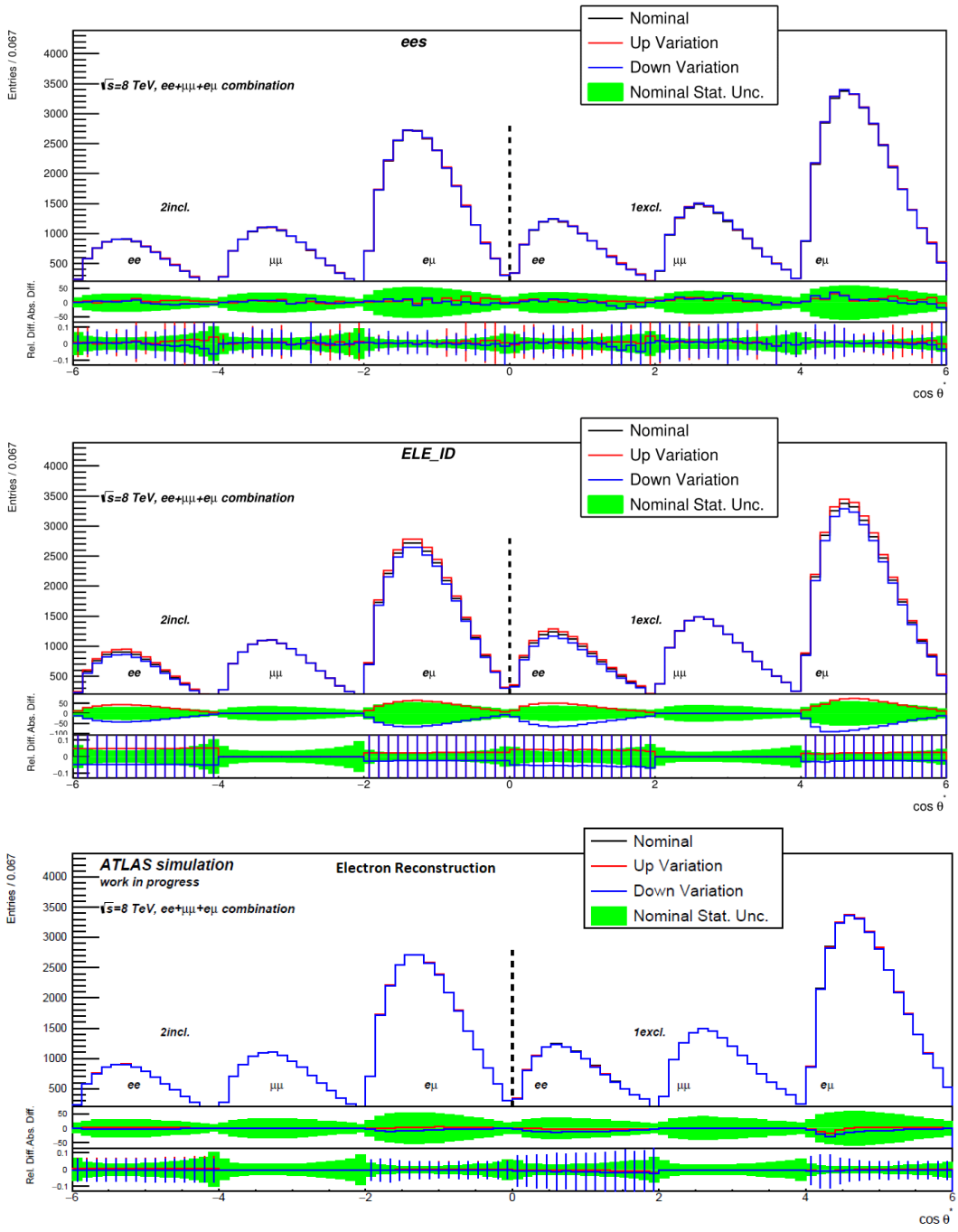

Figure C.1.: Generated pseudo-data for the ee, $\mu\mu$ and $e\mu$ combination for systematic variations and the nominal $t\bar{t}$ sample. The ratio plot shows the absolute and relative difference between the variations and the nominal sample in comparison to the statistical uncertainty of the nominal sample.

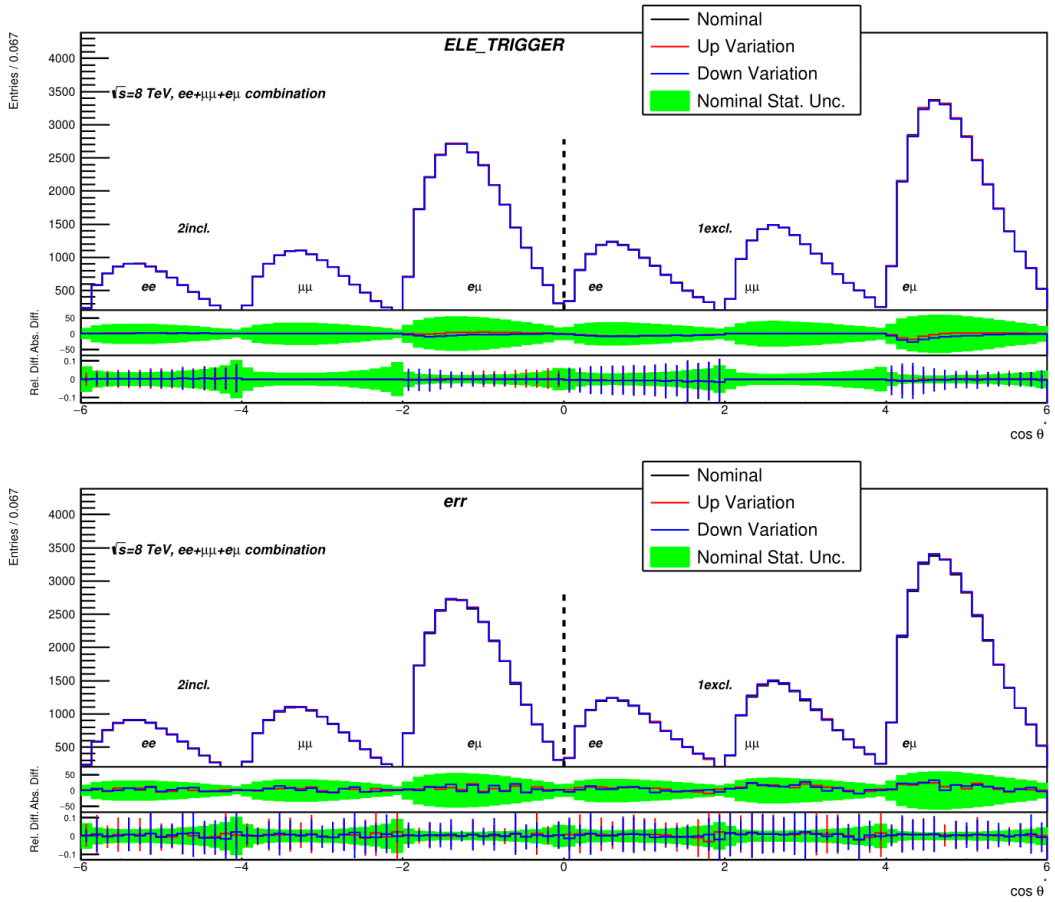

Figure C.2.: Generated pseudo-data for the ee, $\mu\mu$ and $e\mu$ combination for systematic variations and the nominal $t\bar{t}$ sample. The ratio plot shows the absolute and relative difference between the variations and the nominal sample in comparison to the statistical uncertainty of the nominal sample.

C.1.2. Muon Systematics

The plot name definitions:

- mu_idres: muon identification resolution.
- mu_msres: standalone muon resolution
- MUON_ID: muon identification.
- MUON_RECO: muon reconstruction.
- MUON_TRIGGER: muon trigger.
- mu_scale: muon scaling.

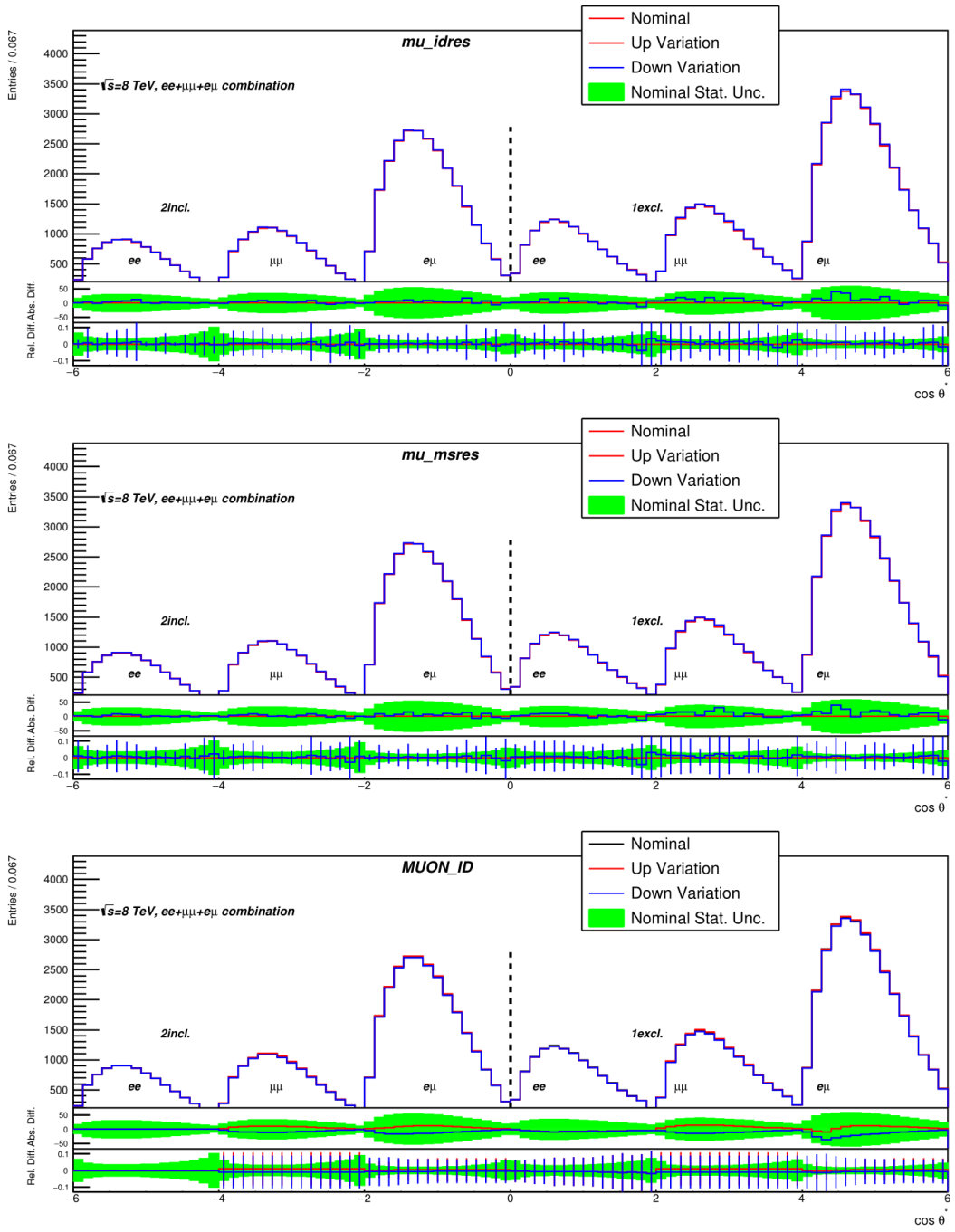

Figure C.3.: Generated pseudo-data for the ee, $\mu\mu$ and $e\mu$ combination for systematic variations and the nominal $t\bar{t}$ sample. The ratio plot shows the absolute and relative difference between the variations and the nominal sample in comparison to the statistical uncertainty of the nominal sample.

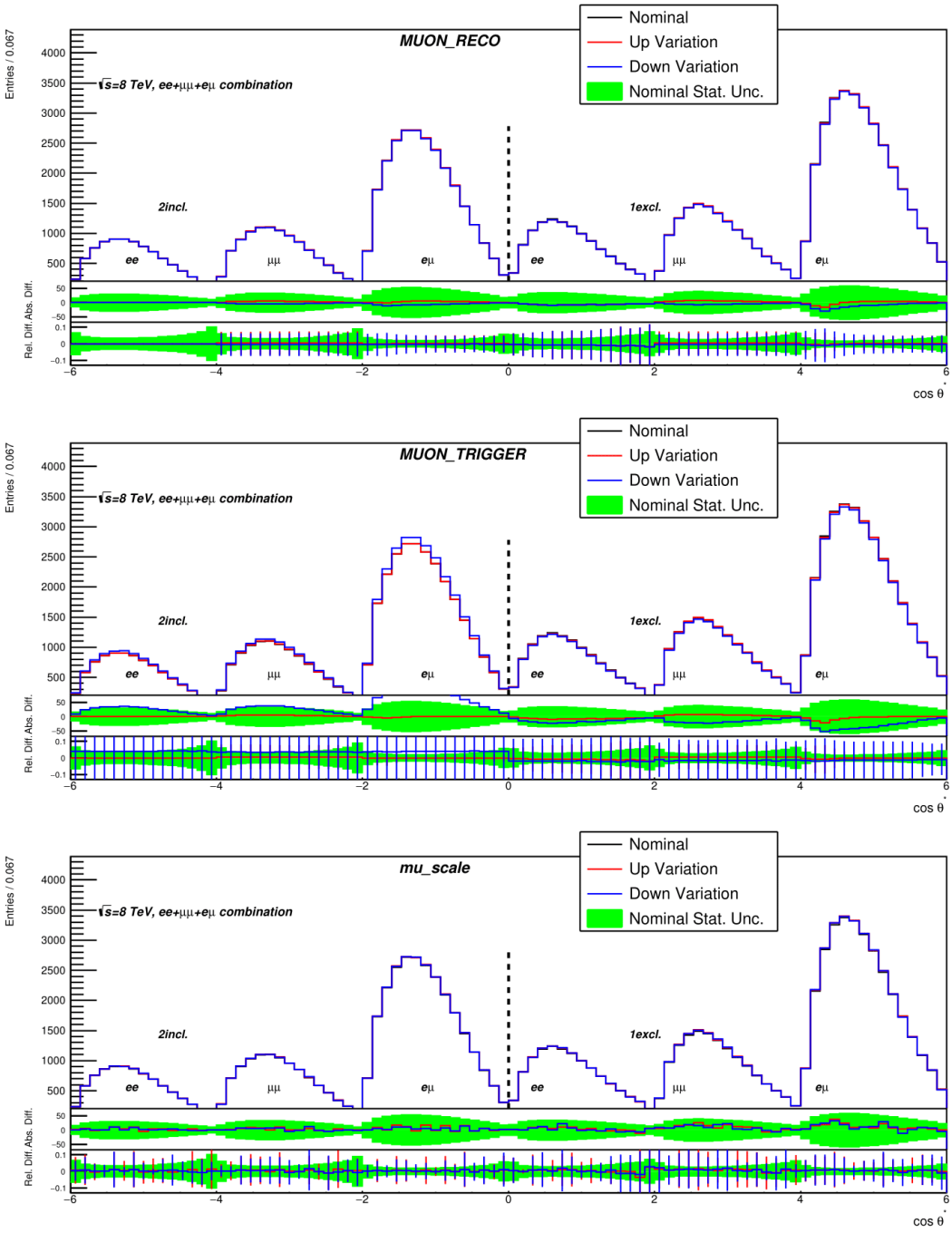

Figure C.4.: Generated pseudo-data for the ee, $\mu\mu$ and $e\mu$ combination for systematic variations and the nominal $t\bar{t}$ sample. The ratio plot shows the absolute and relative difference between the variations and the nominal sample in comparison to the statistical uncertainty of the nominal sample.

C.1.3. Jet Vertex Fraction

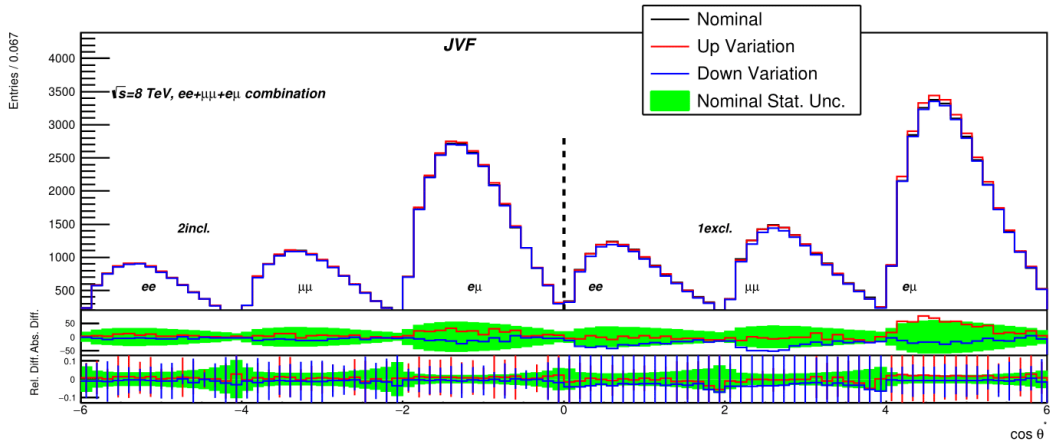

Figure C.5.: Generated pseudo-data for the ee, $\mu\mu$ and $e\mu$ combination for systematic variations and the nominal $t\bar{t}$ sample. The ratio plot shows the absolute and relative difference between the variations and the nominal sample in comparison to the statistical uncertainty of the nominal sample.

C.1.4. Jet Energy Scale (JES)

Individual JES components.

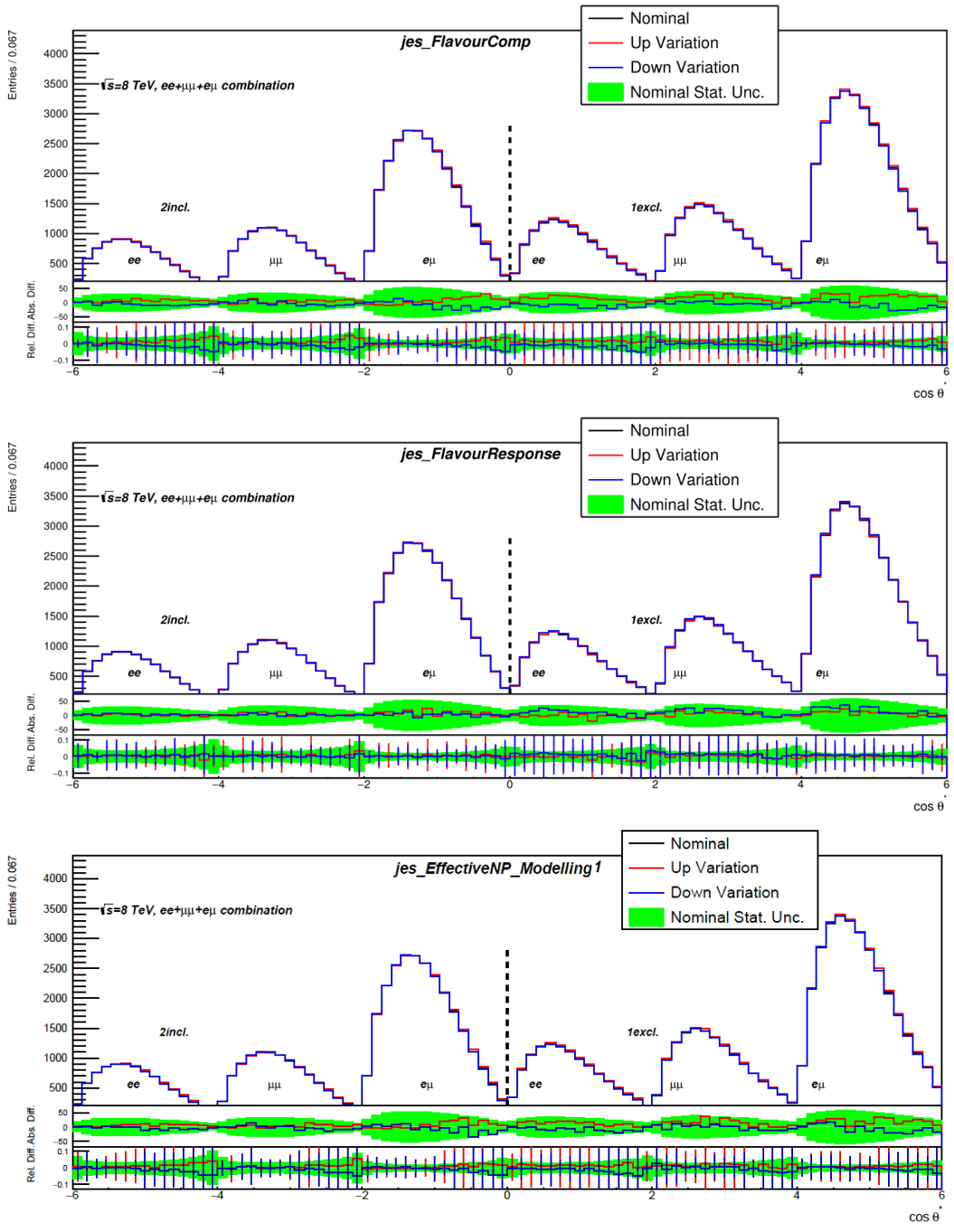

Figure C.6.: Generated pseudo-data for the ee, $\mu\mu$ and $e\mu$ combination for systematic variations and the nominal $t\bar{t}$ sample. The ratio plot shows the absolute and relative difference between the variations and the nominal sample in comparison to the statistical uncertainty of the nominal sample.

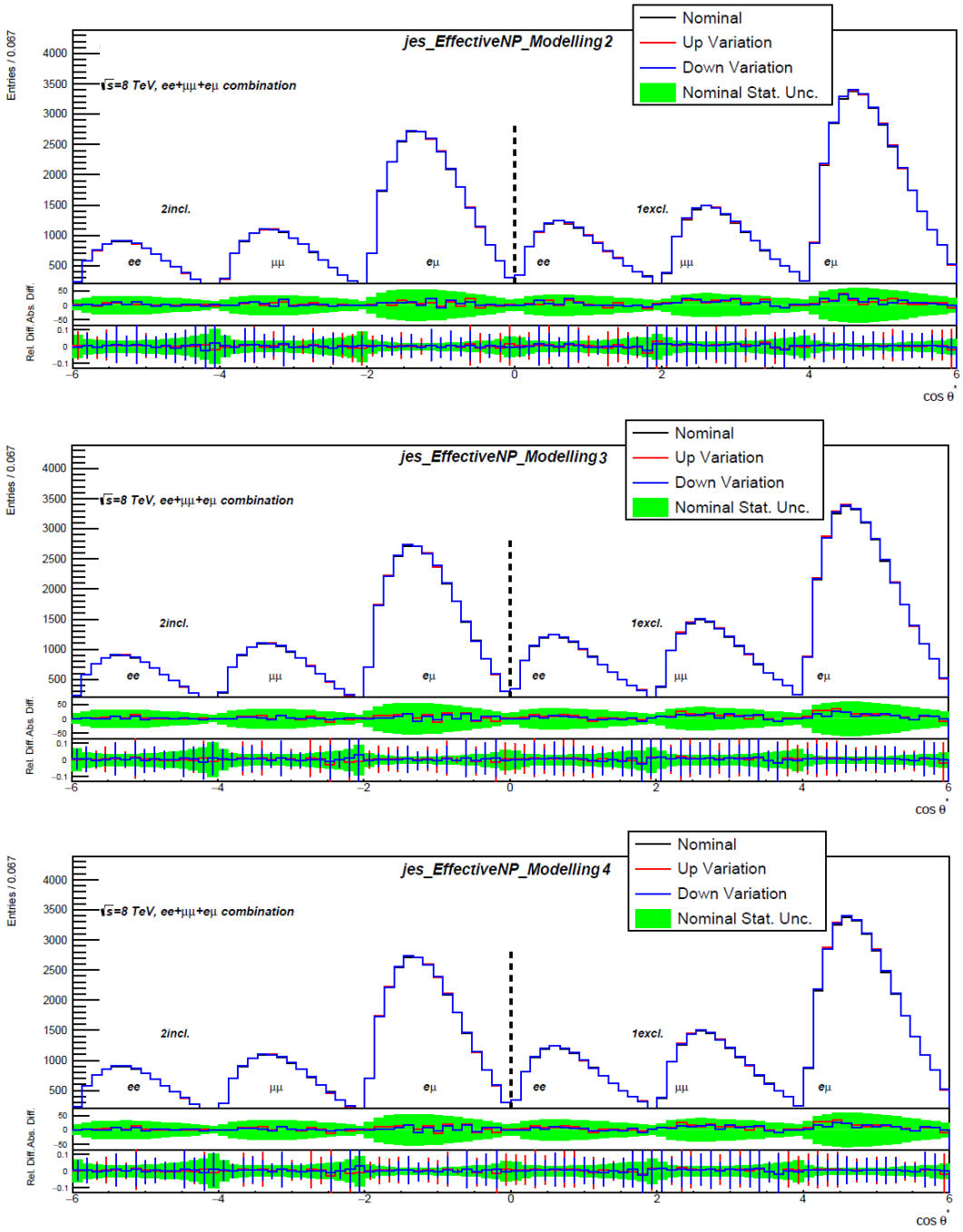

Figure C.7.: Generated pseudo-data for the ee, $\mu\mu$ and $e\mu$ combination for systematic variations and the nominal $t\bar{t}$ sample. The ratio plot shows the absolute and relative difference between the variations and the nominal sample in comparison to the statistical uncertainty of the nominal sample.

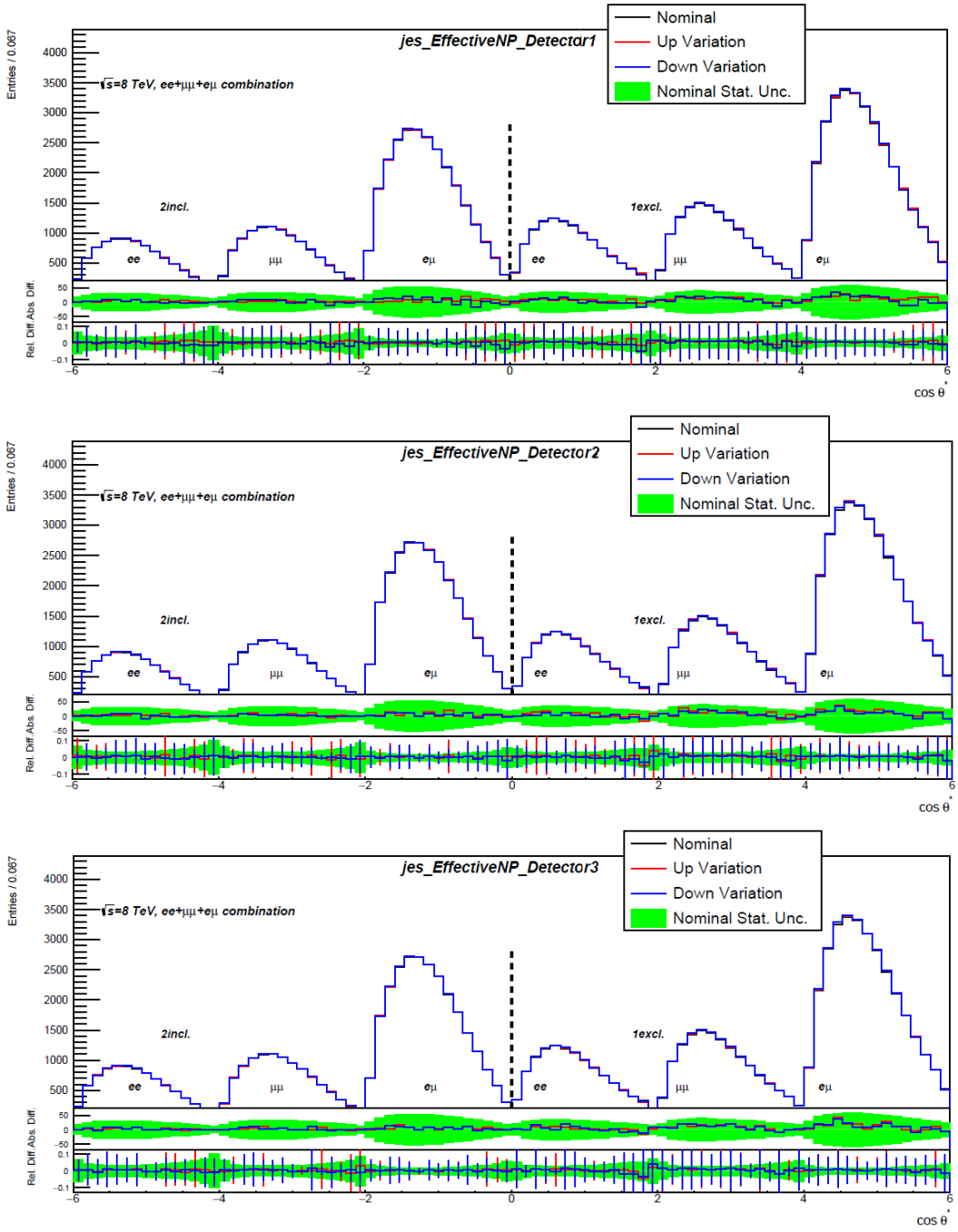

Figure C.8.: Generated pseudo-data for the ee, $\mu\mu$ and $e\mu$ combination for systematic variations and the nominal $t\bar{t}$ sample. The ratio plot shows the absolute and relative difference between the variations and the nominal sample in comparison to the statistical uncertainty of the nominal sample.

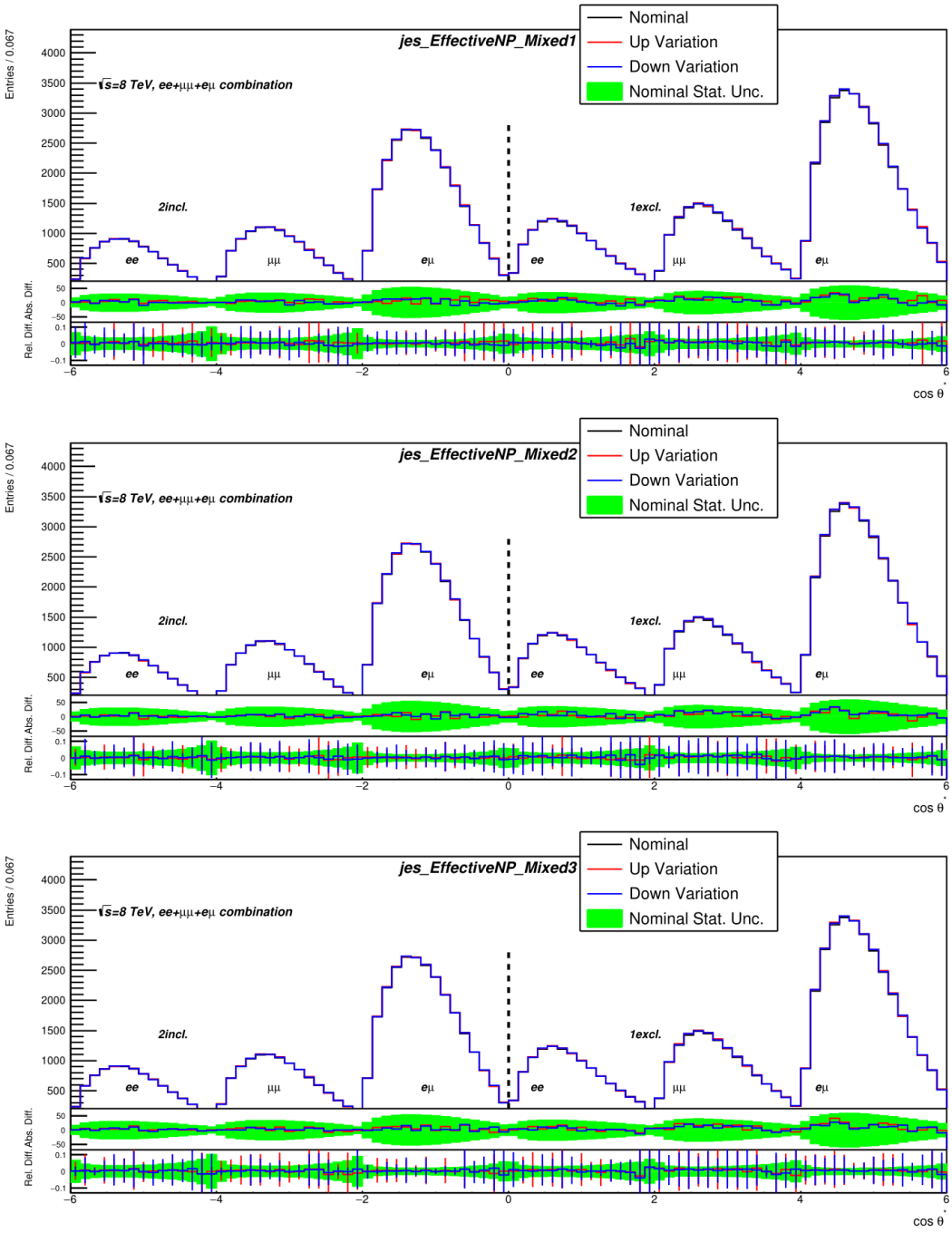

Figure C.9.: Generated pseudo-data for the ee, $\mu\mu$ and $e\mu$ combination for systematic variations and the nominal $t\bar{t}$ sample. The ratio plot shows the absolute and relative difference between the variations and the nominal sample in comparison to the statistical uncertainty of the nominal sample.

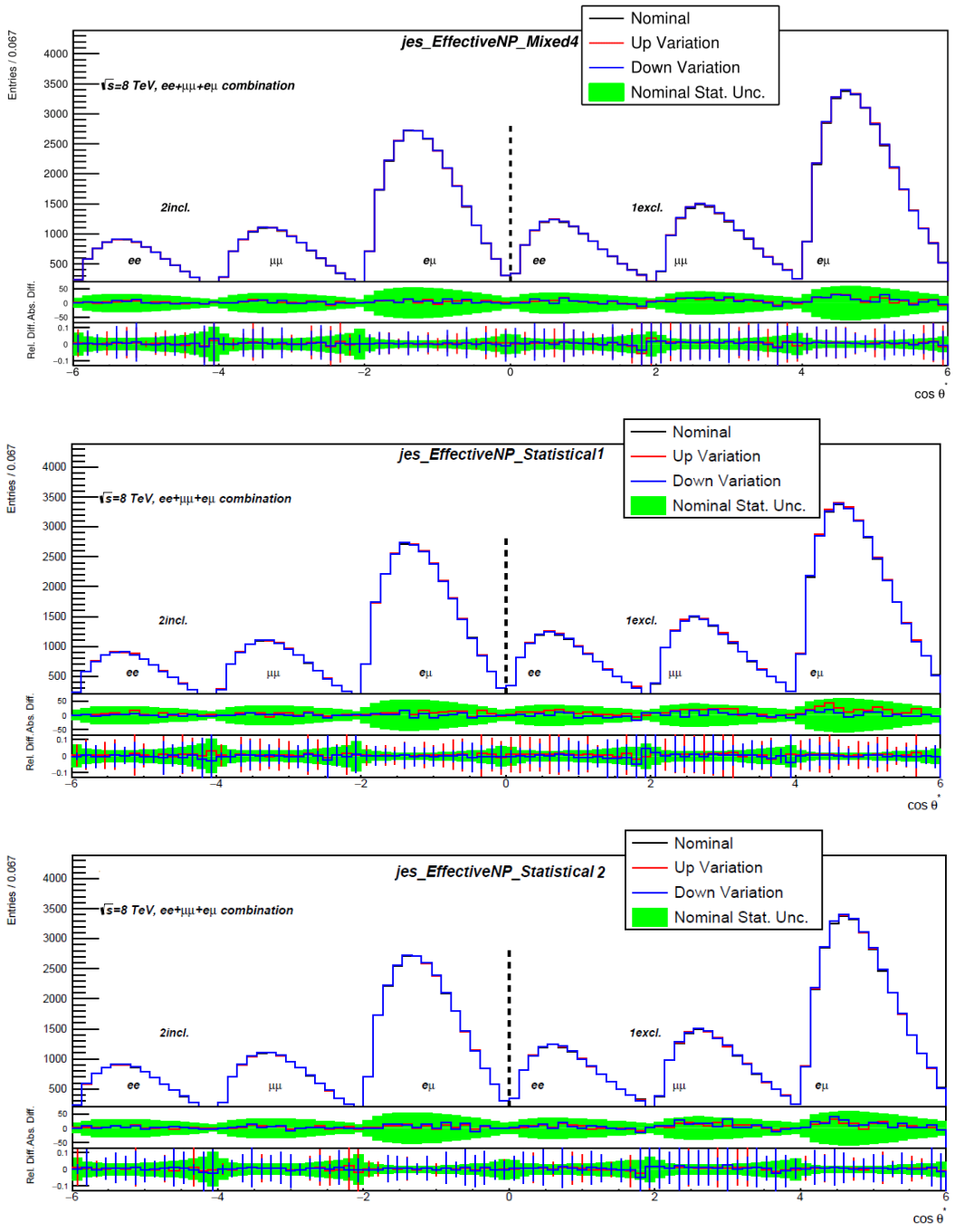

Figure C.10.: Generated pseudo-data for the ee, $\mu\mu$ and $e\mu$ combination for systematic variations and the nominal $t\bar{t}$ sample. The ratio plot shows the absolute and relative difference between the variations and the nominal sample in comparison to the statistical uncertainty of the nominal sample.

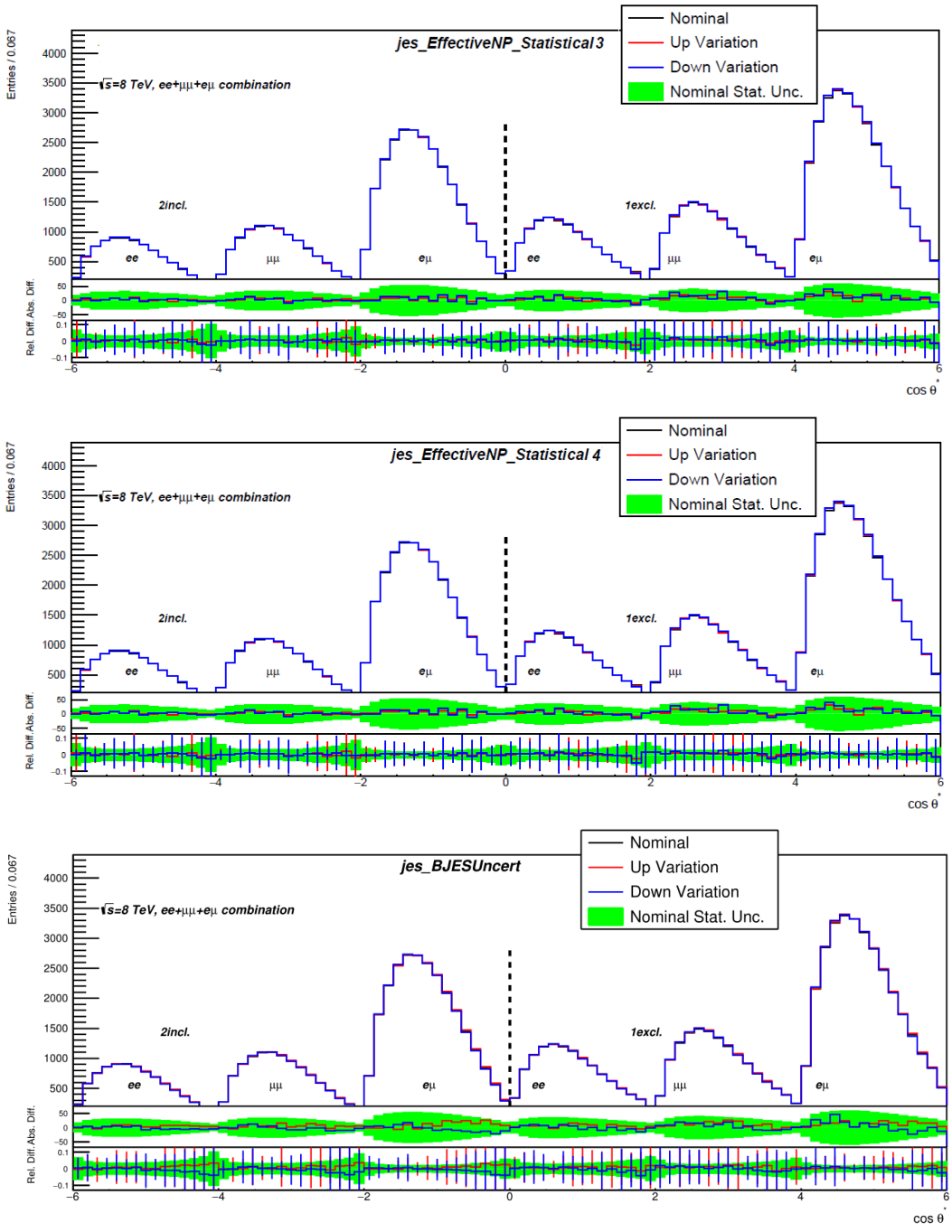

Figure C.11.: Generated pseudo-data for the ee, $\mu\mu$ and $e\mu$ combination for systematic variations and the nominal $t\bar{t}$ sample. The ratio plot shows the absolute and relative difference between the variations and the nominal sample in comparison to the statistical uncertainty of the nominal sample.

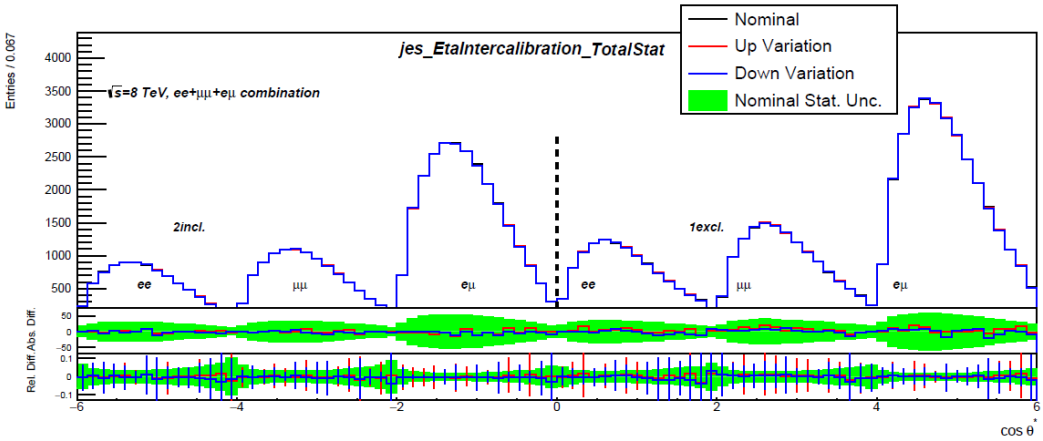

Figure C.12.: Generated pseudo-data for the ee, $\mu\mu$ and $e\mu$ combination for systematic variations and the nominal $t\bar{t}$ sample. The ratio plot shows the absolute and relative difference between the variations and the nominal sample in comparison to the statistical uncertainty of the nominal sample.

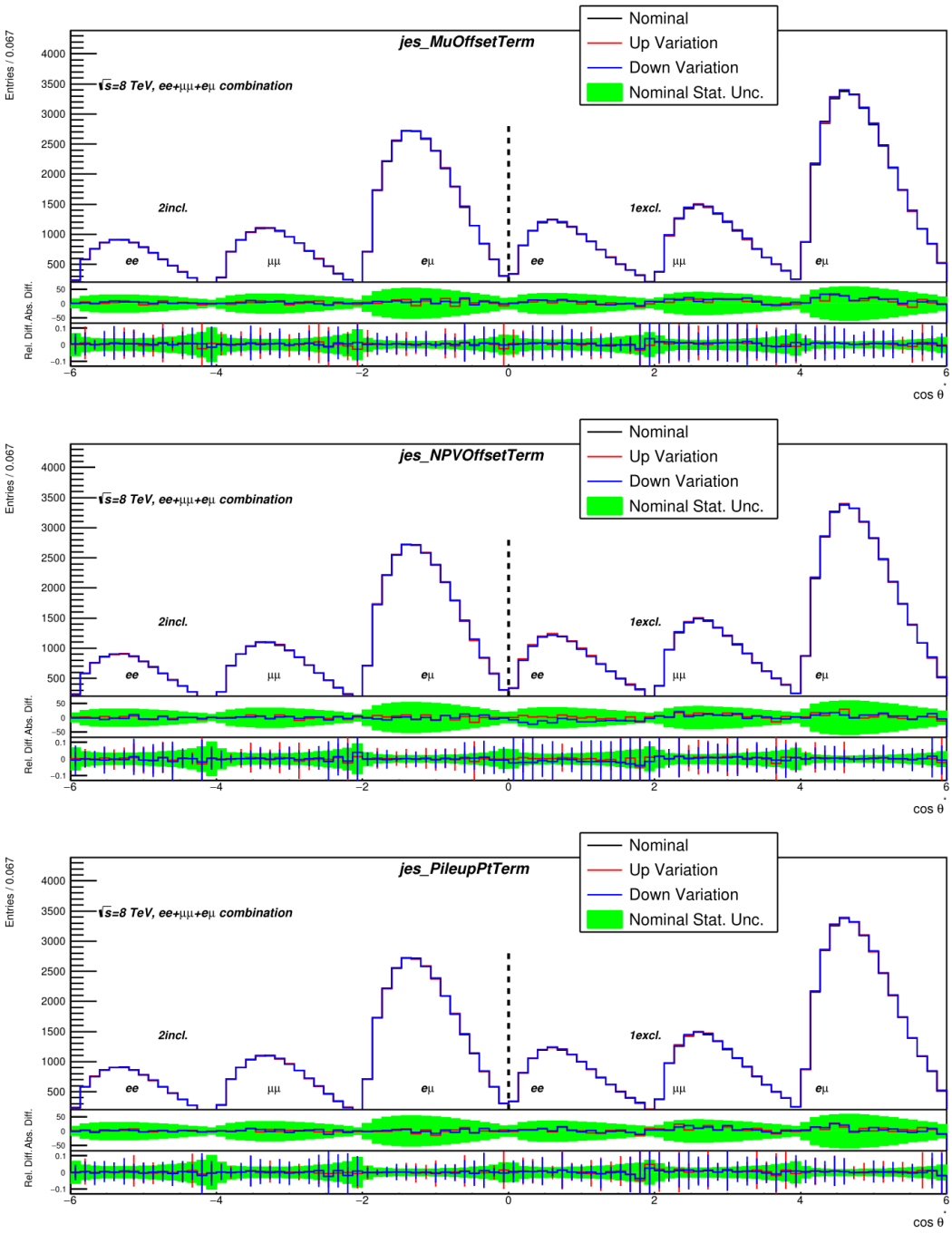

Figure C.13.: Generated pseudo-data for the ee, $\mu\mu$ and $e\mu$ combination for systematic variations and the nominal $t\bar{t}$ sample. The ratio plot shows the absolute and relative difference between the variations and the nominal sample in comparison to the statistical uncertainty of the nominal sample.

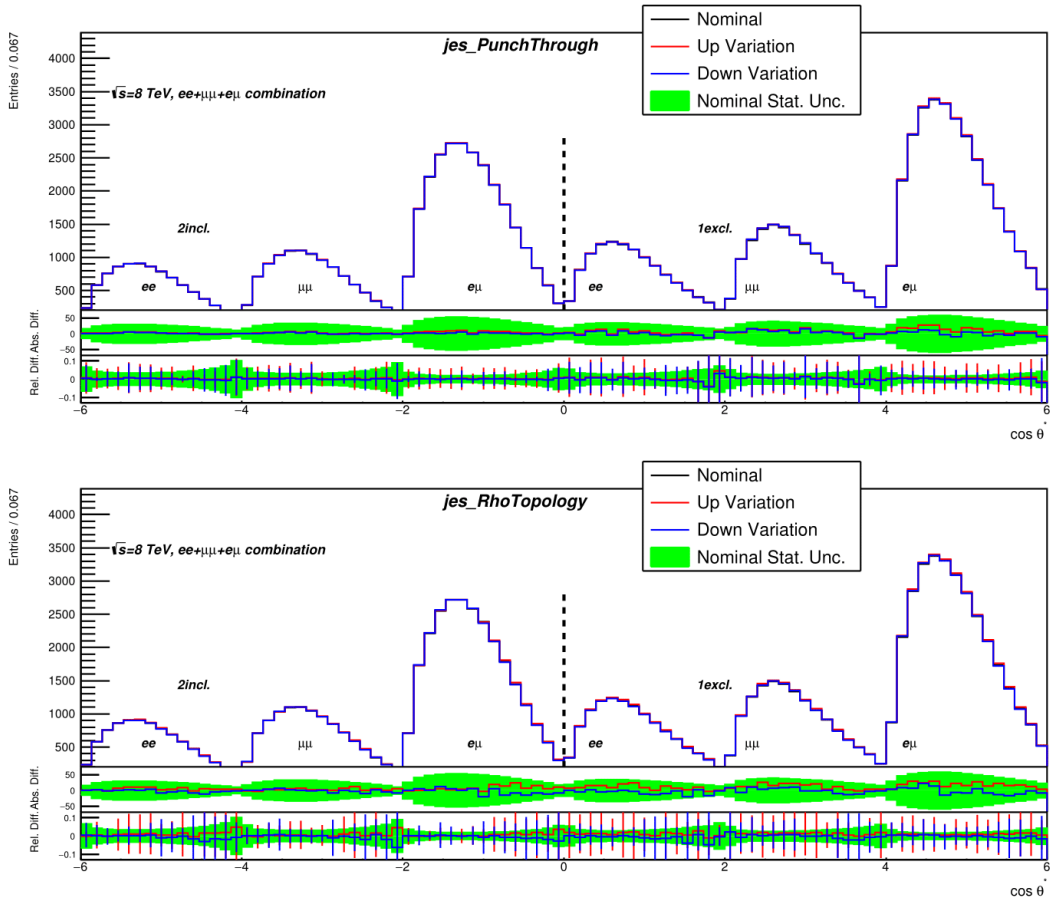

Figure C.14.: Generated pseudo-data for the ee, $\mu\mu$ and $e\mu$ combination for systematic variations and the nominal $t\bar{t}$ sample. The ratio plot shows the absolute and relative difference between the variations and the nominal sample in comparison to the statistical uncertainty of the nominal sample.

C.1.5. Jet Energy Resolution

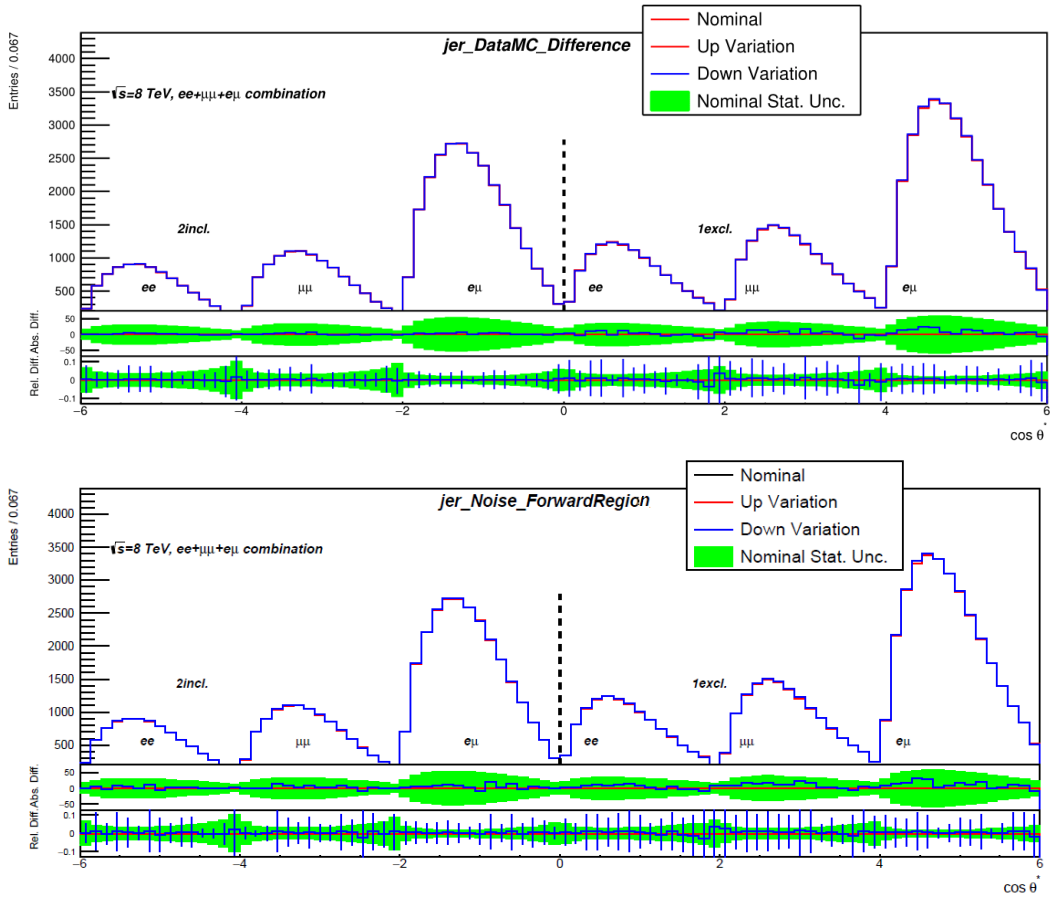

Figure C.15.: Generated pseudo-data for the ee, $\mu\mu$ and $e\mu$ combination for systematic variations and the nominal $t\bar{t}$ sample. The ratio plot shows the absolute and relative difference between the variations and the nominal sample in comparison to the statistical uncertainty of the nominal sample.

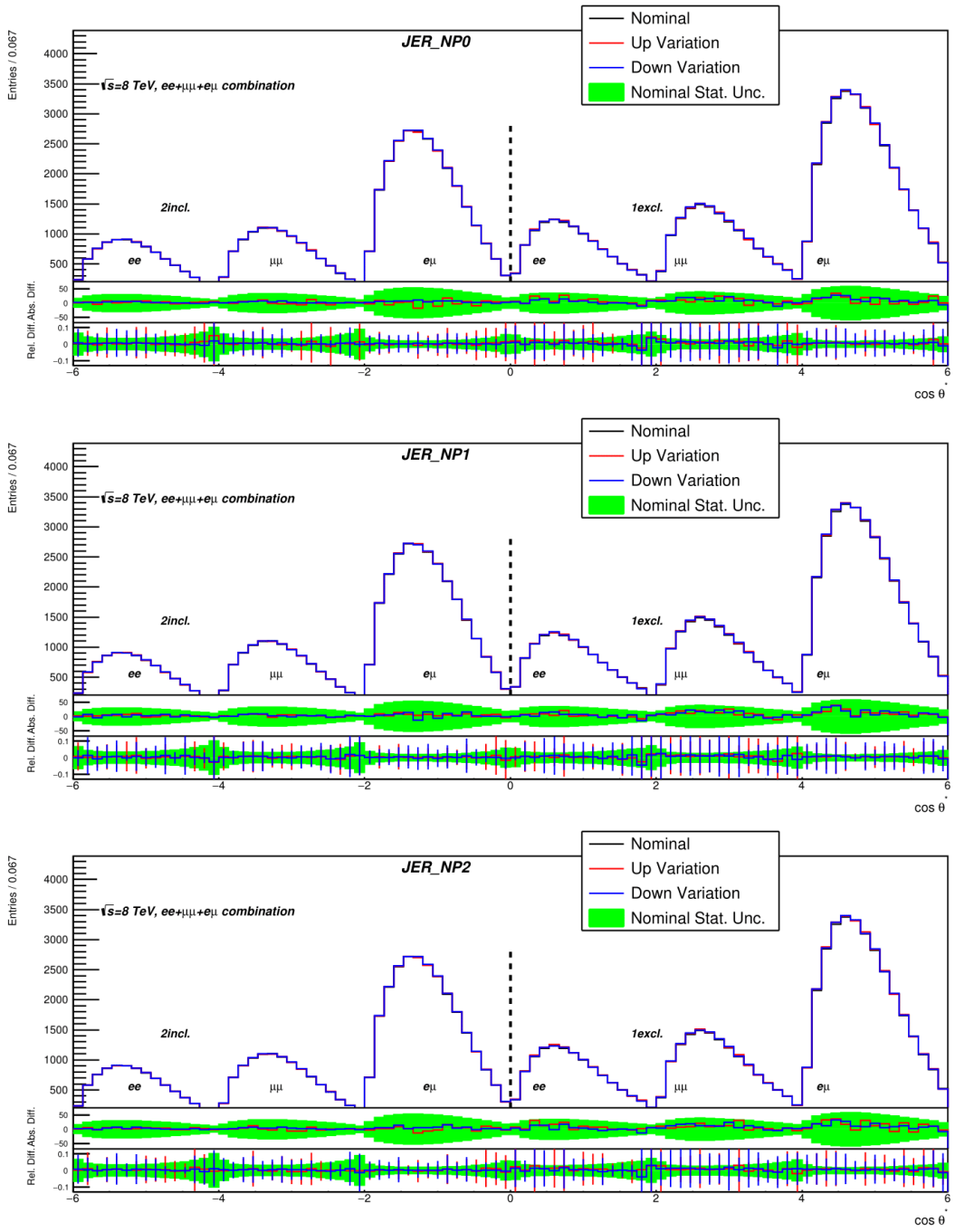

Figure C.16.: Generated pseudo-data for the ee, $\mu\mu$ and $e\mu$ combination for systematic variations and the nominal $t\bar{t}$ sample. The ratio plot shows the absolute and relative difference between the variations and the nominal sample in comparison to the statistical uncertainty of the nominal sample.

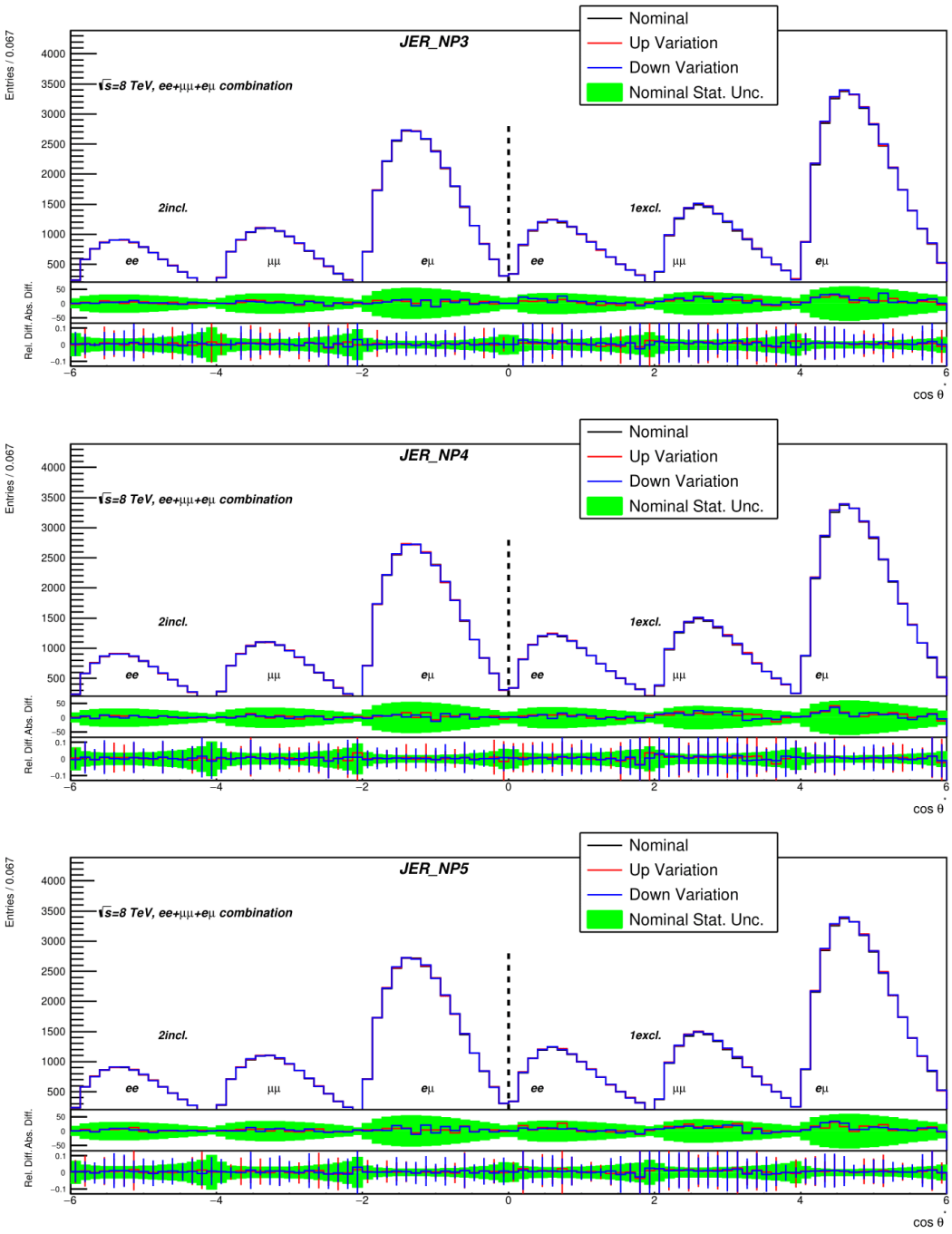

Figure C.17.: Generated pseudo-data for the ee, $\mu\mu$ and $e\mu$ combination for systematic variations and the nominal $t\bar{t}$ sample. The ratio plot shows the absolute and relative difference between the variations and the nominal sample in comparison to the statistical uncertainty of the nominal sample.

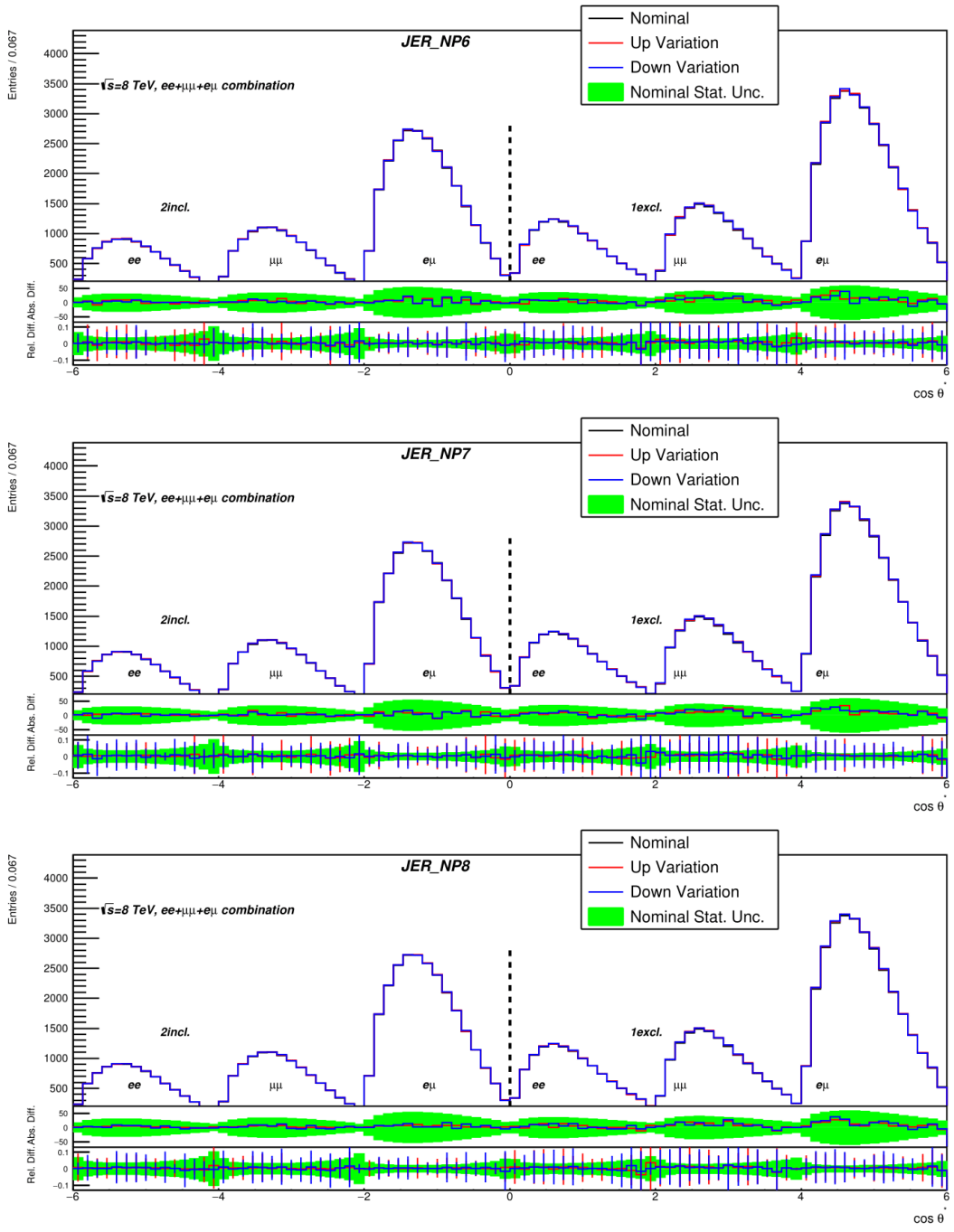

Figure C.18.: Generated pseudo-data for the ee, $\mu\mu$ and $e\mu$ combination for systematic variations and the nominal $t\bar{t}$ sample. The ratio plot shows the absolute and relative difference between the variations and the nominal sample in comparison to the statistical uncertainty of the nominal sample.

C.1.6. Heavy- and Light- Flavor Tagging

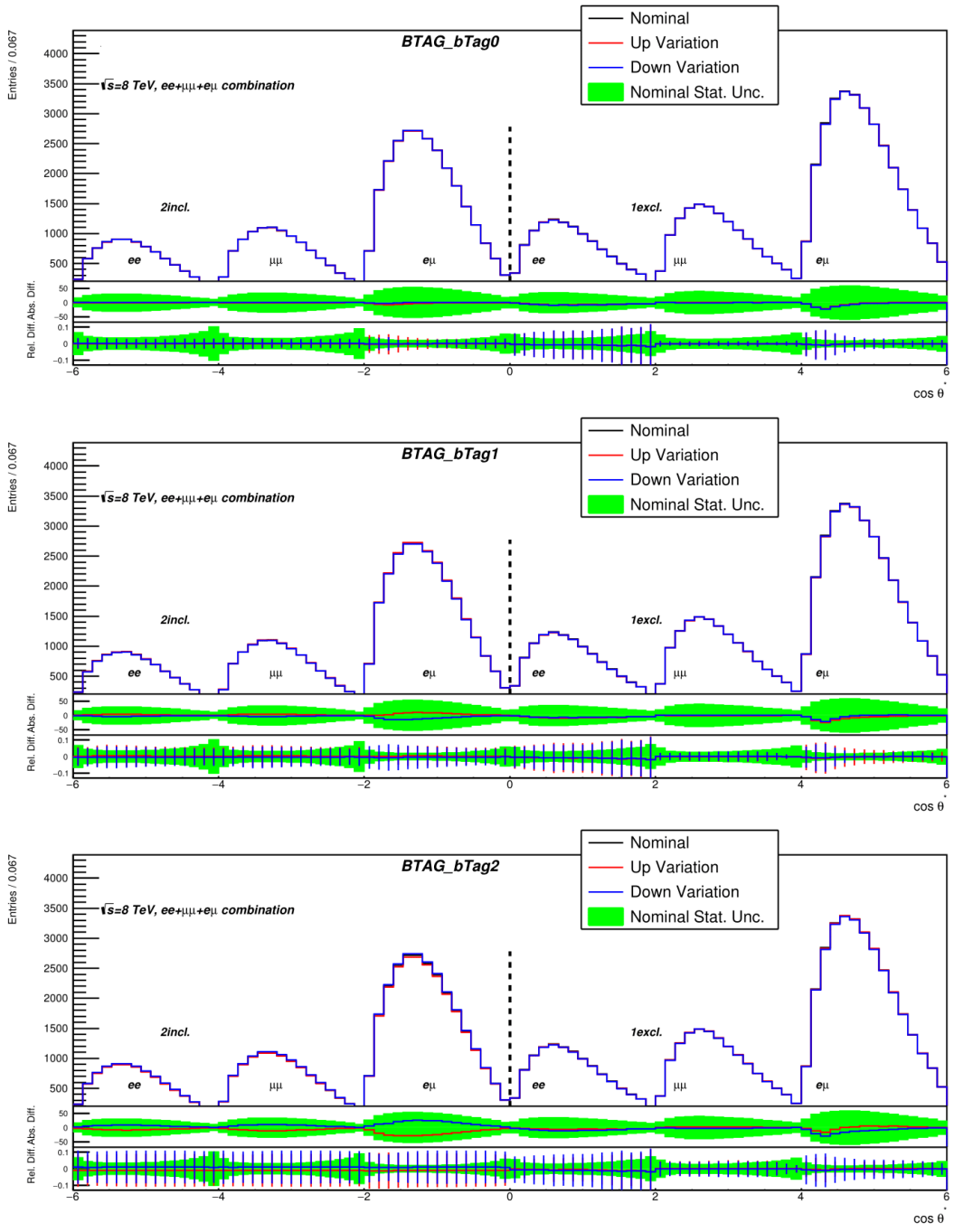

Figure C.19.: Generated pseudo-data for the ee, $\mu\mu$ and $e\mu$ combination for systematic variations and the nominal $t\bar{t}$ sample. The ratio plot shows the absolute and relative difference between the variations and the nominal sample in comparison to the statistical uncertainty of the nominal sample.

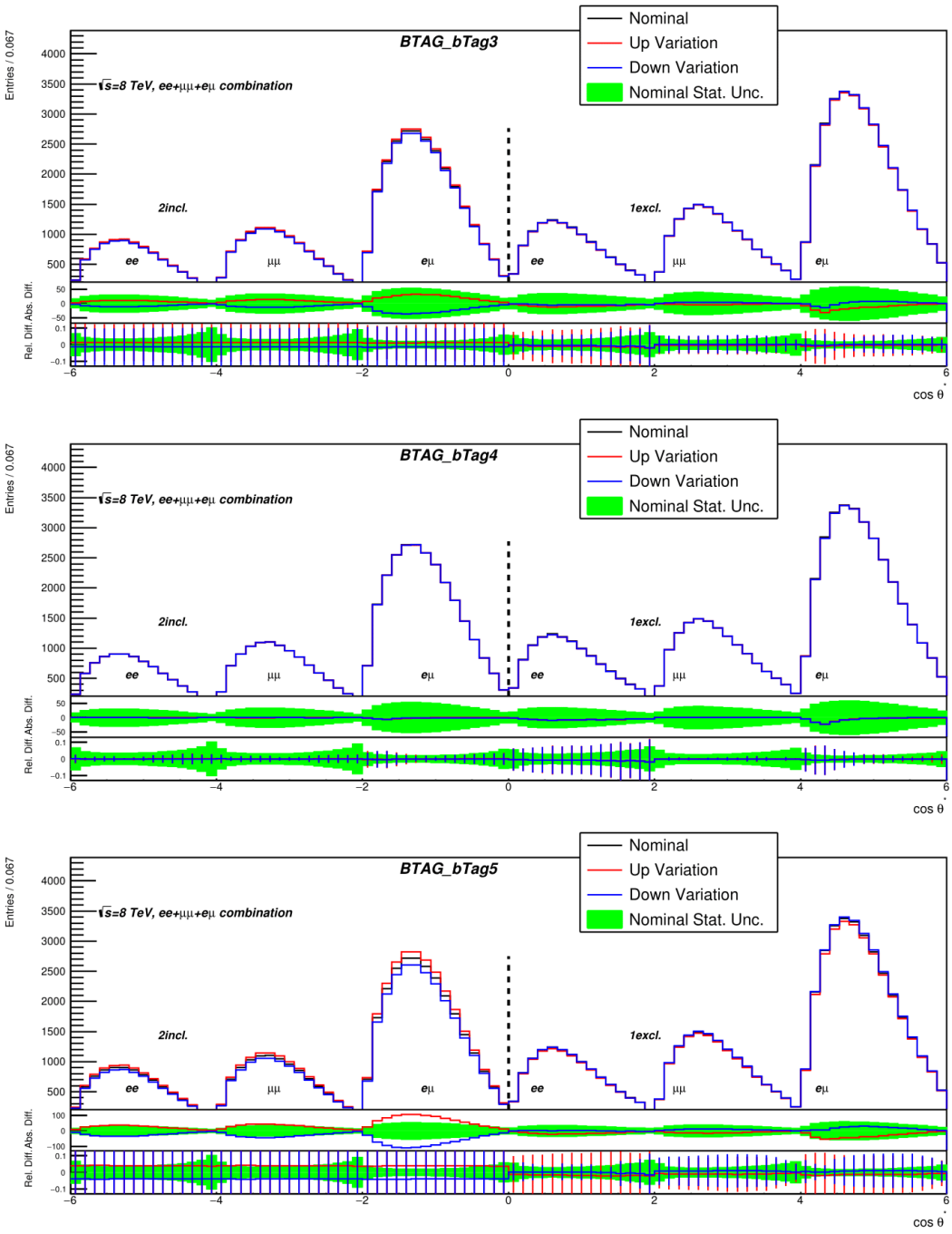

Figure C.20.: Generated pseudo-data for the ee, $\mu\mu$ and $e\mu$ combination for systematic variations and the nominal $t\bar{t}$ sample. The ratio plot shows the absolute and relative difference between the variations and the nominal sample in comparison to the statistical uncertainty of the nominal sample.

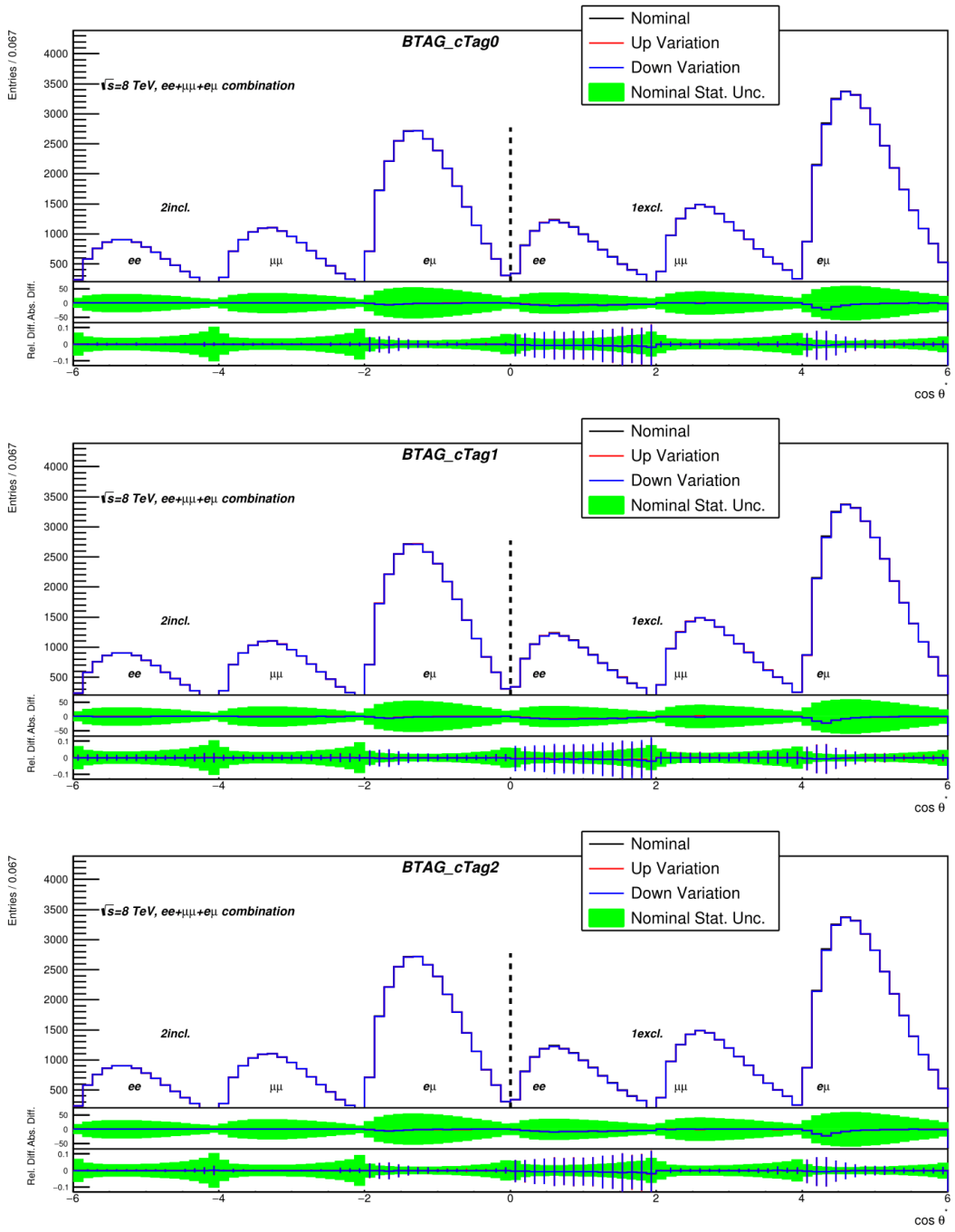

Figure C.21.: Generated pseudo-data for the ee, $\mu\mu$ and $e\mu$ combination for systematic variations and the nominal $t\bar{t}$ sample. The ratio plot shows the absolute and relative difference between the variations and the nominal sample in comparison to the statistical uncertainty of the nominal sample.

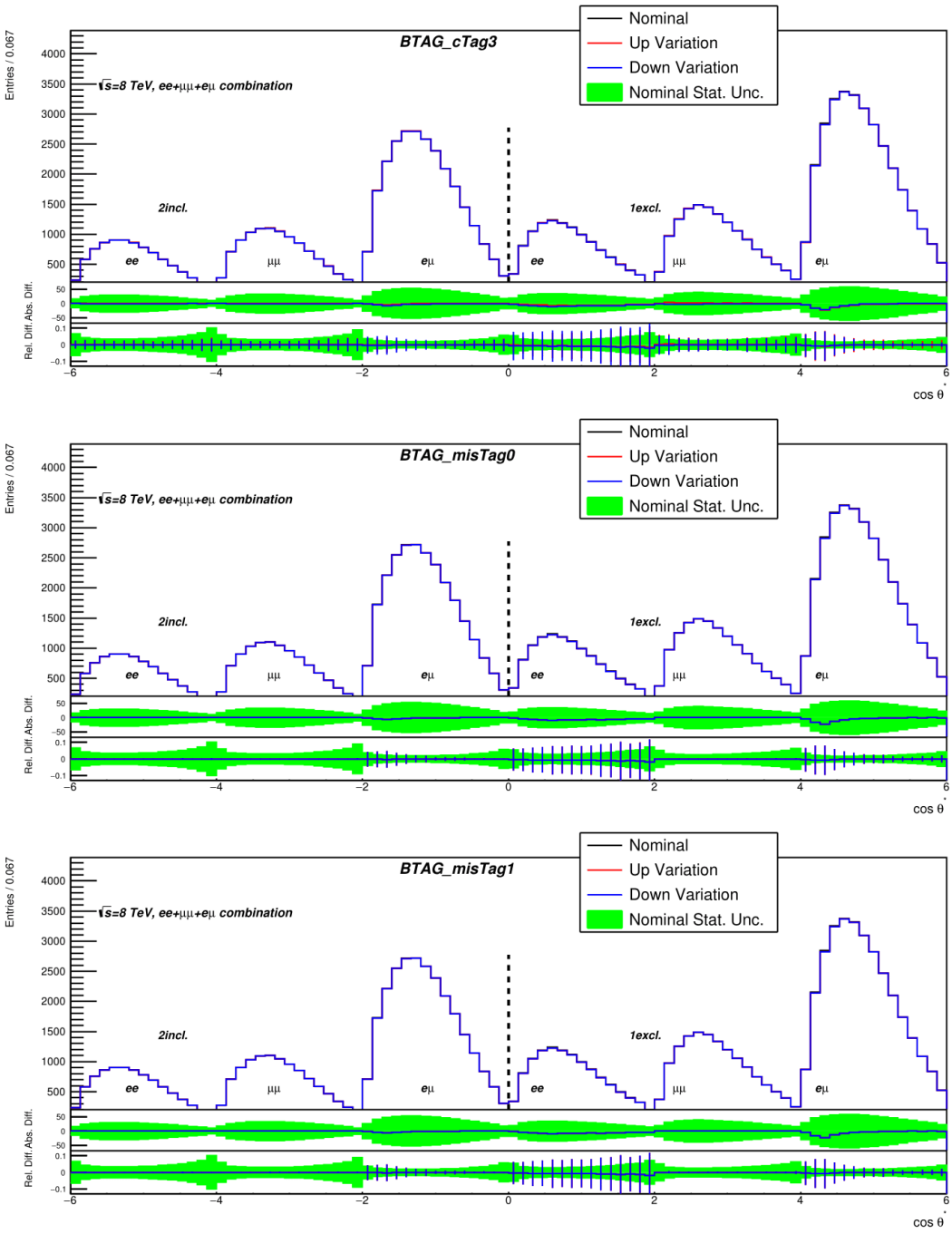

Figure C.22.: Generated pseudo-data for the ee, $\mu\mu$ and $e\mu$ combination for systematic variations and the nominal $t\bar{t}$ sample. The ratio plot shows the absolute and relative difference between the variations and the nominal sample in comparison to the statistical uncertainty of the nominal sample.

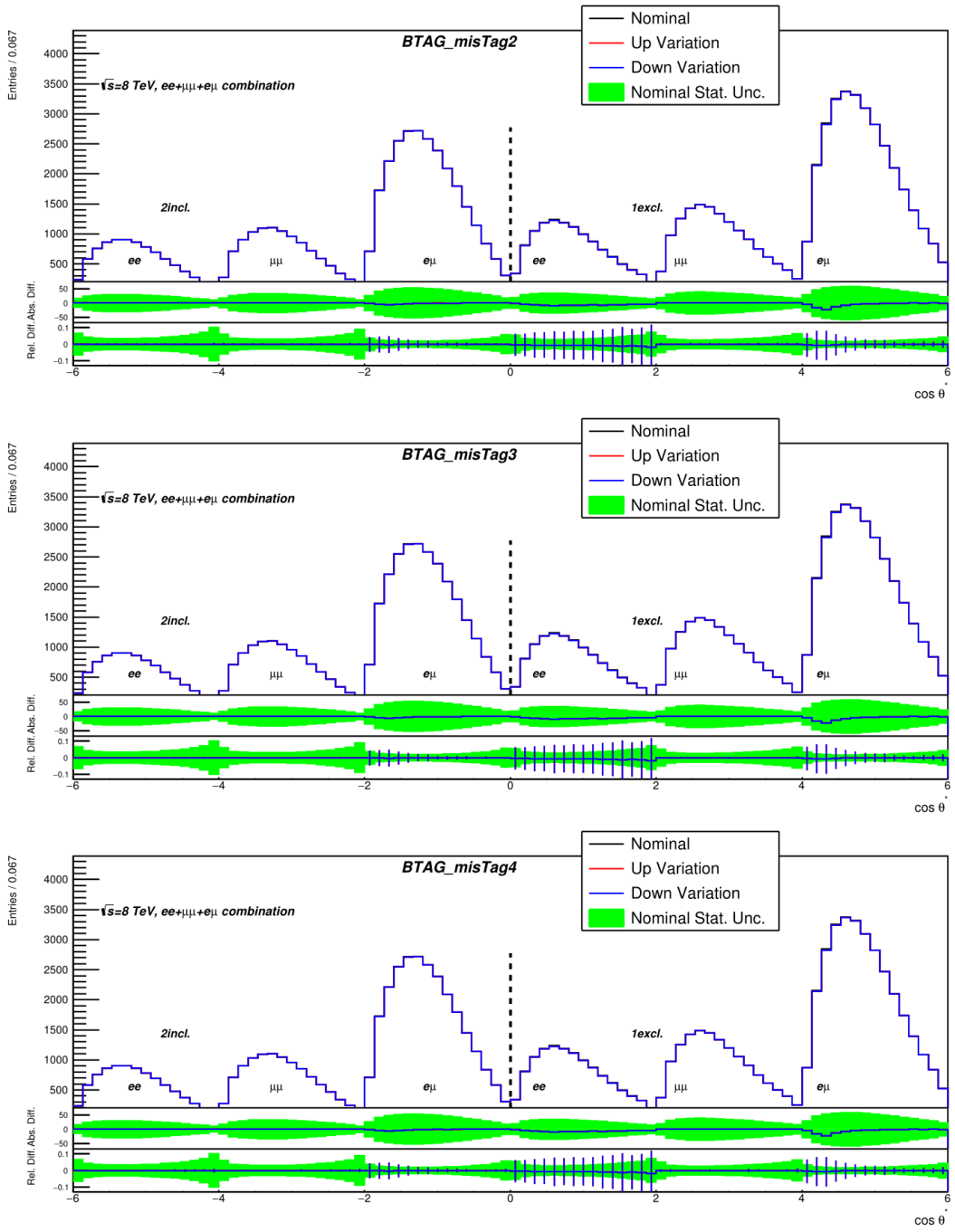

Figure C.23.: Generated pseudo-data for the ee, $\mu\mu$ and $e\mu$ combination for systematic variations and the nominal $t\bar{t}$ sample. The ratio plot shows the absolute and relative difference between the variations and the nominal sample in comparison to the statistical uncertainty of the nominal sample.

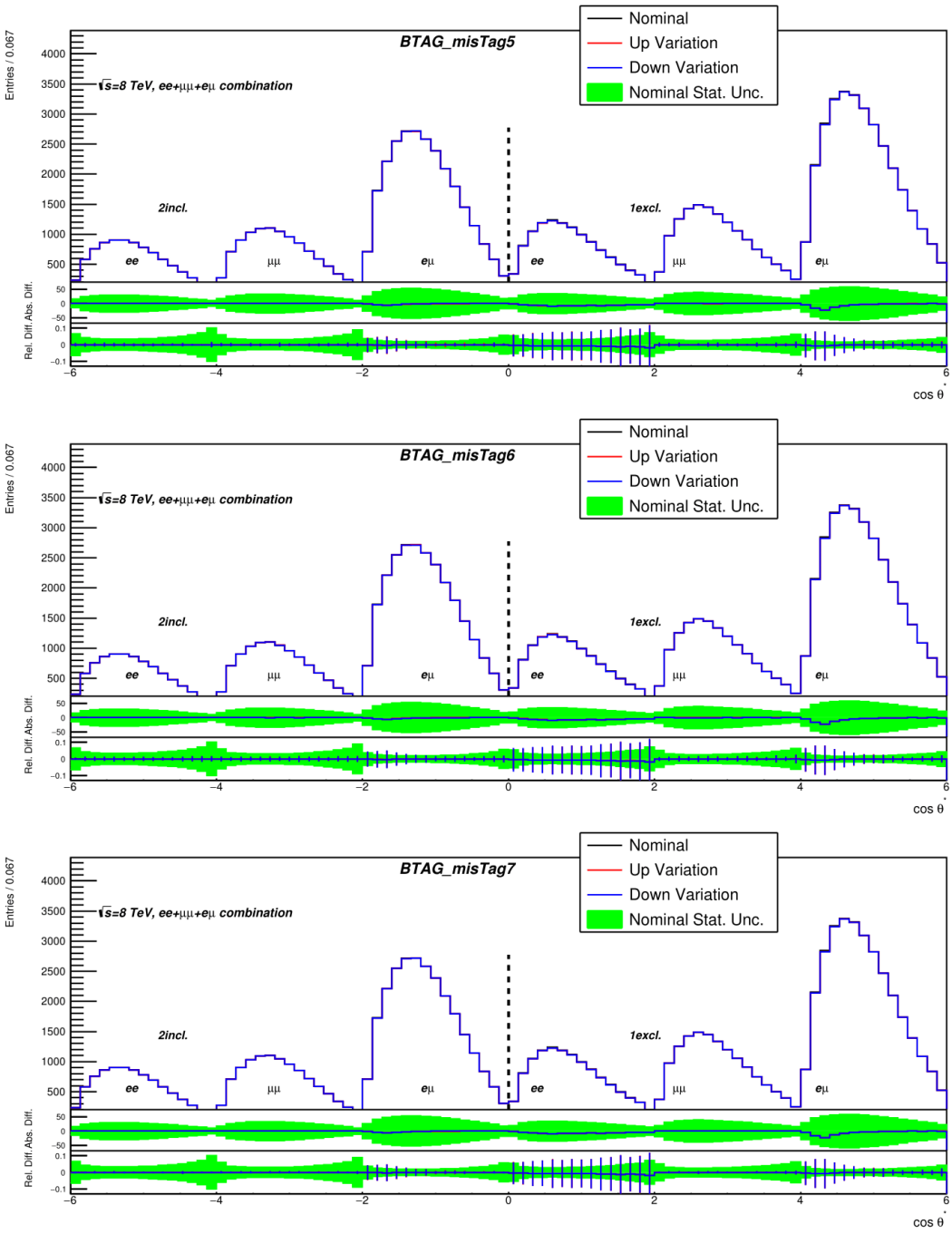

Figure C.24.: Generated pseudo-data for the ee, $\mu\mu$ and $e\mu$ combination for systematic variations and the nominal $t\bar{t}$ sample. The ratio plot shows the absolute and relative difference between the variations and the nominal sample in comparison to the statistical uncertainty of the nominal sample.

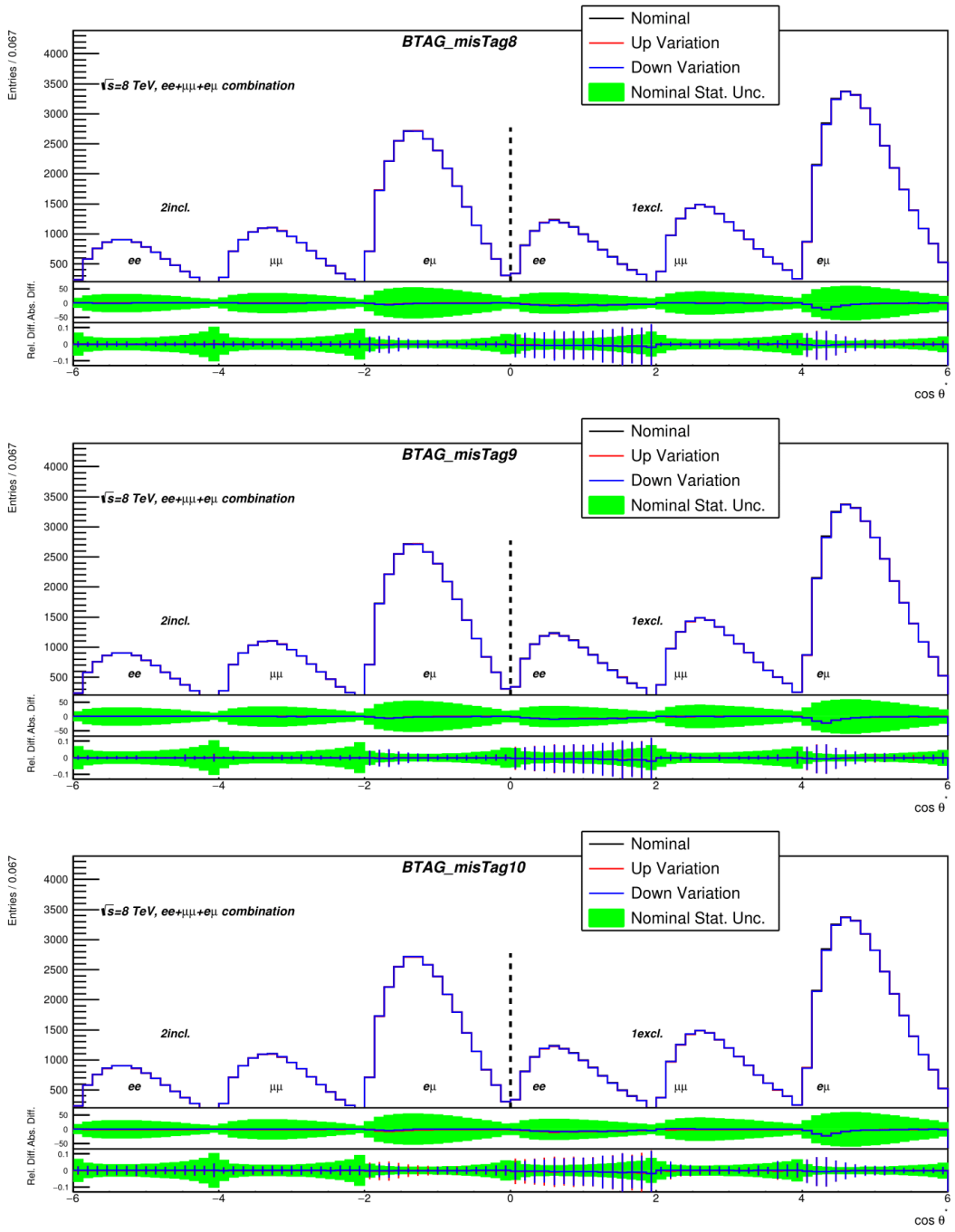

Figure C.25.: Generated pseudo-data for the ee, $\mu\mu$ and $e\mu$ combination for systematic variations and the nominal $t\bar{t}$ sample. The ratio plot shows the absolute and relative difference between the variations and the nominal sample in comparison to the statistical uncertainty of the nominal sample.

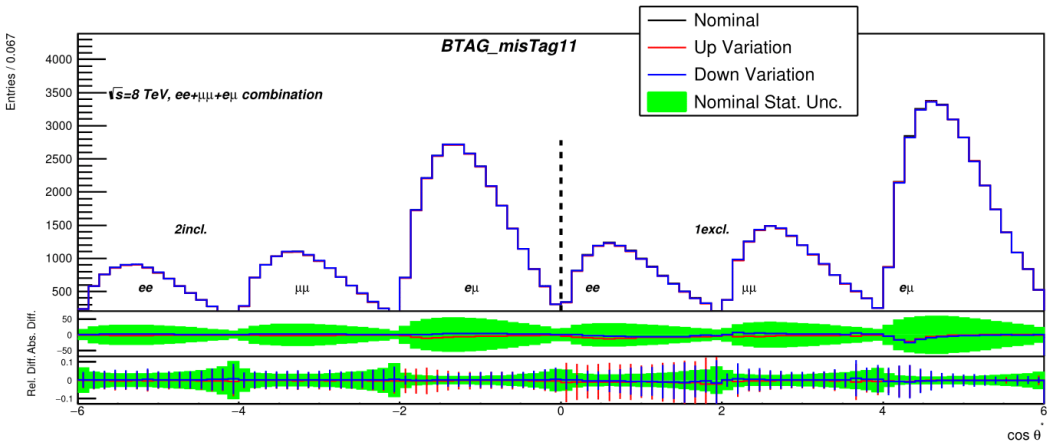

Figure C.26.: Generated pseudo-data for the ee, $\mu\mu$ and $e\mu$ combination for systematic variations and the nominal $t\bar{t}$ sample. The ratio plot shows the absolute and relative difference between the variations and the nominal sample in comparison to the statistical uncertainty of the nominal sample.

C.1.7. Missing Transverse Momentum

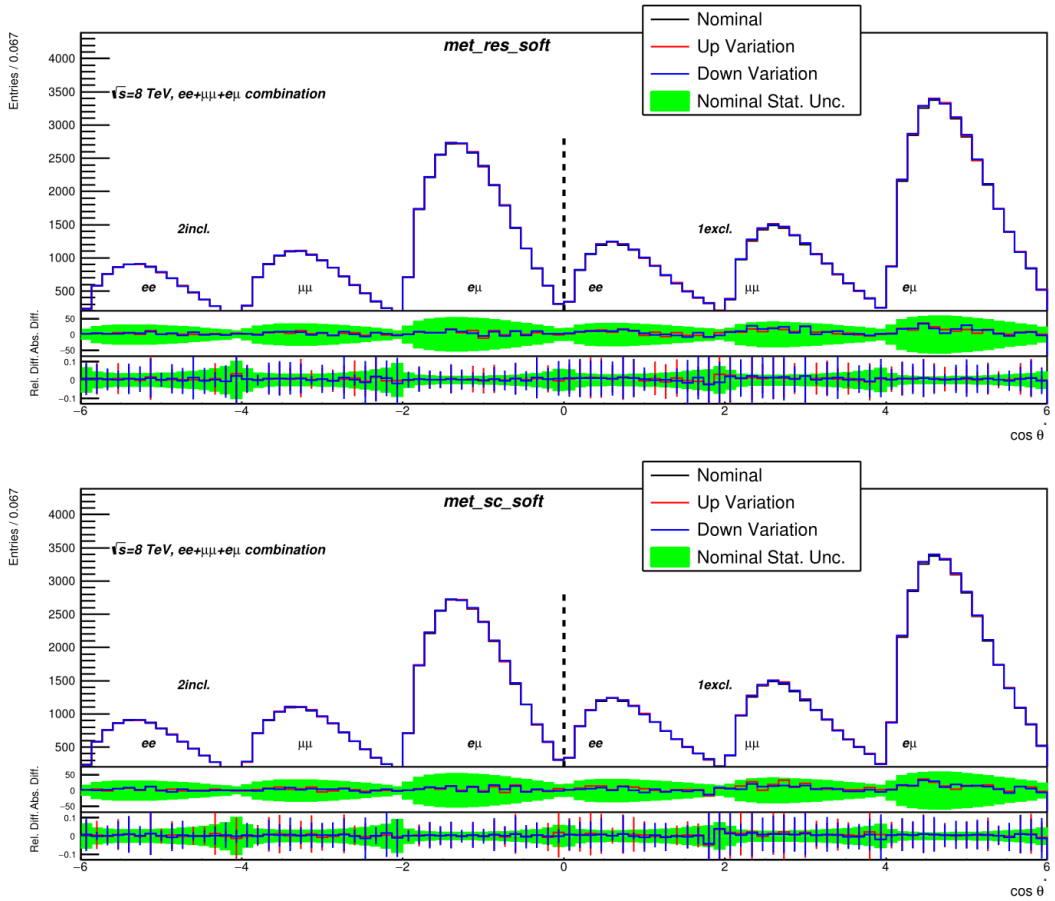

Figure C.27.: Generated pseudo-data for the ee, $\mu\mu$ and $e\mu$ combination for systematic variations and the nominal $t\bar{t}$ sample. The ratio plot shows the absolute and relative difference between the variations and the nominal sample in comparison to the statistical uncertainty of the nominal sample.

C.2. Modelling Systematics

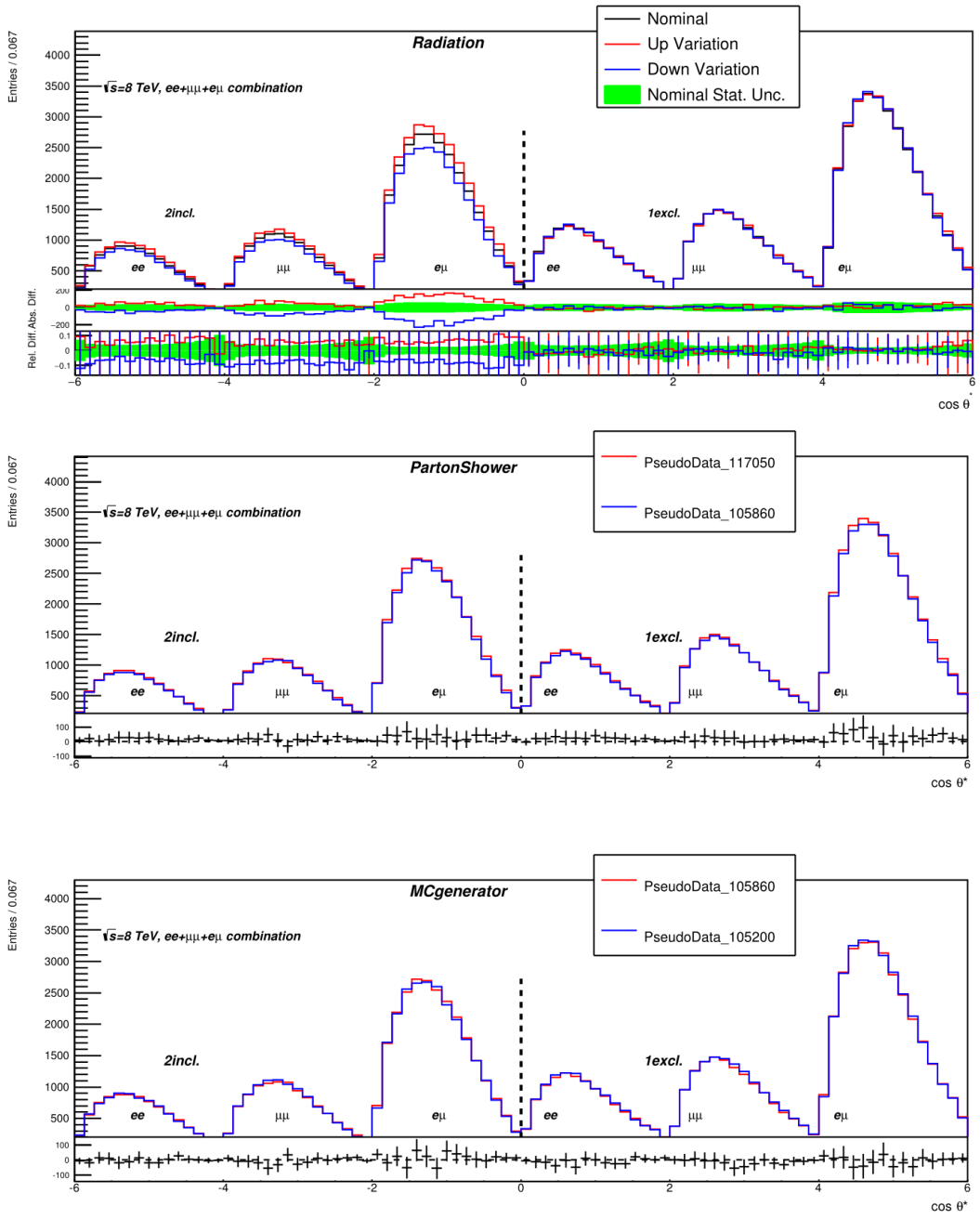

Figure C.28.: Generated pseudo-data for the ee, $\mu\mu$ and $e\mu$ combination for systematic variations and the nominal $t\bar{t}$ sample. The ratio plot shows the absolute and relative difference between the variations and the nominal sample in comparison to the statistical uncertainty of the nominal sample.

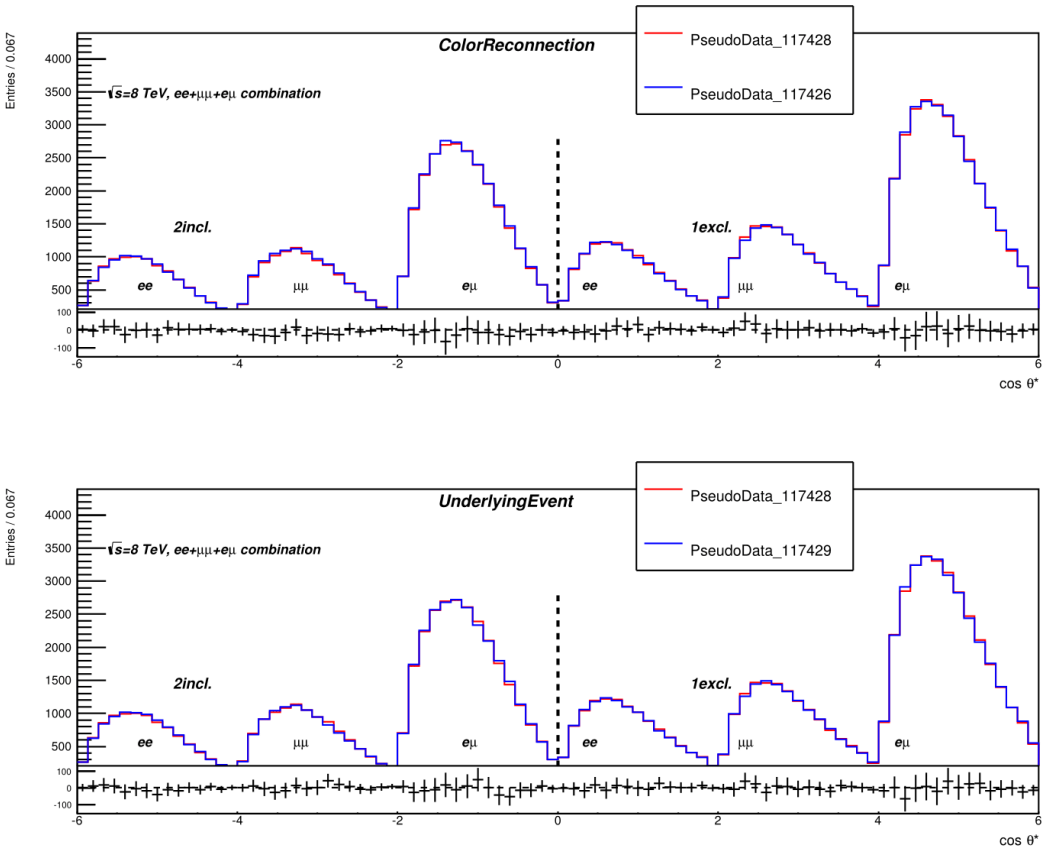

Figure C.29.: Generated pseudo-data for the ee, $\mu\mu$ and $e\mu$ combination for systematic variations and the nominal $t\bar{t}$ sample. The ratio plot shows the absolute and relative difference between the variations and the nominal sample in comparison to the statistical uncertainty of the nominal sample.

APPENDIX D

Systematic Table: Fraction Sum

This appendix contains tables showing the effect of all significant systematic variations evaluated after generating 5000 sets of pseudo-data for the two inclusive and combined one exclusive + two inclusive b-tag, $ee+\mu\mu+e\mu$ region, as well as the sum across helicity fractions for each variation. Event by event, the sum is identically zero, but fits over the Gaussian mean of the generated pseudo-experiments can differ slightly from this identity. Even so, any deviation should be small, and this behaviour is observed. The uncertainties are split into up and down variations where appropriate and categorised according to detector and modelling systematics.

$ee + \mu\mu + e\mu$ 2incl b-tag					
Systematic uncertainty	Up/Down	F_0	F_L	F_R	Sum
Modelling					
ME Generator		0.0116	-0.0041	-0.0079	-0.0001
Parton Shower		0.0148	-0.0050	-0.0099	¡0.0001
Radiation	radHi	-0.0014	0.0037	-0.0023	-0.0001
	radLo	-0.0068	0.0011	0.0057	<-0.0001
Reconstructed Objects					
BTAG_bTagVar_0	up	-0.0011	0.0009	0.0001	-0.0001
	down	-0.0009	0.0006	0.0002	-0.0001
BTAG_bTagVar_1	up	-0.0017	0.0009	0.0007	<-0.0001
	down	-0.0001	0.0004	-0.0005	-0.0001
BTAG_bTagVar_2	up	-0.0003	0.0002	<-0.0001	-0.0001
	down	-0.0014	0.0011	0.0002	-0.0001
BTAG_bTagVar_3	up	-0.0004	0.0007	-0.0003	-0.0001
	down	-0.001	0.0007	0.0003	<-0.0001
BTAG_bTagVar_4	up	-0.0008	0.0008	-0.0002	-0.0002
	down	-0.0007	0.0004	0.0001	-0.0002
BTAG_bTagVar_5	up	-0.0007	0.0002	0.0004	-0.0002
	down	-0.0011	0.0011	-0.0002	-0.0002
BTAG_cTagVar_0	up	-0.0011	0.0009	0.0001	-0.0001
	down	-0.0008	0.0008	<-0.0001	<-0.0001
BTAG_cTagVar_1	up	-0.0009	0.0006	0.0001	-0.0002
	down	-0.0007	0.0005	<-0.0001	-0.0002
BTAG_cTagVar_2	up	-0.0011	0.0006	0.0002	-0.0003
	down	-0.001	0.0008	0.0001	-0.0001
BTAG_cTagVar_3	up	-0.0002	0.0002	-0.0002	-0.0002
	down	-0.0015	0.0011	0.0003	-0.0001
BTAG_misTagVar_0	up	-0.0009	0.0007	0.0001	-0.0001
	down	-0.001	0.0007	0.0002	-0.0001
BTAG_misTagVar_1	up	-0.001	0.0007	0.0002	-0.0001
	down	-0.0009	0.0008	0.0002	0.0001
BTAG_misTagVar_2	up	-0.0011	0.0008	0.0002	<-0.0001
	down	-0.0008	0.0007	0.0001	-0.0001
BTAG_misTagVar_3	up	-0.001	0.0007	0.0002	-0.0001
	down	-0.0008	0.0006	0.0001	-0.0001
BTAG_misTagVar_4	up	-0.0006	0.0006	<-0.0001	<-0.0001
	down	-0.001	0.0009	0.0001	<-0.0001
BTAG_misTagVar_5	up	-0.0009	0.0007	0.0001	-0.0002
	down	-0.001	0.0008	0.0001	<-0.0001
BTAG_misTagVar_6	up	-0.0006	0.0006	<-0.0001	-0.0001
	down	-0.0009	0.0007	0.0001	-0.0001
BTAG_misTagVar_7	up	-0.0009	0.0007	0.0002	<-0.0001
	down	-0.001	0.0009	0.0001	<-0.0001
BTAG_misTagVar_8	up	-0.0011	0.0008	0.0002	-0.0001
	down	-0.0013	0.001	0.0002	<-0.0001
BTAG_misTagVar_9	up	-0.0009	0.0008	<-0.0001	<-0.0001
	down	-0.0008	0.0006	0.0001	-0.0001
BTAG_misTagVar_10	up	-0.0009	0.0007	0.0001	-0.0001
	down	-0.0003	0.0004	-0.0001	<-0.0001
BTAG_misTagVar_11	up	-0.0015	0.001	0.0004	<-0.0001
	down	-0.0002	0.0005	-0.0002	<-0.0001
jes_Modelling1	up	0.0023	0.0035	-0.006	-0.0002
	down	-0.0076	-0.002	0.0098	0.0001
jvf	up	-0.0028	0.0014	0.0014	<-0.0001
	down	-0.0004	-0.0003	0.0006	-0.0001

$ee + \mu\mu + e\mu$ 1excl+2incl b-tag					
Systematic uncertainty	Up/Down	F_0	F_L	F_R	Sum
Modelling					
ME Generator		0.0157	-0.0058	-0.0101	-0.0002
Parton Shower		0.0206	-0.0061	-0.0146	¡0.0001
Radiation	radHi	0.023	-0.0056	-0.0172	0.0001
	radLo	-0.0248	0.0083	0.0165	<-0.0001
Reconstructed Objects					
BTAG_bTagVar_0_6channel.root	up	-0.0015	0.0012	0.0003	0.0001
	down	-0.0006	0.0008	-0.0001	<-0.0001
BTAG_bTagVar_1_6channel.root	up	-0.0009	0.0008	0.0002	<-0.0001
	down	-0.0015	0.0014	0.0002	<-0.0001
BTAG_bTagVar_2_6channel.root	up	-0.0037	0.0022	0.0014	-0.0001
	down	0.0011	<-0.0001	-0.001	0.0001
BTAG_bTagVar_3_6channel.root	up	0.0025	-0.0008	-0.0018	-0.0001
	down	-0.0047	0.0028	0.0019	<-0.0001
BTAG_bTagVar_4_6channel.root	up	-0.0014	0.0013	<-0.0001	-0.0001
	down	-0.0013	0.001	0.0005	0.0001
BTAG_bTagVar_5_6channel.root	up	0.0097	-0.0048	-0.0049	<-0.0001
	down	-0.012	0.0069	0.005	<-0.0001
BTAG_cTagVar_0_6channel.root	up	-0.0013	0.0012	0.0003	0.0001
	down	-0.0015	0.0012	0.0002	<-0.0001
BTAG_cTagVar_1_6channel.root	up	-0.001	0.001	<-0.0001	0.0001
	down	-0.0014	0.0011	0.0003	<-0.0001
BTAG_cTagVar_2_6channel.root	up	-0.0011	0.001	0.0003	0.0001
	down	-0.0012	0.0011	0.0001	<-0.0001
BTAG_cTagVar_3_6channel.root	up	-0.0009	0.0009	0.0001	<-0.0001
	down	-0.0018	0.0014	0.0005	0.0002
BTAG_misTagVar_0_6channel.root	up	-0.0014	0.0012	0.0002	0.0001
	down	-0.0014	0.0013	0.0002	<-0.0001
BTAG_misTagVar_1_6channel.root	up	-0.0013	0.0012	0.0001	<-0.0001
	down	-0.0015	0.0013	0.0002	-0.0001
BTAG_misTagVar_2_6channel.root	up	-0.0012	0.0011	0.0002	0.0001
	down	-0.0014	0.0013	0.0001	0.0001
BTAG_misTagVar_3_6channel.root	up	-0.0015	0.0014	0.0001	<-0.0001
	down	-0.0015	0.0013	0.0002	<-0.0001
BTAG_misTagVar_4_6channel.root	up	-0.0014	0.0012	0.0003	0.0001
	down	-0.0013	0.0011	0.0002	0.0001
BTAG_misTagVar_5_6channel.root	up	-0.0013	0.0011	0.0002	0.0001
	down	-0.0012	0.0011	0.0002	0.0001
BTAG_misTagVar_6_6channel.root	up	-0.0012	0.0011	0.0002	0.0001
	down	-0.0015	0.0012	0.0003	<-0.0001
BTAG_misTagVar_7_6channel.root	up	-0.0009	0.0009	<-0.0001	<-0.0001
	down	-0.0013	0.0011	0.0003	0.0001
BTAG_misTagVar_8_6channel.root	up	-0.0011	0.001	0.0001	<-0.0001
	down	-0.0014	0.0011	0.0003	<-0.0001
BTAG_misTagVar_9_6channel.root	up	-0.0012	0.001	0.0001	-0.0001
	down	-0.0014	0.0012	0.0002	0.0001
BTAG_misTagVar_10_6channel.root	up	-0.0014	0.0014	0.0002	0.0002
	down	-0.0009	0.0008	-0.0001	-0.0001
BTAG_misTagVar_11_6channel.root	up	-0.0031	0.0021	0.0011	0.0001
	down	0.0004	0.0001	-0.0007	-0.0001
jes_Modelling1	up	0.0020	0.0030	-0.0049	-0.0001
	down	-0.0080	-0.0035	0.0115	<-0.0001
jvf	up	-0.0121	0.0047	0.0074	<-0.0001
	down	-0.0113	0.0025	0.0088	<–0.0001

List of Figures

List of Tables